Deployable Synthetic Aperture Radar Reflector

Ö. Soykasap and S. Pellegrino

CUED/D-STRUCT/TR209

Department of Engineering

University of Cambridge

Release date: 13 January, 2004.

Summary

This report presents a new deployable structure concept for a low altitude L or P-Band Synthetic Aperture Radar (SAR) satellite. The structure consists of four cylindrical surfaces formed from thin sheets of carbon-fibre-reinforced-plastic (CFRP) connected by flexible hinges along the edges. The key to forming a cylindrical surface with any required shape is in the cutting/joining profile for the sheets. For a parabolic cylinder, this profile can be found analytically, given the focal length, aperture distance, and offset distance of the reflector.

The structure is folded by first collapsing it essentially flat and then Z-folding it into a compact package. At full scale the reflective surface will be 7.9 m long by 3.2 m wide, and it has been estimated that the whole packaged structure would fit in an envelope of 3.2 m by 1.6 m by 0.3 m. The last dimension depends on the minimum bend radius of CFRP thin sheets, which is estimated theoretically and also measured experimentally. The performance of the connections between different sheets, made with woven-glass tape, has been determined experimentally.

An overall design for a full size reflector is presented, sized for optimal structural performance using the finite element software ABAQUS, and demonstrated by designing, constructing and testing a half-scale high-fidelity demonstrator.

Immediately after construction of this demonstrator a surface error of 3.8 mm RMS was measured; this value improved to 3.4 mm by removing the least accurate 25%of the surface area. The surface error increased to 5.1 mm after folding and deployment, but again improved to 3.3 mm by ignoring 25% of the area.

The typical mass achievable with this concept is 1.3 kg/m^2 of antenna, which represents a saving of the order of two-and-half times on the previous state of the art.

Patent applications on this invention have been filed jointly by EADS Astrium and Cambridge University.

Contents

List of Figures

Chapter 1

Introduction

1.1 Background

The study presented in this report is part of an ongoing collaboration between the Deployable Structures Laboratory at Cambridge University and EADS-Astrium, whose general aim is the development of low-cost technologies for lightweight deployable structures. Some of the technologies that underlie the present study, which were developed at earlier stages of this collaboration, are presented in Pellegrino et al. (2000).

This report presents a new deployable structure concept for a low altitude Synthetic Aperture Radar (SAR) satellite. The satellite is designed to perform low-cost Earth observation missions including land hazards, agriculture, forestry, geology, maritime and infrastructure.

Prior to this study, EADS-Astrium performed satellite/launch vehicle trade-offs (Howard, 2001). The main requirements for the baseline launch vehicle were low cost with good flight heritage and at least one independent backup. Among several candidate launch vehicles, Rockot was chosen as the baseline along with the Vega launcher as a backup. The satellite configuration is shown in Figure 1.1; note the large main reflector surface which is required for this mission. A more detailed view of the flight configuration of the satellite, in one of its viewing modes, is shown in Figure 1.2. The main reflector has an aperture of (6.5×3.2 m^2); the surface itself forms a 3.2 m wide offset parabolic cylinder with arc-length of 7.888 m. This structure needs to be stowed for launch.

The reflector system comprises three functional elements: launch restraint system, supporting structure, and deployable reflector. This report is concerned with only one of these functional elements, namely the reflector structure.

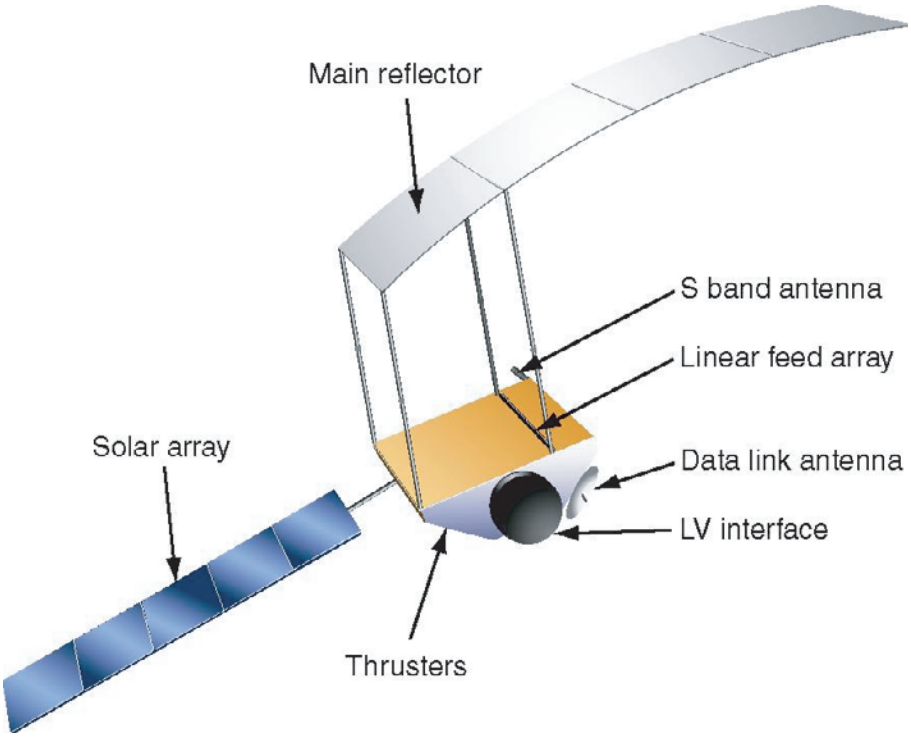

Figure 1.1: Baseline satellite configuration, from Howard (2001).

1.2 Requirements

The design requirements for the offset reflector (Canty, 2002) are summarized as follows:

- Mass: Total mass of reflector shall be less than 108.5 kg.
- Stowed condition: The complete system shall fit within the maximum envelope available in the Rockot launcher, i.e. the shaded area in Figure 1.3. The first natural frequency of the reflector system to be > 40 Hz when stowed.
- Deployment: The reflector system shall deploy in two stages: Stage 1, deployment of the support structure, and Stage 2, deployment of the reflector. After deployment of the support structure, the reflector retention system is released, thus initiating the stage 2 deployment, which results in the deployment of the complete reflector. The maximum time for the deployment of stage 2 is 300 s. Deployment shall not damage the reflector itself or the spacecraft.
- Deployed condition: The projected reflective area shall be at least 6.5×3.2 m^2. The deployed reflector shape shall conform to the parabolic shape shown in Figure 1.4. The maximum permitted deviation from this parabolic shape, due to all error sources —

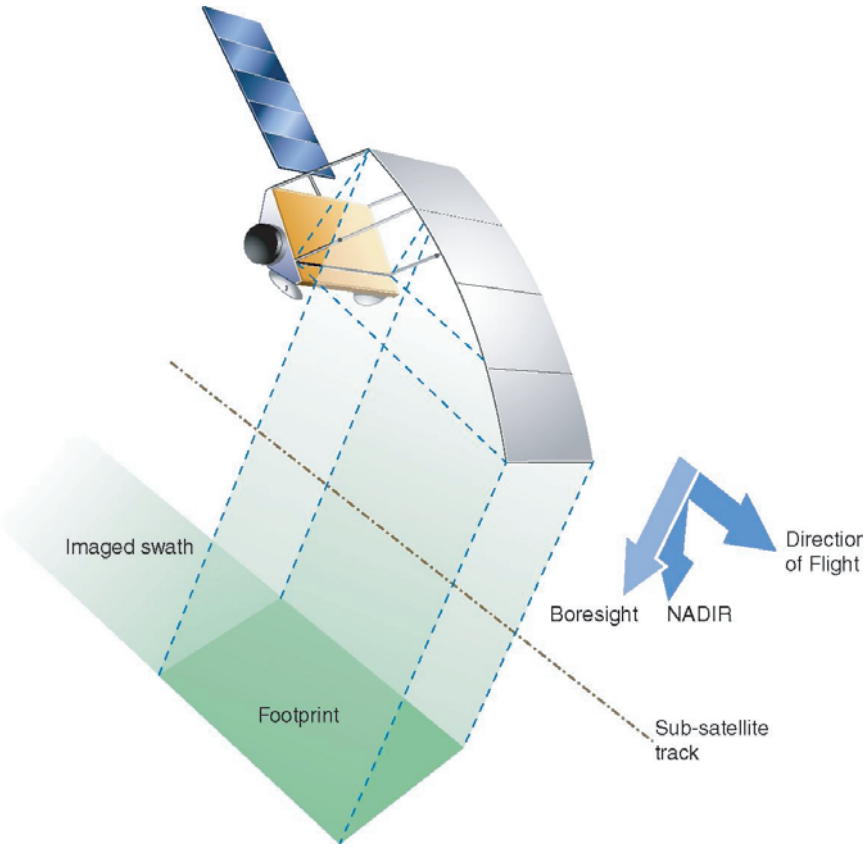

Figure 1.2: Flight configuration, from Howard (2001).

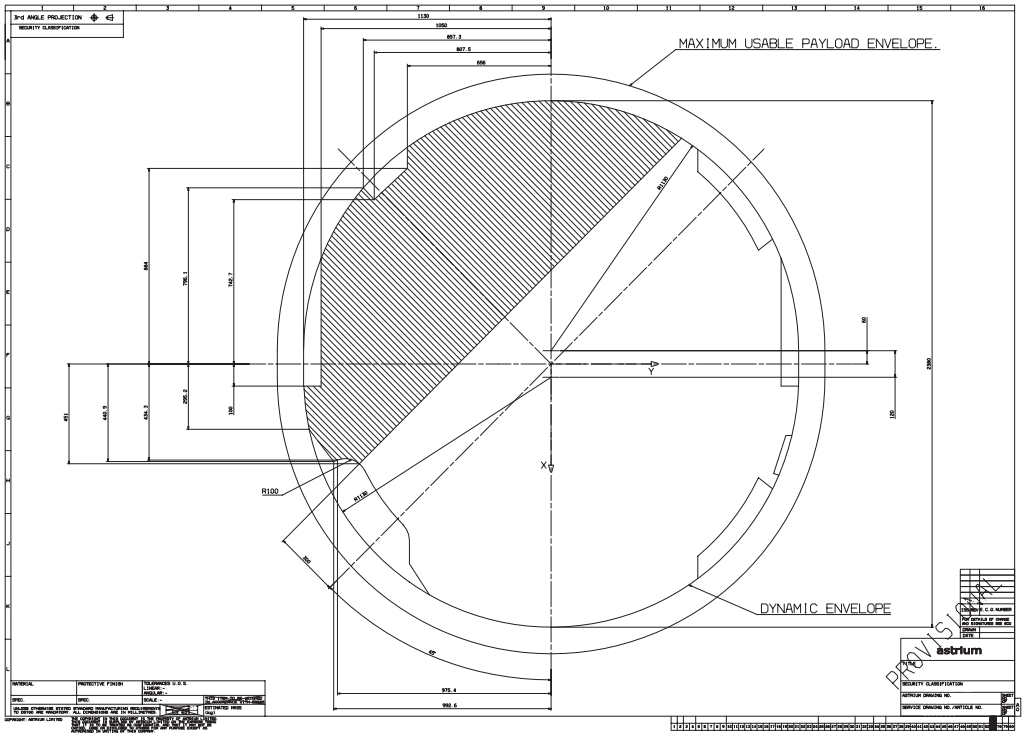

Figure 1.3: Stowed envelope of the deployable reflector

such as manufacturing, deployment, repeatability, reflector surface deformations, thermal distortions— shall be 6 mm. The first natural frequency of the complete reflector system shall be greater than 0.4 Hz (target) in the deployed configuration, although 0.1 Hz may be acceptable.

1.3 Scope and Aims

The original aims of this study were to design, construct and test a physical demonstrator of a deployable reflector structure. Specifically, an outline design of the full-scale flight structure, and the detailed design and manufacture of a half-scale demonstrator were to be produced. The tests were to include measurements of the stiffness and surface accuracy of the demonstrator. A novel concept for this structure was invented during the first part of the study, and so it became necessary to prove this new concept by manufacturing additional scaled models.

The proposed deployable reflector concept is a “hollow solid” that comprises curved surfaces formed from thin sheets hinged along the edges, and supports a continuous reflective surface. The

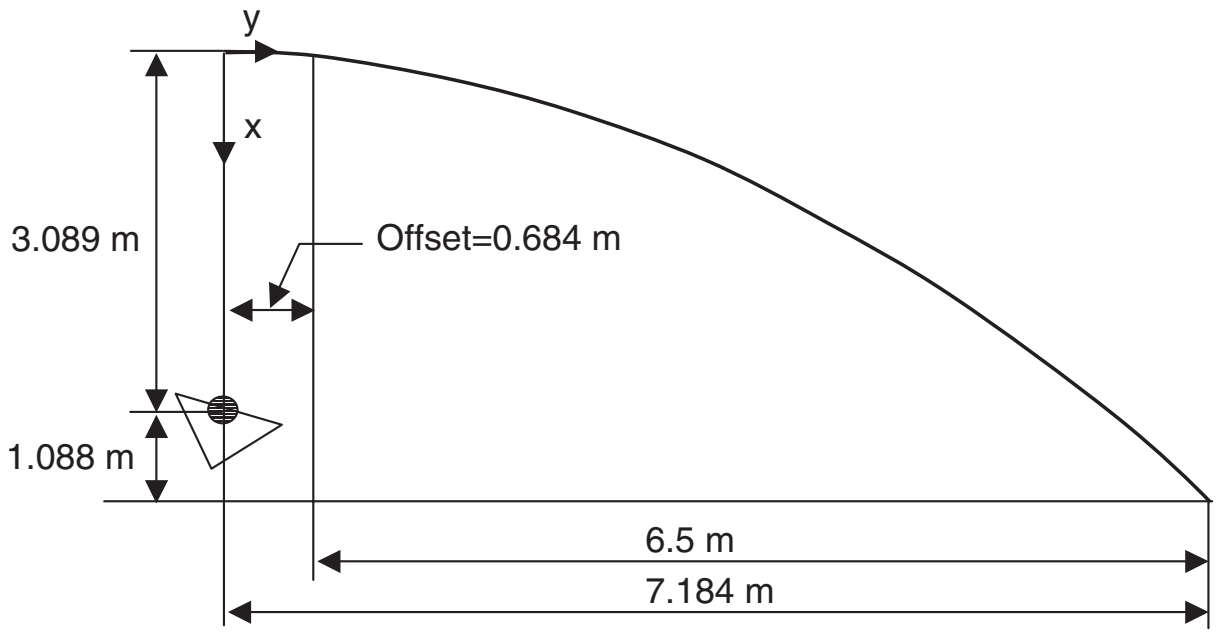

Figure 1.4: Deployable SAR reflector shape (arc-length of reflector surface is 7.888 m).

realization of this concept critically depends on finding a suitable cutting pattern for the sheets. A methodology for finding the cutting pattern is presented, and detailed analytical expressions are obtained, based on given focal length, aperture, and offset distance of the reflector.

An overall design for a full size reflector based on this concept is presented, sized for structural performance, and analysed using the finite element software ABAQUS. A quarter-scale, low-cost-plastic model is used for a preliminary demonstration of the concept, and two different folding schemes are tested: accordion-type, or Z-fold, and coil-type. The first folding scheme is found to be preferable for the present application.

Next, a half-scale demonstrator is designed, modelled in ABAQUS, and constructed from sheets of woven of carbon-fibre-reinforced-plastic. The minimum bend radius that the composite material can undergo without failing is a crucial piece of information in the design of this structure. Its value is initially estimated theoretically, using both the Maximum Strain and Tsai-Wu Criteria for laminated composites, and is then also measured experimentally. The shear stiffness and strength of the connections between the sheets, made with woven-glass tape, are determined experimentally.

The stiffness and surface accuracy of the demonstrator are measured after construction. Then, the structure is packaged and deployed several times, and finally its surface accuracy is measured again.

The design and testing of the half-scale demonstrator thus demonstrates the achievable mass,

stiffness and surface accuracy, assembly and handling process, packaging, material and process viability of the proposed new concept. A partial demonstration of its deployment behaviour is also obtained.

1.4 Layout of Report

Chapter 2 presents the three structural concepts that were considered: thin-foil reflector structures supported by a deployable frame, thin-walled structures that can be folded elastically, and structures consisting of rigid panels connected by hinges. Two variants of the first two concepts are considered, thus giving a total of five options. A trade-off between these five options leads to the selection of one of the thin-walled structures. The geometric details of this chosen concept are then worked out and a preliminary finite element analysis is carried out to verify that it has the potential to deliver a high-performance structure of low mass.

Chapter 3 presents a series of finite-element simulations of a full size reflector structure in orbit. The aim of these studies is to establish a reasonably optimal structural configuration; hence a series of sensitivity analyses are carried out to reduce mass while increasing stiffness and the margin of safety against local or global buckling. Various changes of configuration of the structure are considered. An untapered structure with open ends is found to be optimal.

Chapter 4 presents a study of a half-scale demonstrator, to be tested in the laboratory, under gravity conditions. The overall structural configuration of the demonstrator is obtained by scaling the full-size flight structure while keeping the wall thickness unchanged. The effect of using high-performance carbon fibre composites and the minimal amount of gravity off-loads required for testing the structure in the laboratory are investigated. A more detailed finite-element model is then introduced, which includes cut-outs in the sidewalls of the structure —required to fold it— and stiffeners –to prevent local buckling.

Chapter 5 describes the construction of a quarter-scale low-cost demonstrator. This model is used to investigate the two folding methods that had been proposed during the conceptual study phase, and also to verify the performance of various measures for avoiding damage of the structure when it is folded, to latch it when it is deployed, etc. Many valuable lessons that have been learnt are summarized at the end of the chapter.

In Chapter 6 the folding of the structure is investigated in detail. The minimum bend radius of currently available laminates is investigated, both analytically and experimentally, along with the transverse forces that need to be applied on either side of the fold line. The different types of joints to be used for connecting the sheets are described and are then tested to define their

strength and stiffness under shear loading. The size of the cut-outs in the sidewalls ("windows") is determined. The packaged volume of the structure is estimated, assuming Z-folding.

Chapter 7 describes the detailed design, manufacture and assembly of the half-scale demonstrator. A full description of each part is given and, most importantly, the novel assembly technique is explained in detail.

In Chapter 8 the mass, stiffness and surface accuracy of the demonstrator are measured. The stiffness measurements are compared with results from a finite element model. The surface accuracy in the deployed configuration is measured with photogrammetry software, before packaging the structure for the first time and also after deploying it.

Chapter 9 describes the way in which the structure is packaged in two stages: first by flattening it and then by Z-folding it. Deployment has also been demonstrated. Problems that occurred when the structure was packaged for the first time are discussed.

Chapter 10 concludes the report, and outlines the future work that is required to further advance the proposed new concept.

Chapter 2

Structural Concept

2.1 Schemes Considered and Trade-off

Three structural concepts were considered: two schemes involving thin foil reflective surfaces supported by deployable frames, two thin-walled structures with curved surfaces, four rigid panels connected by self-powered and self-locking hinges.

The first concept is based on a series of identical, rectangular deployable frames, of the kind described in Pellegrino et al. (2000), which provide discrete attachment points for a RF reflective surface consisting of a thin foil, or metallic mesh, that takes up the required parabolic profile when it is stretched out. Two variants of this concept were considered, and models were constructed to visualize them, each consisting of three frames only, see Figures 2.1 and 2.2. Note that both types of frame involve six revolute joints, four at the corners and two in the middle of the shorter sides of the rectangle.

The foldable frames used in the first concept, Figure 2.1, have the property that during deployment there is a 90° rotation of the long edges of the rectangle with respect to the short edges. Hence, the deployment of the right-hand-side frame from Figure 2.1(a) to 2.1(b) causes a 90° rotation between the undeployed two frames and the deployed one. Deployment of the middle frame, from Figure 2.1(b) to 2.1(c), causes a further 90° rotation between the same two frames, which thus become coplanar. The foldable frames shown in Figure 2.2 have a similar behaviour, but the rotations are through 45° instead of 90°, which makes it less efficient in terms of packaging efficiency but easier to avoid interference during deployment between the members of the frame and the reflective foil.

These two deployable frame concepts could potentially offer a very lightweight reflector structure. However they have a number of disadvantages, as follows:

(a)

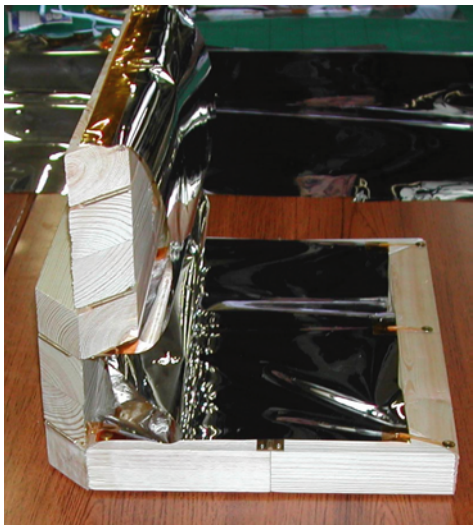

(b)

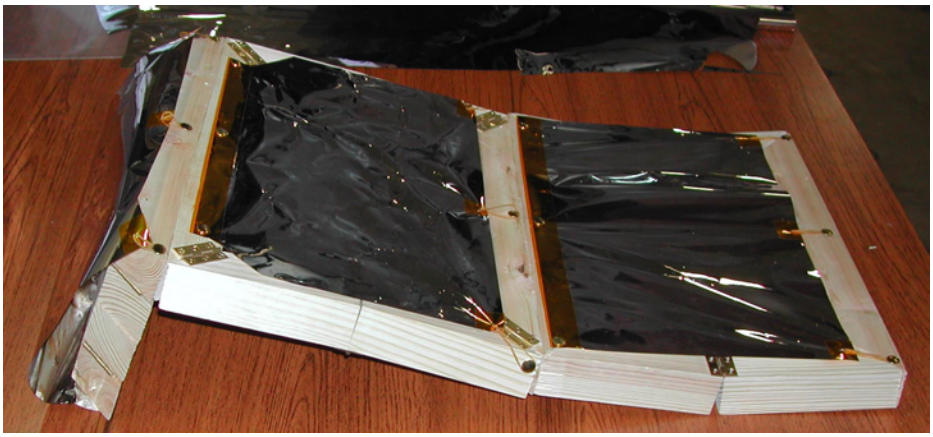

(c)

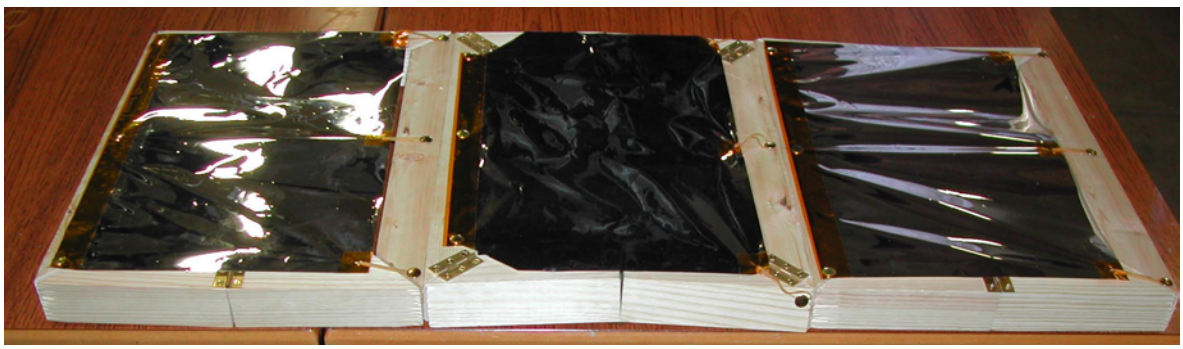

(d)

Figure 2.1: Deployable frame scheme 1.

Figure 2.2: Deployable frame scheme 2.

- They require many joints (six joints per frame);
- they involve complex motions during unfolding;
- the reflective surface cannot be made as a single piece because the distance between the edges of the frames decreases at the end of the deployment process, and hence there will have to be gaps in the reflector, reducing its RF performance;
- they are complex to design and analyse.

The second concept uses thin sheets of in-plane stiff material, with non-straight edges, which are bent to form a series of interconnected curved surfaces. The curvature of the surfaces is determined by the shape of the hinge line that connects the sheets. The cutting pattern for the edges is such that one of the surfaces (called the RF surface henceforth) provides the required parabolic reflective surface. The cutting pattern is designed such that the whole structure can be collapsed into an essentially flat configuration, so that it can then be coiled or Z-folded.

Different types of low-cost, high precision hinges can be used along the edges such as adhesive tape, rolamite hinges, or tape springs. Hence, general features of this concept are lightness, simplicity, no joints, low cost, and self deployment.

Three schemes of this type were studied. Scheme 1 uses two convex surfaces for the top and bottom surfaces and two concave surfaces for the side surfaces, as shown in Figure 2.3. The cutting pattern of the sheets is also shown in the figure. It offers a good support for the profile for the RF surface, but RF blockage resulting from the presence of the top surface in the radiation path would require the use of special non-RF materials for this sheet. Also, the back of the RF surface would require thermal protection to reduce thermal distortion.

Scheme 2 uses two concave surfaces for the top and bottom surfaces and two convex surfaces for the side surfaces, as shown in Figure 2.4. Scheme 2 is similar to Scheme 1, but it yields better RF performance.

Scheme 3, shown in Figure 2.5, is identical to scheme 1 but provides two additional, internal supports for the RF surface. Since this scheme is a variant of a previous one, it is not pursued in the trade-off.

The third concept, shown in Figure 2.6, uses four sandwich panels to form the RF surface. This is not a particularly novel concept, but would use the tape-spring-rolamite-hinge in Pellegrino et al. (2002) along the hinge lines. The element of risk in this solution is relatively small, but it needs a large number of parts and the manufacturing cost would be relatively high.

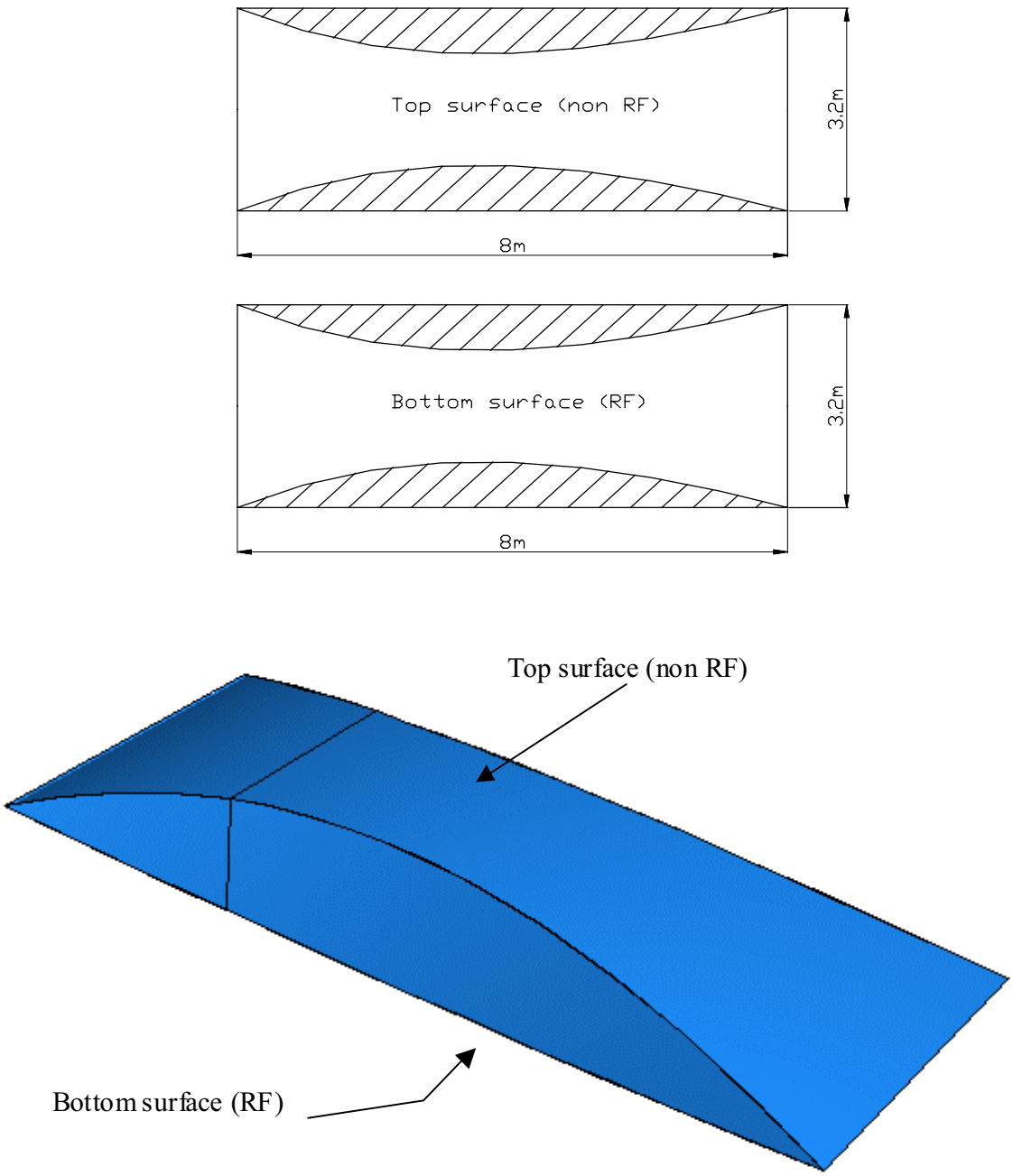

Figure 2.3: Thin-walled structure scheme 1.

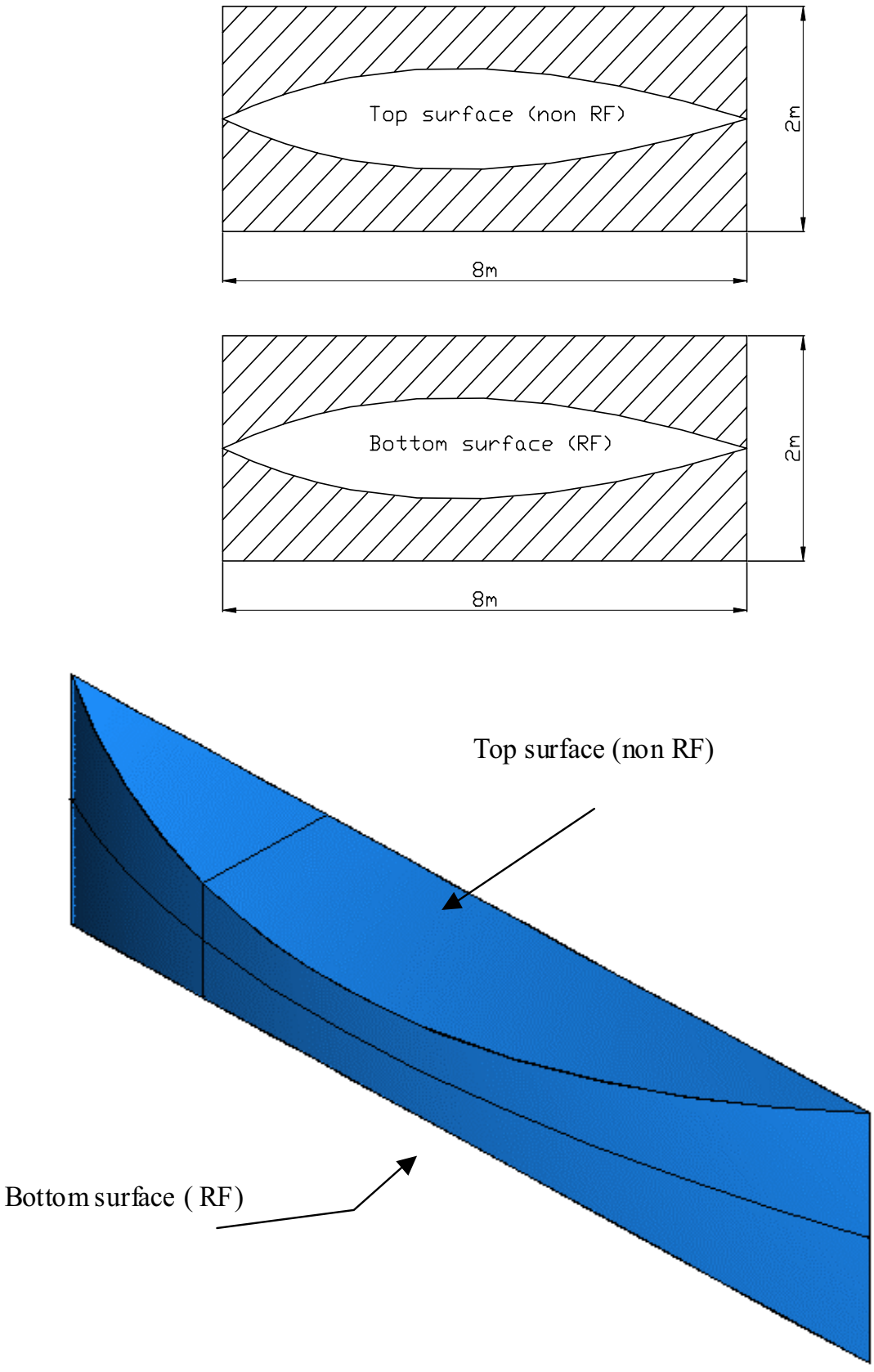

Figure 2.4: Thin-walled structure scheme 2.

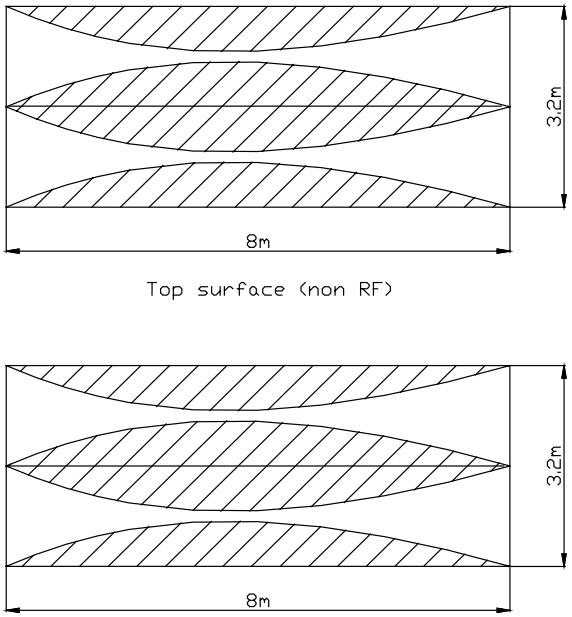

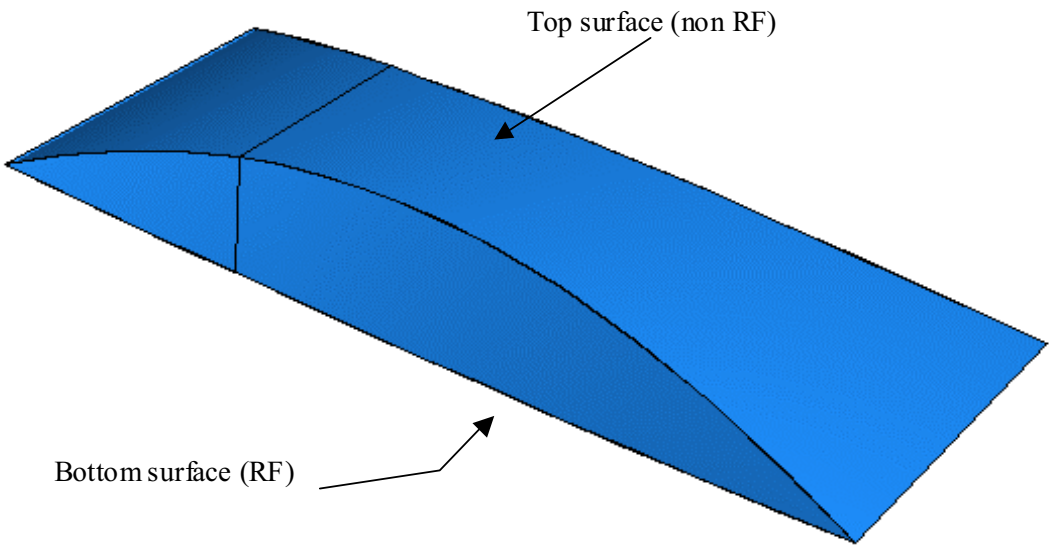

Figure 2.5: Thin-walled structure scheme 3.

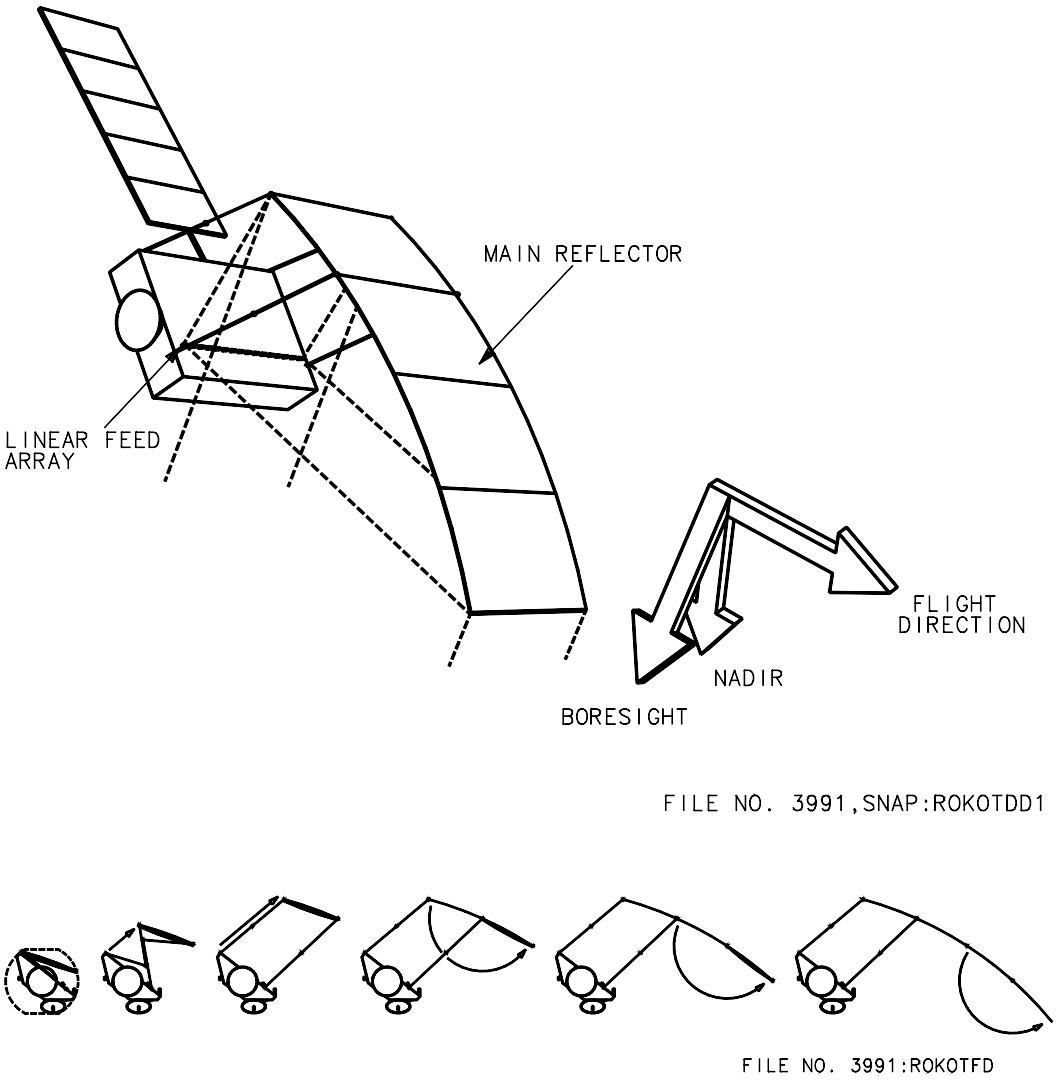

Figure 2.6: Concept with rigid panels.

Type	Weighting	Option 1	Frame		Option 2	Frame	
Feature		Fig 5	concept 1	weighted	Fig 6	concept 2	weighted
High score is best		comment	score	score	comment	score	score
Deployed accuracy	4	Frame gives fixed points, flat shape	7	28	Similar to option 1	7	28
Deployed stiffness	4	ditto	8	32	::	8	32
Repeatability	4	Good frame, cushion not so good	5	20	::	5	20
Packaging for stowage	3	How to hold?	6	18	::	6	18
RF performance	5	Gap between panels	5	25	::	5	25
Thermal performance	3	Lots of joints	6	18	::	6	18
Mass (based on a lightweight goal)	4	lightweight + frame	6	24	::	6	24
Level of development needed	3	lots of modelling needed, -joints	3	9	::	4	12
Repeat Cost	5	many joints	3	15	::	3	15
Acceptability of deployment	3	sequencing needed	3	9	::	4	12
Motive torque	2	tensioning required at end	7	14	::	7	14
Simplicity, reliability	4	lots of joints, secondary deployment reqd	3	12	::	5	20
Ground testing / susceptability to damage	2	difficult to fold	4	8	Better than option 1	5	10
Total				232			248

Option3	Reflector		Option4	Reflector		Option 5	Large folding	
Fig 2	concept 1	weighted	Fig 3	concept 2	weighted	Baseline	panels	weighted
comment	score	score	comment	score	score	comment	score	score
good profile	8	32	similar to Option3	8	32	similar to Option 4	8	32
good/needs evaluation	7	28	freedom for choice of materials	9	36	similar to Option 4	8	32
no frame but better	6	24	similar to Option3	7	28	similar to Option 4	9	36
score TBC	4	12	score TBC	4	12	similar to Option 4	8	24
no gaps but RF blockage	5	25	Excellent	9	45	similar to Option 4	9	45
distortion, hot spots	4	12	can add MLI, carbon upright sections	6	18	similar to Option 4	7	21
light	8	32	needs to be more rigid than option 3	7	28	similar to Option 4	5	20
analysis, make a B/B	5	15	similar to Option3	5	15	similar to Option 4	8	24
better	8	40	similar to Option3	8	40	expensive	6	30
how to stow	8	24	similar to Option3	8	24	similar to Option 4	6	18
no friction	8	16	similar to Option3	8	16	similar to Option 4	8	16
simple	8	32	similar to Option3	8	32	similar to Option 4	7	28
no joints	7	14	similar to Option3	7	14	similar to Option 4	8	16
		306			340			342

Table 2.1: Concept selection trade off.

2.1.1 Trade-off

Five options (deployable frame schemes 1 and 2, thin-walled structure schemes 1 and 2, rigid panels) were examined in terms of deployed accuracy, deployed stiffness, repeatability, packaging for stowage, RF performance, thermal performance, mass, amount of development required, repeat cost (i.e. cost of making additional reflectors, once the tooling has been paid for), acceptability of deployment, motive torque, simplicity and reliability, ground testing/susceptibility to damage.

A table summarizing the trade-off is presented in Table 2.1. The various features that have been considered are listed in the first column, with the corresponding weighting. In the following columns, each option is scored in terms of its features and a total score is obtained.

It is concluded that option 4 (thin-walled surface, scheme 2) and option 5 (rigid panels) are the most favorable. Hence it was decided not to pursue the deployable frame solutions (options 1 and 2). Since the rigid panel scheme could be safely assumed as a back-up and would not require significant additional development, option 4 was selected for further study and hence is covered in this report.

2.2 Geometry of Main Structure

Option 4 —thin-walled surface, scheme 2— was selected as a baseline for this study. The general concept, shown in Figure 2.7, envisages a thin-walled support structure which supports a thin-walled reflector.

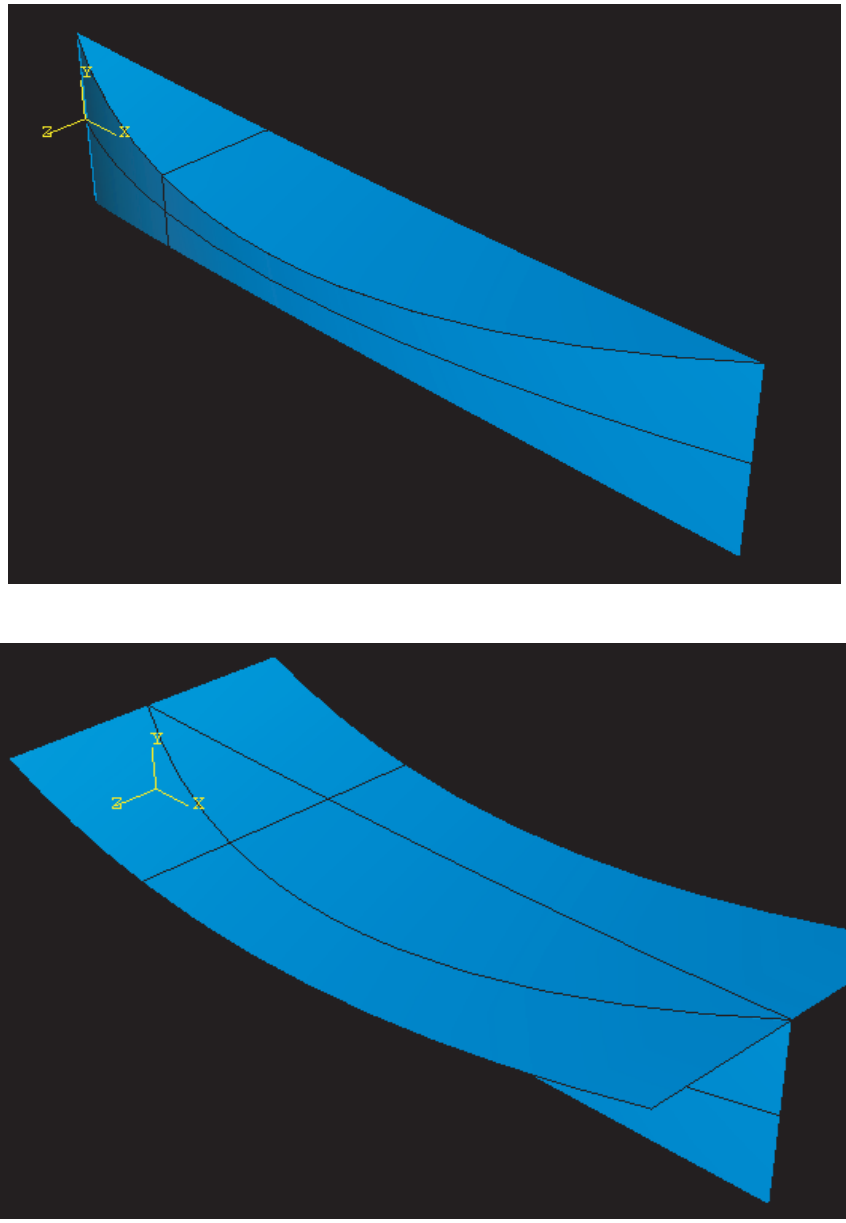

Figure 2.7: Reflector support structure (top), and reflective surface with support structure (bottom).

The support structure consists of two concave surfaces, top and bottom, and two convex surfaces on the sides. All four surfaces have the same parabolic shape of the reflector, as will be

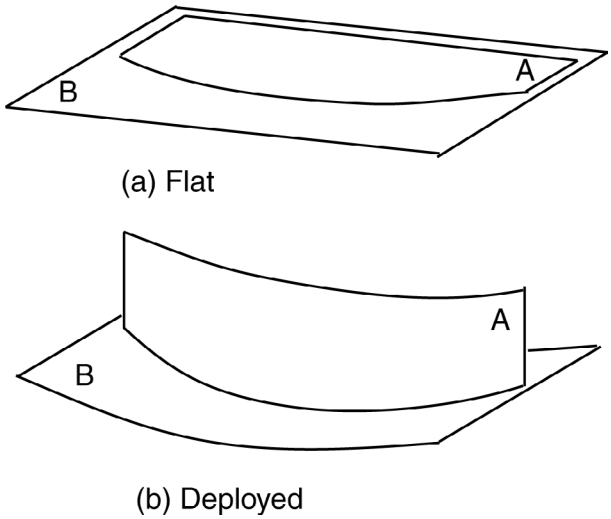

Figure 2.8: Use of a shaped sheet A to form sheet B into a singly-curved surface.

explained next. The RF surface is placed in lieu of either the top or the bottom surface.

2.2.1 Structural Concept

The key geometric ideas behind this concept can be explained as follows.

It is obvious that a flat sheet A can be connected through a straight edge to another, coplanar flat sheet B. If sheet A is then brought out of plane, for example by rotating it through 90°, both sheets remain planar but are now at an angle. Consider the case where sheet A has a non-straight edge, as shown in Figure 2.8. When sheet A is brought out of plane, both sheets become curved, as shown in Figure 2.8(b).

Next consider the "hollow-solid" structure shown in Figure 2.9, which is made by connecting two pairs of identical flat sheets. Sheets A and A', which are identical, are connected to sheets B and B', which are also identical. The shape of the edges is identical in all four sheets. In the configuration shown in Figure 2.9(b) the four sheets form curved surfaces which define a hollow solid. The folded configuration shown in Figure 2.9(a) is obtained by introducing fold lines along the centre lines of sheets A and A' (shown as broken lines in the figure).

The hollow solid structure can be flattened (we will call this stage one of the folding process), as shown in Figure 2.9(a), then it can be folded again (stage two of the folding process) as an accordion, or it can be rolled up into a coil.

The edge profile of sheet A is determined by considering the required shape of sheet B.

Figure 2.10(a) shows a cylindrical surface (corresponding to sheet B in the earlier explana-

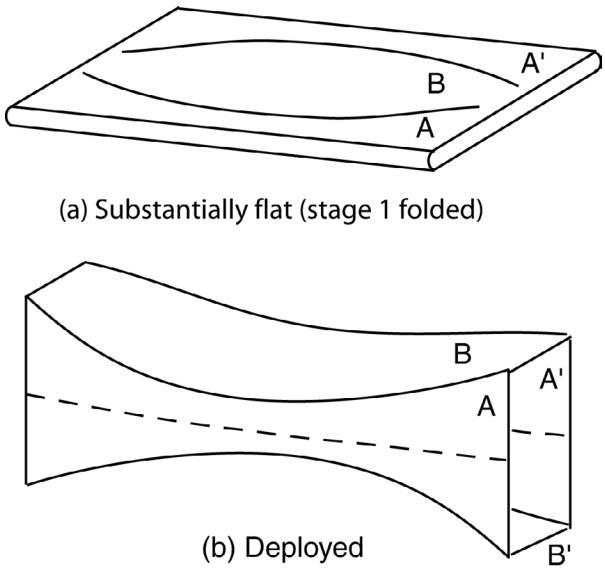

Figure 2.9: Hollow solid structure.

tion). This surface can be generated by considering the two-dimensional curve $z = f(x)$ and by translating this curve along a generator segment which is parallel to the y-axis, for example BC. Note that in Figure 2.10(a) a general point on $z = f(x)$ is point B; also note that the x-axis starts at the origin O, and passes through the end point A of the curve. Finally, note that all points on BC have the same arc-length distance s from the y-axis, and the same distance d from the xy plane.

Let F and D be the projections of B and E onto the xy plane, clearly

$$\overline{\mathrm{BF}} = \overline{\mathrm{DE}} = d$$

Now consider flattening the surface onto the xy-plane while keeping its edge fixed along the y-axis. During this process BC moves in the x and z directions, while remaining parallel to the y-axis. The height d of E above the xy-plane becomes zero.

Next, consider attaching the curved surface B to another curved surface A, as shown in Figure 2.11(a). It is required that

- the surface B has a particular curved shape, defined by $f(x)$ as above, and that
- the two surfaces can be flattened together.

We will now look for the locus of the points E on the surface B defining the curved profile of surface A, and hence the curve along which the two surfaces are attached. It will be assumed that the generator BC is perpendicular to the surface A in the curved configuration (i.e. the

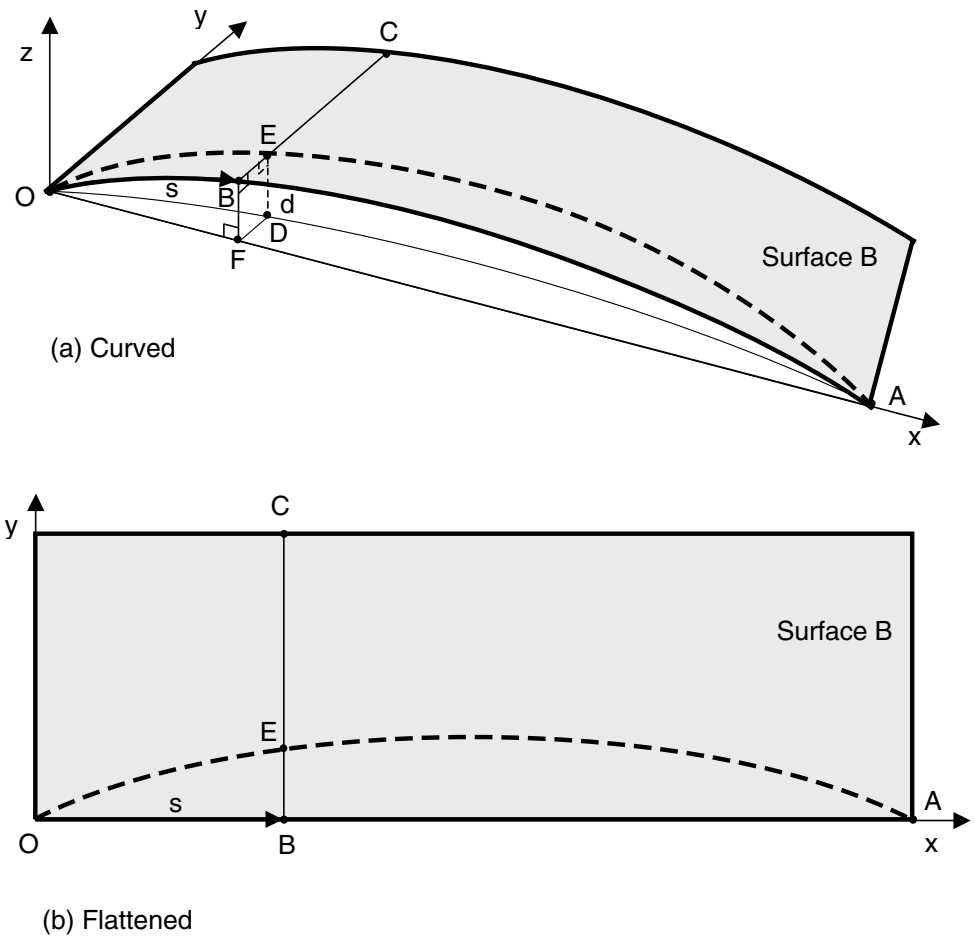

Figure 2.10: Two configurations of a singly-curved surface.

deployed configuration), although a more general situation could be considered. It will also be assumed that the two surfaces are tied to each other at the general point E and there is no relative motion of the tie points during flattening or deployment.

The following conditions apply

- Condition 1: The arc-length of OE, measured on the surface B, is equal to the arc-length of OE measured on the surface A. This condition needs to be satisfied in the two extreme configurations shown in Figure 2.11, and also of course in any intermediate configuration (but intermediate configurations will not be considered).

- Condition 2: When the surfaces are flattened, both points B and D move towards point F, and so B and D coincide when the surfaces are flattened, see Figure 2.11(b). Hence, it follows that

$$\overline{\mathrm{BE}} = \overline{\mathrm{DE}} = d \tag{2.1}$$

The above conditions define the required edge profile of surface A. This profile is defined by $s(x)$ and $d(x)$. *Given a two-dimensional curve $z = f(x)$, $s(x)$ will be the arc length along this curve, and $d(x) = z$.*

Note that, from Equation 2.1, both sheets have the same singly-curved shape in the deployed configuration.

2.2.2 Cutting Pattern

For ease of manufacture, the whole structure is to be made from flat sheets. The concave and convex surfaces will be obtained by bending these sheets.

The required parabolic profile for the reflective surface is shown in Figure 2.12. Following Section 2.2.1, the cutting pattern for the flat sheets requires that the arc length $s(x)$ and the perpendicular distance from the chord line to the parabola $d(x)$ be worked out. These two functions are unchanged in the case of a tapered support structure, hence this more general case has been shown in Figure 2.13,

The equation of a parabola with vertex at (0, 0) is given by

$$y^2 = 4ax \tag{2.2}$$

where a is the focal distance. Equation 2.2 can be rewritten as

$$y = k\sqrt{x} \tag{2.3}$$

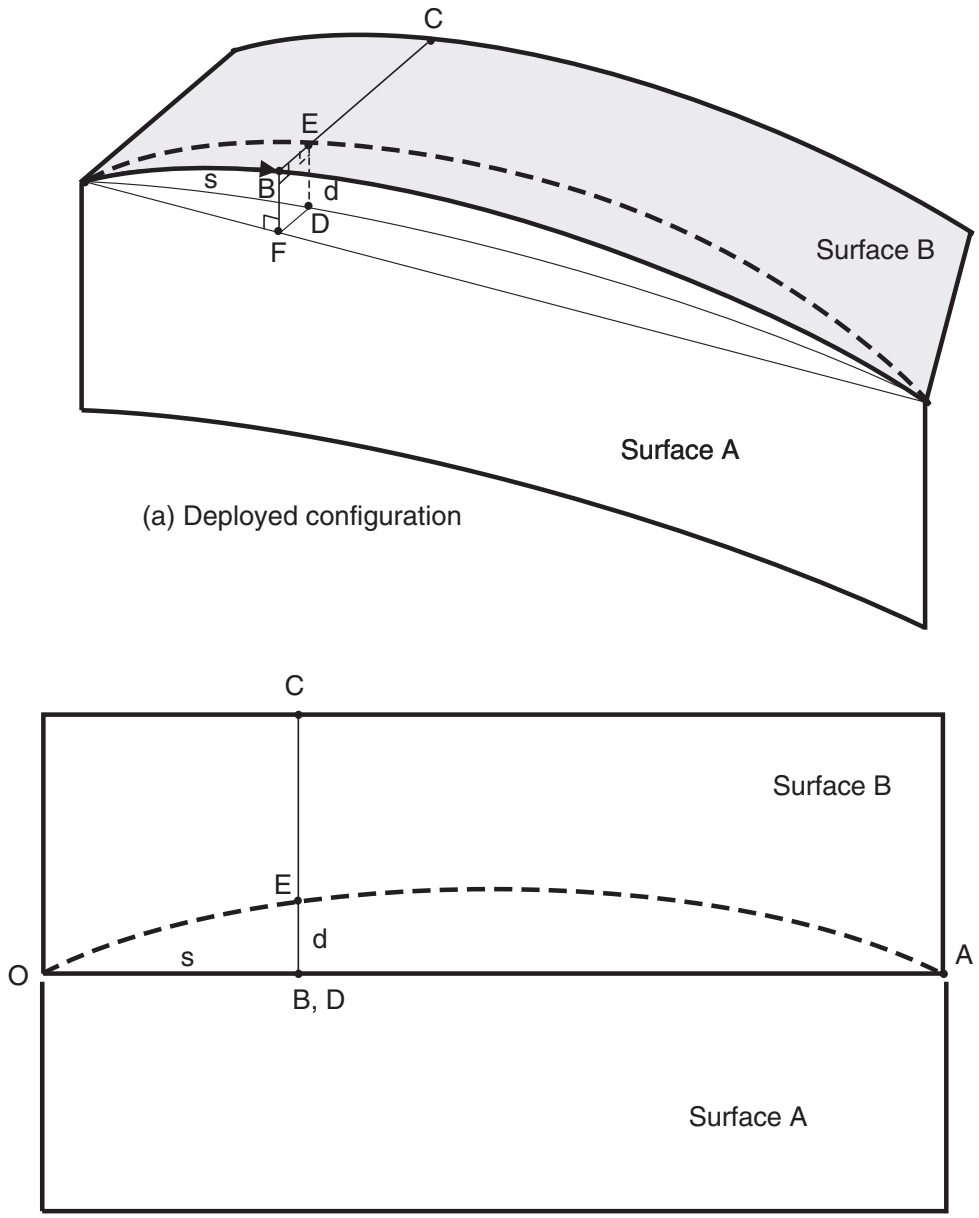

Figure 2.11: Required edge profile of sheet A to shape a singly-curved surface.

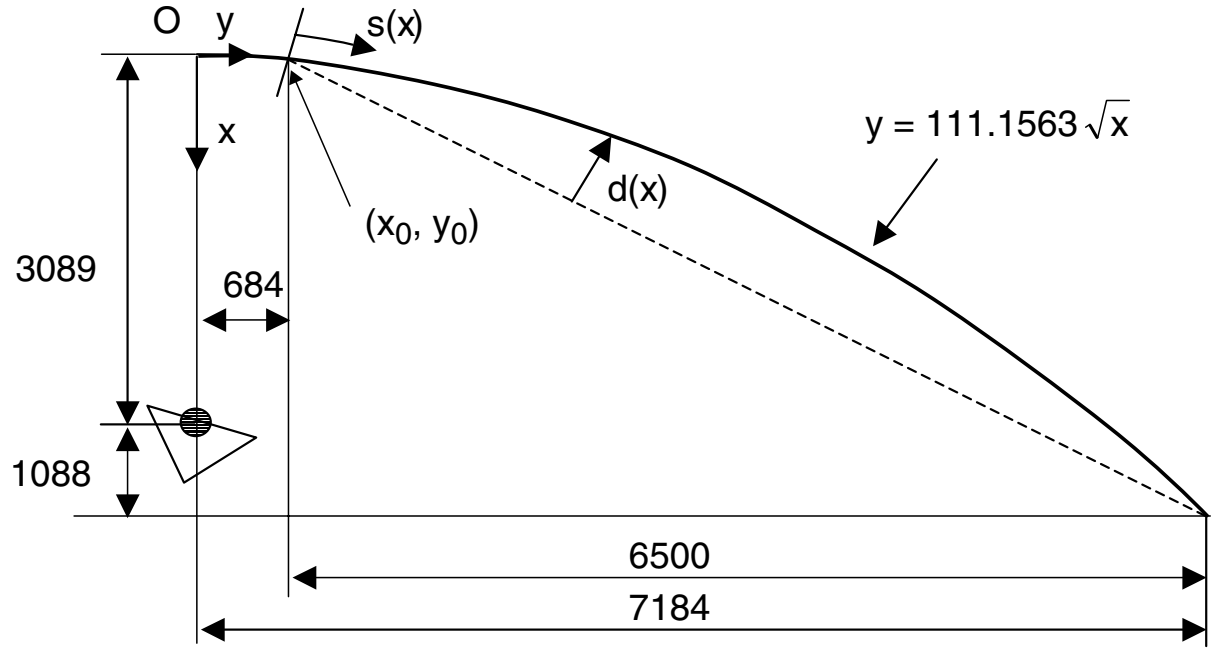

Figure 2.12: Profile of RF surface (all dimension in mm).

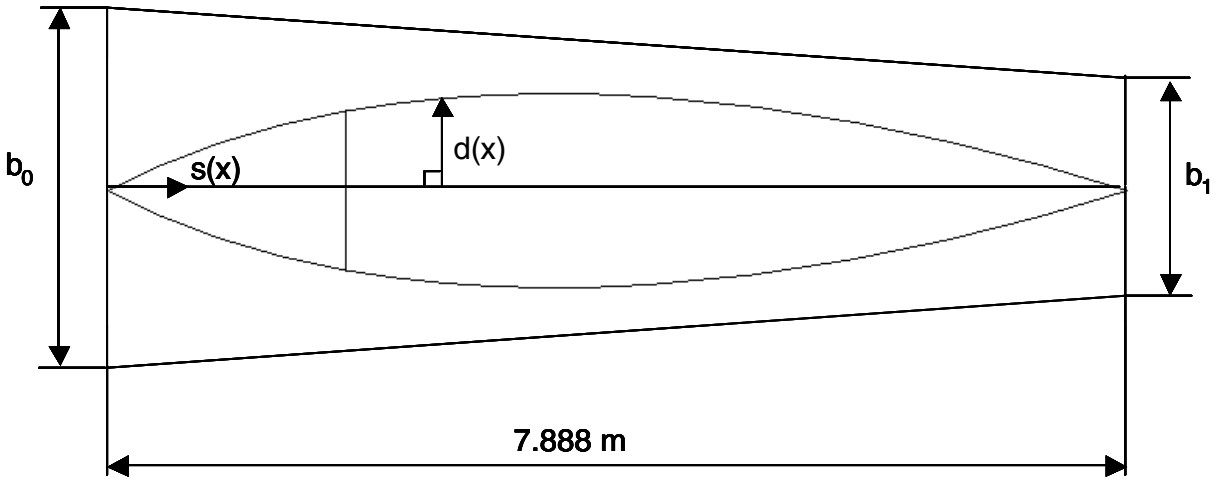

Figure 2.13: Top view of flattened support structure, assuming a tapered design $b_o \neq b_1$.

where $k = 2\sqrt{a}$. The arc length from the offset point (x_0, y_0) to a generic point (x, y) on the parabola is calculated from

$$s(x) = \int_{x_0}^{x} \sqrt{1 + (dy/dx)^2} dx \tag{2.4}$$

Substituting Equation 2.3 into Equation 2.4 and carrying out the integration yields

$$s(x) = \frac{1}{2}\sqrt{x\,(4\,x + k^2)} - \frac{1}{2}\sqrt{x_0\,(4\,x_0 + k^2)} + \frac{k^2}{8}\,\ln\left(\frac{8\,x + k^2 + 4\sqrt{x\,(4\,x + k^2)}}{8\,x_0 + k^2 + 4\sqrt{x_0\,(4\,x_0 + k^2)}}\right) \tag{2.5}$$

Substituting the end point of the parabola (x_f=4177 mm, y_f=7184 mm) into Equation 2.3 yields $k = 111.2$ mm$^{1/2}$, corresponding to a focal length $a = 3089$ mm. This gives the coordinates of the starting point for the reflective surface as $x_0 = 38$ mm at $y_0 = 684$ mm. Substituting x_0 and k into Equation 2.5 yields

$$\begin{aligned} s(x) = \quad & \frac{1}{2}\sqrt{x\,(4\,x + 12355)} - 344 \\ & +1544\,\ln(519 \times 10^{-6}\,x + 0.8017 \\ & +260 \times 10^{-6}\sqrt{x\,(4\,x + 12356)}) \end{aligned} \tag{2.6}$$

The equation of the chord line of the reflector, which joins the start and end points of the reflective surface, is written as

$$y_c = a_0 + a_1 x \tag{2.7}$$

where $a_0 = (y_0 x_f - x_0 y_f)/(x_f - x_0) = 624$ mm, and $a_1 = (y_f - y_0)/(x_f - x_0) = 1.57$ mm/mm.

Consider a generic point on the parabola, A(x, y), and a point on the chord line, B(x_c, y_c). The distance between A and B is

$$d_{AB} = \sqrt{(x - x_c)^2 + (y - y_c)^2} \tag{2.8}$$

Substituting $y = k\sqrt{x}$ and $y_c = a_0 + a_1 x_c$ into Equation 2.8 we obtain

$$d_{AB} = \sqrt{(x - x_c)^2 + (k\sqrt{x} - a_0 - a_1 x_c)^2} \tag{2.9}$$

The shortest distance $d(x)$ between $y(x)$ and the chord line can be obtained by minimizing d_{AB}. Hence we set the first derivative of d_{AB} with respect to x_c equal to zero and solve for x_c

$$\frac{\partial d_{AB}}{\partial x_c} = 0 \tag{2.10}$$

$$x_c = \frac{(x + a_1 k\sqrt{x} - a_0 a_1)}{(1 + a_1^2)} \tag{2.11}$$

The shortest distance $d(x)$ is obtained by substituting Equation 2.11 into Equation 2.9

$$d(x) = \sqrt{\frac{(x\,a_1 + a_0 - k\,\sqrt{x})^2}{1 + {a_1}^2}} \tag{2.12}$$

Substituting numerical values for k, a_0, and a_1 into Equation 2.12 yields

$$d(x) = 0.5371\sqrt{(1.570x - 111.1\sqrt{x} + 624.5)^2} \tag{2.13}$$

2.3 Preliminary Finite Element Analysis

A preliminary analysis of the static and dynamic response of the thin-walled surface scheme 2 was carried out. The structure was modelled in ABAQUS; first a parabolic cylinder was created by translation of the offset parabola profile. Then, the concave and convex surfaces were obtained by cutting the parabolic cylinder with another parabolic cylinder perpendicular to the first one. The support structure is thus a closed hollow solid, which is symmetric with respect to the planes XY and XZ. The following was assumed in the analysis:

- Material: Carbon (T300)/epoxy composite with properties E_1=142 GPa, E2=10.3 GPa, G_{12}=7.2 GPa, ν_{12}=0.27, ρ=1580 kg/m^3.
- Uniform thickness: 1 mm.
- Width in flat position: b_0=b_1=1.5 m, no taper.
- Boundary conditions: the first quarter of the RF surface is assumed to be edgewise pinned.
- Loading: inertial loading of 0.02 m/s^2. It is assumed that the gravity vector is in the XZ plane, has angle of 25.2° from the Z axis. The components of the gravity vector are g_X=8.53 mm/s^2, g_Z=18.09 mm/s^2.

The boundary conditions and loading are defined in Figure 2.14. A linear static analysis was carried out, in which 583 quadrilateral shell elements (S4R) were used to mesh the structure. The displacement magnitude is shown in Figure 2.15 and the stress contours are shown in Figures 2.16 to 2.18. Natural frequency analysis results are presented in Figures 2.19 to 2.21. It was concluded that the mass of the support structure is 50 kg, and the support structure is very stiff (maximum deflection is 9 μm).

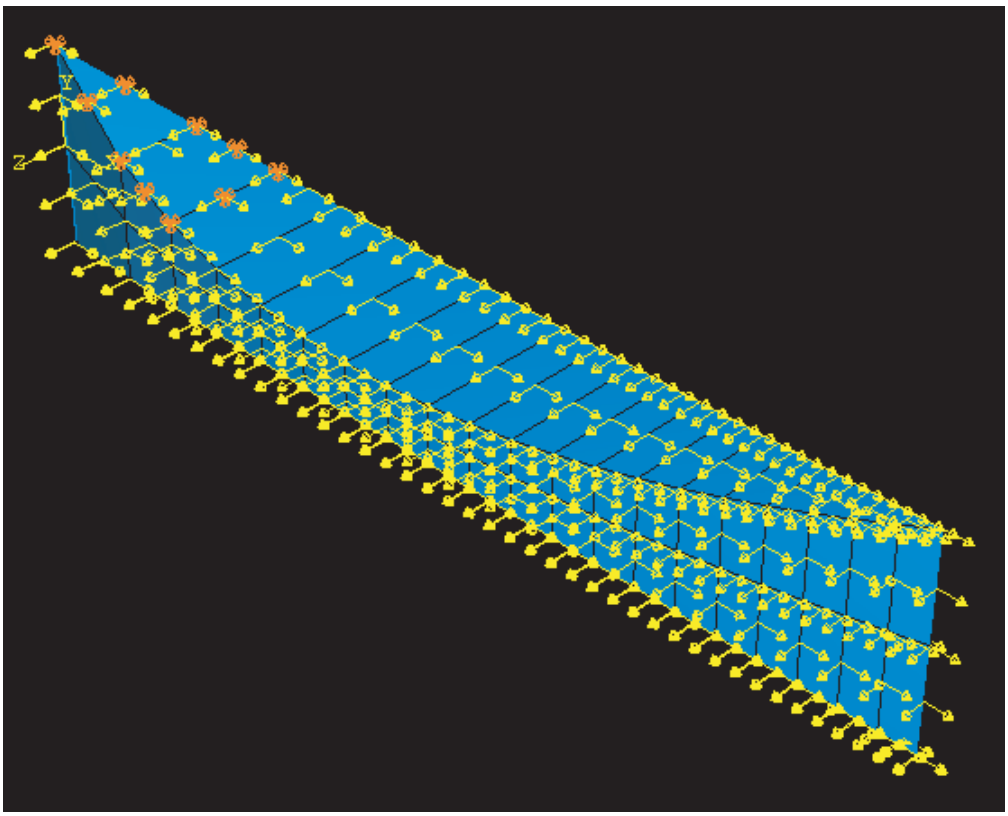

Figure 2.14: Boundary conditions and loading.

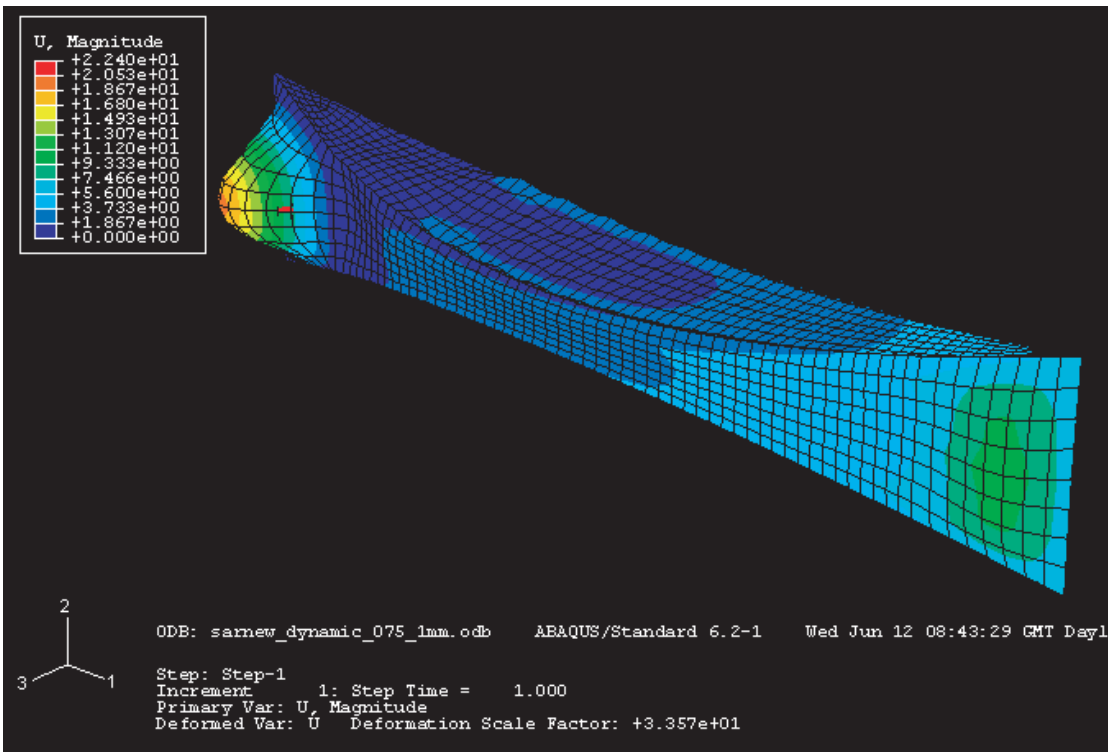

Figure 2.15: Contours of displacement magnitudes (μm).

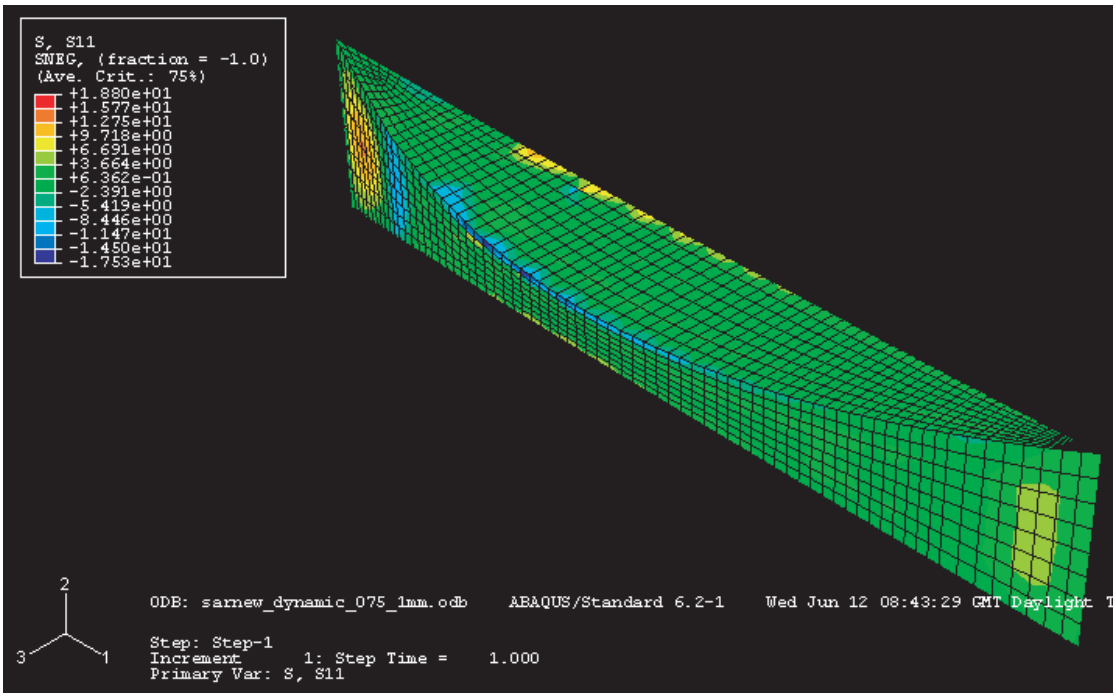

Figure 2.16: Stress contours, S11 (kN/m^2).

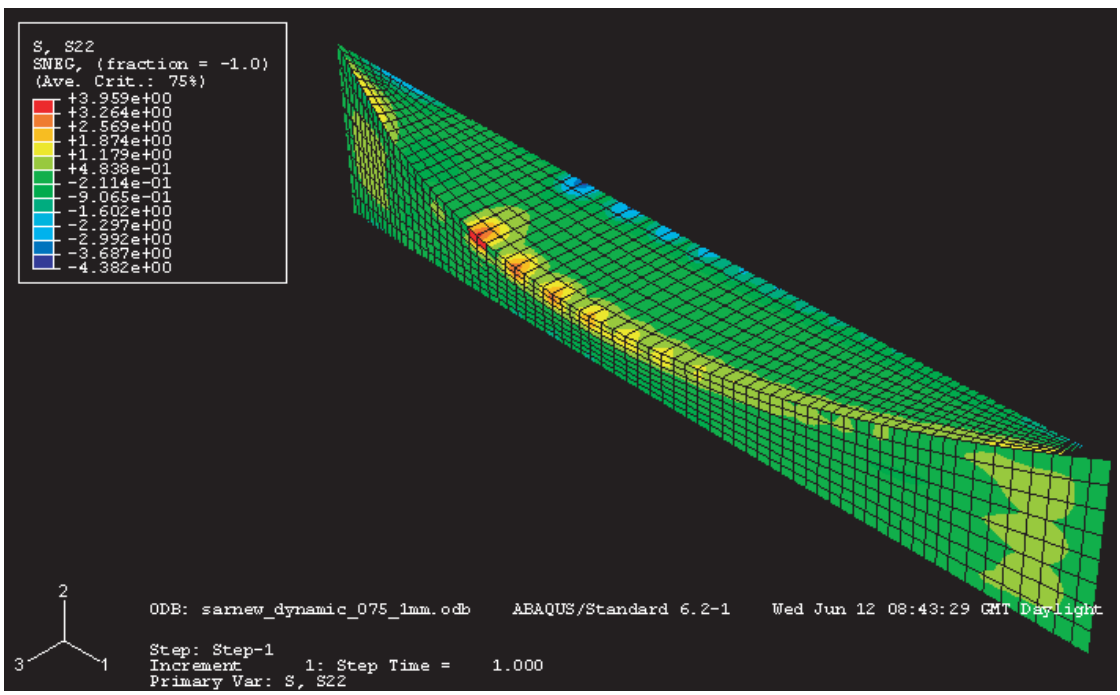

Figure 2.17: Stress contours, S22 (kN/m^2).

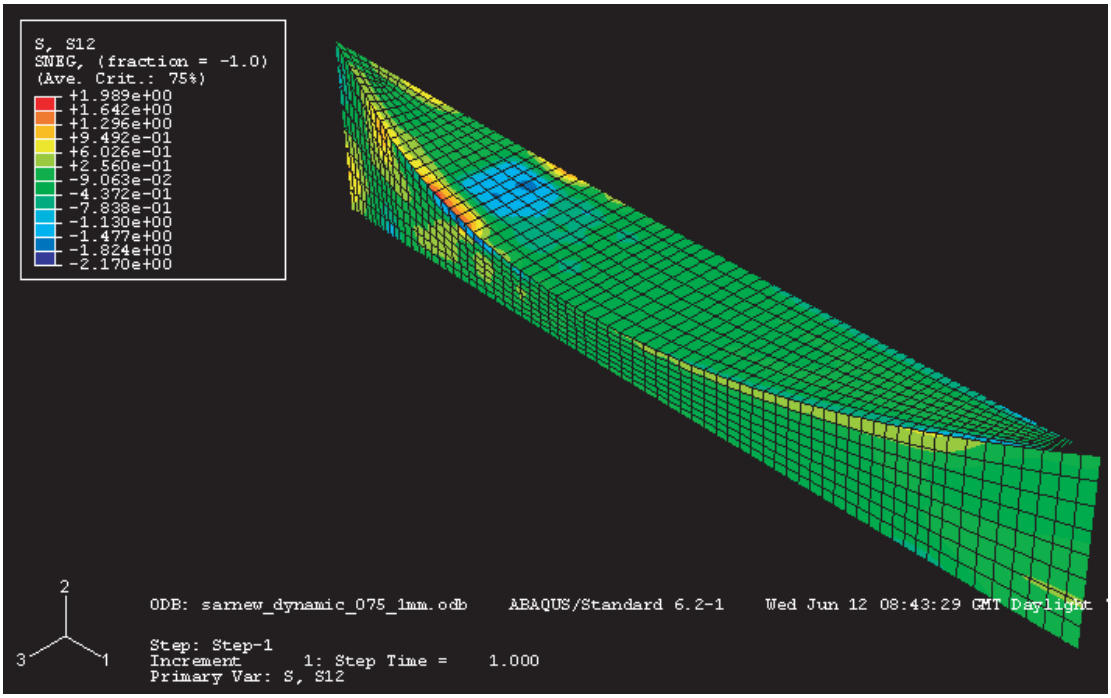

Figure 2.18: Stress contours, S12 (kN/m^2).

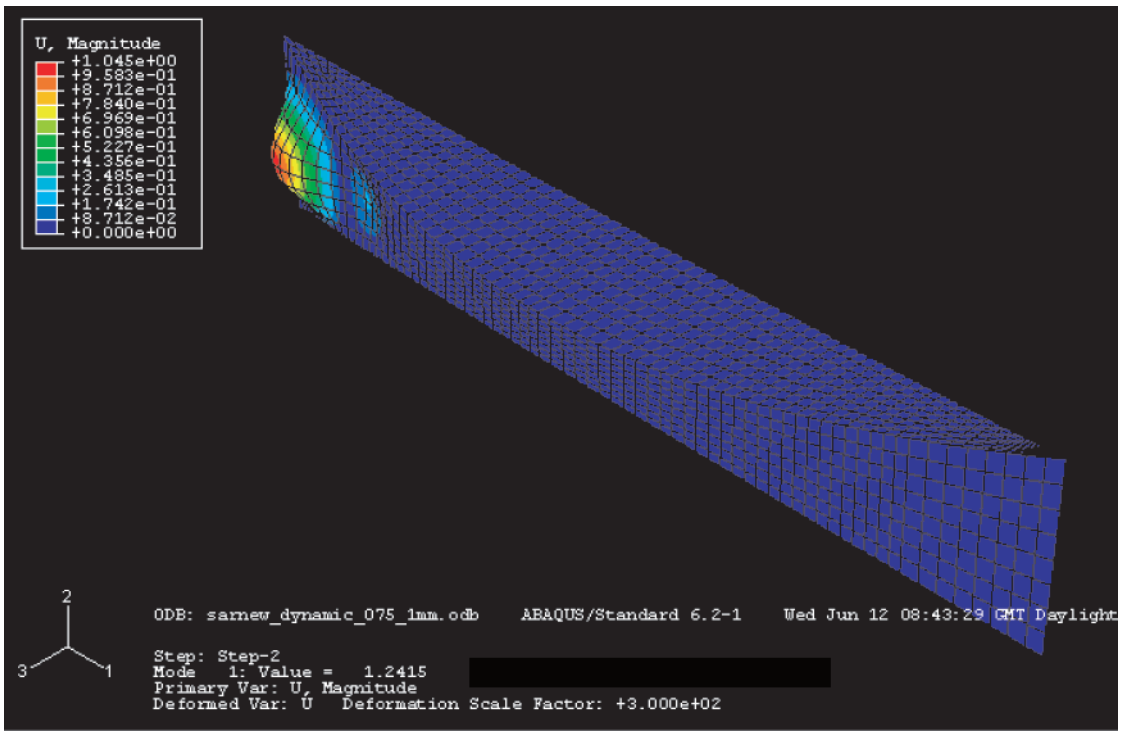

Figure 2.19: Normal mode 1 (frequency= 5.607 Hz).

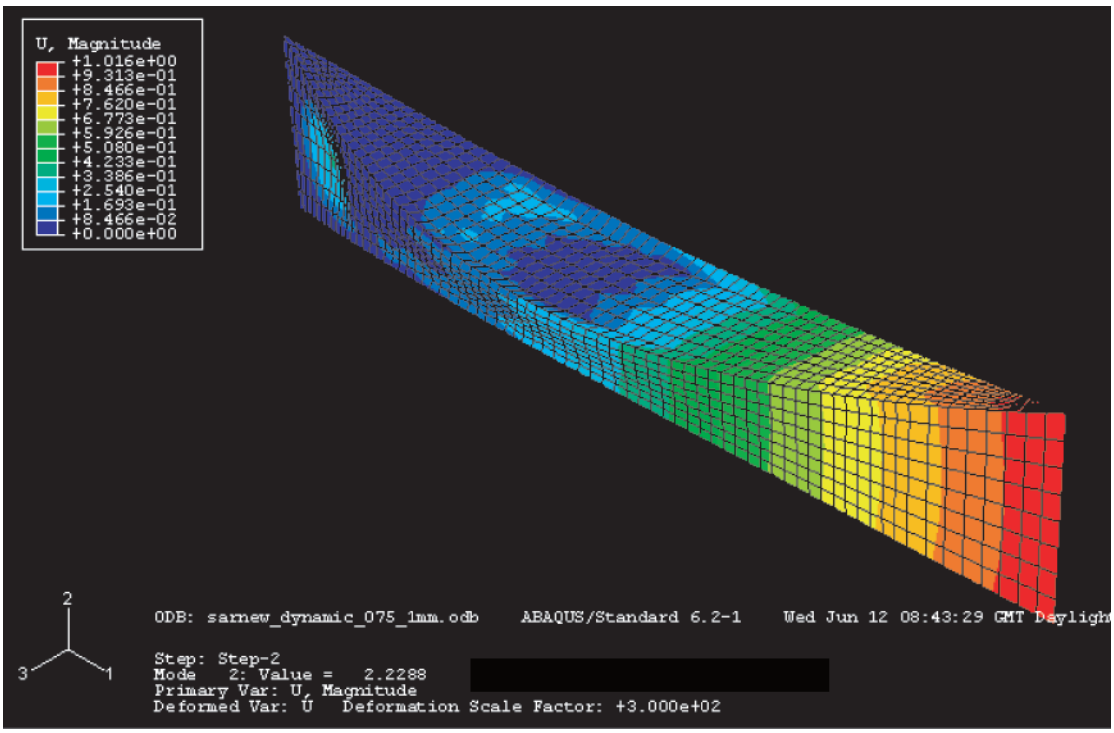

Figure 2.20: Normal mode 2 (frequency= 7.514 Hz).

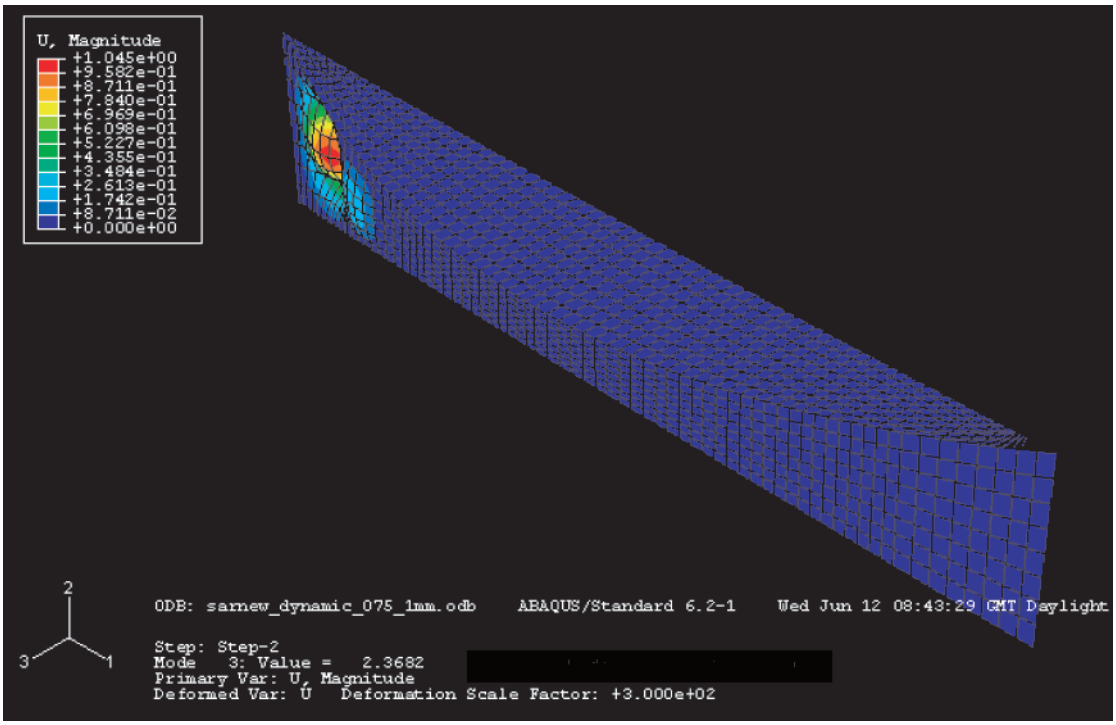

Figure 2.21: Normal mode 3 (frequency= 7.745 Hz).

Chapter 3

Optimization of Structural Configuration

A series of sensitivity studies were carried out to identify modifications of the basic thin-walled surface structure reflector concept scheme 2, shown in Figure 2.4, to improve its performance.

The structure was modelled in ABAQUS, and static, dynamic, and buckling analyses were performed. First, only the structure that supports the RF surface was studied, without the reflective surface; the effect of tapering the support structure was also investigated. Next, the support structure together with the reflector surface was analyzed, but a low-frequency mode appeared in all designs that were considered. Finally, a variant of the basic concept in which the support structure has open ends was analysed, and this was found to perform very satisfactorily.

3.1 Support Structure without Reflective Surface

This section presents a parametric study of the reflector support structure, to consider the effects of varying the thickness t, the width in the flat configuration b_0, and the taper $\lambda = b_1/b_0$. Both an untapered and a tapered support structure are shown in Figure 3.1.

The following was assumed in the analysis:

- Material: all surfaces made of woven carbon (T300) composite with eight layers $(0/45_2/0)_s$. For the sake of simplicity, the analysis assumes a single layer for each surface with the average material properties defined in Table 3.1.
- Uniform thickness.
- Boundary conditions: the first quarter of the RF surface is assumed to be edgewise pinned.

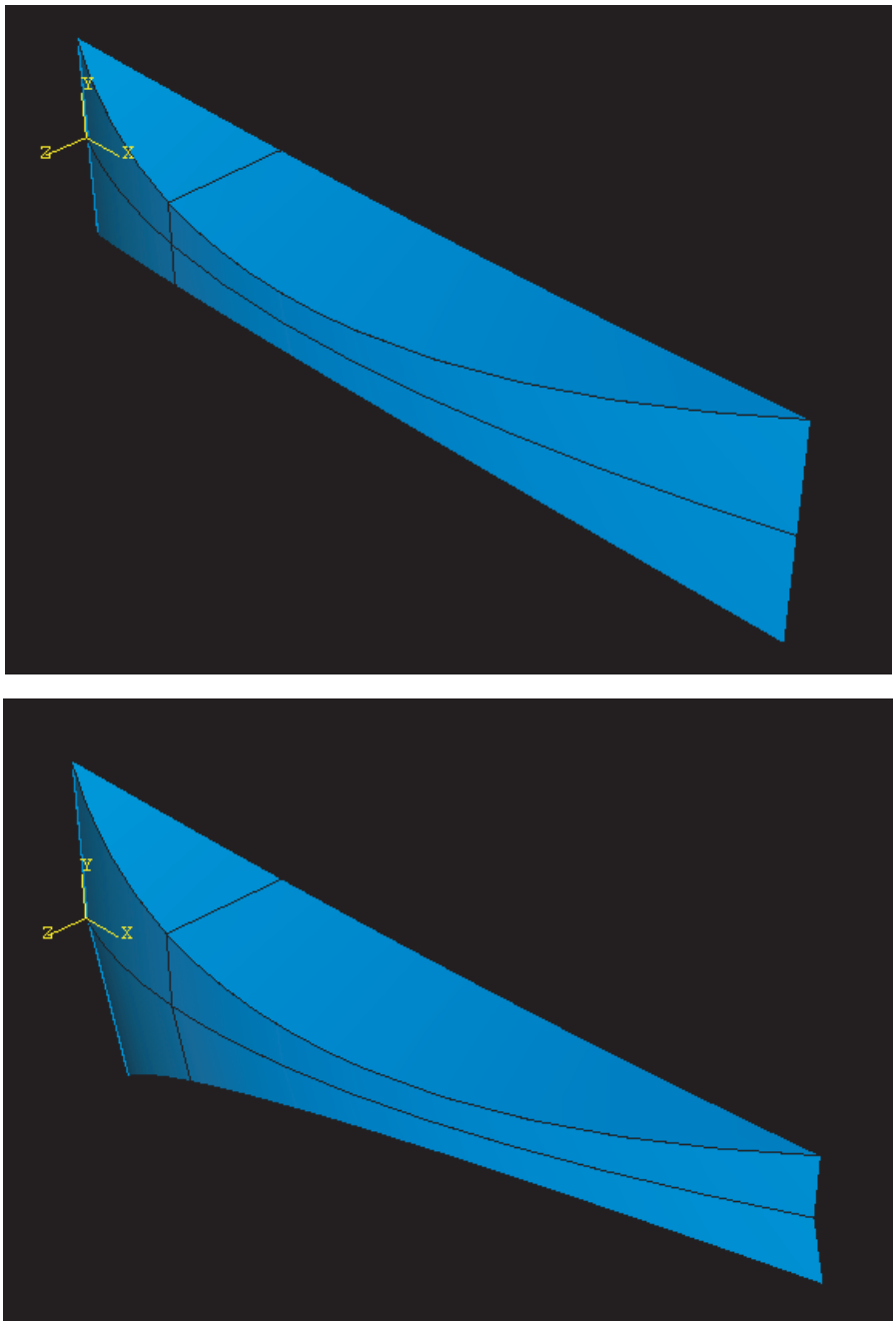

Figure 3.1: Untapered and tapered support structures, in deployed configuration.

Carbon/epoxy woven lamina				$(0/45_2/0)_s$ woven laminate		
Lamina Properties			**Average Laminate Properties**			
$E_1=E_2$	70	GPa		$Ex=E_y$	50.4	GPa
G_{12}	5	GPa		G_{xy}	19.2	GPa
ν_{12}	0.05	-		ν_{xy}	0.316	-
ρ	1.56	g/cm^3		ρ	1.56	g/cm^3
Thickness	0.125	mm		Thickness	1	mm
F_{1t}	800	MPa		F_{1t}	400	MPa
F_{1c}	700	MPa		F_{1c}	300	MPa
F_{2t}	750	MPa		F_{2t}	400	MPa
F_{2c}	650	MPa		F_{2c}	300	MPa
F_6	80	MPa		F_6	60	MPa

Table 3.1: Material properties of 8-ply woven composite.

- Loading: inertial loading of 0.02 m/s^2. It is assumed that the gravity vector is in the XY plane, has angle of 57.5° from the X axis so that the gravity vector is parallel to x axis shown in Figure 2.12. The components of the gravity vector are g_X=10.74 mm/s^2, g_Y=16.87 mm/s^2.

The boundary conditions and loading are shown in Figure 3.2 for a tapered support structure. Table 3.2 summarizes the variation in the total mass of the structure, the maximum displacement due to the applied loading, the fundamental natural frequency of vibration, and the margin against material failure, based on the Tsai-Wu criterion, when the wall thickness, the width in the folded configuration, and the amount of taper are varied.

The same effects are depicted graphically in Figures 3.3 to 3.7. Contour plots of the magnitude of displacement, margin against material failure, and the first three vibration mode shapes are shown in Figures 3.8 to 3.12 for b_o=2 m, λ=1, t = 1 mm.

Figures 3.13 to 3.17 show contour plots of the magnitude of displacement, margin against material failure, and the first three vibration mode shapes for b_0=3 m, λ=1/3, t = 1 mm.

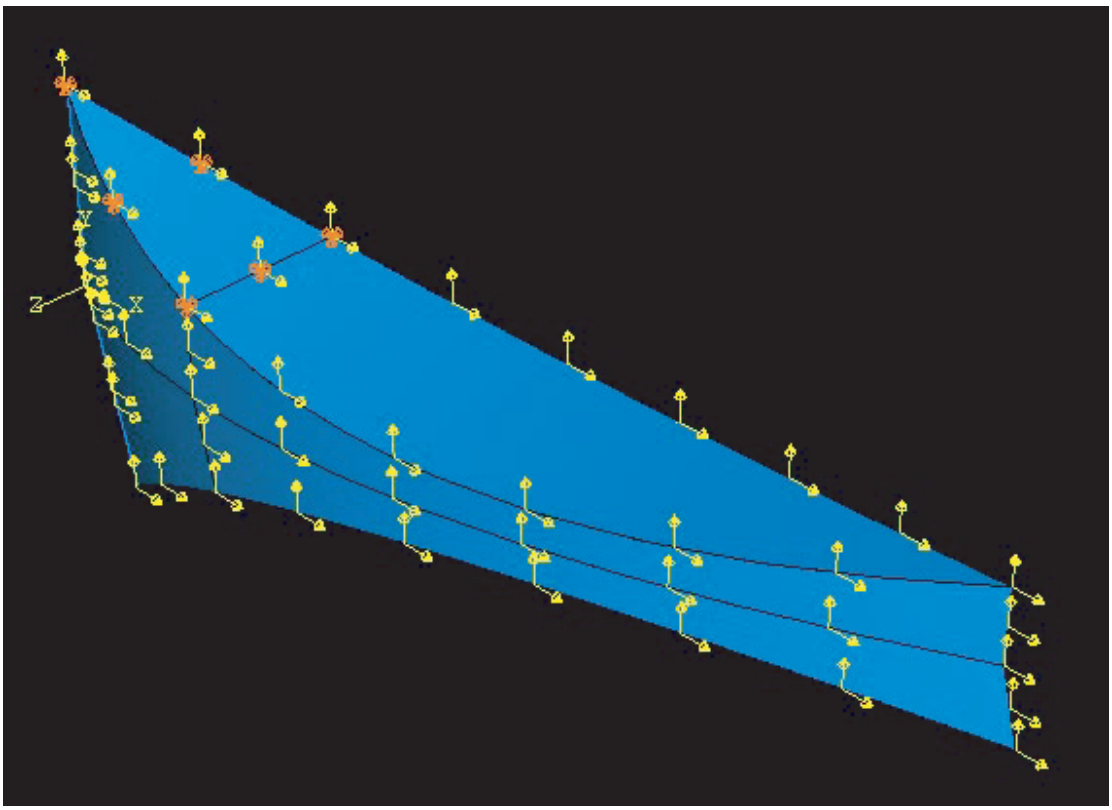

Figure 3.2: Boundary conditions and loading.

t	b_0	b_1	λ	mass	u_{max}	f_0	Tsai-Wu
(mm)	(m)	(m)	-	(kg)	(mm)	(hz)	-
varying thickness							
0.6	2	2	1.000	29.53	0.012	6.412	6.60E-05
0.8	2	2	1.000	39.38	0.010	7.169	6.35E-05
1	2	2	1.000	49.22	0.009	7.573	6.21E-05
1.2	2	2	1.000	59.07	0.009	7.916	6.07E-05
	varying width						
1	**1.8**	1.8	1.000	44.30	0.018	5.657	7.42E-05
1	**2**	2	1.000	49.22	0.009	7.573	6.21E-05
1	**2.2**	2.2	1.000	54.14	0.006	7.435	6.49E-05
			varying taper				
1	3	1	**0.333**	49.22	0.003	10.130	2.84E-05
1	2.5	1.5	**0.600**	49.22	0.005	9.210	3.08E-05
1	2	2	**1.000**	49.22	0.009	7.573	6.21E-05

Table 3.2: Sensitivity of key structural parameters to thickness, width and taper.

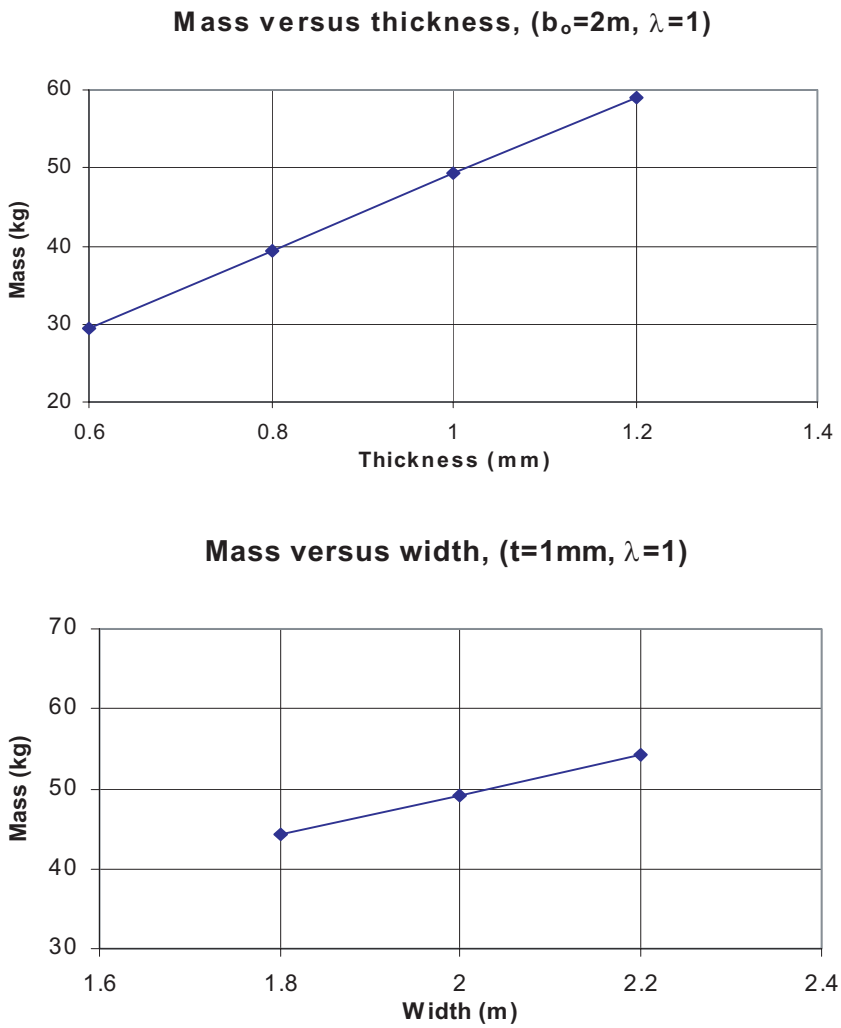

Figure 3.3: Mass versus thickness and width.

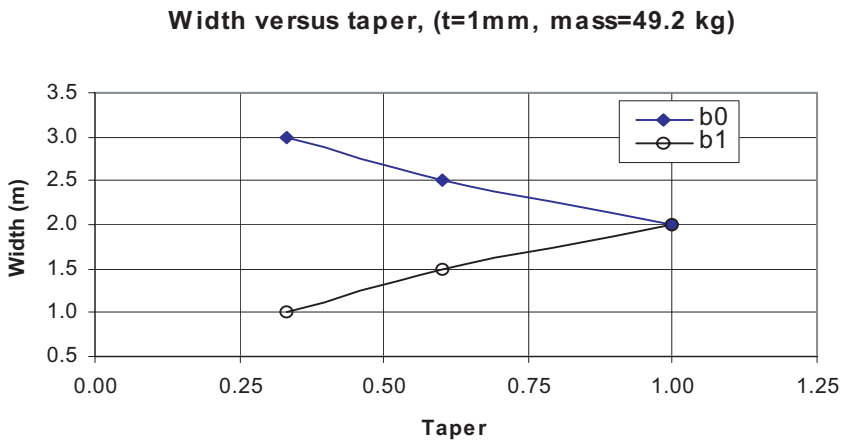

Figure 3.4: Width versus taper.

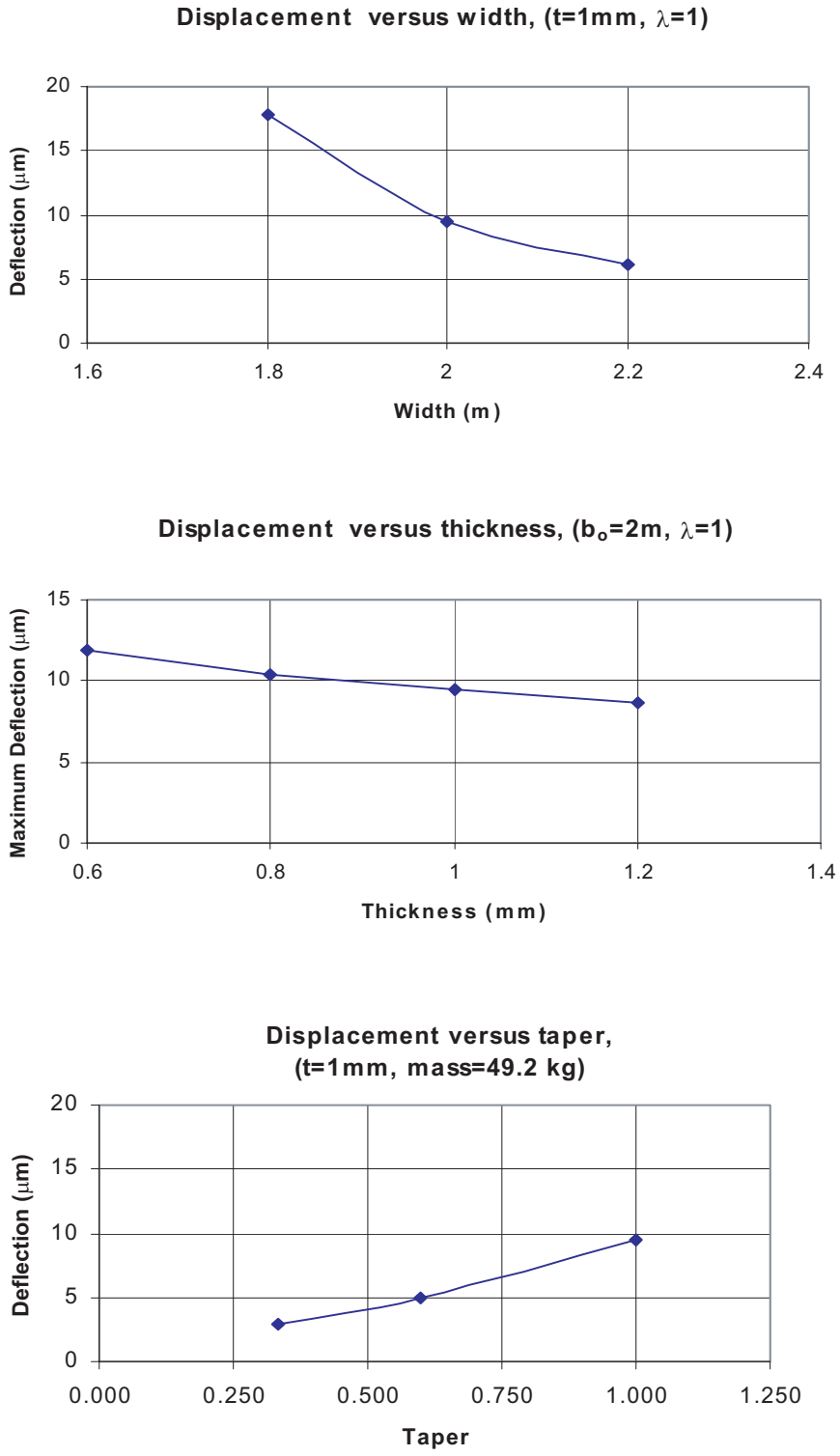

Figure 3.5: Displacement versus width, thickness, and taper.

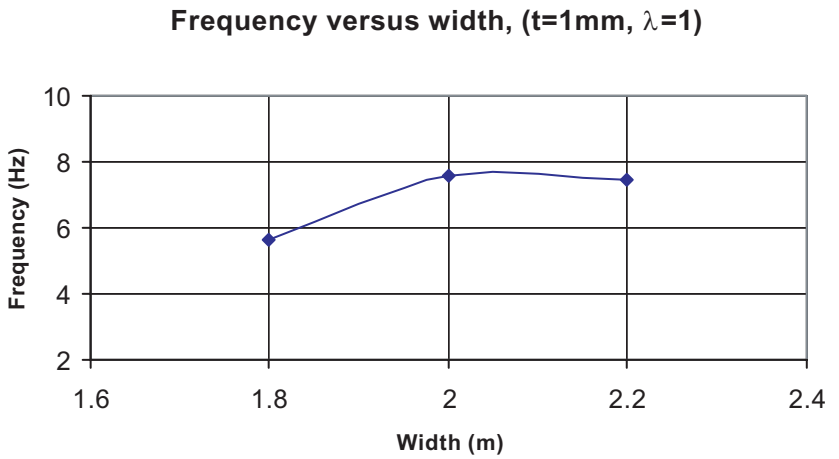

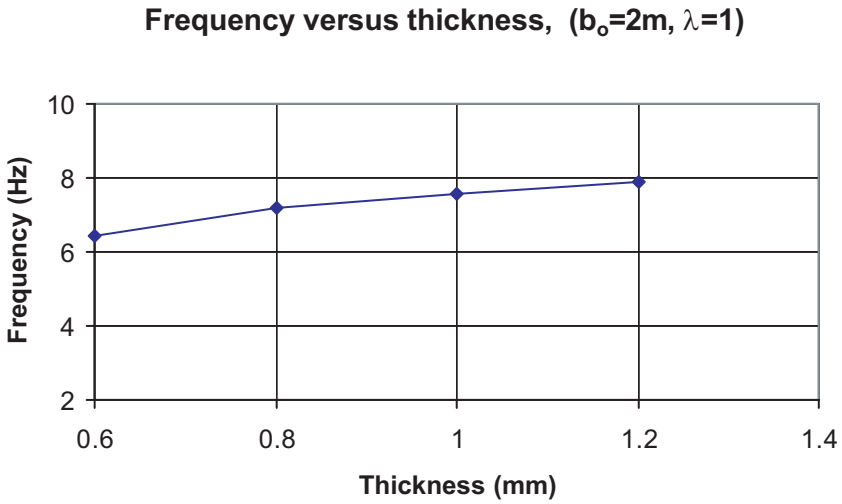

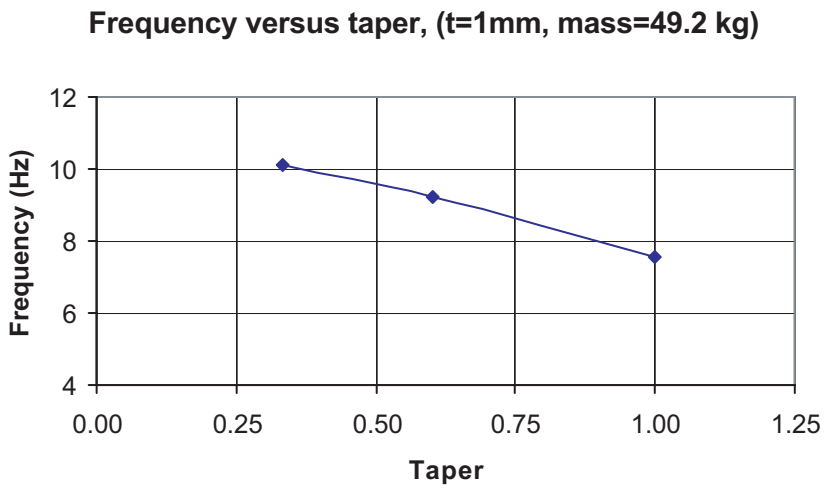

Figure 3.6: Fundamental frequency of vibration versus width, thickness, and taper.

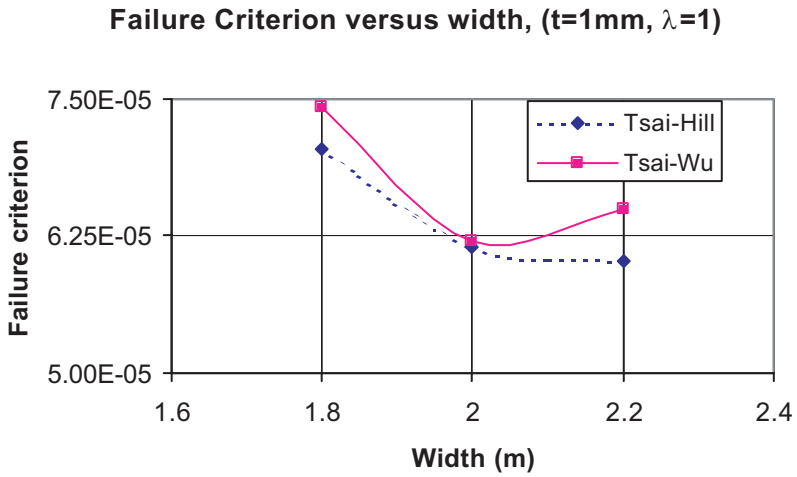

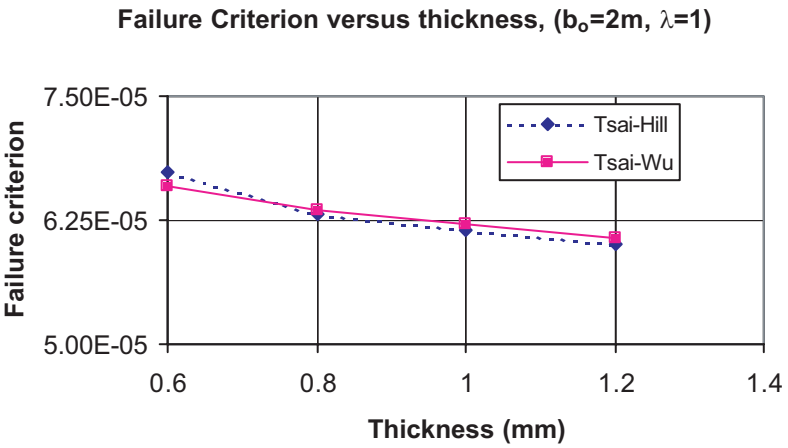

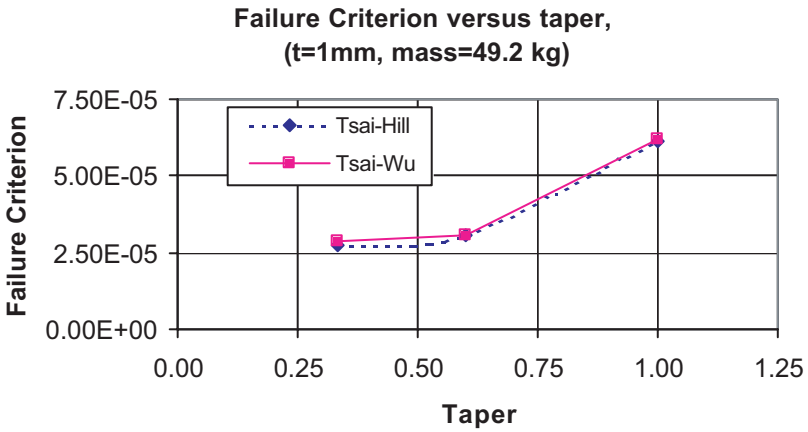

Figure 3.7: Safety margin against material failure versus width, thickness, and taper.

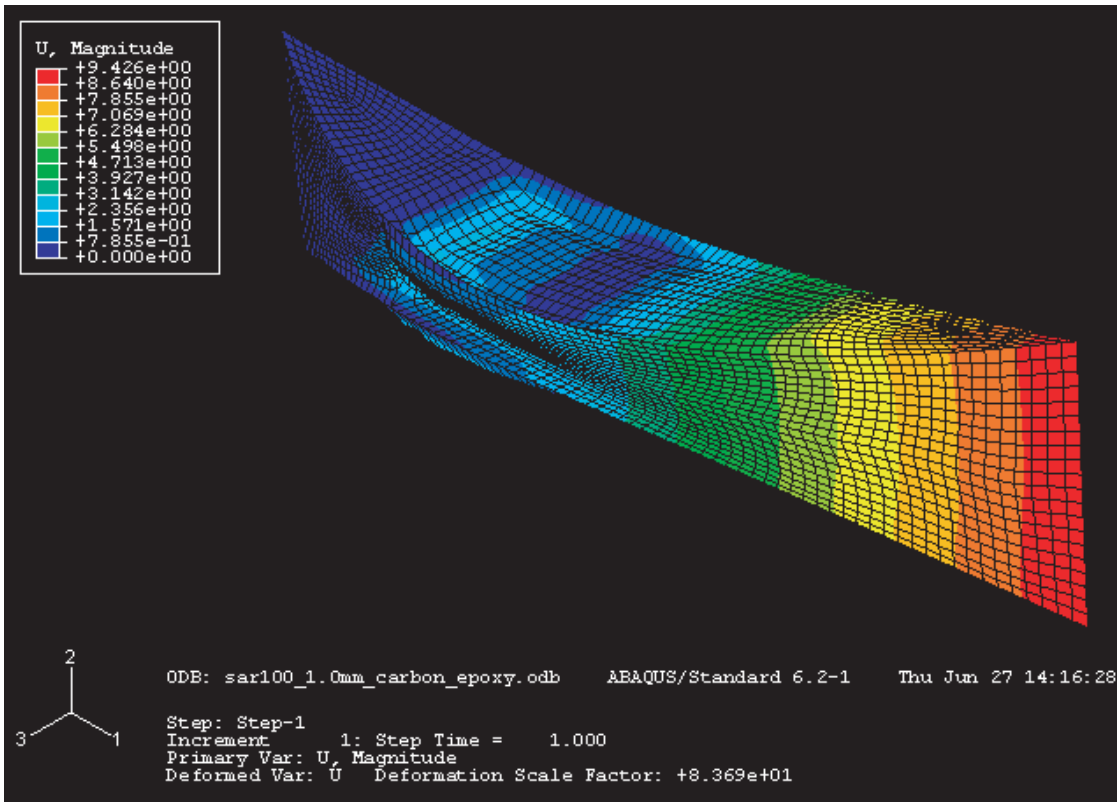

Figure 3.8: Contours of displacement magnitude (μm).

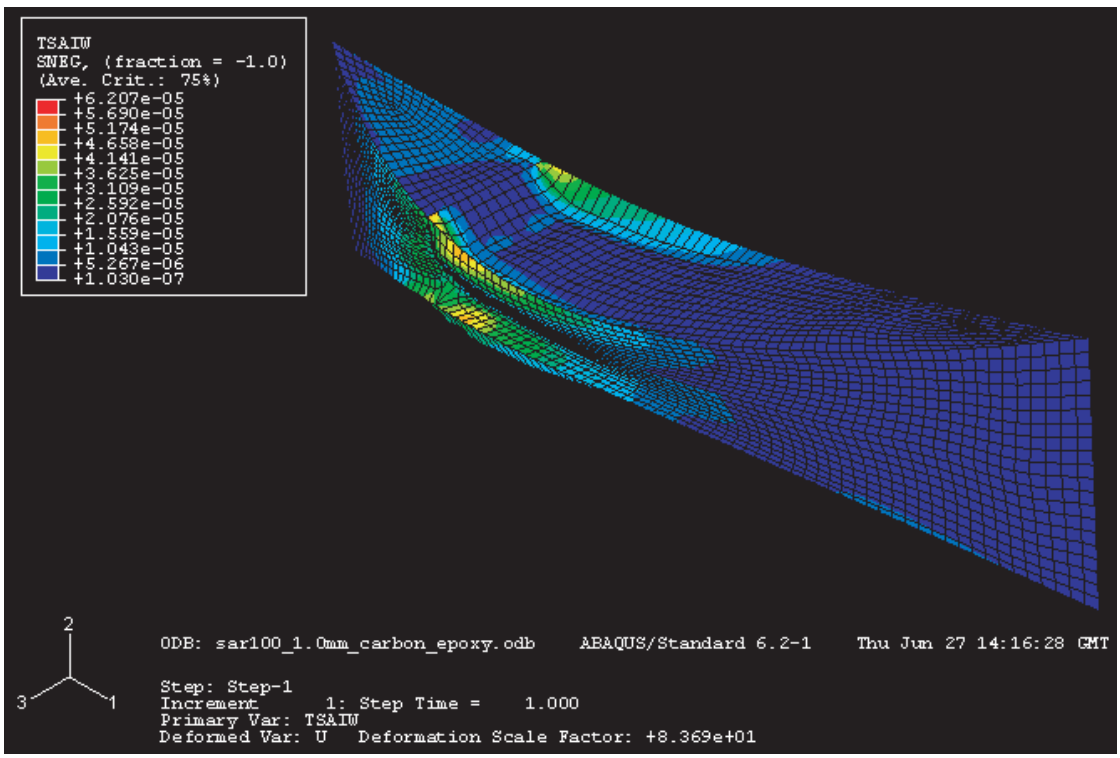

Figure 3.9: Contours of safety margin against material failure (Tsai-Wu criterion).

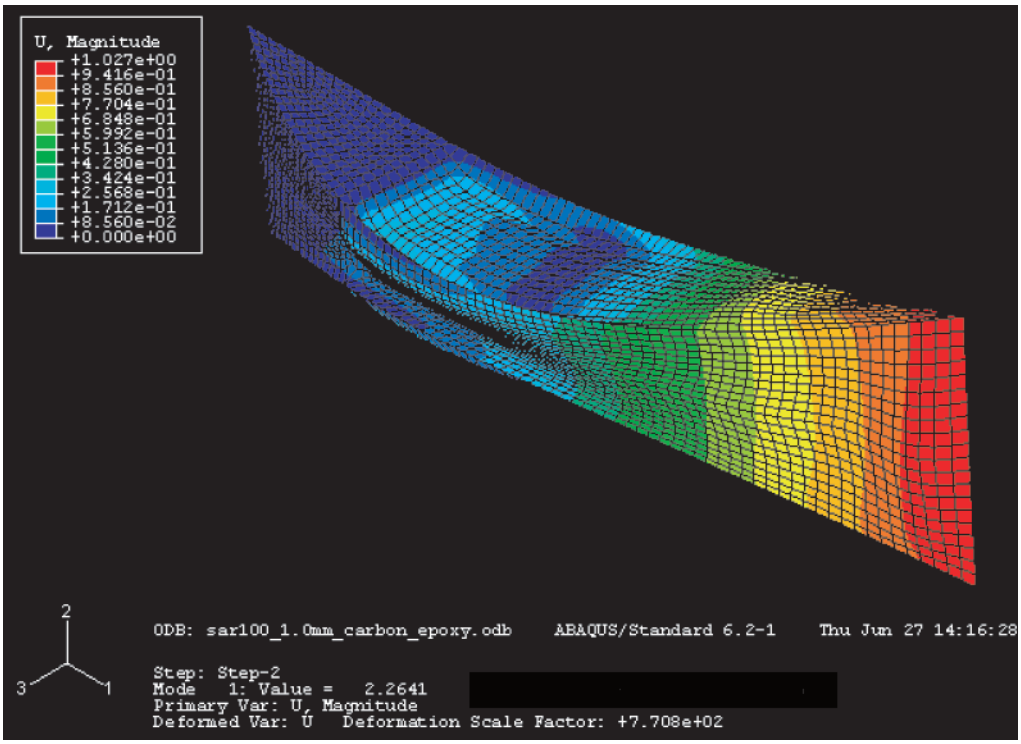

Figure 3.10: First mode (frequency=7.573 Hz).

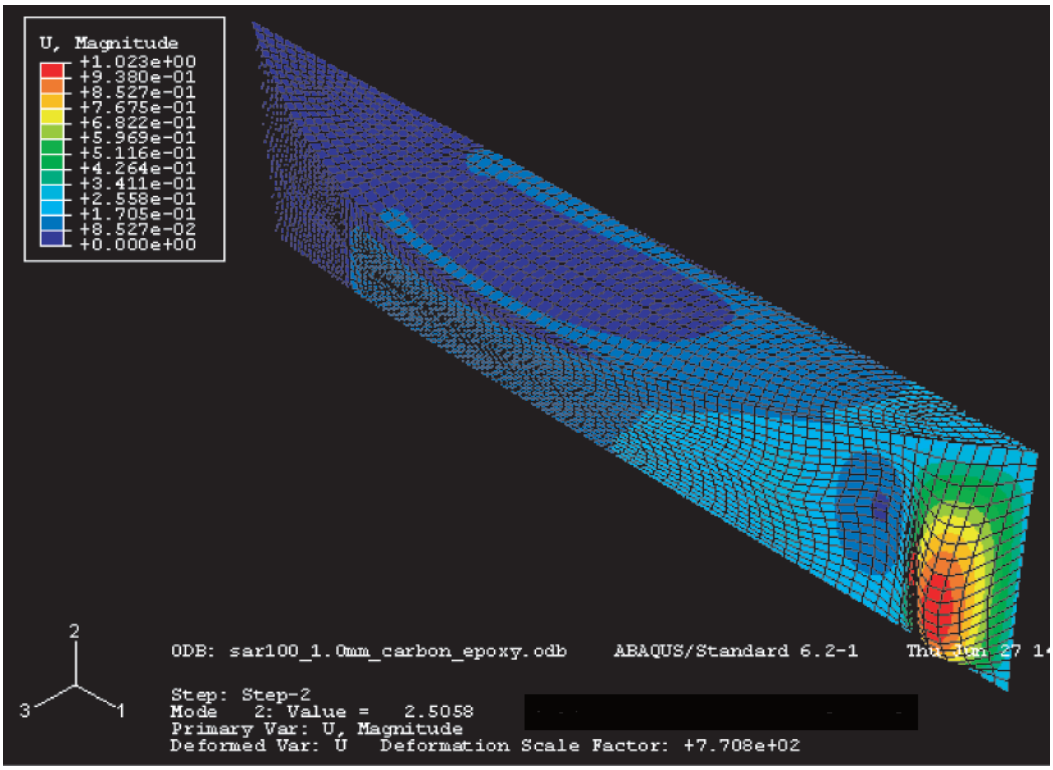

Figure 3.11: Second mode (frequency=7.967 Hz).

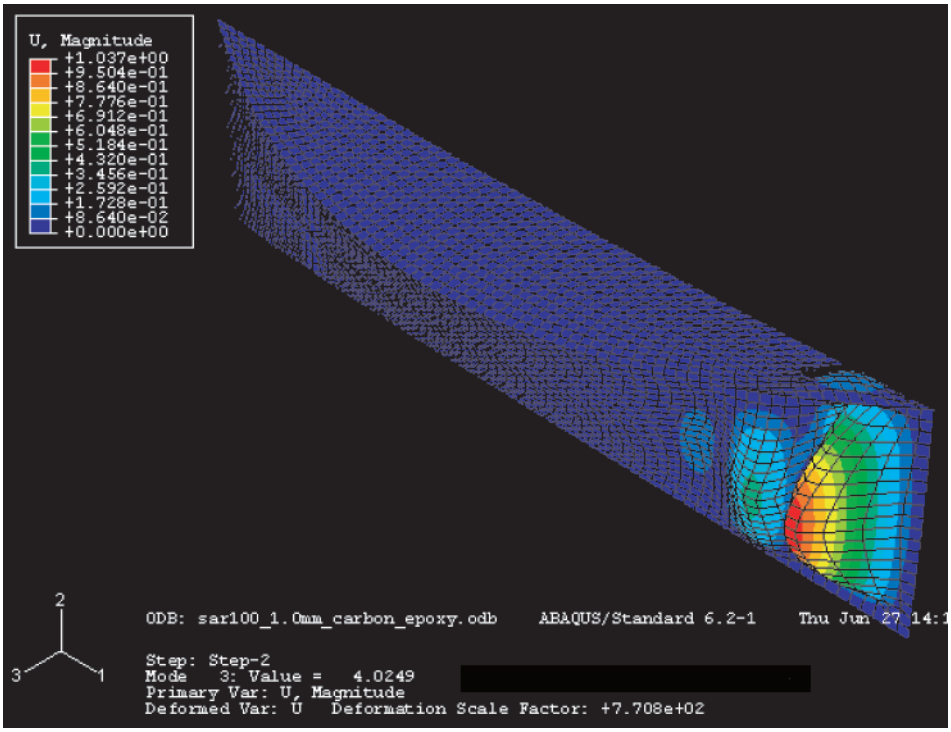

Figure 3.12: Third mode (frequency=10.097 Hz).

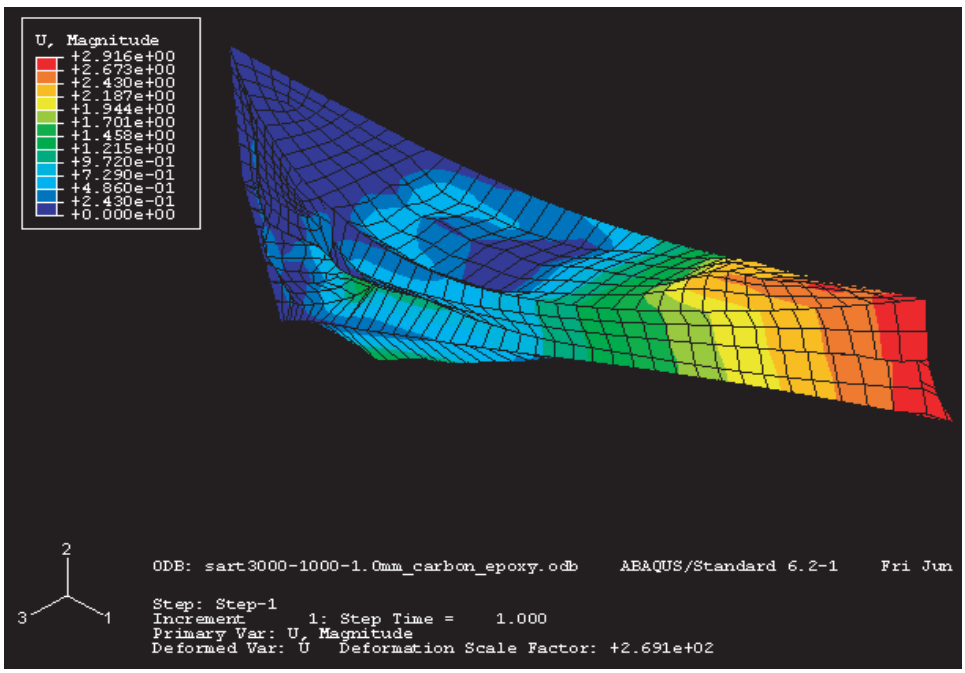

Figure 3.13: Contours of displacement magnitude (μm) for a tapered structure.

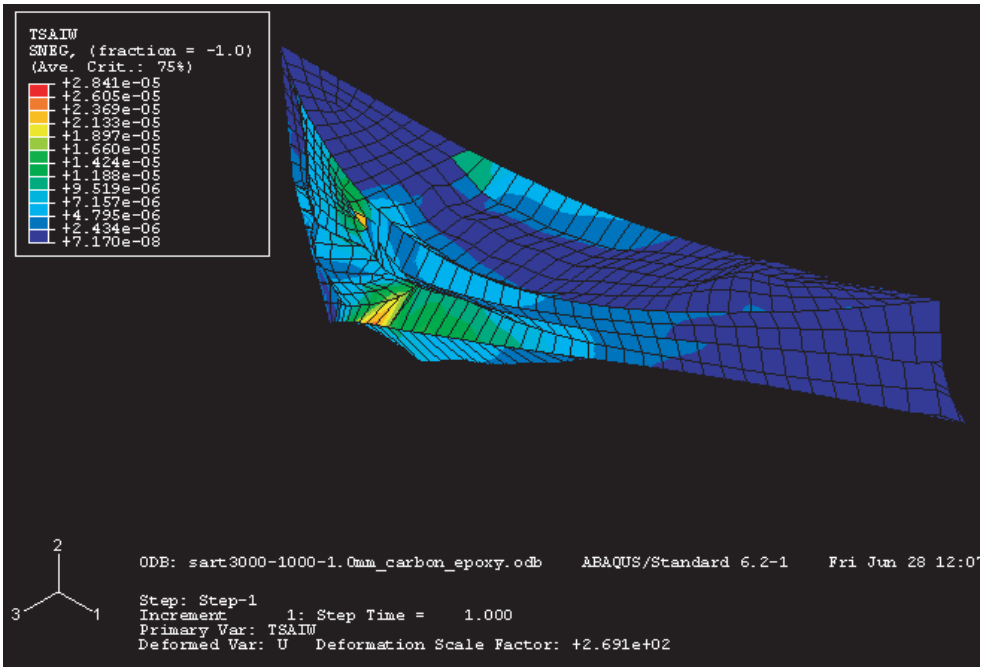

Figure 3.14: Contours of safety margin against material failure (Tsai-Wu criterion) for a tapered structure.

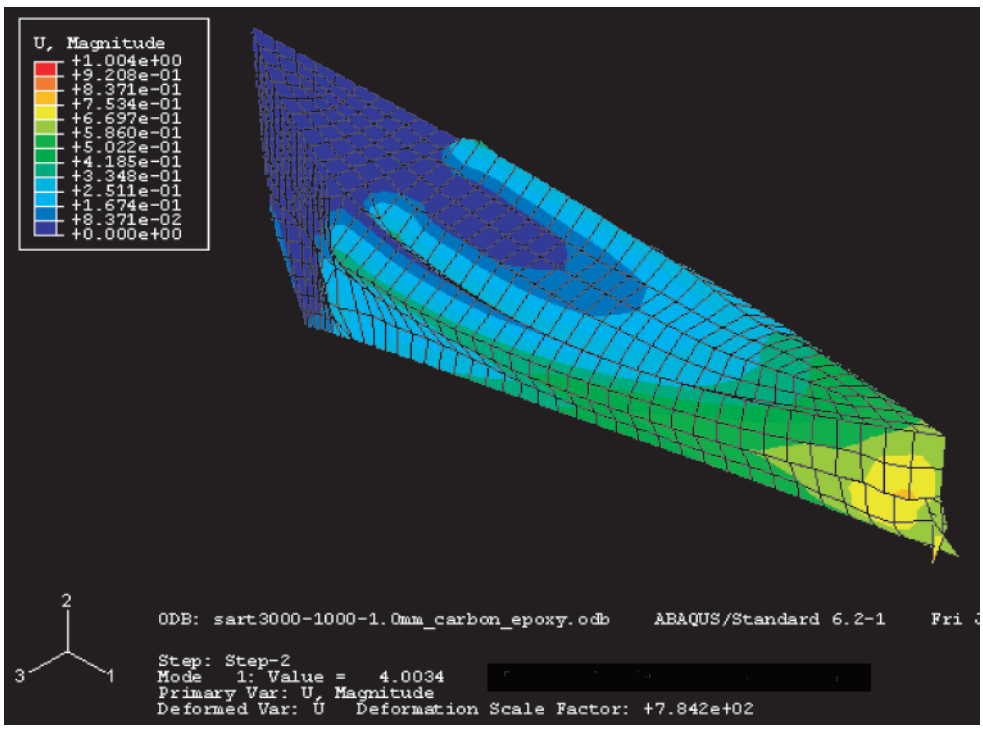

Figure 3.15: First mode (frequency=10.070 Hz).

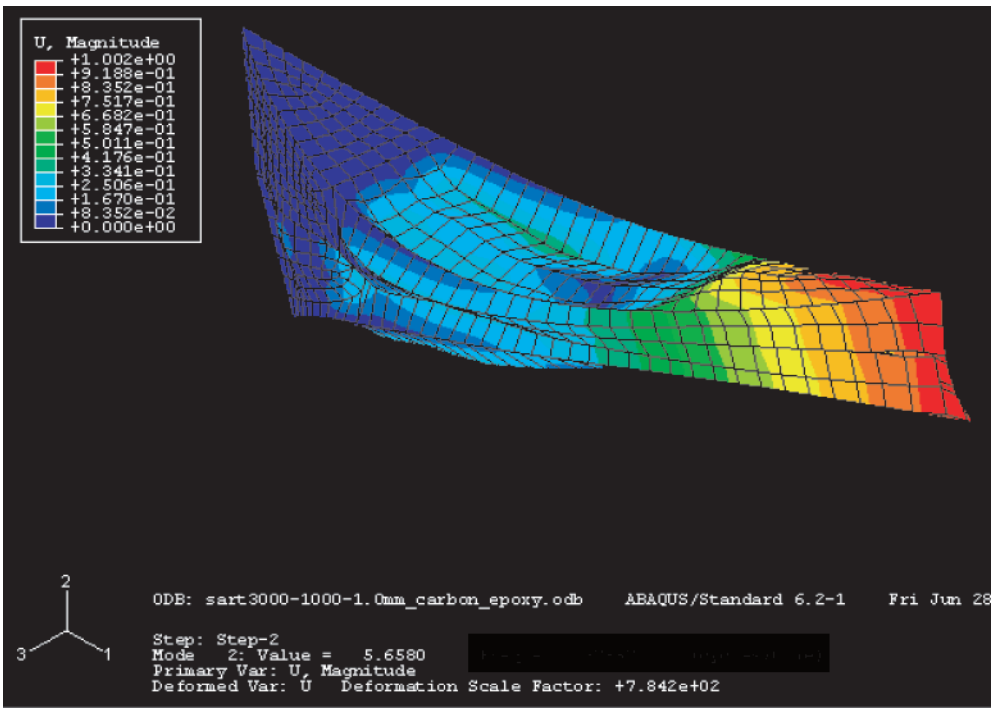

Figure 3.16: Second mode (frequency=11.097 Hz).

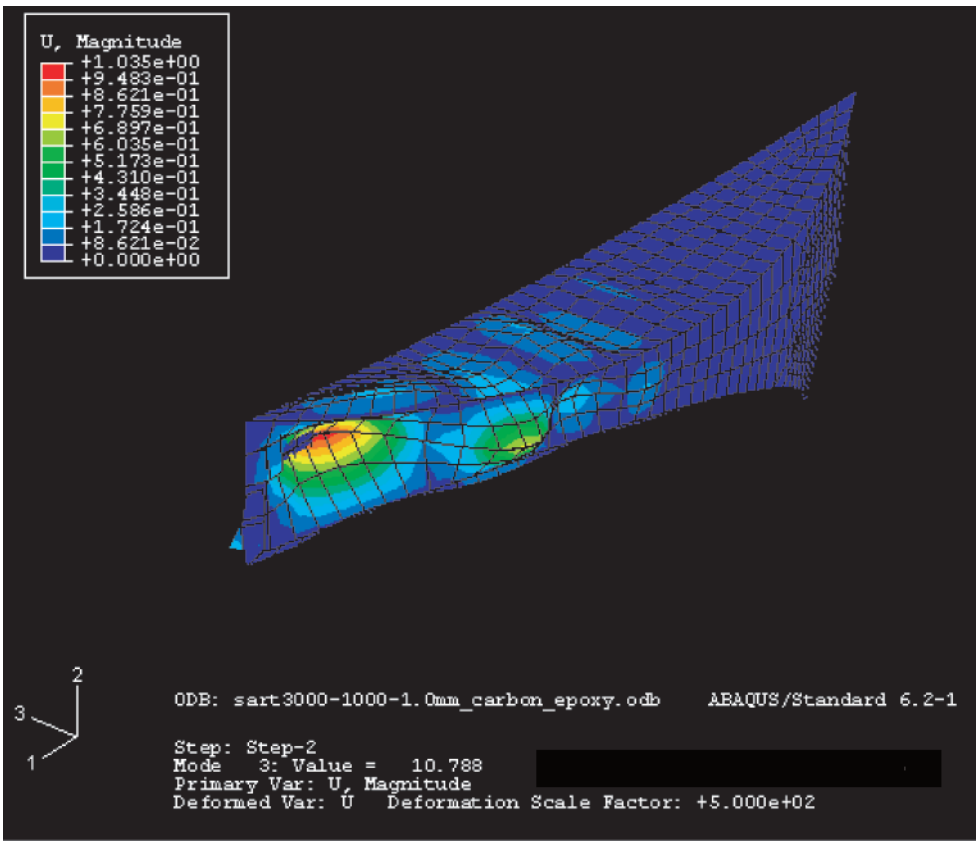

Figure 3.17: Third mode (frequency=16.531 Hz).

3.1.1 Conclusions

Increasing the thickness of the untapered support structure while keeping the width constant yields an increase in mass, fundamental natural frequency and margin against material failure, and a decrease in the magnitude of displacement.

Increasing the flattened width of the untapered support structure while keeping the thickness constant yields an increase in mass, fundamental natural frequency and the margin against material failure, and a decrease in the magnitude of displacement.

Decreasing the taper ratio λ of the support structure while keeping constant the thickness and overall mass yields an increase in natural frequency and in the margin against material failure, and a decrease in the magnitude of displacement. It is concluded that tapering is beneficial for the support structure.

3.2 Support Structure with Reflective Surface (Closed Ends, no Ribs)

This section considers a structure consisting of an untapered "hollow solid" to which the required reflective surface has been attached (in practice, there is no need to increase the thickness of the structure as the reflective surface can also carry out a structural function, but for a preliminary analysis two overlapping layers are simpler to model). The following assumptions were made in all of the analyses that are presented.

- Material: both the reflector surface and the support structure are made of woven carbon (T300) composite with average material properties given in Table 3.1.
- Uniform thickness of the support structure, t_1, and of the reflector surface t_2.
- Boundary conditions: the first quarter of the RF surface is assumed to be edgewise pinned.
- Loading: inertial loading of 0.02 m/s^2. It is assumed that the gravity vector is in the XY plane, and forms an angle of 57.5° with the X-axis so that the gravity vector is parallel to the x-axis shown in Figure 2.12. The components of the gravity vector are g_X=10.74 mm/s^2, g_Y=16.87 mm/s^2.

Table 3.3 presents the variation in the total mass of the structure, the maximum displacement due to the applied loading, the fundamental natural frequency of vibration, and the margin against material failure, using the Tsai-Wu criterion, when the wall thickness is varied.

t_1	t_2	b_0	b_1	λ	mass	u_{max}	f_0	Tsai-Wu
(mm)	(mm)	(m)	(m)	-	(kg)	(mm)	(Hz)	-
1	1	2	2	1	88.6	0.411	1.544	1.95E-03
0.8	0.25	2	2	1	49.22	1.826	0.714	6.73E-03

Table 3.3: Variation of key structural parameters with wall thickness for support structure with reflective surface.

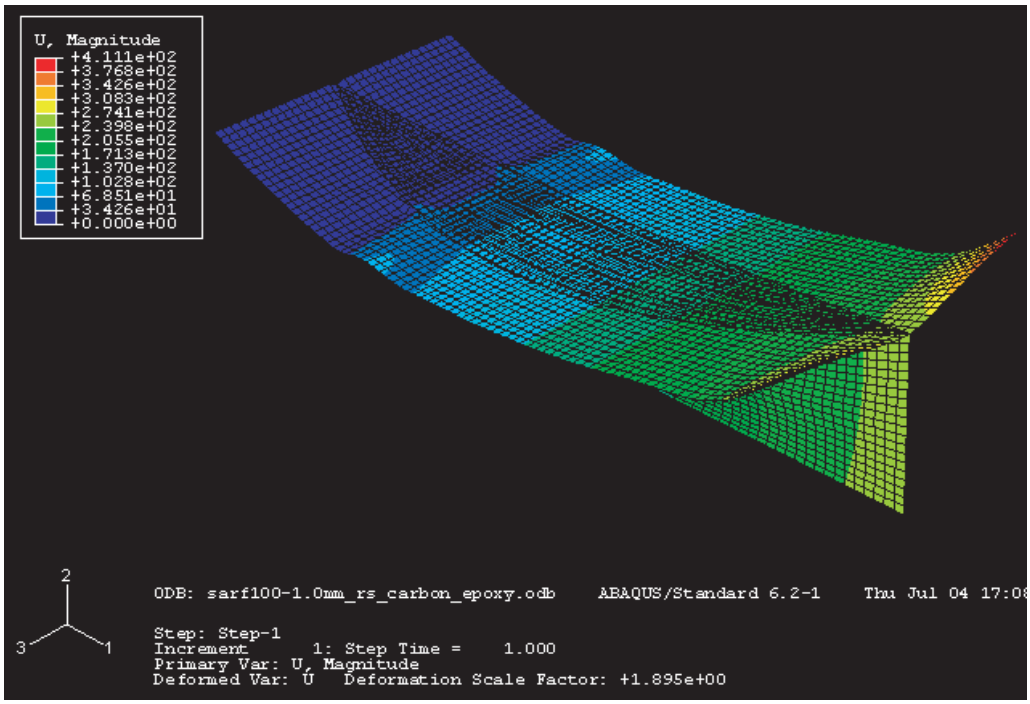

Figure 3.18: Contours of displacement magnitude (μm).

Contours of displacement magnitude, margin against material failure, and frequency are shown in Figures 3.18 to 3.22 for b_o=2m, λ=1, t_1=t_2=1 mm.

In conclusion, adding the reflector surface to the support structure results in a 40-fold increase in the magnitude of static displacement, in a decrease in the margin against material failure (by two orders of magnitude) and a decrease in the first natural frequency (by one order of magnitude).

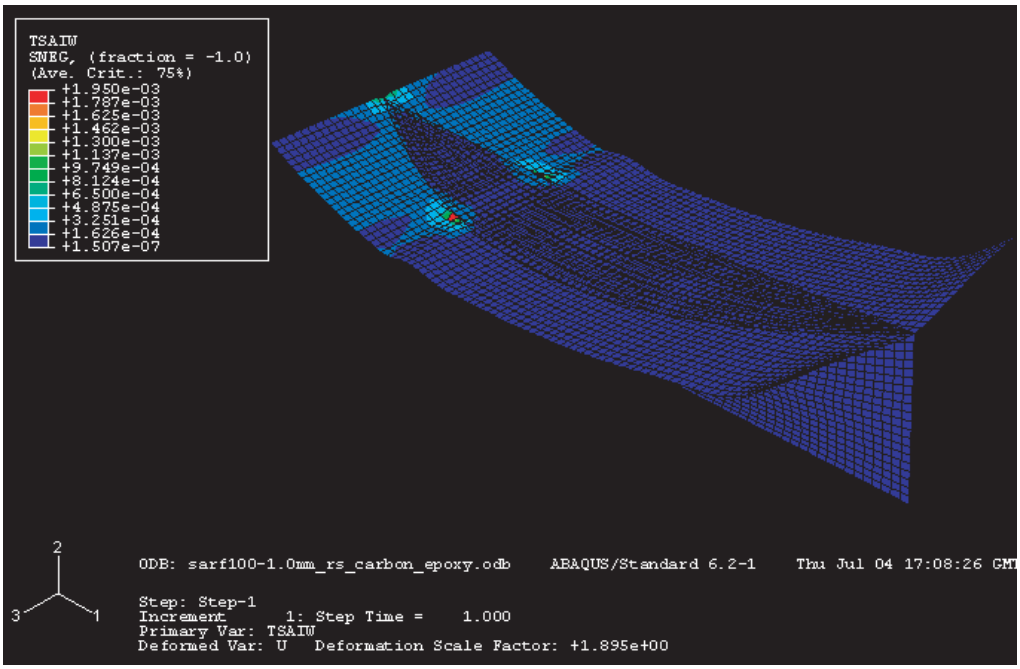

Figure 3.19: Contours of safety margin against material failure (Tsai-Wu criterion).

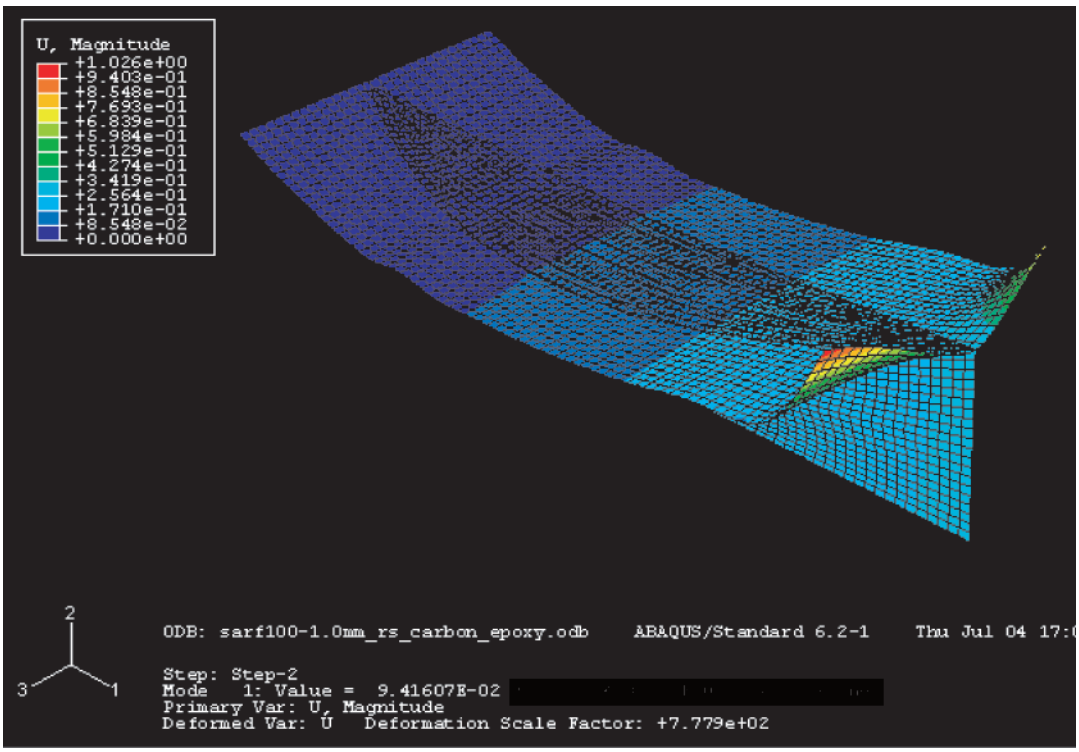

Figure 3.20: First mode (frequency=1.544 Hz).

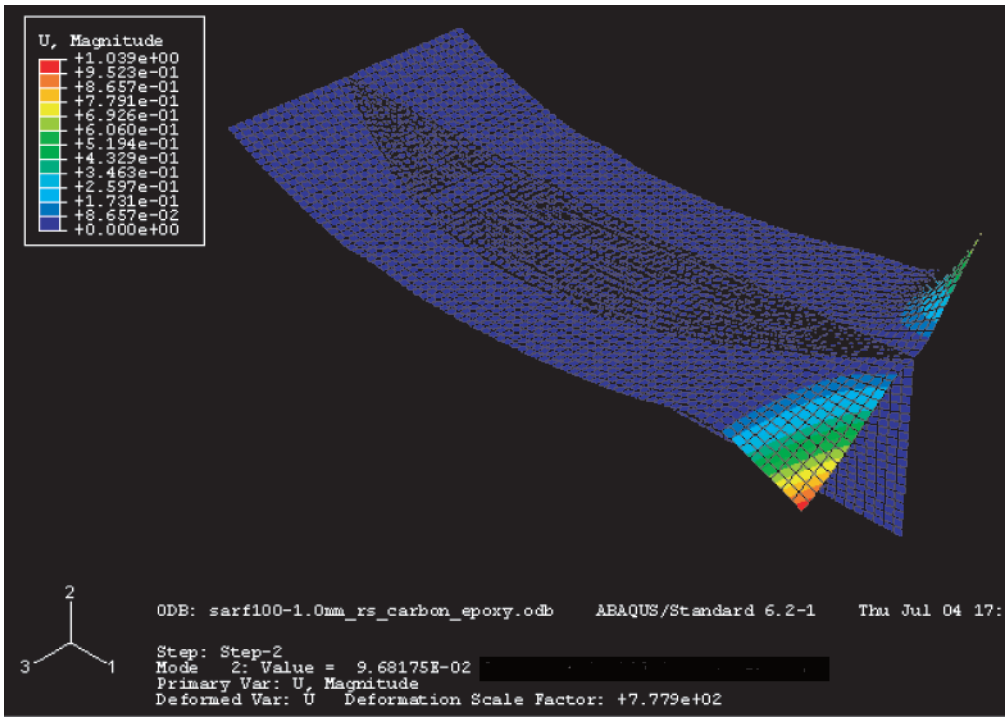

Figure 3.21: Second mode (frequency=1.566 Hz).

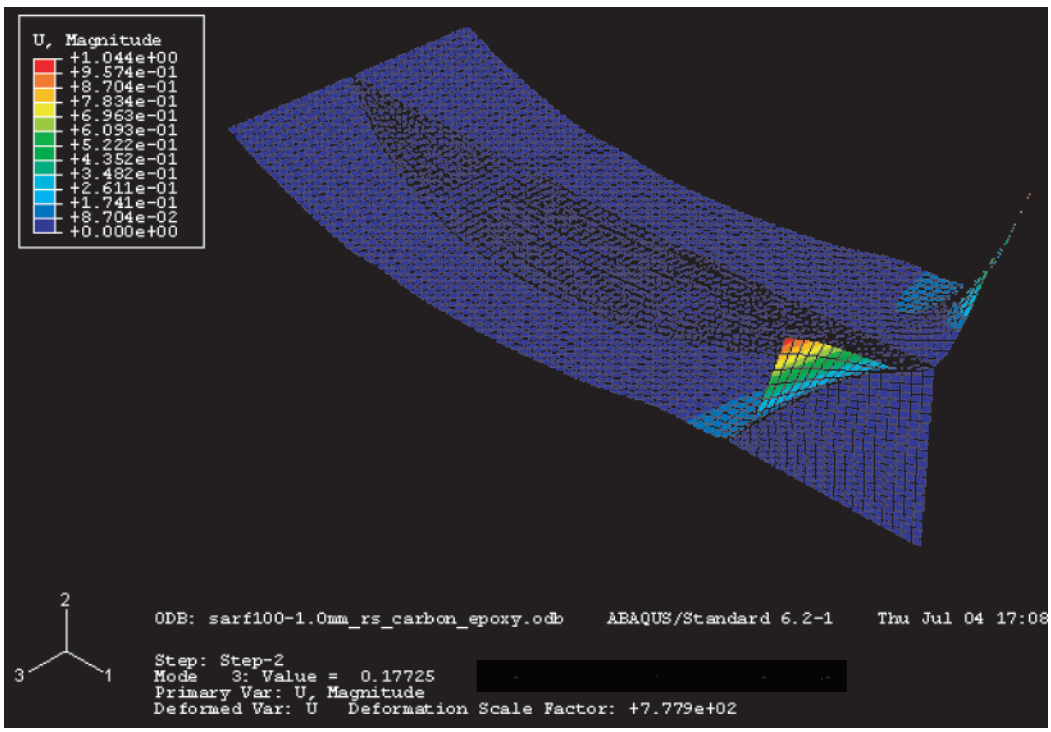

Figure 3.22: Third mode (frequency=2.119 Hz).

t_1	t_2	b_0	b_1	λ	mass	u_{max}	f_0	Tsai-Wu
(mm)	(mm)	(m)	(m)	-	(kg)	(mm)	(Hz)	-
1	1	2	2	1	89.08	0.168	1.648	6.11E-03
0.8	0.25	2	2	1	49.71	0.292	1.391	5.02E-03

Table 3.4: Variation of key structural parameters for reflective surface with ribs.

3.3 Support Structure with Reflective Surface (Closed Ends, Ribs)

Having found a large increase in the maximum displacement of the structure and a large decrease in the margin against material failure, a series of stiffeners (ribs) were added to the reflector surface. The following was assumed in the analysis:

- Lateral ribs (0.125 mm×10 mm×3.2 m) added to the structure analysed in the previous section. They are evenly distributed over the reflector surface (at 100 mm spacing) see Figure 3.23).
- Material: the whole structure, including ribs, made of woven carbon (T300) composite with average material properties as given in Figure 3.1.
- Uniform thickness of the reflector surface, t_1, and the support structure, t_2.
- Boundary conditions: the first quarter of the RF surface is edgewise pinned.
- Loading: inertial loading of 0.02 m/s^2. It is assumed that the gravity vector lies in the XY plane, and forms an angle of 57.5° with the X-axis so that the gravity vector is parallel to the x axis shown in Figure 2.12. The components of the gravity vector are g_X=10.74 mm/s^2, g_Y=16.87 mm/s^2.

Table 3.4 presents the variation in the total mass of the structure, the maximum displacement due to the applied loading, the fundamental natural frequency of vibration, and the margin against material failure, using the Tsai-Wu criterion, when the wall thickness is varied.

Contours of displacement magnitude, margin against material failure, and frequency are shown in Figures 3.24 to 3.28 for b_o=2 m, λ=1, t_1=t_2=1 mm.

In conclusion, supporting the reflective surface on closely spaced ribs has the effect of reducing the maximum deflection to about 40% and of slightly increasing the fundamental natural frequency. However, there is still a large difference in the magnitude of displacement, the margin

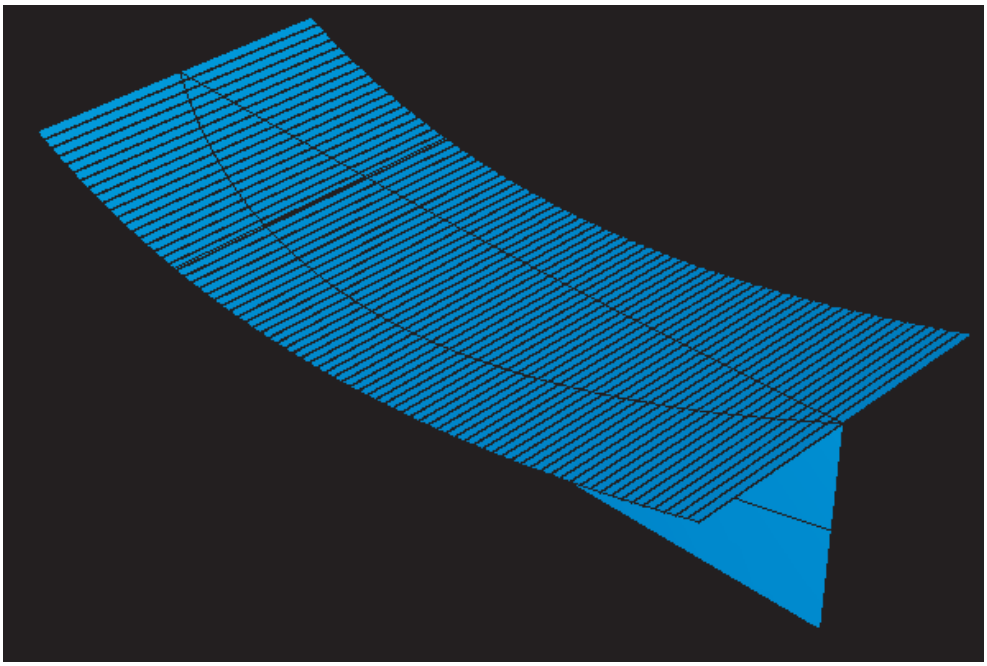

Figure 3.23: Reflective surface with ribs.

against material failure (by two orders of magnitude), and in the first natural frequency (by one orders of magnitude) when compared to the results of the support structure by itself.

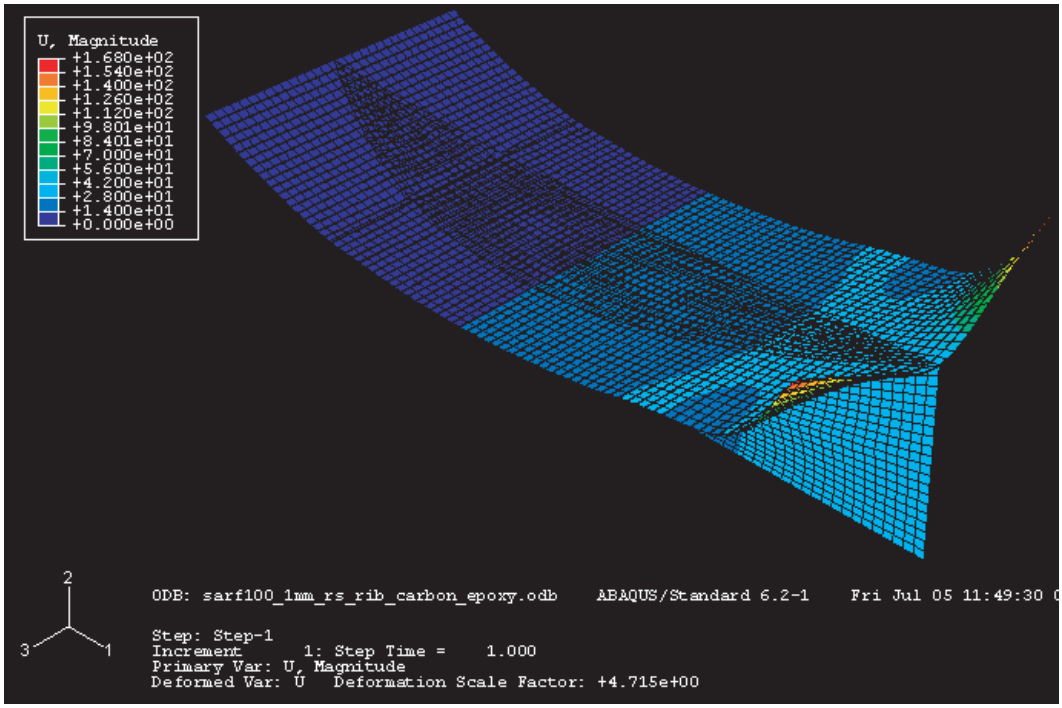

Figure 3.24: Contours of displacement magnitude (μm) for ribbed reflective surface.

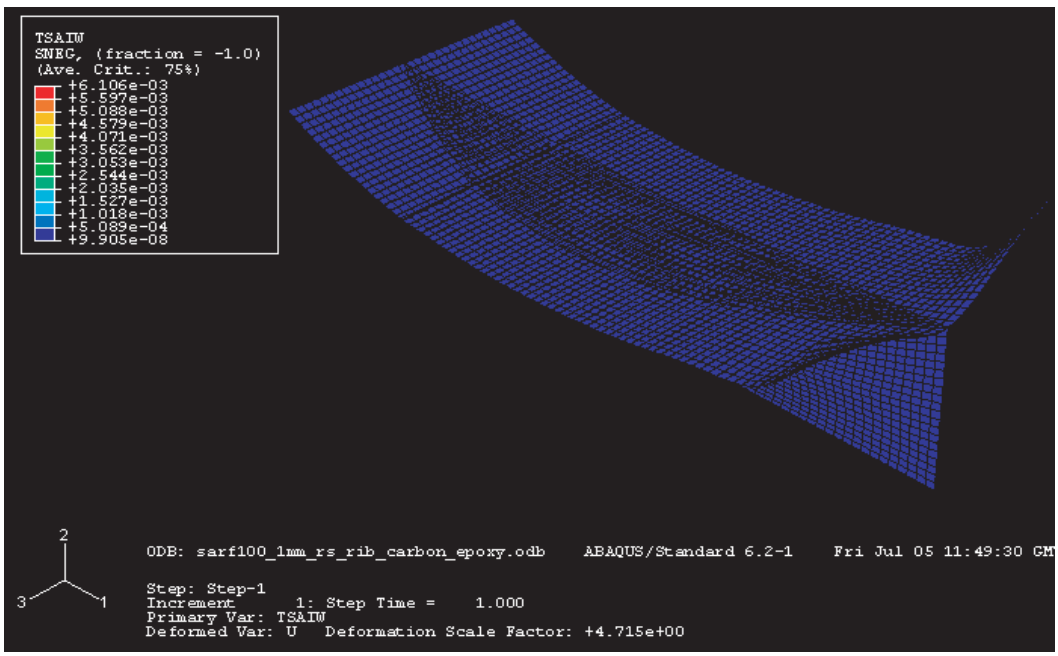

Figure 3.25: Contours of safety margin against material failure (Tsai-Wu criterion) for ribbed reflective surface.

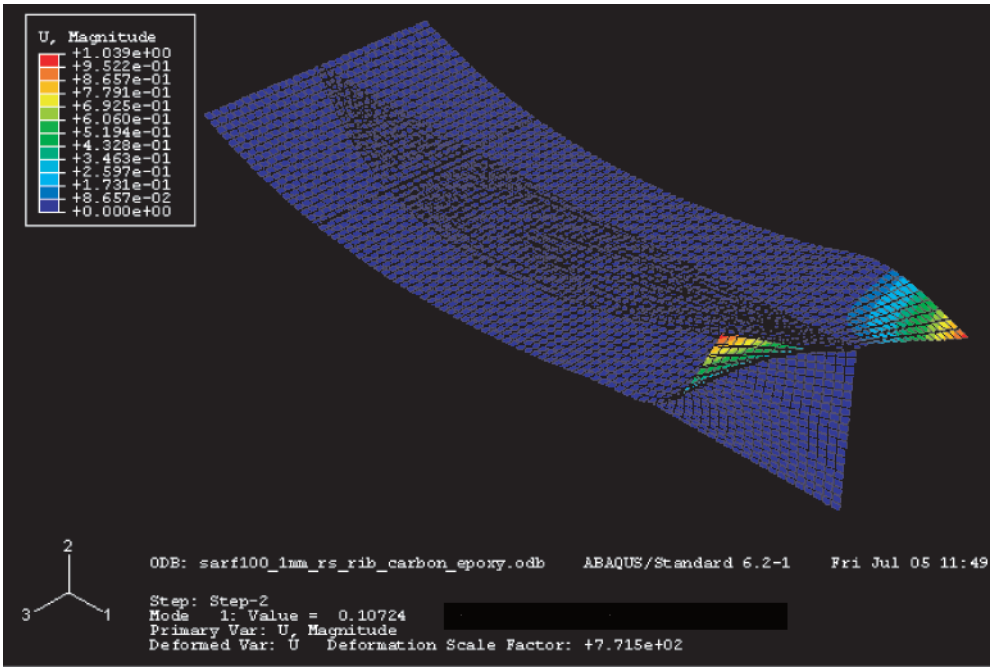

Figure 3.26: First mode (frequency=1.648 Hz).

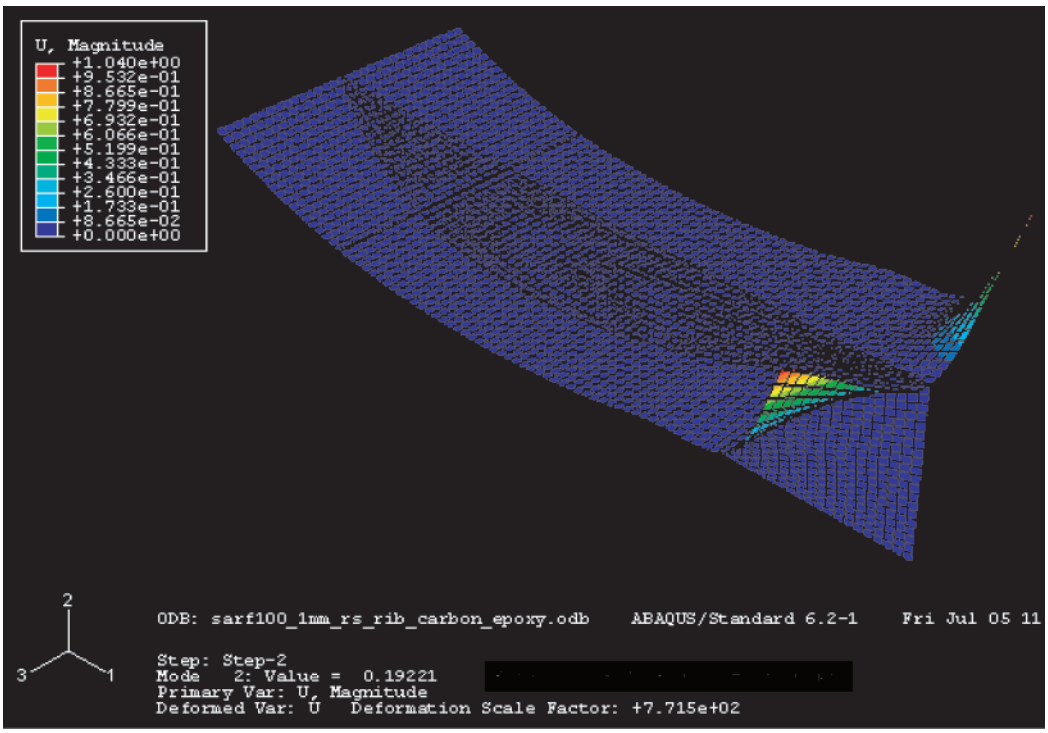

Figure 3.27: Second mode (frequency=2.207 Hz).

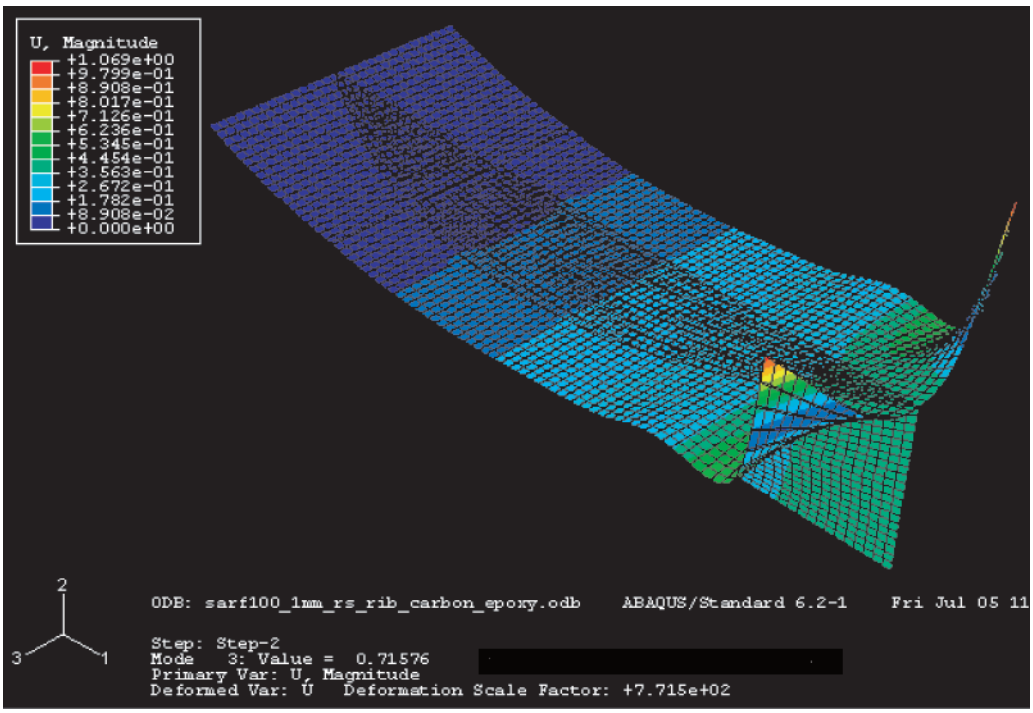

Figure 3.28: Third mode (frequency=4.258 Hz).

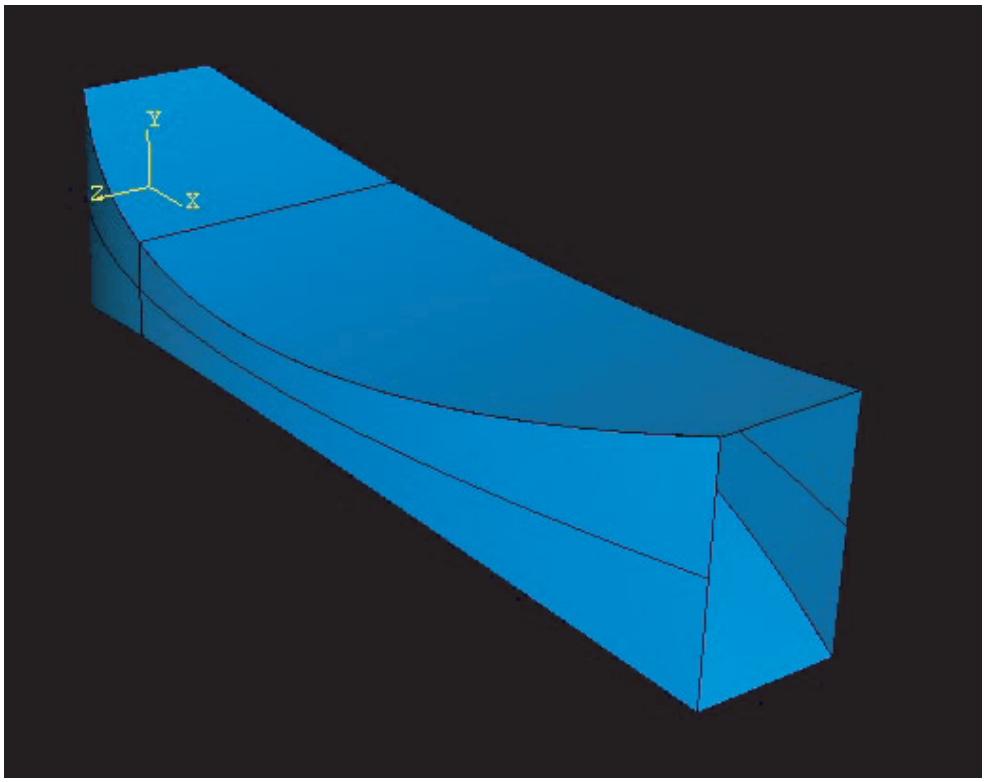

Figure 3.29: Support structure with open ends.

3.4 Support Structure with Reflective Surface (Open Ends)

Comparing the response of the complete structure (reflective surface plus support), in Sections 3.2 and 3.3 with that of the support structure itself, in Section 3.1, shows that there are large differences in deflection, frequency and margin against material failure.

The support structure firmly holds the reflective surface along two hinge lines. However the two hinge lines meet at the ends, and hence here the reflective surface is supported only at a single point. This allows the ends of the reflective surface freedom to rotate.

To increase the stiffness against this deformation mode, an alternative configuration of the support structure was investigated. This new "open-ended" configuration, shown in Figure 3.29 is obtained by moving apart the sidewalls of the support structure outward. It will be assumed that the end separation between the two sidewalls is such that, when the structure is flattened, it has the same width as the RF surface.

It was also decided to extend the analysis, to check against overall and local buckling. Finally, in order to compare different designs quantitatively, the following multi-objective performance

criterion was defined

$$F = K_1\frac{m_{ref}}{m} + K_2\frac{u_{ref}}{u} + K_3\frac{f_0}{f_{0ref}} + K_4\frac{F_{TWref}}{F_{TW}} + K_5\frac{B_{Lref}}{B_L} + K_6\frac{B_{Gref}}{B_G} \tag{3.1}$$

where K_i is a weighting factor; m is the total mass of the reflector; u is the maximum deflection magnitude; f_0 is the first natural frequency of the reflector; F_{TW} is the margin against material failure given by the Tsai-Wu criterion; B_L is the margin against local buckling; B_G is the margin against global buckling; the subscript ref represents the reference values of the objectives.

Note that there are two buckling terms in the criterion: global buckling and local buckling. The first estimate for buckling is obtained by finite element analysis, and represents the buckling behavior of the whole structure. It is called global buckling although the buckling mode may not be global. To carry out a buckling analysis in ABAQUS, the model used for static and/or natural vibration analysis needs to be modified, which makes the evaluation of this performance criterion expensive.

A simple, preliminary estimate of the buckling margin can be obtained from the standard formula based on the classical analysis of isotropic cylinders (Peery and Azar 1982)

$$\sigma_{cr} = 0.606\frac{Et}{R} \tag{3.2}$$

where E is the Young's modulus, t the thickness of the cylinder, and R its local radius of curvature. This equation is used for checking the buckling margin of individual surfaces of the reflector, and the smallest value is the margin against local buckling used in Equation 3.2.

According to the static analysis results from ABAQUS, the maximum compression stress occurs in the first quarter region of the reflector (near the root support). The average radius of curvature of the surfaces in this region is 10 m. The buckling margin is calculated for the thinnest surface in this region, as the ratio between the maximum stress from the static analysis and the buckling stress.

The following assumptions were made in the analysis:

- Material: Reflector surface, beams and support structure all made of woven carbon (T300) composite with average material properties as given in Figure 3.1.
- Upper surface of single thickness, reflector surface of uniform thickness t_1 and support structure of uniform thickness t_2.
- Boundary conditions: the first quarter of the RF surface is edgewise pinned.
- Loading: inertial loading of 0.02 m/s^2. It is assumed that the gravity vector is in the XY plane, and forms angle of 57.5° with the X-axis so that the gravity vector is parallel to the

closed ends

support structure+reflector surface (3.2mx7.888m), (1/4 of the reflector surface edgewise pinned)

t_1	t_2	b_0	b_1	λ	mass	u_{max}	f_0	Tsai-Wu	L.Buckling	Performance
(mm)	(mm)	(m)	(m)	-	(kg)	(mm)	(hz)	-	%	(maximize)
0.36	0.36	2	2	1	27.49	0.617	0.877	1.65E-04	3.34	0.65

open ends

support structure+reflector surface (3.2mx7.888m)(1/4 of the reflector surface edgewise pinned)

t_1	t_2	b_0	b_1	λ	mass	u_{max}	f_0	Tsai-Wu	L.Buckling	Performance
(mm)	(mm)	(m)	(m)	-	(kg)	(mm)	(hz)	-	%	(maximize)
0.3	0.3	2	2	1	27.49	0.245	0.5213	1.46E-04	4.77	0.63

closed ends

support structure+reflector surface (3.2mx7.888m)+root and tip beams (r=10mm,t=1mm) (1/4 of the reflector surface edgewise pinned)

t_1	t_2	b_0	b_1	λ	mass	u_{max}	f_0	Tsai-Wu	L.Buckling	Performance
(mm)	(mm)	(m)	(m)	-	(kg)	(mm)	(hz)	-	%	(maximize)
0.36	0.36	2	2	1	28.09	0.047	1.518	1.20E-04	3.32	0.91

open ends

support structure+reflector surface (3.2mx7.888m)+root and tip beams (r=10mm,t=1mm) (1/4 of the reflector surface edgewise pinned)

t_1	t_2	b_0	b_1	λ	mass	u_{max}	f_0	Tsai-Wu	L.Buckling	Performance
(mm)	(mm)	(m)	(m)	-	(kg)	(mm)	(hz)	-	%	(maximize)
0.3	0.3	2	2	1	29.06	0.038	3.3088	1.58E-04	5.16	1

Table 3.5: Comparison of reflector structures with closed or open ends.

x axis shown in Figure 2.12. The components of the gravity vector are g_X=10.74 mm/s^2, g_Y=16.87 mm/s^2.

- The end opening of the support structure is $3.2 - b_0$.

3.4.1 Closed or Open Ends?

Ignoring global buckling (the effect of which will be considered later), the weighting factors are taken to be K_1=10/25, K_2=7/25, K_3=5/25, K_4=1/25, K_5=2/25. The reference values for these performance parameters are based on the reflector with open ends and tubular beams, $t_1 = t_1$ =0.3 mm, $b_0 = b_1$=2 m, whose performance is defined to be unity. To improve the performance, tubular beams (radius=10 mm, thickness=1 mm) are added to the root and tip of the reflector surface. The results are compared, for untapered support structure, in Table 3.5.

In Table 3.5, t_1 is the thickness of the support structure; t_2 is the thickness of the reflective surface; b_0 is the depth at the root; b_1 is the depth at the tip; λ is the taper ratio b_1/b_0.

According to the results presented in the table, when there is no stiffening at the ends of the reflective surface, the reflector with closed ends performs slightly better than the reflector with open ends. However if the ends of the reflective surface are stiffened, the reflector with open

open ends

support structure+reflector surface (3.2mx7.888m)+root and tip beams (r=5mm) (1/4 of the reflector surface edgewise pinned)

t_1	t_2	b_0	b_1	λ	mass	u_{max}	f_0	Tsai-Wu	L.Buckling	Performance
(mm)	(mm)	(m)	(m)	-	(kg)	(mm)	(hz)	-	%	(maximize)
0.6	0.125	2	2	1	38.34	0.049	1.4289	1.59E-04	6.49	0.71
0.6	0.25	2	2	1	43.26	0.044	1.4108	9.59E-05	3.63	0.78

support structure+reflector surface (3.2mx7.888m)+root and tip beams (r=10mm) (1/4 of the reflector surface edgewise pinned)

t_1	t_2	b_0	b_1	λ	mass	u_{max}	f_0	Tsai-Wu	L.Buckling	Performance
(mm)	(mm)	(m)	(m)	-	(kg)	(mm)	(hz)	-	%	(maximize)
0.6	0.125	2	2	1	44.52	0.05	2.7624	1.94E-04	7.96	0.73
0.6	0.25	2	2	1	49.44	0.036	3.9696	1.16E-04	4.36	0.93
0.4	0.25	2	2	1	38.99	0.041	3.9914	1.50E-04	6.05	0.91

support structure+reflector surface (3.2mx7.888m)+root and tip beams (r=10mm,t=1mm) (1/4 of the reflector surface edgewise pinned)

t_1	t_2	b_0	b_1	λ	mass	u_{max}	f_0	Tsai-Wu	L.Buckling	Performance
(mm)	(mm)	(m)	(m)	-	(kg)	(mm)	(hz)	-	%	(maximize)
0.4	0.25	2	2	1	32.32	0.036	3.1835	1.18E-04	4.7	0.99

Table 3.6: Reflectors with different end beams.

ends performs much better than the reflector with closed ends.

3.4.2 Effect of End Beams

The effect of different end beams on the performance of the reflector structure was studied in greater detail. The use of solid or thin walled cylindrical beams is compared in Table 3.6 for an open-ended reflector.

First, the beams were assumed to be a solid cylinder with cross-sectional radius of either $r = 5$ mm or $r = 10$ mm. When the thickness and depth of the reflector are kept constant, the solid cylindrical beams with $r = 10$ mm give better performance. Then, thin-walled cylindrical beams ($r = 10$ mm, $t = 1$ mm) were considered, and it was found that they give better results than solid beams.

3.4.3 Optimization of Reflector with Open Ends

The reflector with open ends and thin-walled beams was further studied by varying the design parameters that relate to thickness, depth, and taper. Overall buckling of the reflector was taken into account along with local buckling. The results are shown in Table 3.7.

The weighting factors in Equation 3.1 were taken as K_1=10/27, K_2=7/27, K_3=5/27, K_4=1/27, K_5=2/27, and K_6=2/27. The reference values of the performance parameters are based on the reflector with open ends and tubular beams with $t_1 = t_1$=0.3 mm, $b_0 = b_1 = 2$ m, whose performance is defined to be unity.

From Table 3.7, it is concluded that thinner structures are best and it is not worth using

support structure+reflector surface (3.2mx7.888m)+root and tip beams (r=10mm,t=1mm) (1/4 of the reflector surface edgewise pinned)											
t_1	t_2	b_0	b_1	λ	mass	u_{max}	f_0	Tsai-Wu	L.Buckling	G.Buckling	Performance
(mm)	(mm)	(m)	(m)	-	(kg)	(mm)	(Hz)	-	%	%	(maximize)
0.21	0.21	2	2	1	20.81	0.048	3.5334	1.85E-04	8.50	2.10	1.04
0.3	**0.3**	**2**	**2**	**1**	**29.06**	**0.038**	**3.3088**	**1.58E-04**	**5.16**	**1.21**	**1.00**
0.4	0.25	2	2	1	32.32	0.036	3.1835	1.18E-04	4.70	1.56	0.97
0.4	0.4	2	2	1	38.22	0.033	2.9949	1.38E-04	3.45	0.76	1.02
0.3	0.3	1.6	1.6	1	27.51	0.204	1.6692	4.32E-04	17.66	2.82	0.60
0.4	0.4	1.6	1.6	1	36.18	0.173	1.8180	3.71E-04	11.52	1.67	0.56
0.3	0.3	1.8	1.8	1	28.28	0.061	3.1136	2.27E-04	7.66	1.27	0.86
0.4	0.4	1.8	1.8	1	37.2	0.052	2.8130	1.98E-04	5.03	0.80	0.86
0.3	0.3	2.5	1.5	0.6	27.12	0.049	3.4349	1.34E-04	3.07	1.50	1.02
0.4	0.25	2.5	1.5	0.6	29.76	0.054	3.1717	1.08E-04	2.75	2.03	0.96
0.3	0.3	2	1.5	0.75	27.12	0.07	3.2440	2.41E-04	6.81	1.33	0.87

Table 3.7: Effect of design variables on performance.

tapered designs.

- **The second design ($t_1 = t_1$=0.3 mm, $b_0 = b_1$=2 m), with a mass of 29 kg + 15% for fittings is selected for the full size design of the reflector.**
- **The lightest design is estimated to have an overall mass of 21 kg + 15% for fittings, however a heavier option has been selected for ease of manufacturing (and potentially lower cost).**

Contour plots of displacement magnitude, margin against material failure, vibration and buckling mode shapes are given in Figures 3.30 to 3.37 for $t_1 = t_2$=0.3 mm, $b_0 = b_1$=2 m; in Figures 3.38 to 3.41 for $t_1 = t_2$=0.3 mm, $b_0 = b_1$=1.6 m; in Figures 3.42 to 3.45 for $t_1 = t_2$=0.3 mm, $b_0 = b_1$=1.8 m; and in Figures 3.46 to 3.49 for $t_1 = t_2$=0.3 mm, b_0 = 2.5 m, b_1=1.5 m.

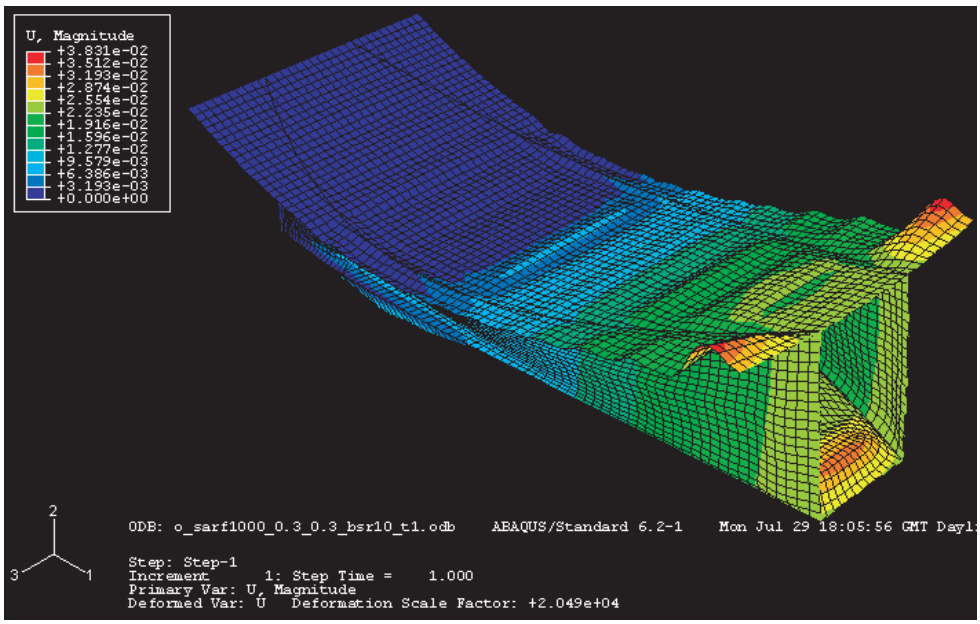

Figure 3.30: Displacement magnitudes for $t_1 = t_2$=0.3 mm, $b_0 = b_1$=2 m.

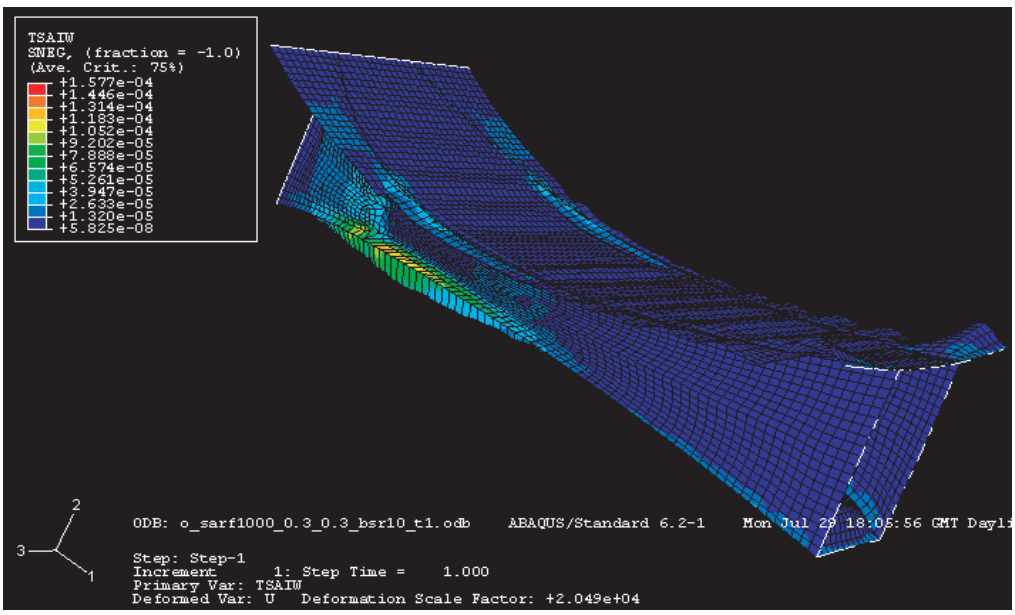

Figure 3.31: Tsai-Wu failure margin for $t_1 = t_2$=0.3 mm, $b_0 = b_1$=2 m.

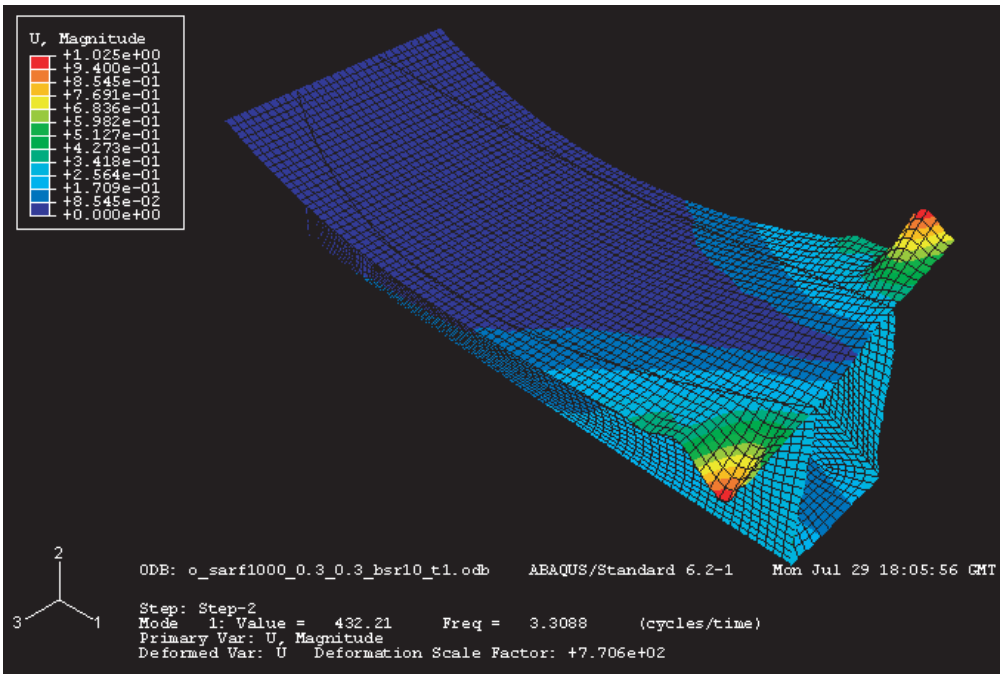

Figure 3.32: First vibration mode (frequency=3.309 Hz) for $t_1 = t_2$=0.3 mm, $b_0 = b_1$=2 m.

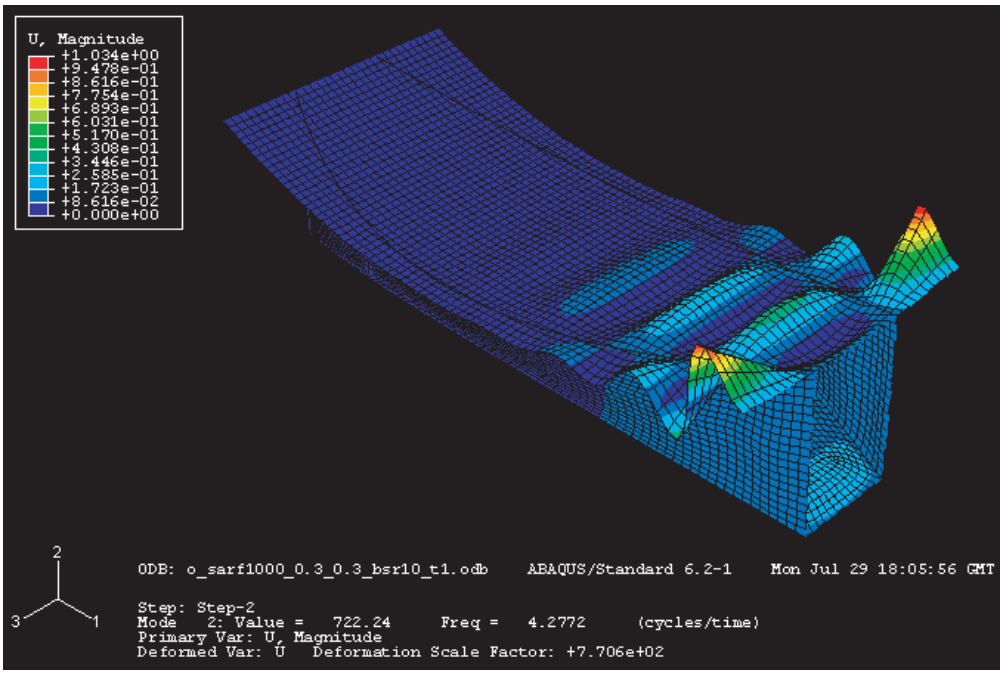

Figure 3.33: Second vibration mode (frequency=4.277 Hz) for $t_1 = t_2$=0.3 mm, $b_0 = b_1$=2 m.

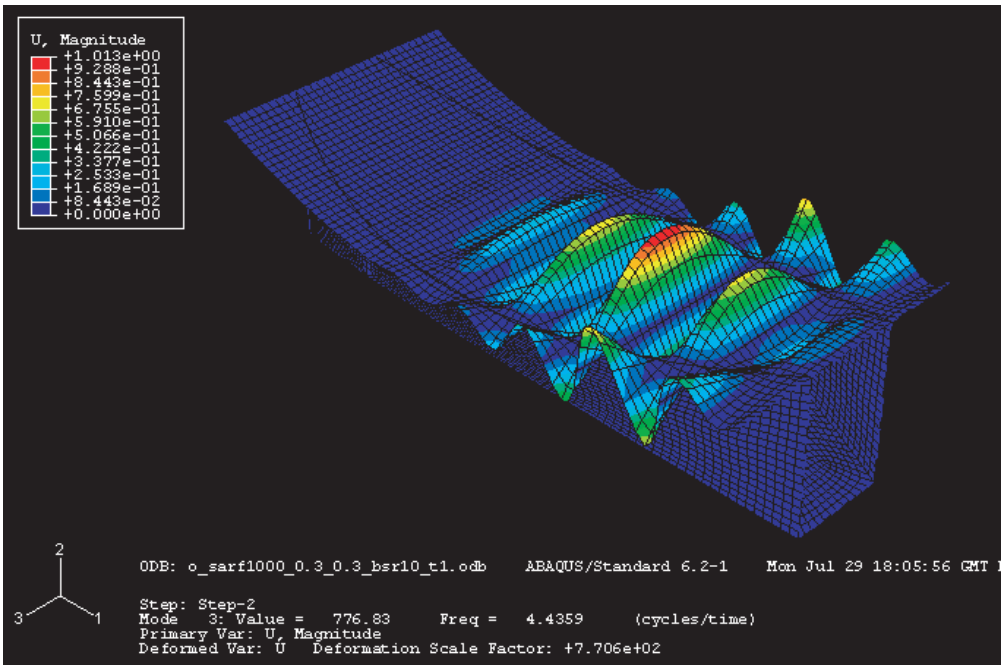

Figure 3.34: Third vibration mode (frequency=4.436 Hz) for $t_1 = t_2$=0.3 mm, $b_0 = b_1$=2 m.

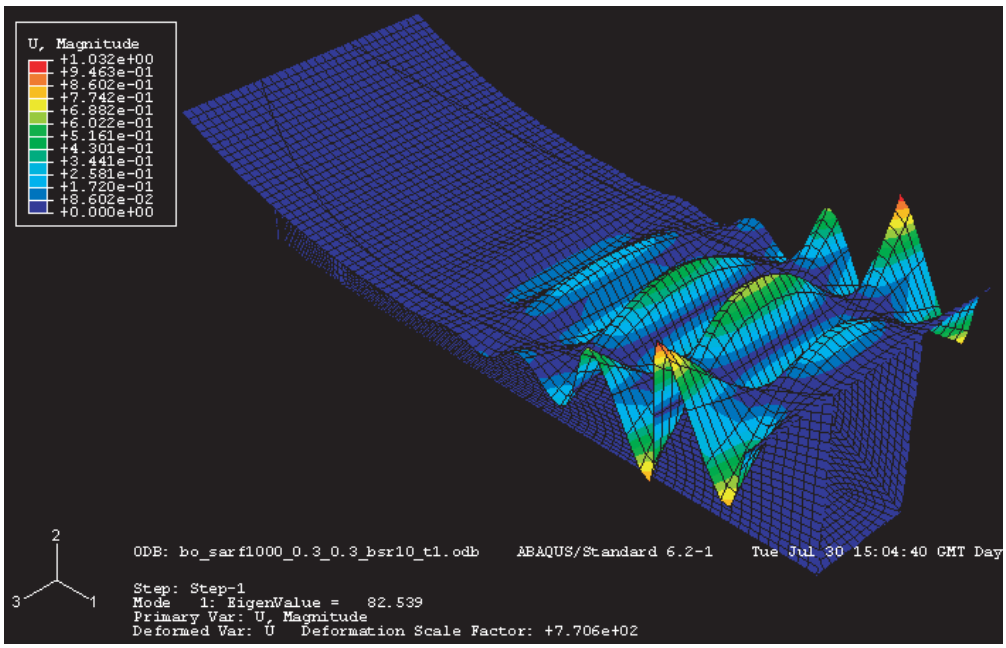

Figure 3.35: Overall buckling (first mode, eigenvalue=82.539) for $t_1 = t_2$=0.3 mm, $b_0 = b_1$=2 m.

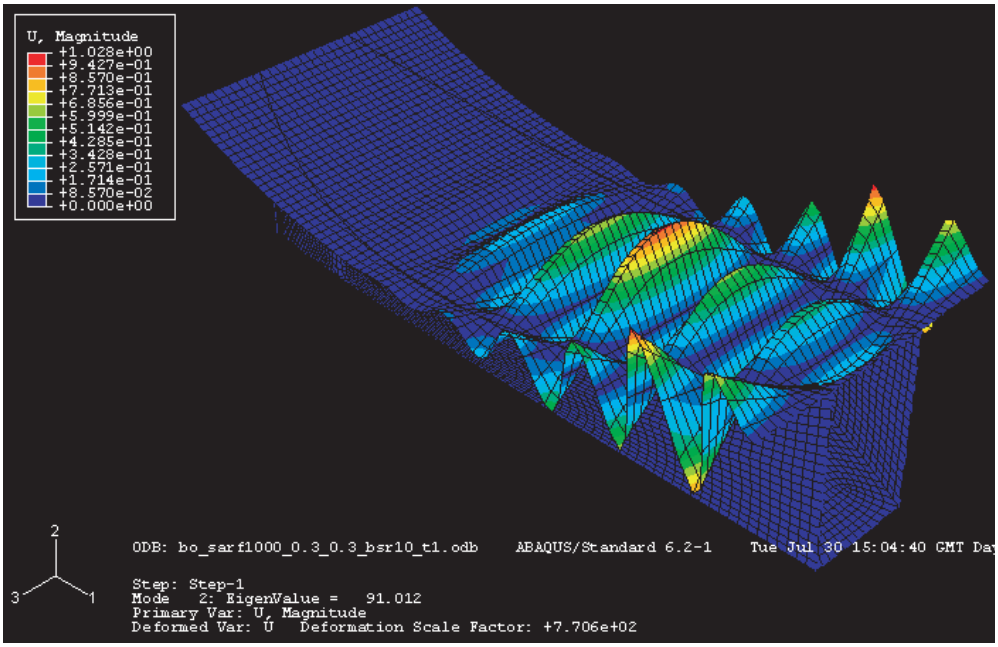

Figure 3.36: Overall buckling (second mode, eigenvalue=91.012) for $t_1 = t_2$=0.3 mm, $b_0 = b_1$=2 m.

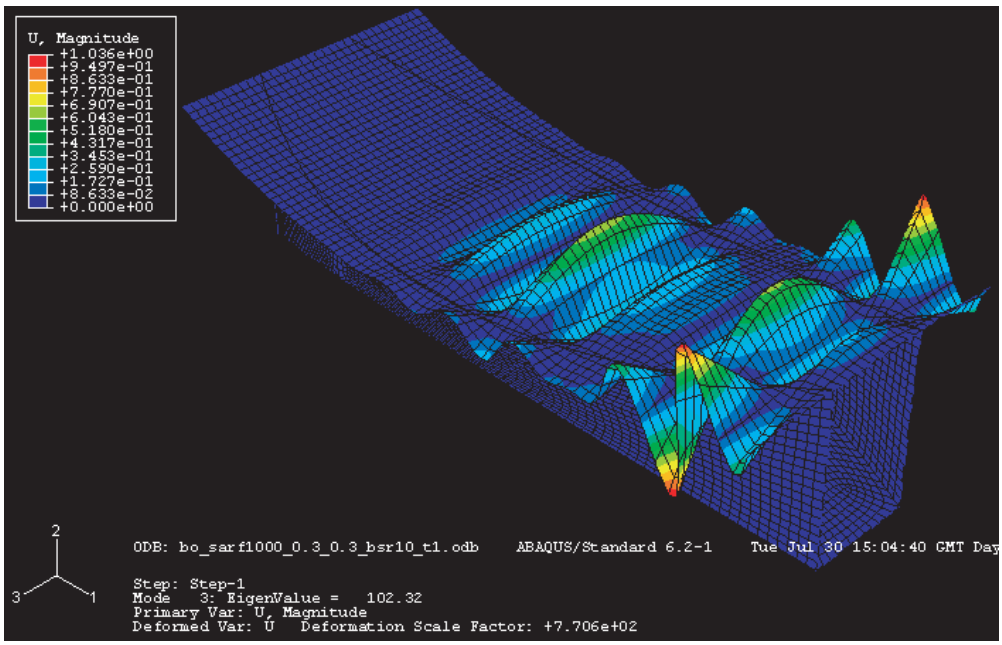

Figure 3.37: Overall buckling (third mode, eigenvalue=102.32) for $t_1 = t_2$=0.3 mm, $b_0 = b_1$=2 m.

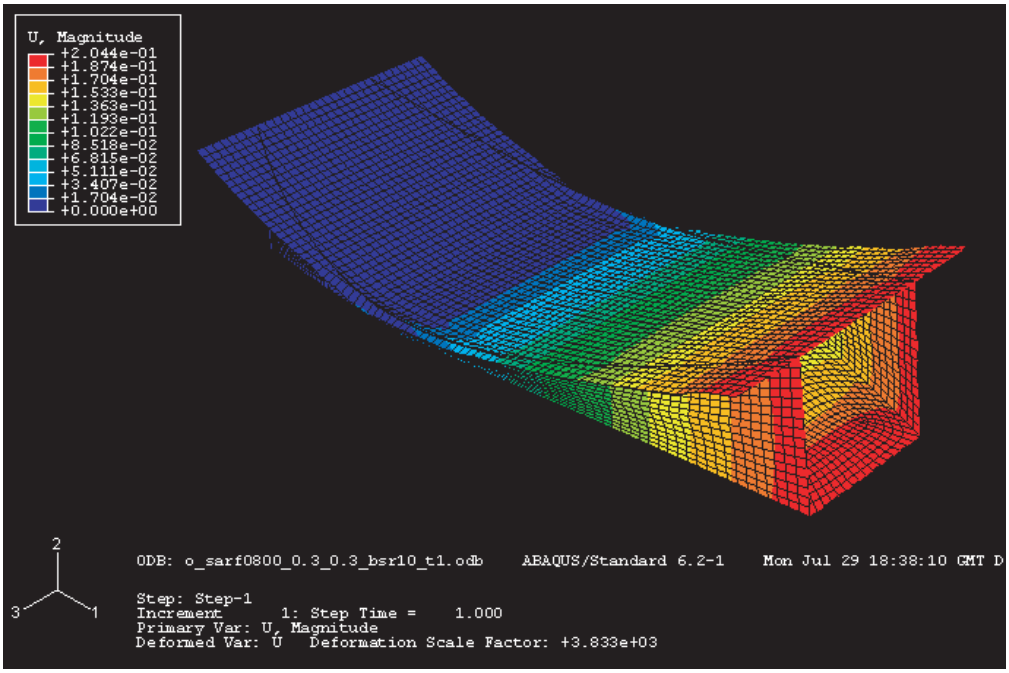

Figure 3.38: Displacement magnitudes for $t_1 = t_2$=0.3 mm, $b_0 = b_1$=1.6 m.

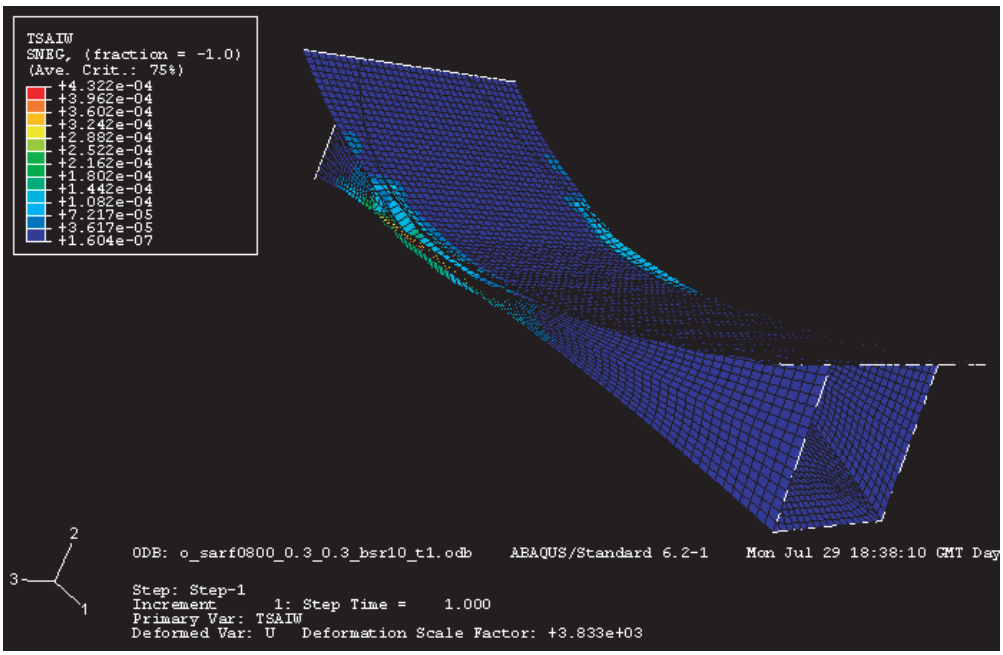

Figure 3.39: Tsai-Wu failure margin for $t_1 = t_2$=0.3 mm, $b_0 = b_1$=1.6 m..

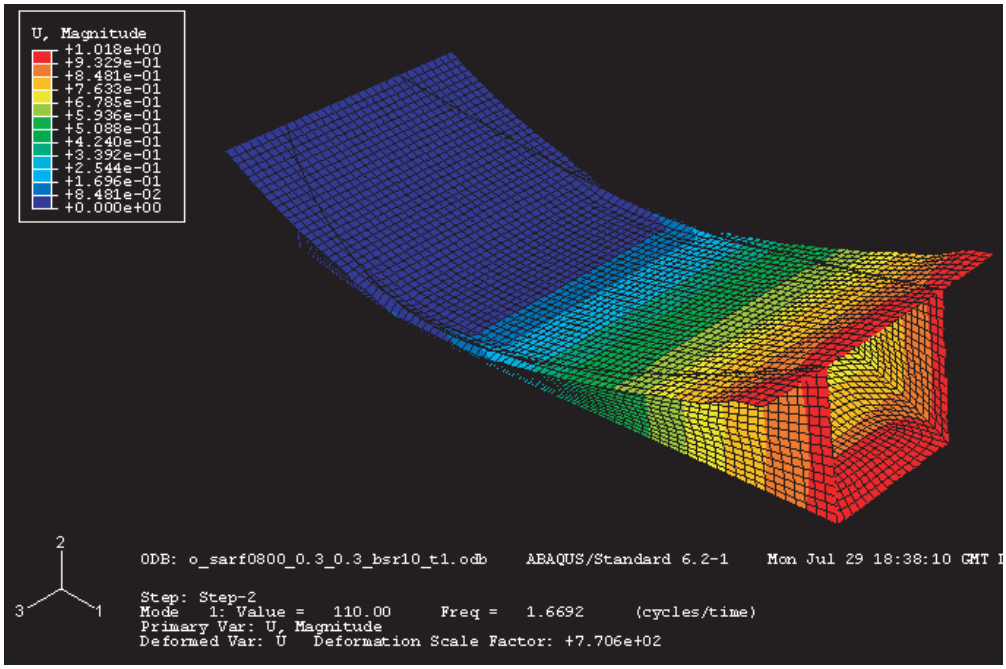

Figure 3.40: First vibration mode (frequency=1.669 Hz) for $t_1 = t_2$=0.3 mm, $b_0 = b_1$=1.6 m.

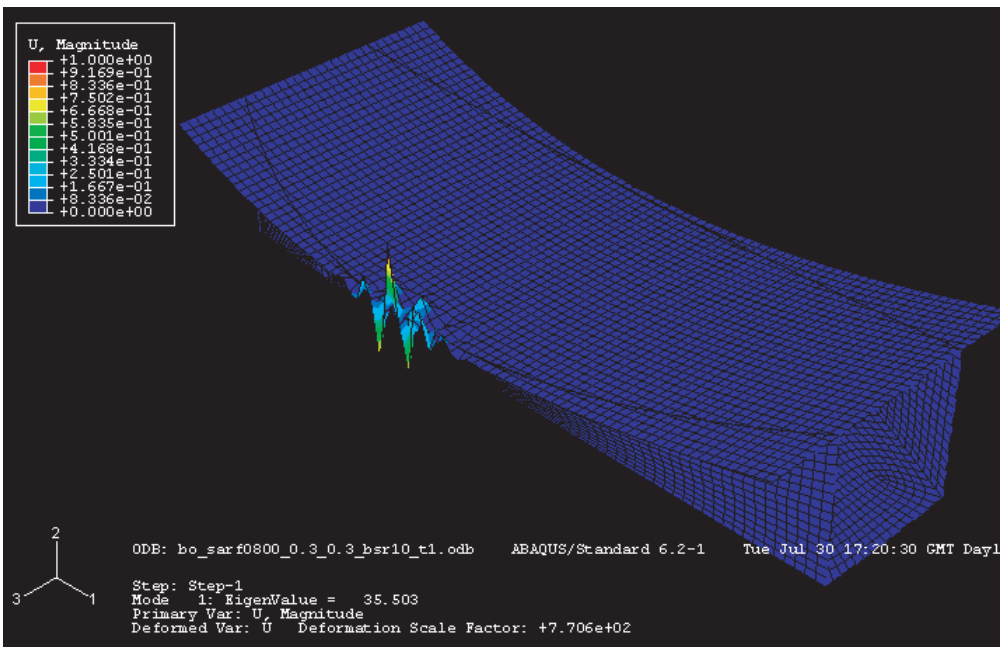

Figure 3.41: Overall buckling (first mode, eigenvalue=35.503) for $t_1 = t_2$=0.3 mm, $b_0 = b_1$=1.6 m.

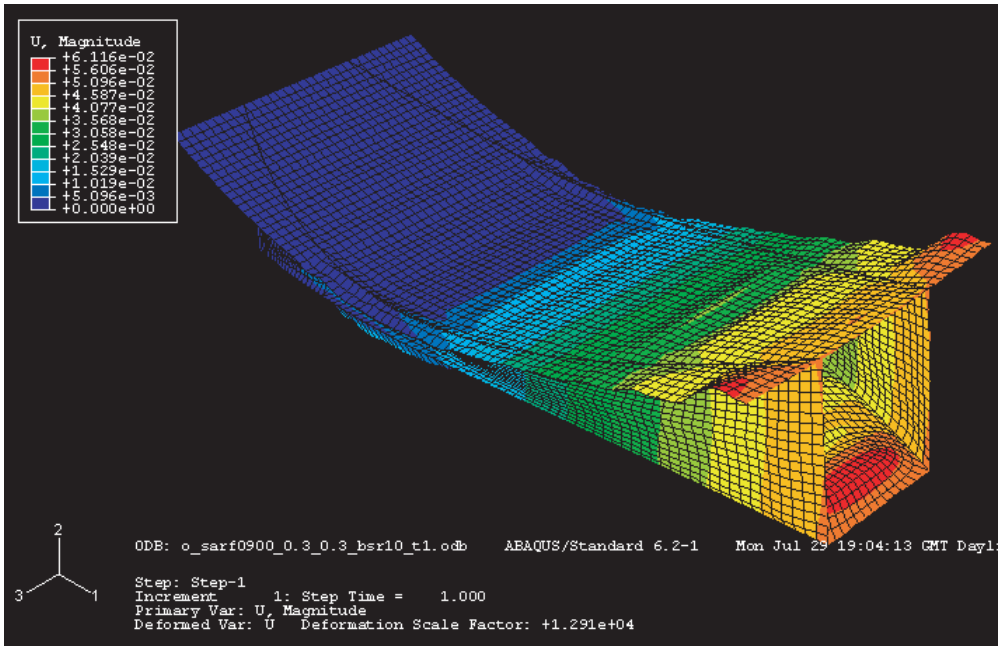

Figure 3.42: Displacement magnitudes for $t_1 = t_2$=0.3 mm, $b_0 = b_1$=1.8 m.

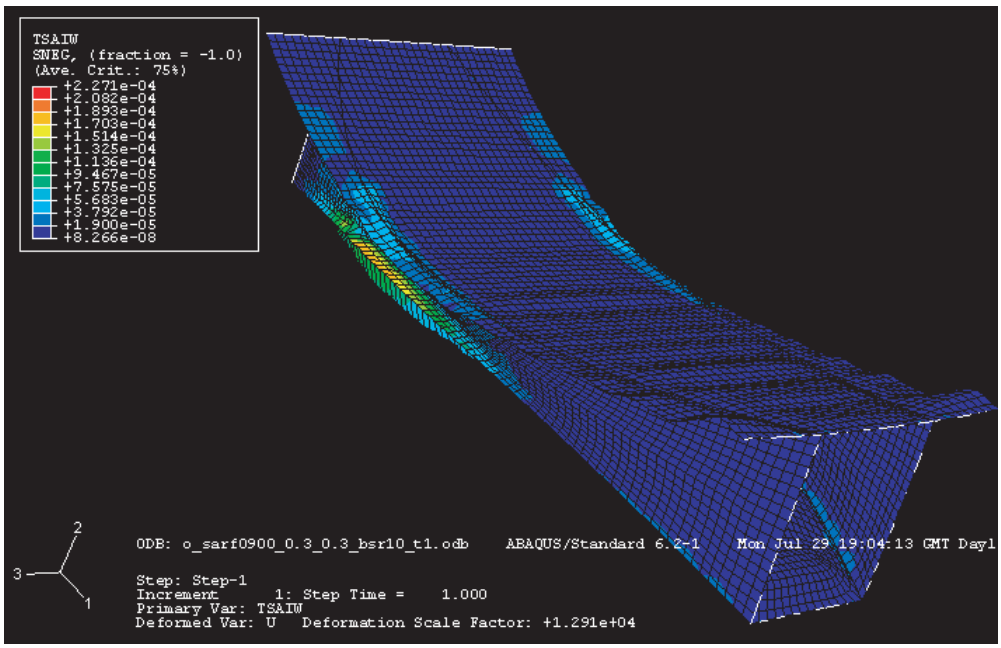

Figure 3.43: Tsai-Wu failure margin for $t_1 = t_2$=0.3 mm, $b_0 = b_1$=1.8 m.

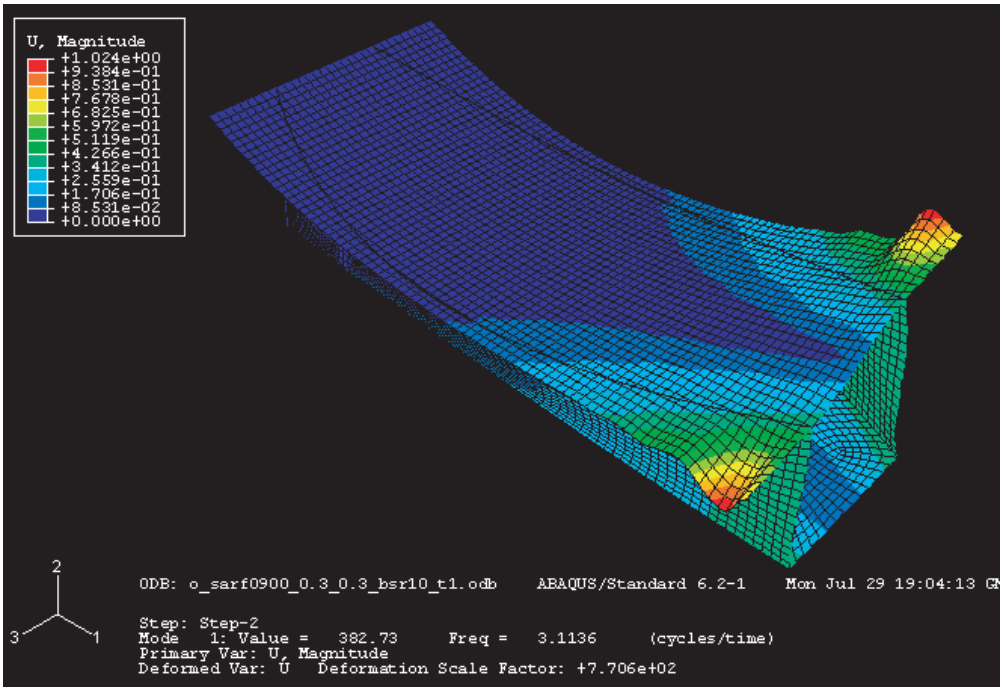

Figure 3.44: First vibration mode (frequency=3.114 Hz) for $t_1 = t_2$=0.3 mm, $b_0 = b_1$=1.8 m.

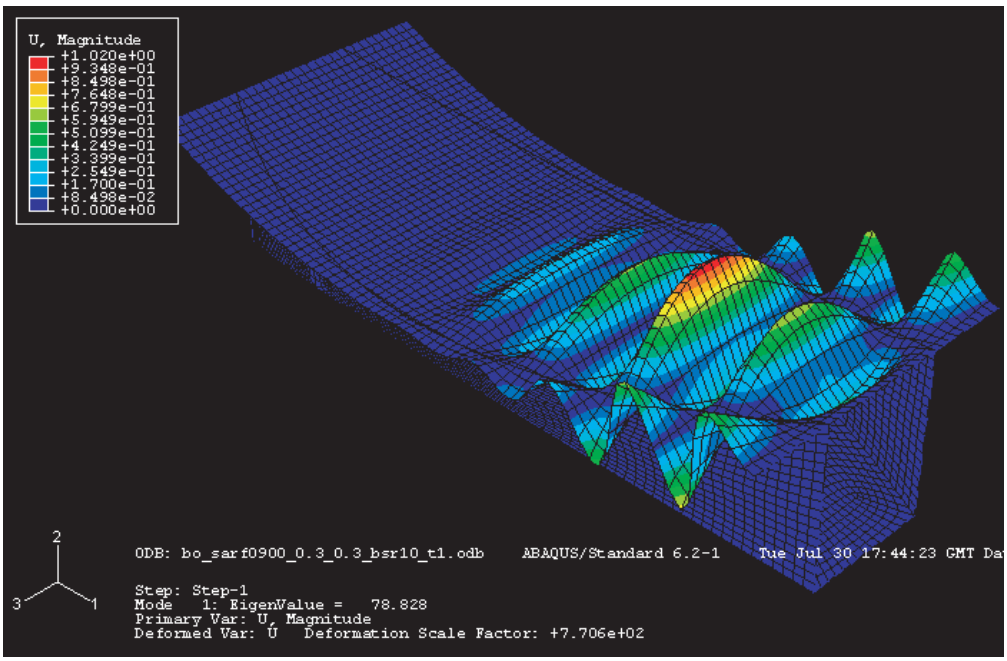

Figure 3.45: Overall buckling (first mode, eigenvalue=78.828) for $t_1 = t_2$=0.3 mm, $b_0 = b_1$=1.8 m.

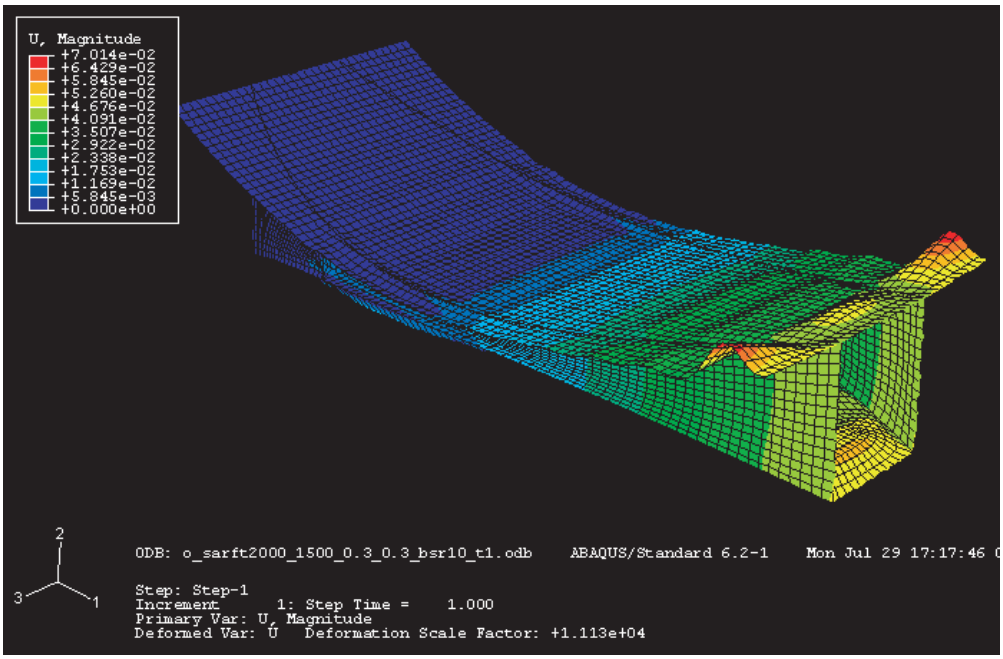

Figure 3.46: Displacement magnitudes for $t_1 = t_2$=0.3 mm, b_0 = 2.5 m, b_1=1.5 m.

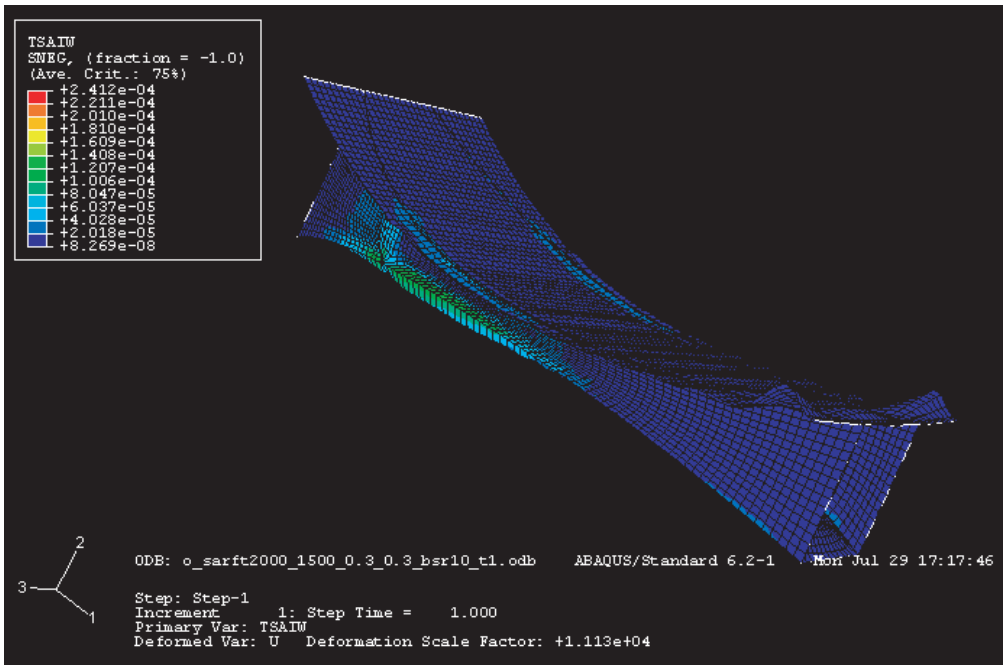

Figure 3.47: Tsai-Wu failure margin for $t_1 = t_2$=0.3 mm, b_0 = 2.5 m, b_1=1.5 m.

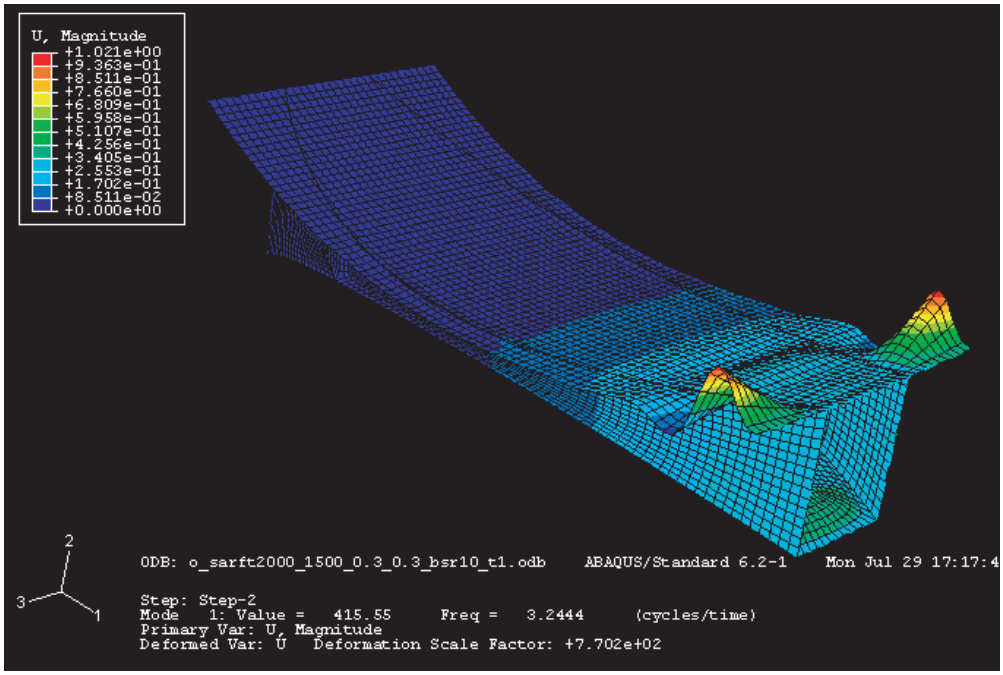

Figure 3.48: First vibration mode (frequency=3.244 Hz) for $t_1 = t_2$=0.3 mm, b_0 = 2.5 m, b_1=1.5 m.

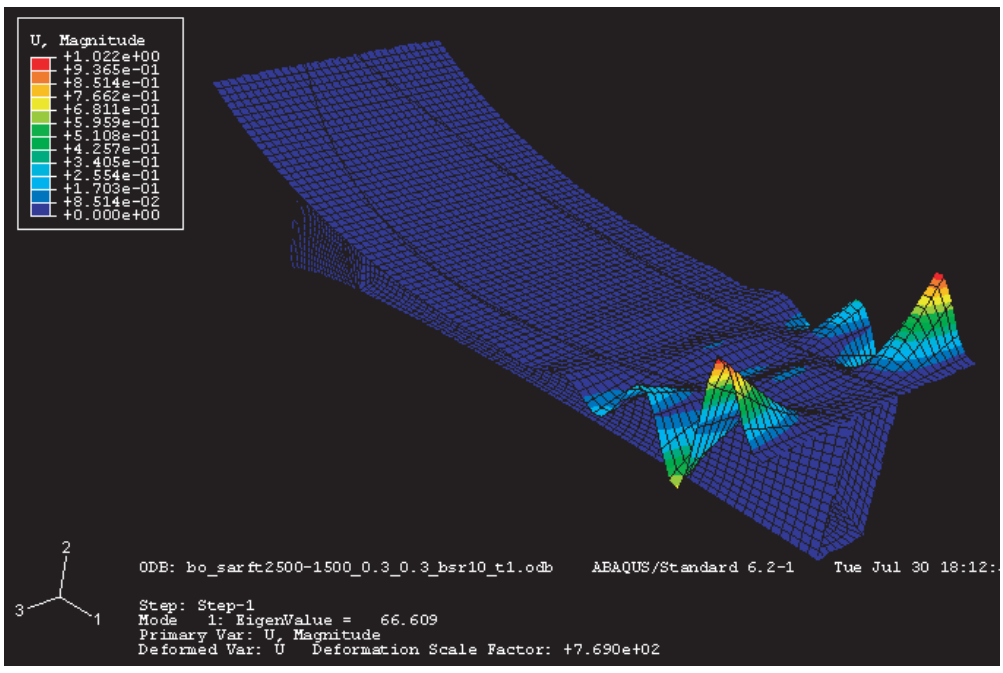

Figure 3.49: Overall buckling (first mode, eigenvalue=66.609) for $t_1 = t_2$=0.3 mm, b_0 = 2.5 m, b_1=1.5 m.

Chapter 4

Analysis of Half-Scale Demonstrator

A half-size demonstrator model of the reflector structure was analyzed under $1g$ loading conditions, as shown in Figure 4.1. The geometry of this structure is defined as an exact half-scale replica of the full-size reflector defined in Section 1.2, e.g. the focal length is half.

Gravity offload is provided by means of two vertical tubes ($r = 5$ mm, $t = 0.5$ mm), parallel to the Z-axis. One of these tubes is attached to the tip of the reflector; the other tube is attached to a point at a distance from the root end of five-eights of the arc-length of the parabolic profile. Both tubes are assumed to be connected to the edge of the reflective surface.

4.1 Initial Analysis

The following assumptions were made:

- Material: Reflective surface, beams, tubes and support structure all made of woven carbon fibre (T300) composite with average material properties as given in Table 3.1.
- Uniform thickness for both reflective surface and support structure, no taper.
- Boundary conditions: The first quarter of the RF surface is edgewise pinned. The tubes are pinned at one end, and connected to the reflective surface at the other end.
- Loading: inertial loading of 9.8 m/s^2 parallel to the Z-axis.

Table 4.1 presents a comparison of the behaviour of structures of three different wall thicknesses. Note that the last two columns indicate that the designs with thinner surfaces may be unsafe against buckling. Since the local buckling estimate is based on a preliminary analytical estimate, which may well not be very accurate, the global buckling estimate —obtained from

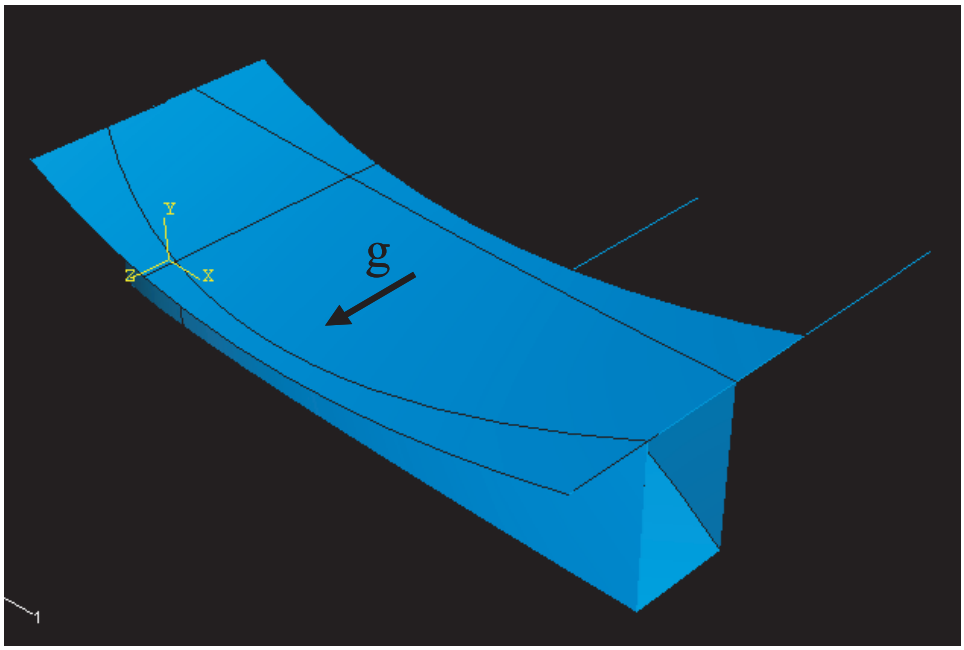

Figure 4.1: Half-scale demonstrator.

Half size model										
support structure+reflector surface (1.6mx3.94m)+root and tip beams (r=5mm,t=0.5mm)										
(1/4 of the reflector surface edgewise pinned										
t_1	t_2	b_0	b_1	λ	**mass**	u_{max}	f_0	**Tsai-Wu**	**L.Buckling**	**G.Buckling**
(mm)	(mm)	(m)	(m)	-	(kg)	(mm)	(Hz)	-	%	%
0.3	0.3	1	1	1	7.12	1.582	10.404	1.62E-02	**331.94**	99.8
0.6	0.6	1	1	1	13.99	1.953	10.558	1.62E-02	**121.06**	36.6
0.8	0.8	1	1	1	18.57	2.226	10.341	1.56E-02	77.31	25.04

Table 4.1: Preliminary comparison of half-scale structures of different thicknesses.

ABAQUS— is expected to be more reliable. However, even for the more accurate estimate the margin against buckling is clearly too small.

Since it is desirable to make the demonstrator from thin-walled sheets of the same thickness as the full size model, it was decided to increase the margin against buckling not by using thicker sheets, but by re-designing some structural details. Hence, the parameters $t_1 = t_2$=0.3 mm, $b_0 = b_1$=1 m were selected for the half-scale model.

Contours of displacement magnitude, margin against material failure, and the vibration and buckling modes for the chosen parameters (t_1=t_2=0.3 mm, b_0=b_1=1 m) are given in Figures 4.2 to 4.9.

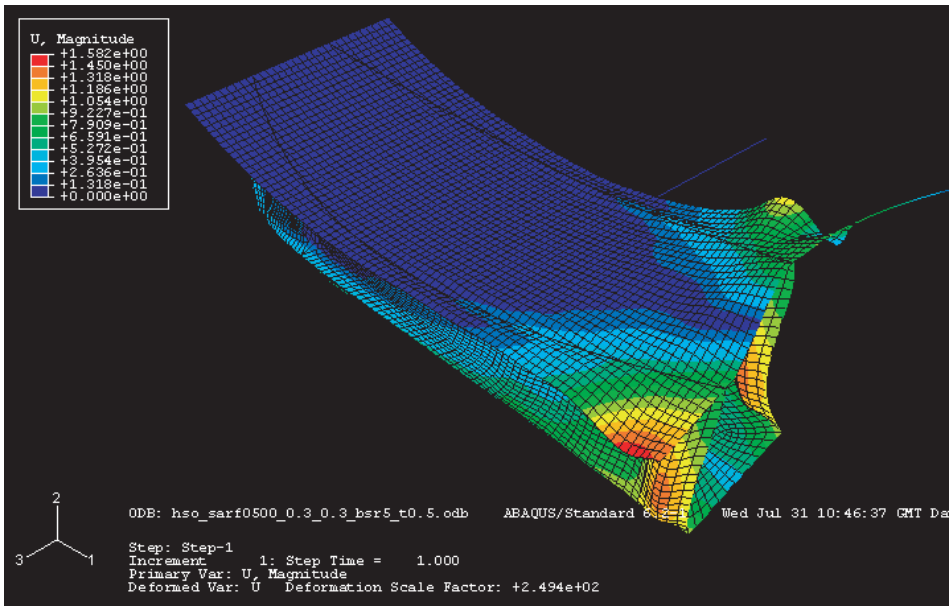

Figure 4.2: Displacement magnitudes of half-scale demonstrator preliminary design.

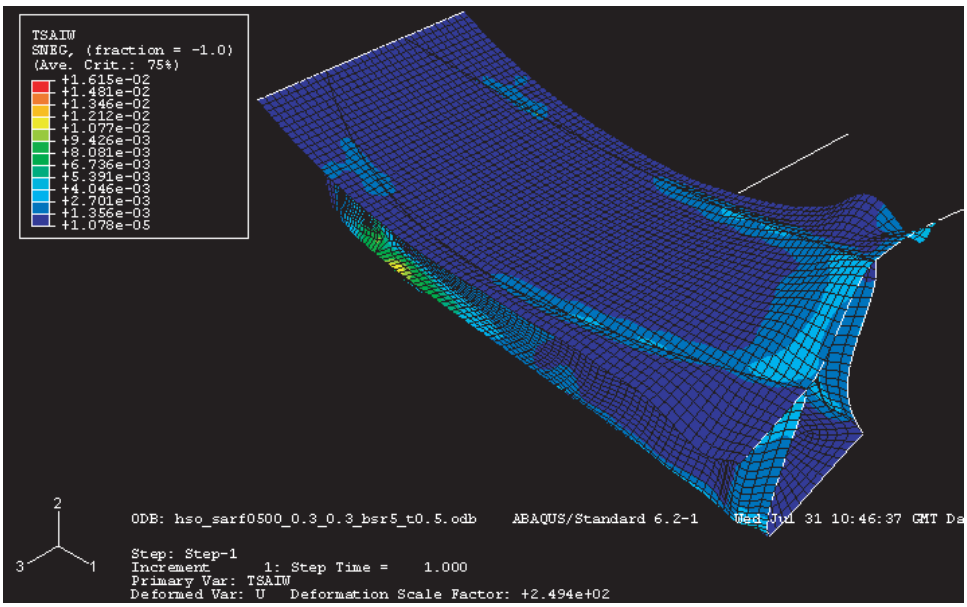

Figure 4.3: Contours of Tsai-Wu failure criterion for half-scale demonstrator preliminary design.

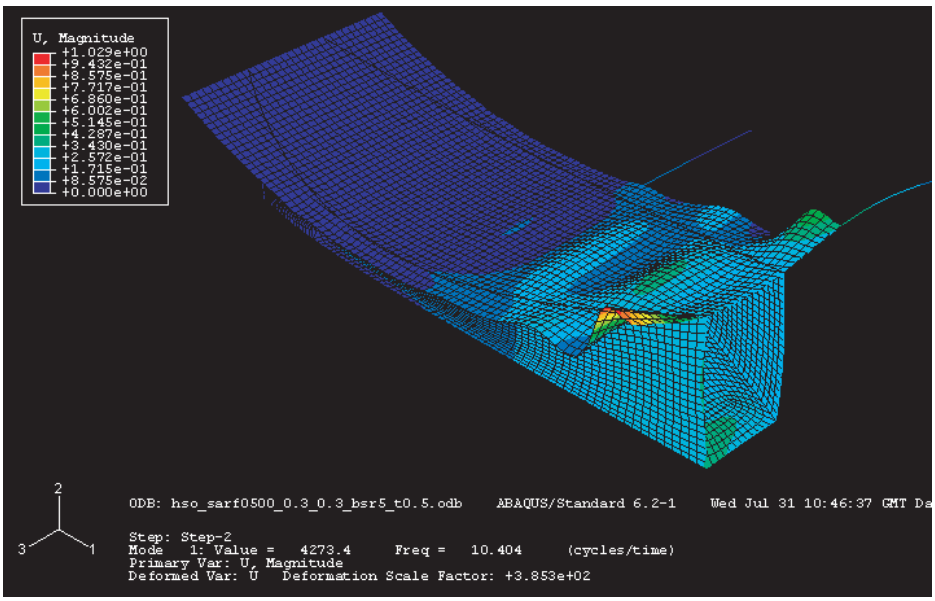

Figure 4.4: First vibration mode (frequency=10.404 Hz) for half-scale demonstrator preliminary design.

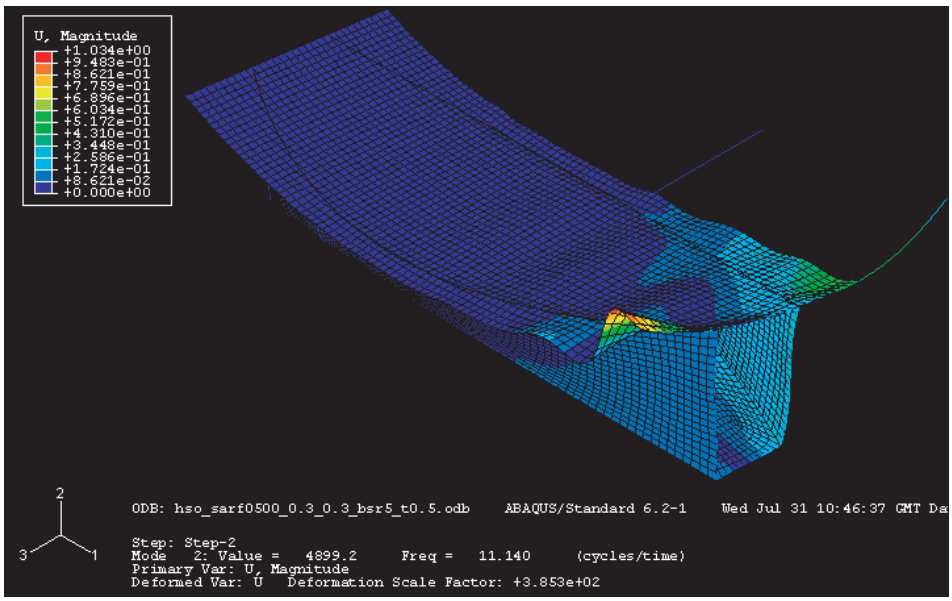

Figure 4.5: Second vibration mode (frequency=11.140 Hz) for half-scale demonstrator preliminary design.

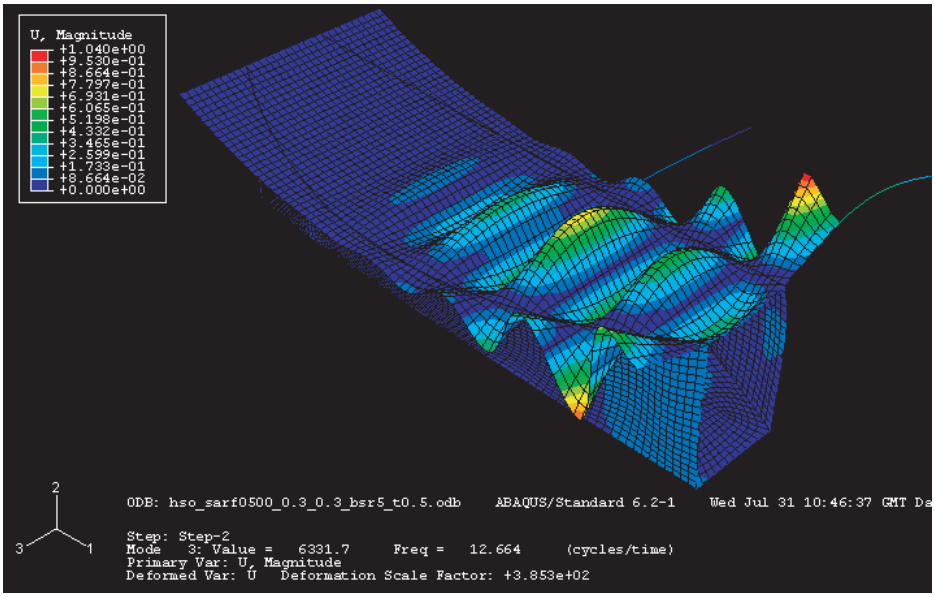

Figure 4.6: Third vibration mode (frequency=12.664 Hz) for half-scale demonstrator preliminary design.

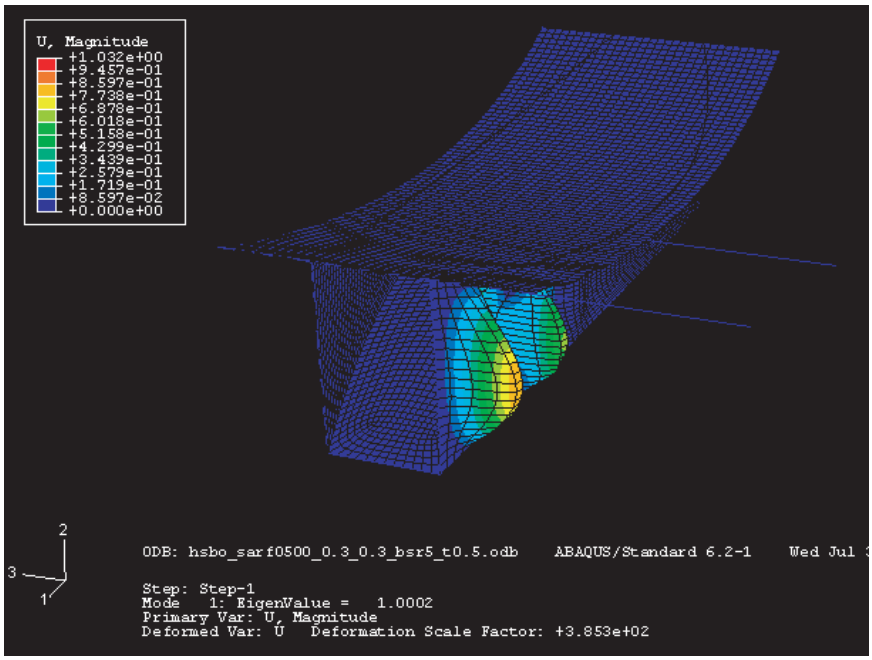

Figure 4.7: Overall buckling (first mode, eigenvalue=1.002) for half-scale demonstrator preliminary design.

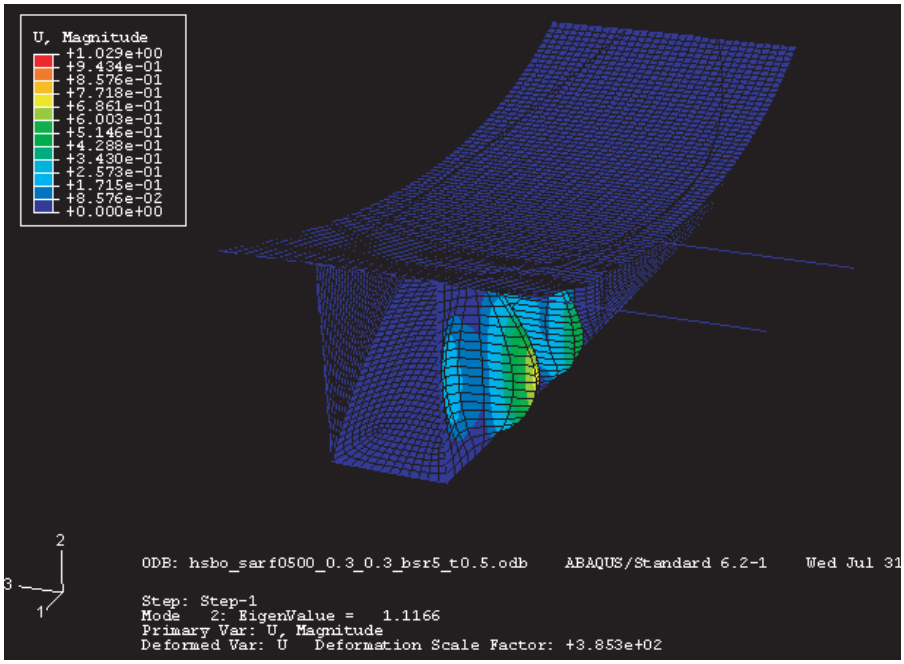

Figure 4.8: Overall buckling (second mode, eigenvalue=1.1166) for half-scale demonstrator preliminary design.

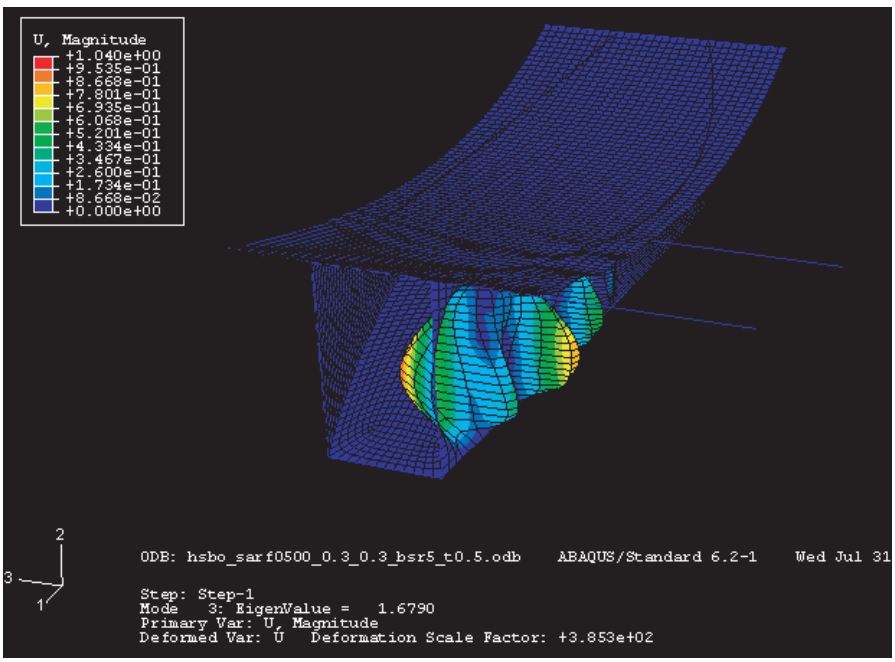

Figure 4.9: Overall buckling (third mode, eigenvalue=1.6790) for half-scale demonstrator preliminary design.

M55J Carbon woven lamina				$(0/45_2/0)_s$ woven laminate		
Lamina Properties				**Average Laminate Properties**		
$E_1=E_2$	150	GPa		$Ex=E_y$	103	GPa
G_{12} =	4.7	GPa		G_{xy} =	38.9	GPa
ν_{12} =	0.027	-		ν_{xy} =	0.33	-
ρ =	1.43	g/cm^3		ρ =	1.43	g/cm^3
Thickness	0.07	mm		Thickness	0.56	mm
F_{1t}	620	MPa		F_{1t}	300	MPa
F_{1c}	322	MPa		F_{1c}	150	MPa
F_{2t}	564	MPa		F_{2t}	300	MPa
F_{2c}	316	MPa		F_{2c}	150	MPa
F_6	60	MPa		F_6	50	MPa

Table 4.2: Material properties of M55J carbon woven composite.

4.1.1 Effect of Stiffer Material and Different Gravity Off-load

The use of M55J carbon woven composite for the half-scale demonstrator was investigated. M55J carbon fibres are about twice as stiff as T300 fibres.

Either one or two gravity off-loads were considered, the mid-tube being removed in the former case.

The following assumptions were made:

- Material: Reflector surface, beams, tubes and support structure all made of M55J carbon woven carbon composite with average material properties as given in Table 4.2.
- Uniform thickness for both reflector surface and support structure.
- Boundary conditions: The first quarter of the reflective surface is edgewise pinned. The tubes of the gravity-off load system are pinned at one end, and connected to the reflective surface at the other end.
- Loading: inertial loading of 9.8 m/s^2 parallel to the Z-axis.

The results of these analyses are presented in Table 4.3. Compared to the results in Table 4.1, it is clear that increasing the stiffness of the material yields a better performance. Using one gravity off-load tube to hold the reflector is preferable, since the effects of the second tube seem negligible in terms of performance and would result in additional manufacturing complexity. However, to reduce the cost of the demonstrator, T300 was chosen.

Half scale model (2-gravity off-loads)										
support structure+reflector surface (1.6mx3.94m)+root and tip beams (r=5mm,t=.5mm)										
(1/4 of the reflector surface edgewise pinned)										
t_1	t_2	b_0	b_1	λ	mass	u_{max}	f_0	Tsai-Wu	L.Buckling	G.Buckling
(mm)	(mm)	(m)	(m)	-	(kg)	(mm)	(hz)	-	%	%
0.3	0.3	1	1	1.000	6.52	0.709	15.547	2.38E-02	149.67	44.50
0.6	0.6	1	1	1.000	12.82	0.876	15.765	1.98E-02	54.35	16.30
0.8	0.8	1	1	1.000	17.02	0.998	15.442	1.81E-02	34.66	11.16
1	1	1	1	1.000	21.22	1.098	15.229	1.71E-02	24.24	8.77
Half scale model (1-gravity off-load at tip)										
support structure+reflector surface (1.6mx3.94m)+root and tip beams (r=5mm,t=.5mm)										
(1/4 of the reflector surface edgewise pinned)										
t_1	t_2	b_0	b_1	λ	mass	u_{max}	f_0	Tsai-Wu	L.Buckling	G.Buckling
(mm)	(mm)	(m)	(m)	-	(kg)	(mm)	(hz)	-	%	%
0.6	0.6	1	1	1.000	12.80	0.872	15.579	1.98E-02	54.35	15.89
0.8	0.8	1	1	1.000	17.00	0.993	15.350	1.81E-02	34.66	10.57
1	1	1	1	1.000	21.20	1.093	15.184	1.69E+00	24.22	7.79

Table 4.3: Performance of structure made from M55J carbon woven composite.

4.2 Further Analysis

A more detailed finite-element model of the structure was set up to refine the analysis and address the buckling issues highlighted by the previous analysis.

This model includes also, a series of "windows" in the sidewalls (required to fold the structure), slots for the interface frame, and tape springs to latch the structure in the deployed configuration. The following assumptions were made:

- Material: Reflector surface, beams, tubes and support structure all made of woven T300 carbon fibre composite with average material properties as given in Table 4.4. Note that a different lay-up is now being used.

- Uniform thickness for both reflector surface and support structure, t_1=t_2=0.3 mm, and no taper, b_0=b_1=1 m.

- Boundary conditions: The reflective surface is connected to a rectangular, rigid interface frame which overlaps with the first quarter of the surface. The reflective surface is pinned to the longer sides (in the transverse direction for the reflective surface) of this rectangular frame. The tubes of the gravity off-load system are pinned to an external foundation, and are connected to the reflective surface and/or to the bottom surface of the reflector at the other end.

- Loading: inertial loading of 9.8 m/s^2 with gravity vector parallel to the Z-axis.

Carbon/epoxy woven lamina				(0/45/0) woven laminate		
Lamina Properties				**Average Laminate Properties**		
E_1=E_2	70	GPa		Ex=E_y	58	GPa
G_{12} =	5	GPa		G_{xy} =	14.4	GPa
ν_{12} =	0.05	-		ν_{xy} =	0.213	-
ρ =	1.56	g/cm^3		ρ =	1.56	g/cm^3
Thickness	0.125	mm		Thickness	0.3	mm
F_{1t}	800	MPa		F_{1t}	400	MPa
F_{1c}	700	MPa		F_{1c}	300	MPa
F_{2t}	750	MPa		F_{2t}	400	MPa
F_{2c}	650	MPa		F_{2c}	300	MPa
F_6	80	MPa		F_6	60	MPa

Table 4.4: Material properties of woven T300.

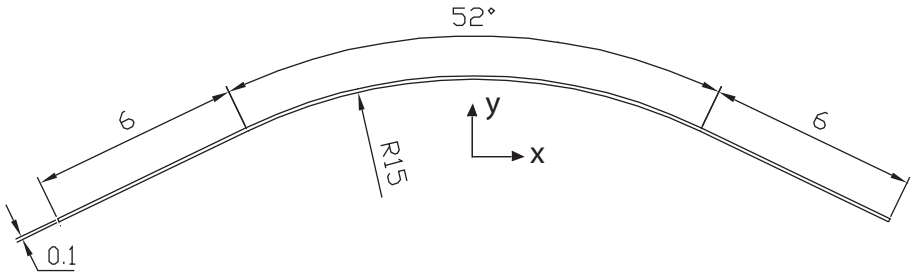

Figure 4.10: Cross section of tape spring (dimensions in mm).

- Tape springs: made from "Contractor Grade" steel tape measure supplied by Sears, Roebuck and Co. (Pellegrino et al. 2002). Their cross-section is shown in Figure 4.10. The principal second moments of area are $I_{xx} = 4.2865$ mm^4 and $I_{yy} = 124.0697$ mm^4, and the cross-sectional area is 2.55 mm^2. The material properties are assumed to be $E = 207$ GPa, $G = 79$ GPa, ν=0.3, ρ=7800 kg/m^3. The tape springs are modelled as beams with general cross-section in ABAQUS.

The performance with and without windows is compared in Table 4.5. The inclusion of windows in the sidewalls slightly affects the buckling margin, which is 1.7% worse. The first buckling mode is shown in Figure 4.11. Note that buckling is localized in one of the sidewalls, between the third cut-out —counting from the root— and the tip.

To prevent buckling, a transverse tubular stiffener —of rectangular cross-section— made of woven T300 carbon fibre is added, between the third cut-out and the end of the sidewall. The performance of the structure with this stiffener is summarised in the bottom part of Table 4.5; note that the presence of this stiffener improves the buckling margin to 70%. The first buckling mode is shown in Figure 4.12.

Half scale model (2-gravity off-loads at bottom surface)
support structure+reflector surface (1.6mx3.94m)+root and tip beams (rectangle a=b=10mm,t=.5mm)
(1/4 of the reflector surface edgewise pinned, only transverse)

t_1	t_2	b_0	b_1	λ	mass	u_{max}	f_0	Tsai-Wu	G.Buckling
(mm)	(mm)	(m)	(m)	-	(kg)	(mm)	(hz)	-	%
0.3	0.3	1	1	1.000	7.18	0.760	10.836	6.29E-03	95.09

Half scale model (2-gravity off-loads at bottom surface) with windows (210x50)
support structure+reflector surface (1.6mx3.94m)+root and tip beams (rectangle a=b=10mm,t=.5mm)
(1/4 of the reflector surface edgewise pinned, only transverse)

t_1	t_2	b_0	b_1	λ	mass	u_{max}	f_0	Tsai-Wu	G.Buckling
(mm)	(mm)	(m)	(m)	-	(kg)	(mm)	(hz)	-	%
0.3	0.3	1	1	1.000	7.15	0.754	10.566	6.43E-03	96.79

Half scale model (2-gravity off-loads at RF surface)
with windows (210x50)+1rib(a=b=10mm, t=0.5mm,L=776mm)
support structure+reflector surface (1.6mx3.94m)+root and tip beams (rectangle a=b=10mm,t=.5mm)
(1/4 of the reflector surface edgewise pinned, only transverse)

t_1	t_2	b_0	b_1	λ	mass	u_{max}	f_0	Tsai-Wu	G.Buckling
(mm)	(mm)	(m)	(m)	-	(kg)	(mm)	(hz)	-	%
0.3	0.3	1	1	1.000	7.16	0.753	10.561	6.44E-03	69.95

Table 4.5: Performance of half-scale demonstrator with and without windows in sidewalls.

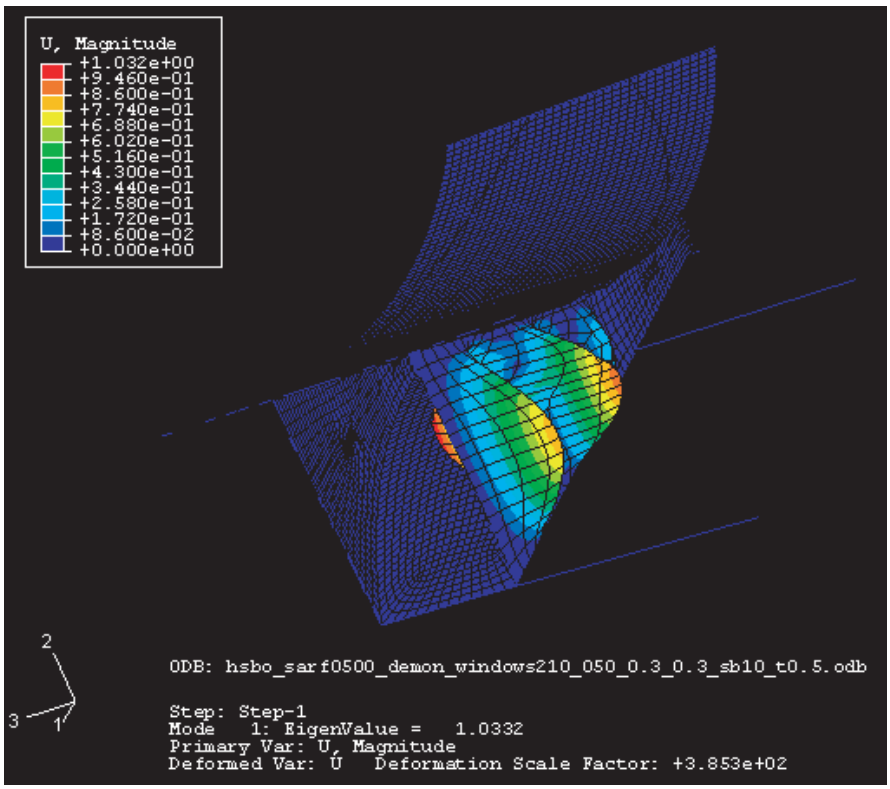

Figure 4.11: First buckling mode of half-scale demonstrator with windows in sidewalls.

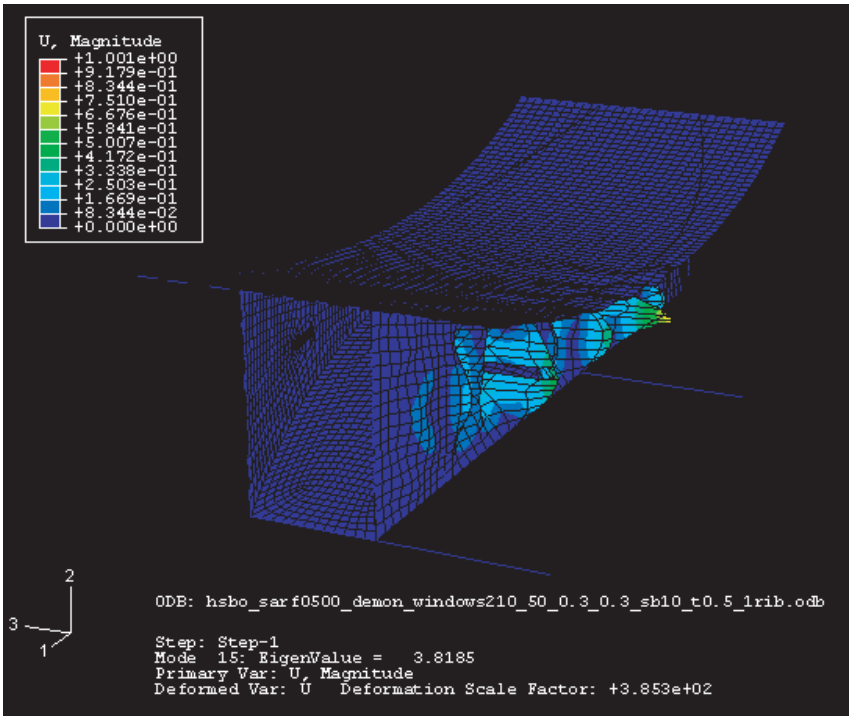

Figure 4.12: First buckling mode of reflector with windows and a stiffener.

To investigate buckling further, the two gravity compensation tubes were removed, and instead two concentrated forces were applied to the edges of the reflector surface and sidewall, in the Z-direction. The corresponding buckling ratio was found to be 96%. Another, extreme case that was analysed involved pinning the edges of the reflective surface and sidewalls to an external foundation, to simulate a fully-distributed gravity off-loading, and this gave a buckling ratio of 83%.

Stiffening the sidewalls was found to be a better way of improving the buckling margin. However, any stiffeners must be foldable like the sidewalls; tape springs are suitable for this application.

The next phase of the study aimed to remove all gravity compensation forces or elements, and to add steel tapes as stiffening elements. Slots for the interface frame were also included at this stage. The use of foldable tapes leads to additional windows in the sidewalls, to provide the necessary space for the bend region of the tape; hence an additional, small cut-out, of dimensions 35 mm $\times$ 75 mm, was added between the third cut-out and the tip end of each sidewall.

Some other steel tapes were placed inside the large windows (210 mm wide) with a 5 mm clearance from the edge of the windows. For symmetry, both sidewalls were stiffened with steel tapes.

Half scale model with windows (210x75) and interface slot(20x238)+tape spring

support structure+reflector surface (1.6mx3.94m)+root and tip beams (rectangle a=b=10mm,t=.5mm)

(1/5.122 of the reflector surface edgewise pinned, only transverse), g is in z direction

t_1	t_2	b_0	b_1	λ	mass	u_{max}	f_0	Tsai-Wu	G.Buckling
(mm)	(mm)	(m)	(m)	-	(kg)	(mm)	(hz)	-	%
no tape									
0.3	0.3	1	1	1.000	7.07	6.711	6.833	2.07E-02	101.05
2 tape springs between third window and tip with window (35x75)									
0.3	0.3	1	1	1.000	7.10	6.678	6.817	2.08E-02	71.38
4 tape springs (2 tapes between third window and tip with window (35x75)+2 tapes in third window)									
0.3	0.3	1	1	1.000	7.13	6.669	6.817	2.09E-02	66.29
6 tape springs (2 tapes between third window and tip with window (35x75)+4 tapes in third window)									
0.3	0.3	1	1	1.000	7.15	6.661	6.821	2.09E-02	66.40
14 tape springs (2 tapes between third window and tip with window (35x75)+4x3 tapes in three window)									
0.3	0.3	1	1	1.000	7.20	6.685	6.842	1.57E-02	51.54

Table 4.6: Performance of demonstrator with stiffened sidewalls.

All of these changes were incorporated in the model, and the results are presented in Table 4.6. Stiffening the sidewalls improves the buckling ratio to 50%. The first buckling mode of the reflector with stiffened sidewalls is shown in Figure 4.13.

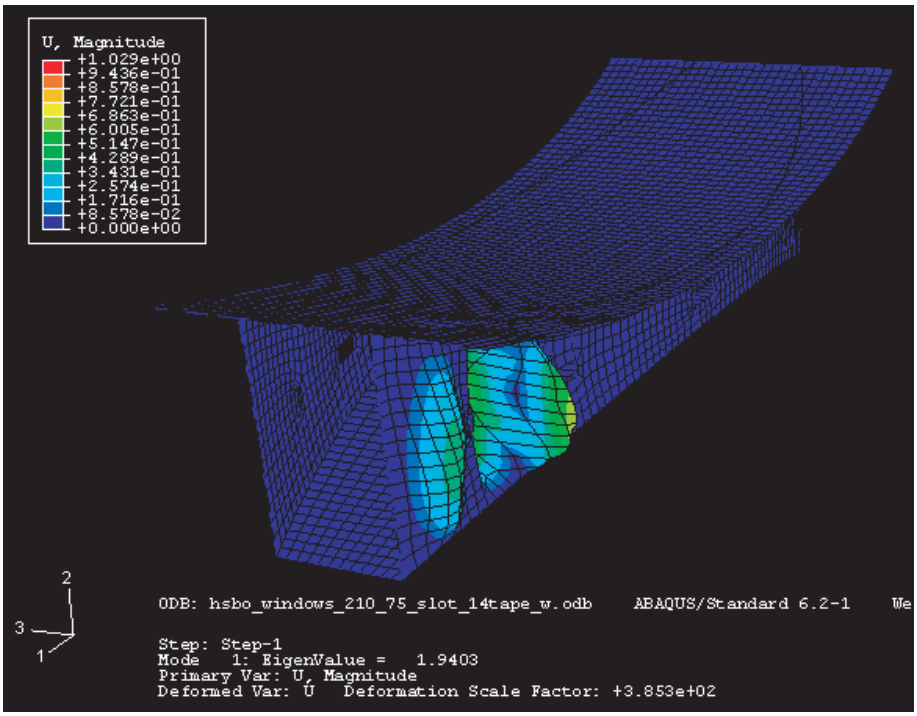

Figure 4.13: First buckling mode of demonstrator with windows, interface slot, and steel tapes.

Chapter 5

Quarter-Scale Proof of Concept Model

5.1 Manufacture

A quarter-scale low-cost model of the reflector was made from 0.75 mm thick sheets of clear thermoplastic (VIVAK). The cutting pattern for this model is given in Figure 5.1. The windows were sized and positioned so that the same model could be used to demonstrate both Z-type and coil-type folding.

A template for this cutting pattern was plotted at 1:1 scale. Then, the RF surface, the top surface and the sidewalls were cut by hand with a sharp blade, after laying the templates underneath the plastic sheets. 30 mm long by 1 mm wide slots were cut in the RF surface, at a spacing of 25 mm, for the T-connections.

Steel tape springs with a thickness of 0.1 mm and a transverse radius of curvature of 15 mm were riveted to the sidewalls, to increase the stiffness of the structure in the deployed configuration. A pair of cylindrical spacers with a radius of 15 mm and a total height of 30 mm were positioned near each cut-out, to prevent plastic deformation of the sidewall material. 3M 79 woven glass tape was used for connecting the sheets.

The model was assembled as follows. First, both sidewalls were connected with woven tape to the RF surface in the flat configuration. This joint is called a T-connection, and consists of 50 mm long pieces tapes attached to the sidewalls and to the front of the RF surface, which pass through the slots previously cut in the RF surface. The strength of this connection is determined in Section 6.3.2. Next, the top surface was connected to one of the sidewalls with woven tape, still in the flat configuration. Finally, the whole structure was set in the deployed configuration

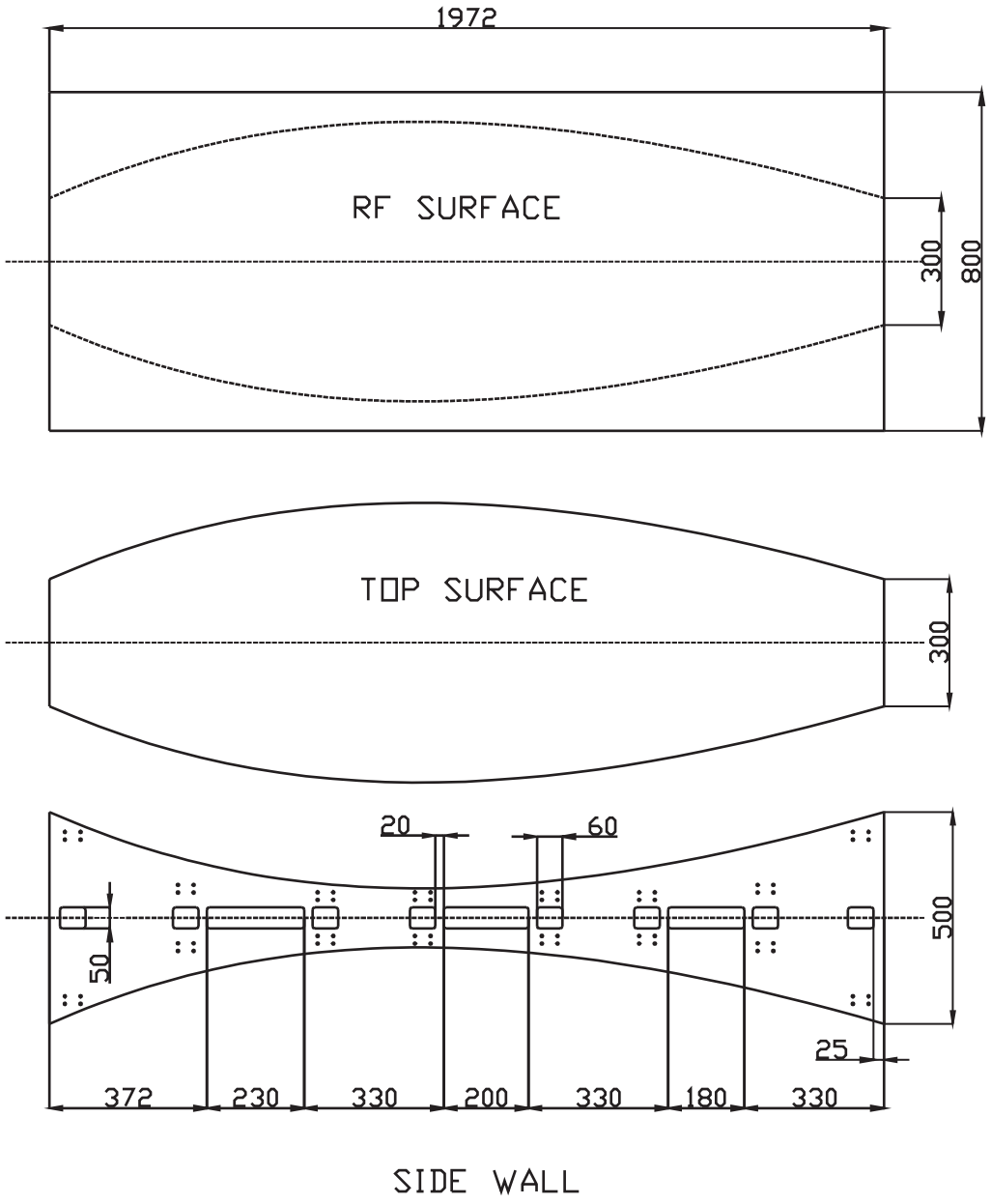

Figure 5.1: Cutting pattern for quarter-scale model (dimensions in mm).

and the final connection was made between a sidewall and the top surface.

The last two sets of connections were made with 70 mm long pieces of tape applied to the outer surfaces of both sidewall and top surface, along the cutting pattern. This joint is called an L-connection and its strength will also be determined in Section 6.3.2. Consecutive pieces of tape were overlapped by 10 mm. Pictures of the complete structure, in the deployed configuration, are given in Figure 5.2.

5.2 Folding

Both Z-folding and coiling of the structure were demonstrated using this model. The two stowed configurations are shown in Figures 5.3 and 5.4. In both cases it was found that the model deploy well, and even under gravity it requires only little help, to reach the expected parabolic shape.

Several advantages and disadvantages of Z-folding and coiling were identified, and are summarized as follows:

- Z-folding:
  - Larger stowed volume
  - Deployment easier to control
  - Requires equal size and evenly positioned sidewall windows
- Coil-type:
  - Smaller stowed volume
  - Deployment more difficult to control
  - Requires unevenly distributed sidewall windows

5.3 Lessons Learned

The quarter-scale model proved to be an invaluable aid to the design and construction of the half-scale model. Many lessons were learned from it, which were later incorporated in the design and construction of the half-scale model. The following is a list of the main lessons learnt:

- Connections: the spacing of the T and L connections needs to be minimized to avoid local buckling of unsupported parts of the thin-walled surface. The strength and stiffness of

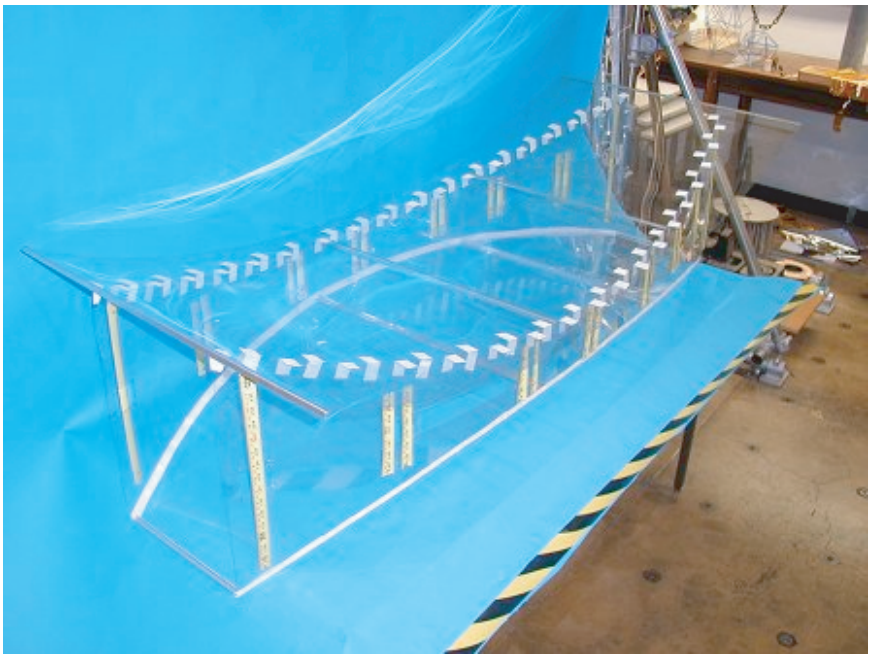

Figure 5.2: Quarter-scale model reflector, deployed.

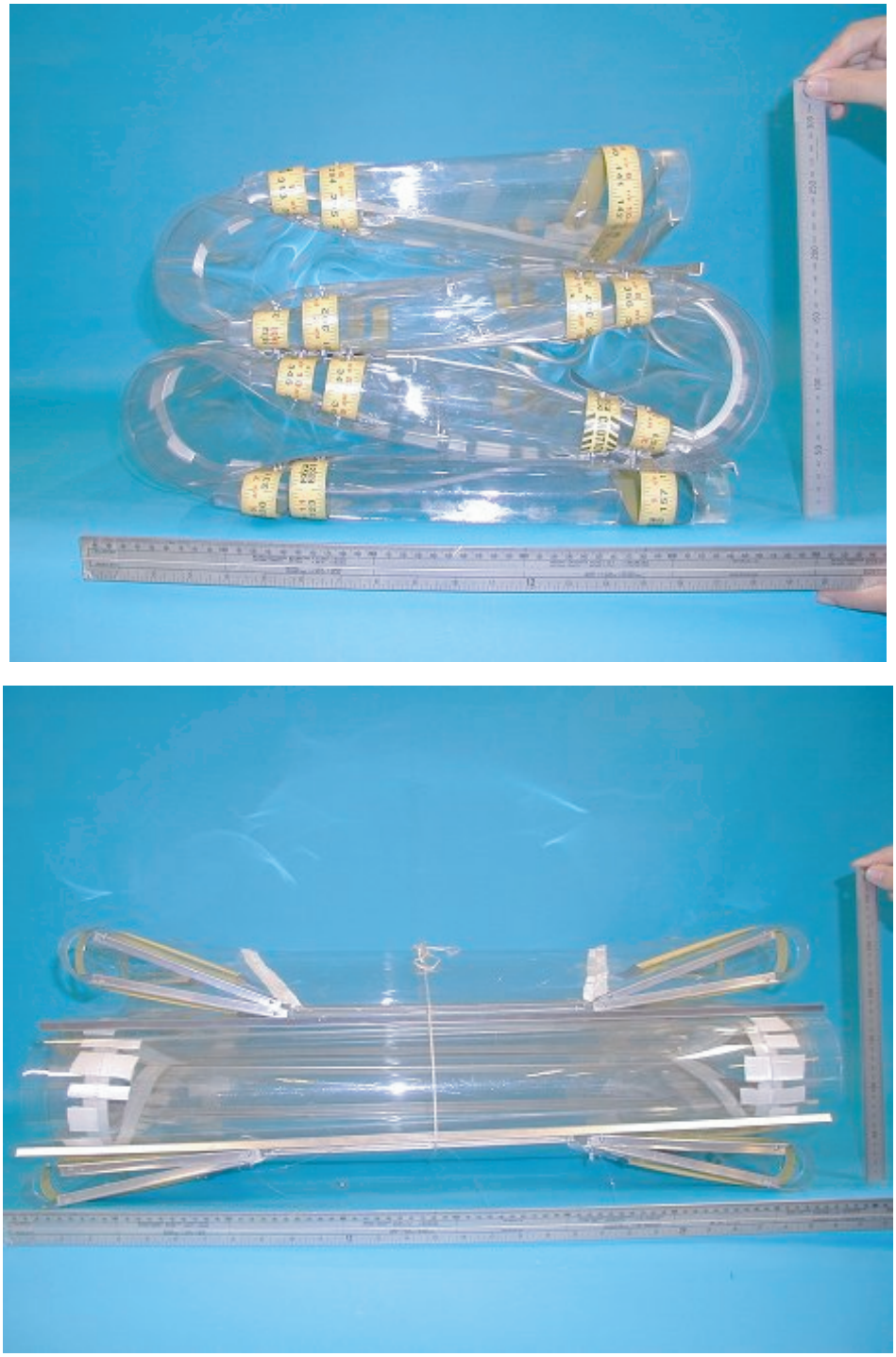

Figure 5.3: Quarter-scale model, Z-folded (side views).

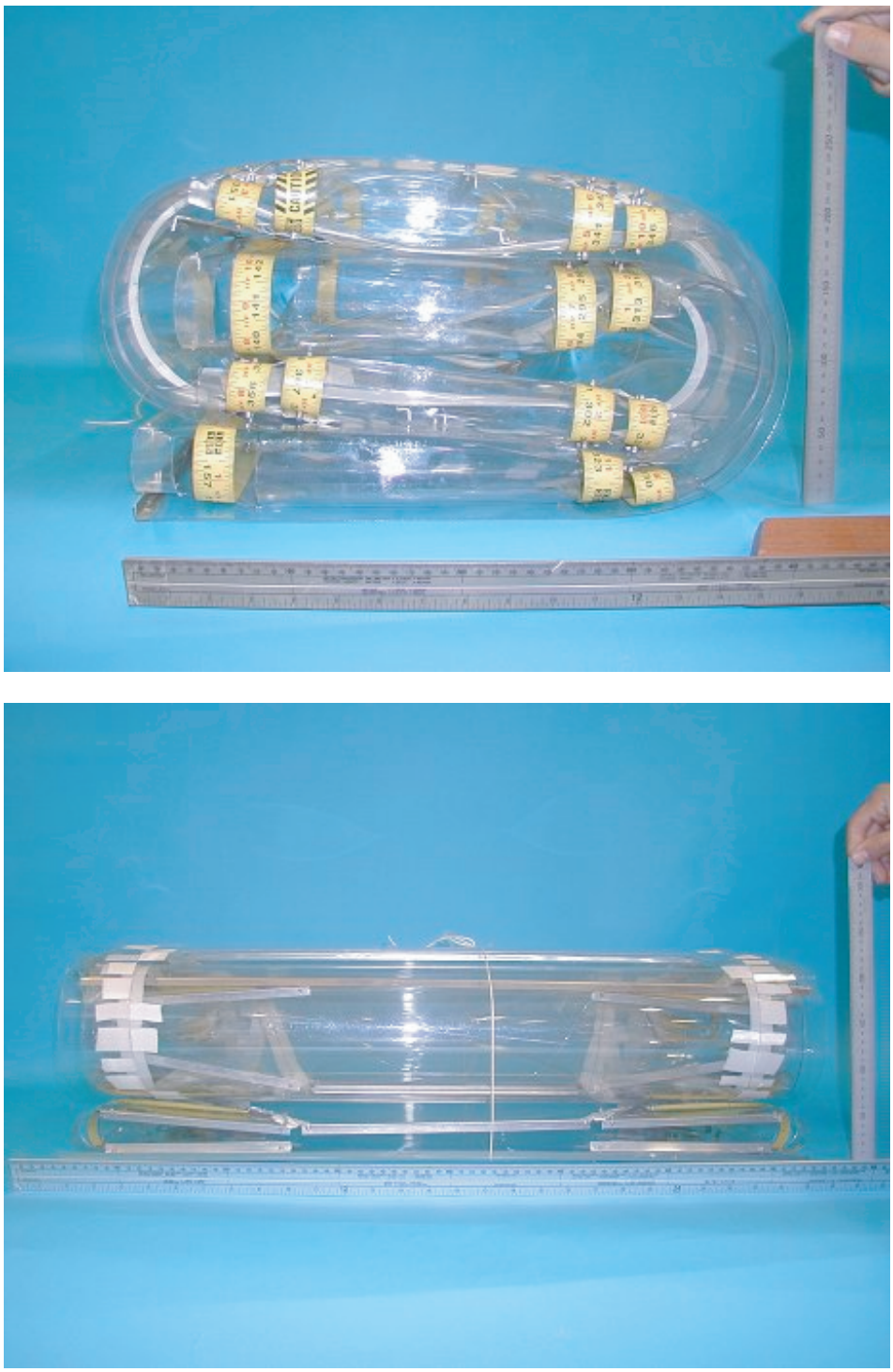

Figure 5.4: Quarter-scale model, coiled (side views).

Figure 5.5: Quarter-scale model, stowed (perspective views): Z-folded at top, coiled at bottom.

these connections needs to be investigated experimentally, ideally on small size samples of the connections.

Both T and L connections were found to be weak under shear loading. The possibility of changing the orientation of the tape such that the fibres are at 45° to the connection needs to be investigated.

- Tape-springs: they increase the deployment moment and the stiffness of the sidewalls in the deployed configuration. However they also increase the mass of the structure due to the high density of steel. The number of tape springs and the distance between the points where they are attached to the sidewall need to be optimized. Curved washers might be used to prevent flattening of the tape-spring at the attachment points. Bolts and nuts can be used as alternative to rivets.

- Windows: windows are needed along the sidewalls, to reduce the high strains resulting from the cross-over of the longitudinal and transverse hinge lines when the structure is folded. The width of the windows depends on the minimum bend radius of the sidewall material. The length of the windows depends on both the minimum bend radius and the type of folding that is used. The position of the windows also depends on how which mode of folding is chosen for the structure, i.e. Z-folding or coiling. All of these issues need to be analysed in greater detail as part of the final design of the half-scale demonstrator.

- Stiffening: the model was found to be insufficiently stiff when first completed, but it became much stiffer when localised stiffening measures were introduced, as follows. Cross bracing wires were introduced at both ends of the model, vertical stiffeners (thin gauge Al-alloy angles) were added along the edges of the sidewalls, and also transversally underneath the RF surface and the top surface.

- Minimum bend radius: some plastic deformation of the Vivak sheets occurred in the quarter-scale model, as the yield strain appears to be lower than in the supplier datasheet. In future, the sheets used for the structure need to be tested to determine their minimum bend radius, and an appropriate factor of safety against yielding needs to be used.

- Spacers have been successful in preventing the sidewall material from becoming over-stressed.

Chapter 6

Design for Folding

This chapter presents the analysis and detailed testing of those elements of the reflector structure that need to deform in order to allow folding of the structure. A full-scale, geometrically non-linear finite-element analysis of these components was not feasible within the timescale of the present study.

6.1 Minimum Bend Radius of Laminated Plates

To ensure that no material failure occurs during folding of the reflector, the minimum bend radius of the material was measured experimentally and also estimated by laminate strength analyses.

Laminate strength analyses, based on classical laminate theory, are an extension of lamina failure criteria, and are applied on a ply-by-ply basis. The maximum strain criterion and the Tsai-Wu failure criterion are used to estimate the minimum bend radius. The results obtained from both criteria are compared to experimental results.

6.1.1 Maximum Strain Criterion

The maximum strain criterion assumes that failure occurs when the in plane strains along the principal material direction exceed the ultimate strains of the material (Gibson, 1994)

$$\begin{aligned} -\epsilon_L^{(-)} < \epsilon_1 < \epsilon_L^{(+)} \\ -\epsilon_T^{(-)} < \epsilon_2 < \epsilon_T^{(+)} \\ \mid \gamma_{12} \mid < \epsilon_{LT} \end{aligned} \tag{6.1}$$

where $\epsilon_L^{(-)}$ and $\epsilon_L^{(+)}$ are the longitudinal ultimate strains in compression and tension; $\epsilon_T^{(-)}$ and $\epsilon_T^{(+)}$ are the transverse ultimate strains in compression and tension; and ϵ_{LT} is the ultimate

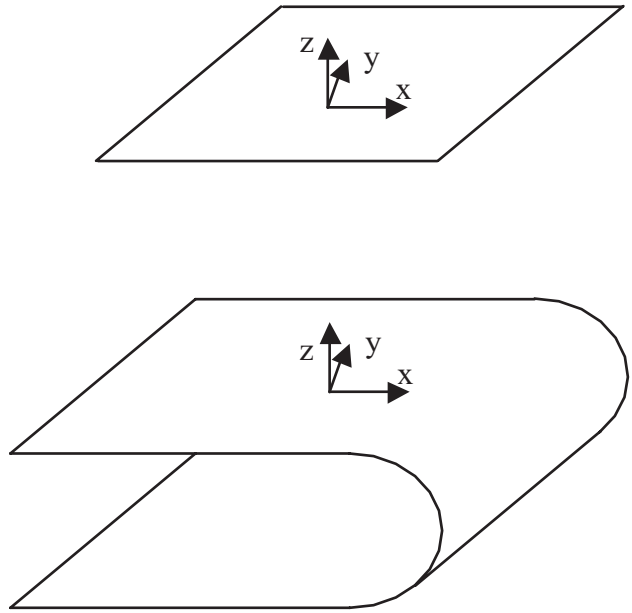

Figure 6.1: Folding of a thin plate.

shear strain.

The in-plane strains in a laminated plate can be written as, see Figure 6.1,

$$\begin{aligned} \epsilon_x &= \epsilon_x^0 + z\kappa_x \\ \epsilon_y &= \epsilon_y^0 + z\kappa_y \\ \gamma_{xy} &= \gamma_{xy}^0 + z\kappa_{xy} \end{aligned} \tag{6.2}$$

where ϵ_x^0, ϵ_y^0, and γ_{xy}^0 are the strains of the middle surface; κ_x, κ_y, and κ_{xy} are the curvatures of the middle surface. The in-plane strains along the principal material direction of the k-th lamina can then be written as

$$\left\{ \begin{array}{c} \epsilon_1 \\ \epsilon_2 \\ \gamma_{12}/2 \end{array} \right\}_k = [T] \left\{ \begin{array}{c} \epsilon_x \\ \epsilon_y \\ \gamma_{xy}/2 \end{array} \right\} \tag{6.3}$$

where $[T]$ is the transformation matrix

$$[T] = \left[\begin{array}{ccc} c^2 & s^2 & 2cs \\ s^2 & c^2 & -2cs \\ -cs & cs & c^2 - s^2 \end{array} \right] \tag{6.4}$$

and where $c = \cos\theta$ and $s = \sin\theta$. θ is the angle between the x-axis and the principal material direction.

Consider a flat, balanced, symmetric laminated plate, initially unstressed. A large curvature along the x-axis is imposed and, since the in-plane stiffness of the plate prevents it from stretching, the plate deforms into a purely cylindrical surface (apart form narrow regions near the edges), as shown in Figure 6.1. Clearly, since $\kappa_x \neq 0$, $\epsilon_x^0 = \epsilon_y^0 = \gamma_{xy}^0 = \kappa_y = \kappa_{xy} = 0$, the in-plane strains along the principal material directions become

$$\left\{ \begin{array}{c} \epsilon_1 \\ \epsilon_2 \\ \gamma_{12}/2 \end{array} \right\}_k = \left[\begin{array}{c} zc^2 \\ zs^2 \\ -zcs \end{array} \right] \left\{ \begin{array}{c} \kappa_x \\ \kappa_x \\ \kappa_x \end{array} \right\} \tag{6.5}$$

To check for material failure one needs to substitute the results obtained from Equation 6.5 into Equation 6.1. This gives

$$\begin{array}{c} -\epsilon_L^{(-)} < zc^2\kappa_x < \epsilon_L^{(+)} \\ -\epsilon_T^{(-)} < zs^2\kappa_x < \epsilon_T^{(+)} \\ \mid -2zcs\kappa_x \mid < \epsilon_{LT} \end{array} \tag{6.6}$$

The first ply failure occurs when Equation 6.6 is violated.

In an isotropic plate, and also in the case of a unidirectional composite plate bent along its principal material direction, the maximum strain occurs on the outer edges of the plates, hence at $z = \pm t/2$. It would seem natural to compare these peak bending strains with the ultimate strains for the fibres. However, extensive experiments on thin laminates made from woven CFRP composites (Yee and Pellegrino 2003, Gerngross 2003) have shown that these laminates are able to survive peak bending strains that are much larger than those obtained from the above approach. Therefore, here it will be assumed that *a woven lamina in bending fails when the strain at the centre of the yarn reaches the ultimate value*:

$$\begin{array}{l} \epsilon_x = \pm z\kappa_x \\ \epsilon_y = \gamma_{xy} = 0 \end{array} \tag{6.7}$$

where z is the distance of the centre of the outermost yarn from the mid-plane. Therefore, the minimum radius of curvature can be obtained from the ultimate strain ϵ_{max} (which is equal to the smaller of $\epsilon_L^{(-)}$ or $\epsilon_L^{(+)}$, in the case of a laminated composite)

$$\mathrm{R}_{min} = \frac{1}{\kappa_x} = \frac{z}{\epsilon_{max}} \tag{6.8}$$

The minimum bend radii were estimated for the following composite plates made of woven T300 carbon fibre in LTM45 epoxy resin, supplied by Brookhouse Paxford Ltd:

- 200 gsm 2 × 2 twill, 0.2 mm thick. According to the supplier, this material has the material properties: $E_1 = E_2$=65 GPa, G_{12}=5 GPa, ν_{12}=0.06, V_f=0.55, $\epsilon_L^{(+)} = 1\%$, $\epsilon_L^{(-)} = 1\%$

Material	Layup	Length	Width	Thickness	R_{min}
-	-	(mm)	(mm)	(mm)	(mm)
200 gsm 2x2 twill, 3k	0	62	15.0	0.2	5.0
200 gsm 2x2 twill, 3k	0/0	99	15.0	0.4	15.0
94 gsm plain weave	0/45/0	85	14.3	0.33	13.7
94 gsm plain weave	45/0/45	65	14.8	0.33	6.8

Table 6.1: Minimum bend radius estimates from maximum strain criterion.

- and 94 gsm plain weave, 0.33 mm thick, which has the following material properties: $E_1 = E_2$=56 GPa, G_{12}=3 GPa, ν_{12}=0.05, V_f=0.48, $\epsilon_L^{(+)} = 1\%$, $\epsilon_L^{(-)} = 1.1\%$.

The minimum radius of curvature, for an assumed ultimate shear strain $\epsilon_{LT} = 3.6\%$ for both materials (Gerngross 2003), is given in Table 6.1.

The 2×2 twill, single ply laminate fails due to both tension and compression strains at $R =$ 5 mm, whereas the two ply laminate fails for tension strain in the upper layer and compression strain in the lower layer at $R = 15$ mm.

For the plain weave 0/45/0, the top layer fails due to tension strain at $R = 13.7$ mm. For the plain weave 45/0/45, the top and bottom layers fail due to shear strain at $R = 6.8$ mm.

6.1.2 Tsai-Wu Criterion

The Tsai-Wu criterion assumes that material failure of a lamina occurs when

$$F_{11}\sigma_1^2 + F_{22}\sigma_2^2 + F_{66}\sigma_6^2 + F_1\sigma_1 + F_2\sigma_2 + 2F_{12}\sigma_1\sigma_2 \geq 1 \tag{6.9}$$

where $F_{11} = 1/(s_L^{(+)}s_L^{(-)})$, $F_{22} = 1/(s_T^{(+)}s_T^{(-)})$, $F_1 = 1/s_L^{(+)} - 1/s_L^{(-)}$, $F_2 = 1/s_T^{(+)} - 1/s_T^{(-)}$, $F_{66} = 1/s_{LT}^2$, and $F_{12} = -(F_{11}F_{22})^{1/2}/2$, $\sigma_6 = \tau_{12}$. $s_L^{(+)}$ and $s_L^{(-)}$ are the longitudinal strengths of the lamina in tension and compression, whereas $s_T^{(+)}$ and $s_T^{(-)}$ are the transverse strengths of the lamina in tension and compression. Note that $s_L^{(-)}$ and $s_T^{(-)}$ are assumed to be positive.

The lamina stress-strain relationships are given by

$$\left\{ \begin{array}{c} \sigma_1 \\ \sigma_2 \\ \tau_{12} \end{array} \right\}_k = [Q] \left\{ \begin{array}{c} \epsilon_1 \\ \epsilon_1 \\ \gamma_{12}/2 \end{array} \right\} \tag{6.10}$$

where $[Q]$ is the lamina stiffness matrix, defined as

$$[Q] = \left[\begin{array}{ccc} Q_{11} & Q_{12} & 0 \\ Q_{21} & Q_{22} & 0 \\ 0 & 0 & 2Q_{66} \end{array} \right] \tag{6.11}$$

The components of $[Q]$ are related to the engineering constants by

$$\begin{aligned} Q_{11} &= \frac{E_1}{1-\nu_{12}\nu_{21}} \\ Q_{12} = Q_{21} &= \frac{\nu_{12}E_2}{1-\nu_{12}\nu_{21}} \\ Q_{22} &= \frac{E_2}{1-\nu_{12}\nu_{21}} \\ Q_{66} &= G_{12} \end{aligned} \tag{6.12}$$

The lamina principal stresses can be expressed in terms of the off-axis strains as

$$\left\{ \begin{array}{c} \sigma_1 \\ \sigma_2 \\ \tau_{12} \end{array} \right\}_k = [Q]\,[T] \left\{ \begin{array}{c} \epsilon_x \\ \epsilon_y \\ \gamma_{xy}/2 \end{array} \right\} \tag{6.13}$$

For a laminate in pure bending, with$\kappa_x \neq 0$, $\epsilon_x^0 = \epsilon_y^0 = \gamma_{xy}^0 = \kappa_y = \kappa_{xy} = 0$, the principal stresses are given by

$$\left\{ \begin{array}{c} \sigma_1 \\ \sigma_2 \\ \tau_{12} \end{array} \right\}_k = [Q]\,[T] \left\{ \begin{array}{c} z\kappa_x \\ 0 \\ 0 \end{array} \right\} \tag{6.14}$$

The principal stresses in the k-th layer can be written in terms of the curvature κ_x as

$$\begin{aligned} \sigma_1 &= (Q_{11}c^2 + Q_{12}s^2)z\kappa_x \\ \sigma_2 &= (Q_{12}c^2 + Q_{22}s^2)z\kappa_x \\ \tau_{12} &= (-Q_{66}cs)z\kappa_x \end{aligned} \tag{6.15}$$

Substituting Equation 6.15 into Equation 6.9 gives a quadratic equation in κ_x

$$b_2\kappa_x^2 + b_1\kappa_x - 1 = 0 \tag{6.16}$$

where

$$\begin{aligned} b_2 &= \left[F_1(Q_{11}c^2 + Q_{12}s^2) + F_2(Q_{12}c^2 + Q_{22}s^2)\right] z \\ b_1 &= \left[F_{11}(Q_{11}c^2 + Q_{12}s^2)^2 + F_{22}(Q_{12}c^2 + Q_{22}s^2)^2 + 2F_{12}(Q_{11}c^2 + Q_{12}s^2)(Q_{12}c^2 + Q_{22}s^2)\right] z^2 \end{aligned}$$

According to the supplier, 2×2 twill T300/LTM45 200 gsm has $S_L^{(+)}$=650 MPa, $S_L^{(-)}$=600 MPa; an in-plane shear strength S_{LT}=55 MPa is assumed. The plain weave T300/LTM45 94 gsm has $S_L^{(+)}$=650 MPa and $S_L^{(-)}$=670 MPa, and the in-plane shear strength S_{LT}=111 MPa has been measured by Gerngross (2003).

In analogy with the previous section, the Tsai-Wu criterion has been applied at the *centre of the yarn* that is nearest to the surface of the laminate. The minimum bend radii thus estimated are listed in Table 6.2.

Material	Layup	Length	Width	Thickness	R_{min}
-	-	(mm)	(mm)	(mm)	(mm)
200 gsm 2x2 twill, 3k	0	62	15.0	0.2	10.4
200 gsm 2x2 twill, 3k	0/0	99	15.0	0.4	15.1
94 gsm plain weave	0/45/0	85	14.3	0.33	11.9
94 gsm plain weave	45/0/45	65	14.8	0.33	6.8

Table 6.2: Minimum bend radius estimates from Tsai-Wu criterion.

Figure 6.2: Bending test for thin composites.

2×2 twill single ply fails due to compression stress at $R = 10.4$ mm, whereas for a two-ply laminate the bottom layer fails due to compression stress at $R = 15.1$ mm. For a plain weave laminate 0/45/0, the top layer fails at $R = 11.9$ mm due to tension stress. For the plain weave laminate 45/0/45 the mid-layer fails due to shear stress at $R = 6.8$ mm.

6.1.3 Measurements of Minimum Bend Radius

Bending tests were carried out to measure the minimum radius of curvature of LTM45/CFO300 woven laminates (T300 grade). The laminates were made from 200 gsm 2×2 twill, 0.2 mm thick, and from 94 gsm plain weave, 0.11 mm thick. All laminates were supplied by Brookhouse Paxford Ltd.

Thin, woven composites can be bent into very small radii, and hence standard three-point and four-point bending tests are found to be unsuitable to measure the minimum bend radius. An alternative test that allows large displacements was devised, see Figure 6.2.

Material	Layup	Length	Width	Thickness	R_{min}
-	-	(mm)	(mm)	(mm)	(mm)
200 gsm 2x2 twill, 3k	0	62	15.0	0.2	4.0
200 gsm 2x2 twill, 3k	0/0	99	15.0	0.4	12.5
94 gsm plain weave	0/45/0	85	14.3	0.33	10.4
94 gsm plain weave	45/0/45	65	14.8	0.33	5.6

Table 6.3: Measurements of minimum bend radius of LTM45/CFO300 woven laminates.

Strip specimens with a width of 15 mm are attached to circular rods with a diameter of 15 mm, in turn connected to an Instron materials testing machine, using 50 mm long strips of 3M 79 tape. The specimens are $\pi R_{min} + 30$ mm long, where R_{min} is our initial estimates of the minimum radius of curvature, in order to ensure that failure takes place roughly in the configuration shown in the figure.

The tests were done with a cross-head speed of 5 mm/min, during which a Sony DCR-PC110E digital video camera recorded images of the specimen. Once the specimen had failed, the minimum bend radius was measured using one or more images captured just before failure. In the case of specimen being too long, the ends of the specimen come into contact without failure and the test is repeated with a shorter specimen.

Results from this test are presented in Table 6.3. For a unidirectional layup, the minimum bend radius increases when the thickness of the material increases. The use of angle plies significantly affects the minimum bend radius. Comparing these results with the theoretical estimates in Tables 6.1 and 6.2, it can be seen that the estimates based on the maximum strain criterion are generally quite accurate.

To see what effect the presence of a longitudinal connection has on the minimum radius of curvature of two sheets that are first folded on top of one another before being bent about an axis perpendicular to the connection, an additional test was carried out. Two sheets were put alongside each other, and connected over their full length using 3M 79 tape that covered half of the width of each specimen. One sheet was folded on top of the other and then the resulting "double-thickness" specimen was tested in the usual way. Results from this test are presented in Table 6.4. When compared to the results for a single strip, the effect of this longitudinal connection on the minimum radius of curvature is negligible.

The transverse force required to fold the above LTM45/CFO300 woven laminates, and also a Vivak sheet for comparison, was measured on 15 mm wide, 125 mm long strips using a similar setup to that described in Section 6.1.3. Measured plots of folding force versus bend radius are

Material	Layup	Length	Width	Thickness	R_{min}
-	-	(mm)	(mm)	(mm)	(mm)
200 gsm 2x2 twill, 3k	0	62	15	0.2	4
200 gsm 2x2 twill, 3k	0/0	99	15	0.4	13

Table 6.4: Measured minimum bend radius of two LTM45/CFO300 woven laminates with a longitudinal connection.

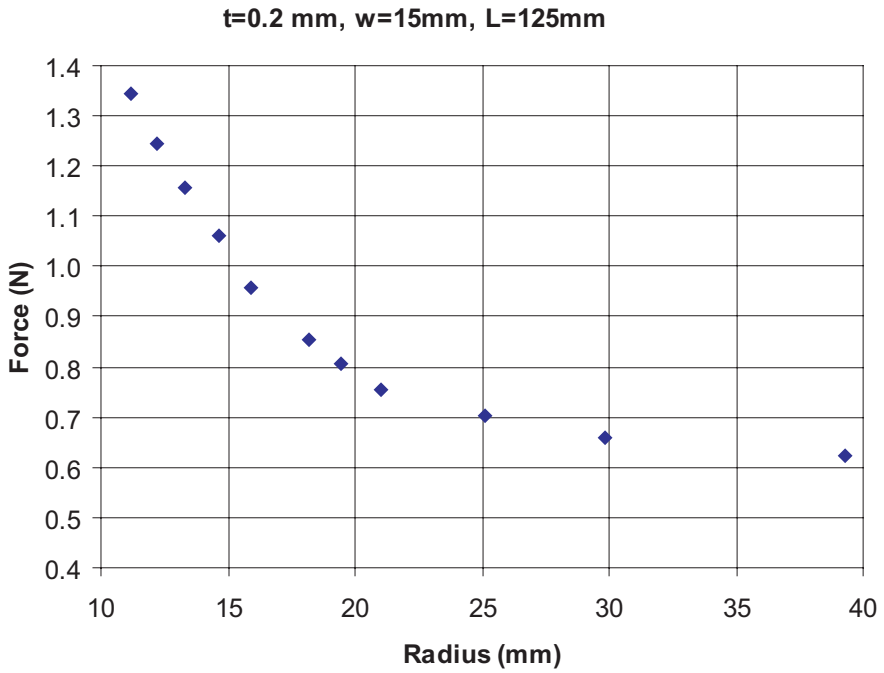

Figure 6.3: Folding force versus bend radius for 0.2 mm thick LTM45/CFO300.

given in Figure 6.3 for a 2 × 2 twill, 0.2 mm thick laminate, and in Figure 6.4 for 2 × 2 twill, 0.4 mm thick laminate. The values of the folding force at a bend radius of 20 mm (Figure 6.5) are compared in Table 6.5. The corresponding folding force can be estimated from

$$F = \frac{E_{fx} I_{yy}}{Rd} \tag{6.17}$$

where $d = 43.6$ mm is the moment arm; E_{fx} is the flexural modulus in the x-direction; I_{yy} is the second moment of area about the neutral axis.

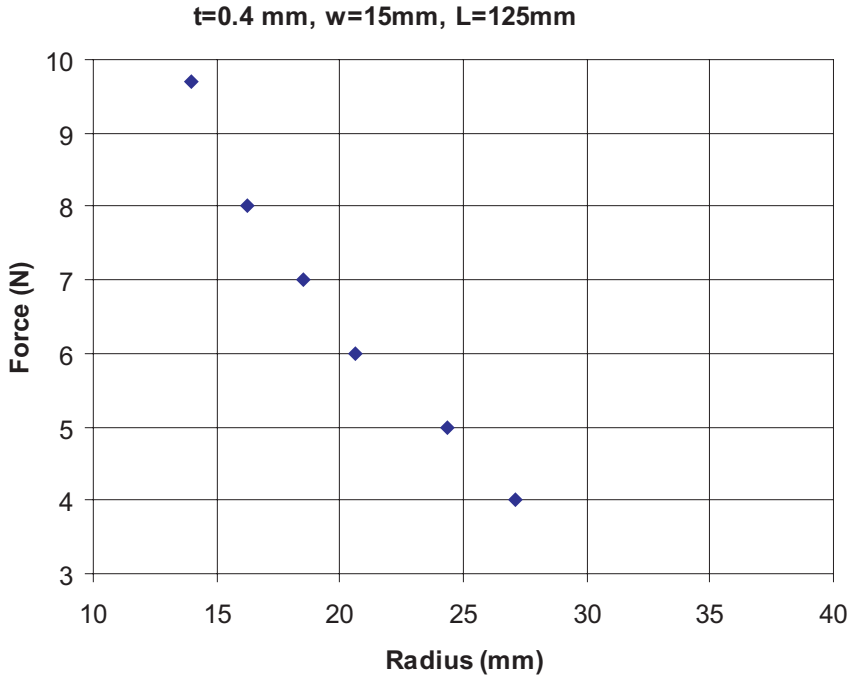

Figure 6.4: Folding force versus bend radius for 0.4 mm thick LTM45/CFO300.

						Test	Estimate
Material	Layup	E_{fx}	Length	Width	Thickness	Force	Force
-	-	(N/mm^2)	(mm)	(mm)	(mm)	(N)	(N)
200 gsm 2x2 twill, 3k	0	65000	125	15	0.2	0.78	0.75
200 gsm 2x2 twill, 3k	0/0	65000	125	15	0.4	6.30	5.96
94 gsm plain weave	0/45/0	55103	125	15	0.33	2.77	2.84
94 gsm plain weave	45/0/45	19392	125	15.5	0.33	1.68	1.03
Vivak	-	2050	125	15	0.75	1.97	1.24

Table 6.5: Folding force comparison.

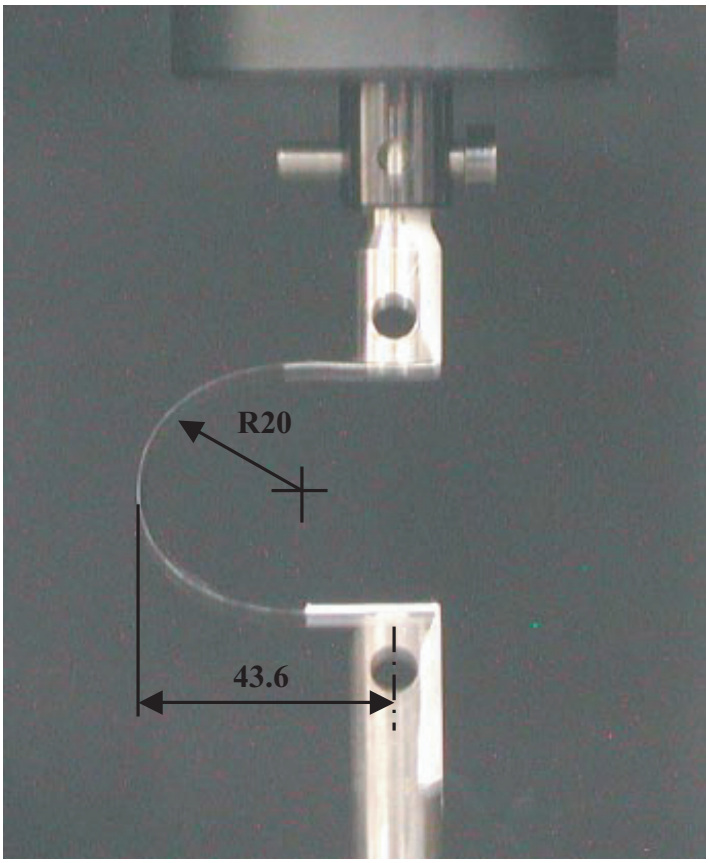

Figure 6.5: Folding force measurement.

6.2 Connections

The joints of the reflector structure must be strong enough to transfer the loads from one surface to another, and also flexible enough to allow folding and unfolding of the structure. Two types of connections have been used, see Figure 6.6:

- surface-to-surface connections, which keep two separate sheets of material in very close proximity, but allow them to rotate with respect to one another;
- flexible connections, which allow two parts of the same sheet to describe an essentially rigid-body relative rotation, while the connecting region deforms elastically.

The first type of connection can be made with adhesive tape, this is a lightweight solution that provides a uniform stress distribution across the two sheets being connected. For an L-connection, one-sided tape can be applied on the inner and/or outer surfaces of the sheets to be joined. For a T-connection (and also a stronger L-connection), the sheets can be stitched by using a double sided tape instead. In this case, the tape would go from the inner surface of the first sheet to the outer surface of the second sheet, then a separate piece of tape would go from the outside of the first sheet to the inside of the second one. This connection resembles a rolamite hinge; ideally the edges of the sheet should be rounded to avoid cutting the tape.

The second type of connection is achieved by careful design of the parts of the structure that have to flex and by controlling the curvature to which they are subjected. In simple terms, the maximum strain imposed by the folding process (which can be reduced by reducing the thickness of the connection and/or the maximum curvature) has to be smaller than a threshold value, which depends on the properties of the sheet.

Figure 6.6 shows where each type of connections was used in the half-scale SAR reflector structure. The same type of connections were used also in the quarter-scale model.

Either of these types of connection can be made to latch in one particular configuration by fastening steel tape springs (i.e. lengths of carpenter tape) on the same side of the two sheets, by means of rivets or bolts and nuts. Note that a cut-out is required under each tape spring to provide the clearance needed for it to fold without being overstressed.

Cut-outs are required to reduce the maximum strain in the region where a hinge line crosses another hinge line in the same sheet of material. It is desirable for these cut-outs to be as small as possible, to reduce the loss of stiffness of the structure. Stress concentrations near the edges of a cut-out need to be avoided, e.g. by reinforcing the structure in the immediate vicinity of the cut-out (Niu 1990). A simple cut-out shape is a rectangle with rounded corners, as used in

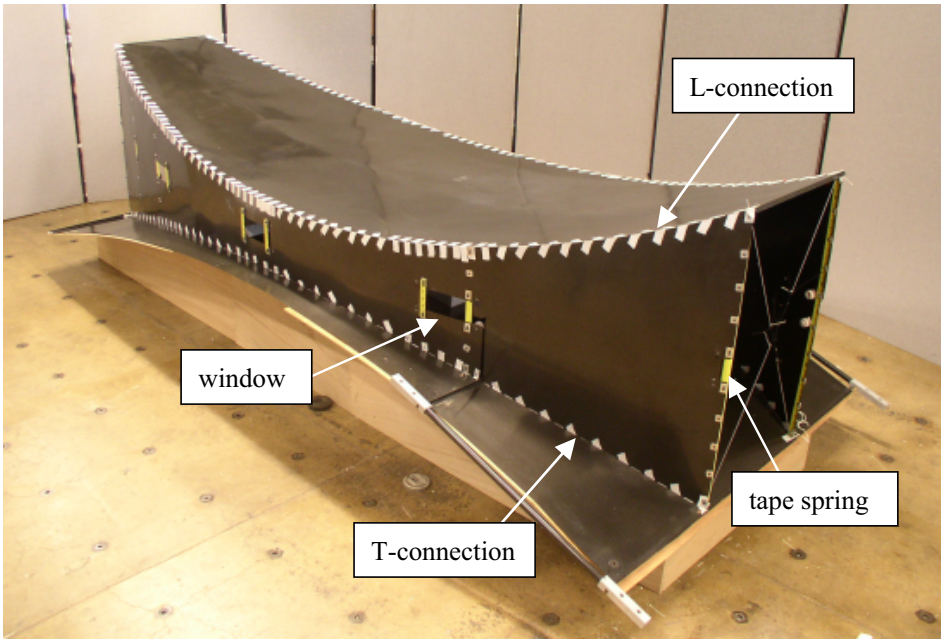

Figure 6.6: Connections in half-scale model.

the sidewalls of the reflector structure.

Some of the connections described above are shown in Figure 6.7.

6.3 Properties of Tape Connections

Structural connections made with 3M 79 woven glass tape were tested in order to measure their stiffness and strength. The tape is a white glass cloth, with acrylic pressure sensitive adhesive.

The manufacturer's datasheet lists the following properties for the tape: thickness of 0.177 mm, width of 25 mm, tensile strength of 26 N/mm, adhesion to steel of 0.33 N/mm, elongation at break 5%.

6.3.1 Shear Testing of Two Coplanar Plates

This test measures the stiffness and strength of an L-connection when the connected surfaces are coplanar (this arrangement corresponds to the folded configuration of the reflector).

Two coplanar steel plates at a distance of 1 mm were connected with tape in two different orientations, 0° and 45°, see Figure 6.8. The plates were connected to an Instron materials testing machine to measure their load-displacement response for a cross-head speed of 5 mm/min.

The vertical displacement of the plates was measured both from the cross-head displacement of the Instron and with an LE-05 laser extensometer using two retro-reflective strips. It was

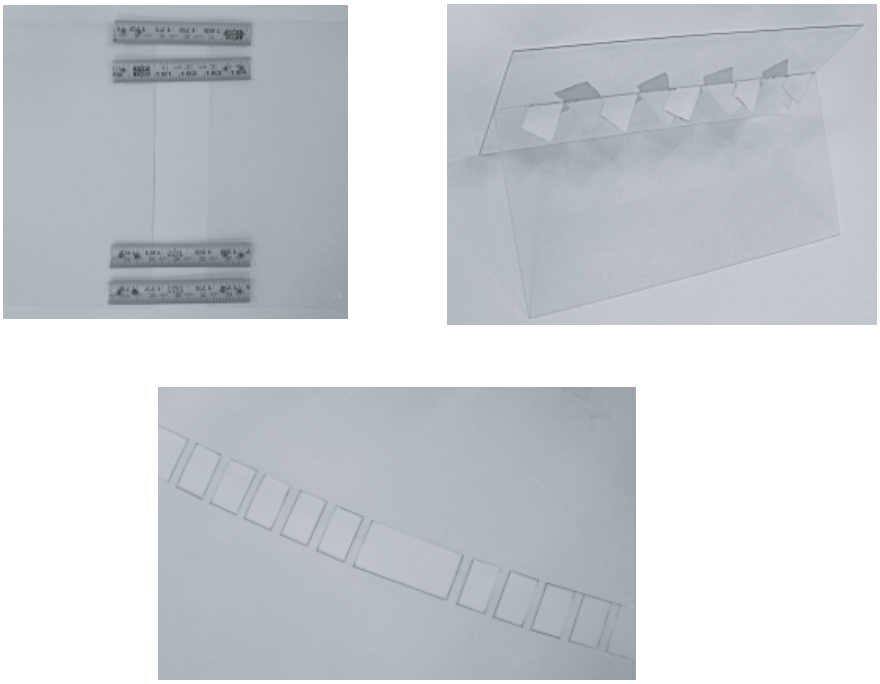

Figure 6.7: Pictures of joints for connecting surfaces (tape springs on top left, woven tape T-connection on top tight, and windows at bottom).

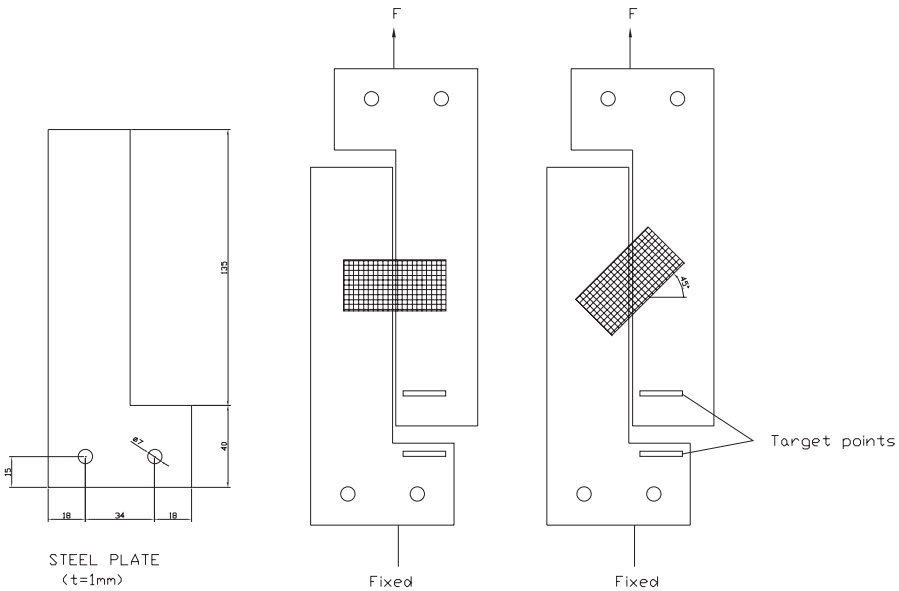

Figure 6.8: Shear testing of two coplanar plates.

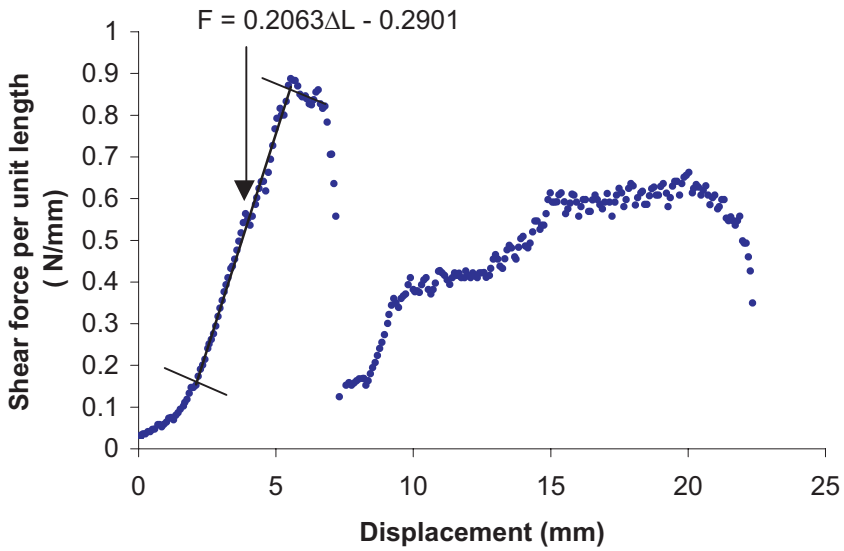

Figure 6.9: Shear test of coplanar plates connected with 0° tape (specimen 1).

found that the displacements measured by the extensometer were essentially identical to those from the Instron, hence only the measurements from the extensometer will be presented.

Plots of shear force per unit length versus displacement are given in Figures 6.9 to 6.11, for connections made with a single 50 mm long tape. Results for connections made with three 60 mm long tapes, at 0° to the steel plates are shown in Figure 6.12.

Least square fits have been obtained for each test, to compare the stiffness of the different types of connections. Note that arranging the tape at 45° yields a connection that is about 4 times stronger and stiffer.

6.3.2 Shear Testing of L- and T-Connections

An L-connection in the unfolded configuration was obtained by rotating one of the steel plates through 90° around the axial direction, as seen in Figure 6.13.

Having found in the previous test that the displacements measured with the laser extensometer were identical to those from the cross-head displacement of the Instron, this time only the cross-head displacements were obtained. 60 mm long tapes were applied to the same steel plates as in the previous test, at 0° and ±45°, and tested at a cross-head speed of 5 mm/min.

Plots of shear force per unit length versus displacement are given in Figure 6.14 for a single tape at 0°, and in Figure 6.15 for a single tape at 45°. Least squares fits are obtained to compare the stiffness of the specimens. Arranging the tape at 45° yields a connection that is about 4 times stronger and stiffer than a connection made by single tape.

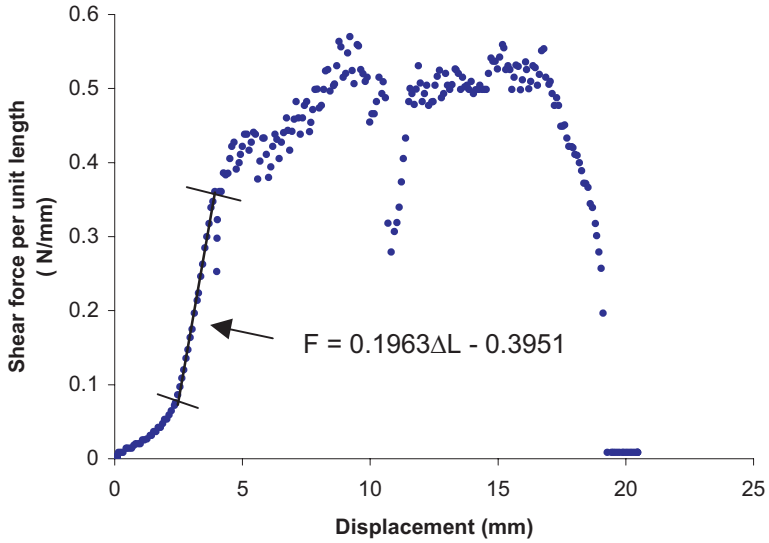

Figure 6.10: Shear test of coplanar plates connected with 0° tape (specimen 2).

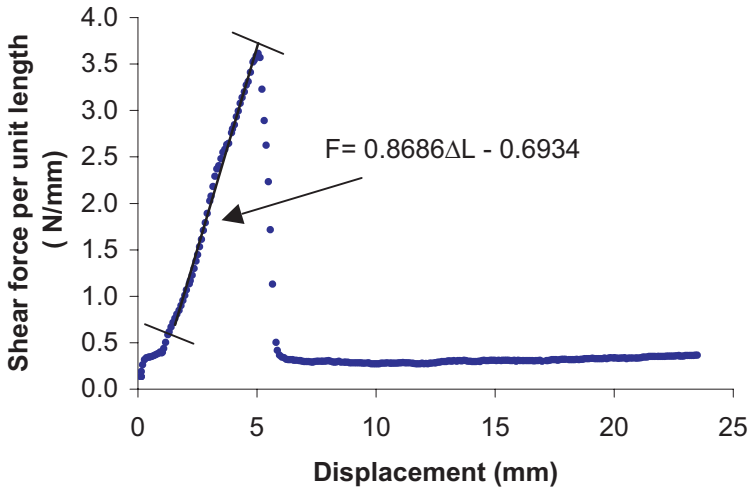

Figure 6.11: Shear test of coplanar plates connected with tape at 45°.

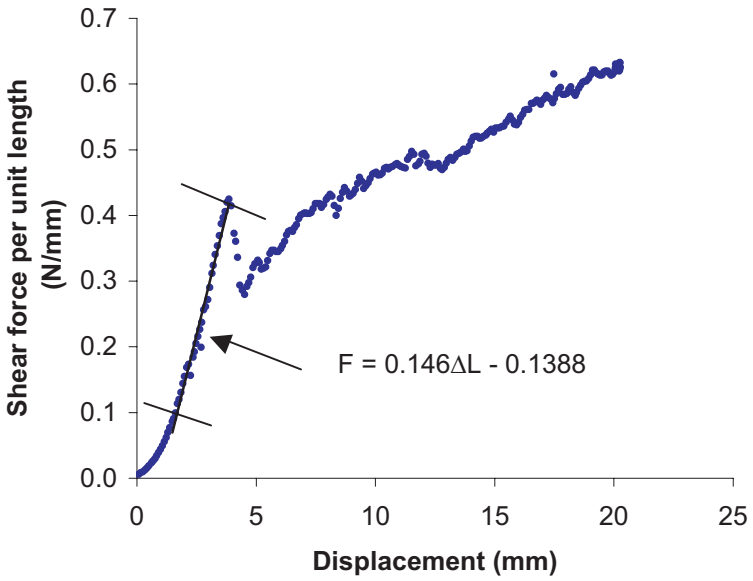

Figure 6.12: Shear test of coplanar plates connected with three tapes at 0°.

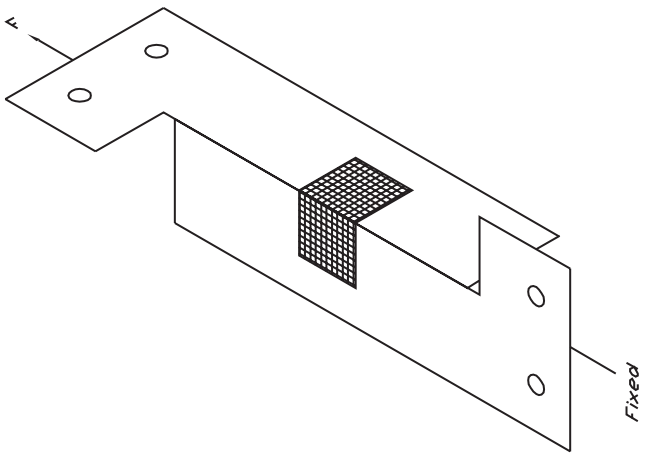

Figure 6.13: Shear testing of an L-connection.

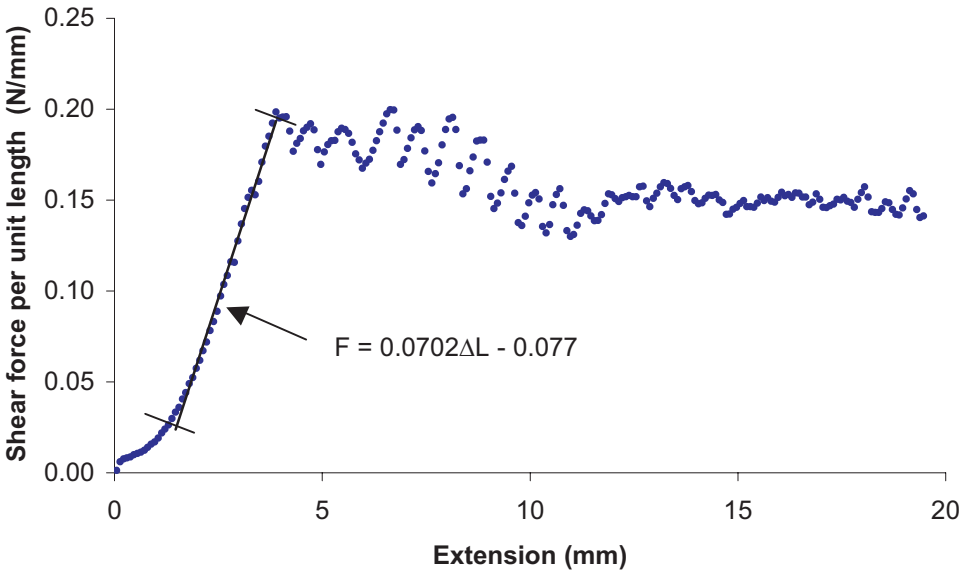

Figure 6.14: Shear test of L-connection with single tape at 0°.

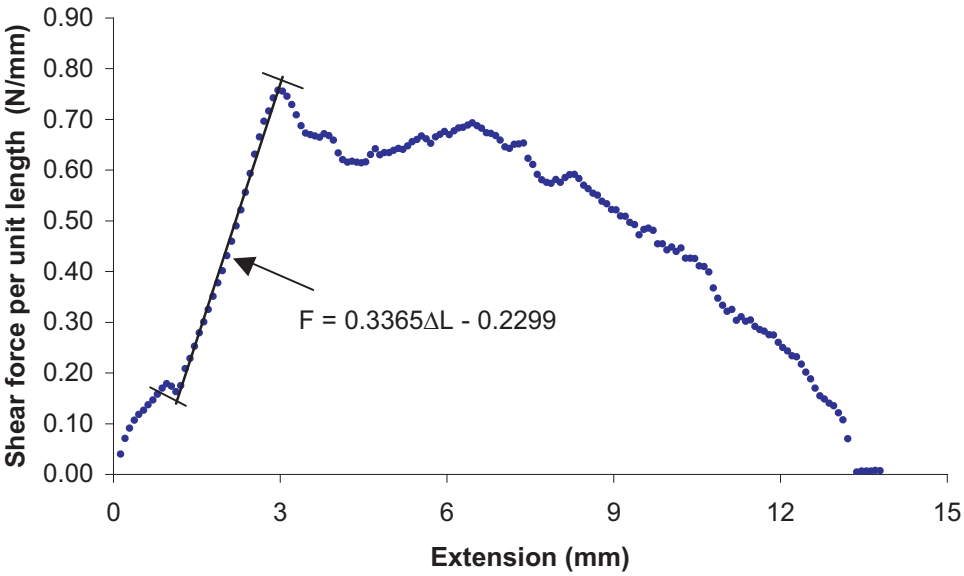

Figure 6.15: Shear test of L-connection with single tape at 45°.

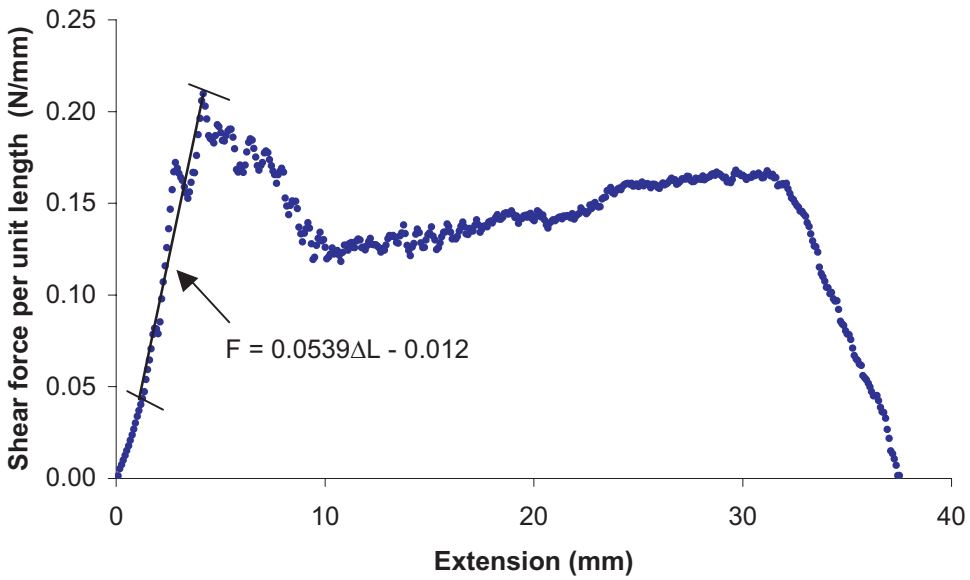

Figure 6.16: Shear test of L-connection with a pair of tapes at 0°.

Results for connections made with a pair of tapes at 0° and at ±45° are given in Figures 6.16 and Figures 6.17, respectively. Arranging the tape at ±45° yields about 2.5 times more strength and stiffness when compared to tapes at 0°.

To measure the strength and stiffness of T-connections, two steel plates were prepared as shown in Figure 6.18. In one of the plates, four 27 mm long by 1 mm wide slots were cut at a spacing of 10 mm. Woven tapes were applied to the plates by passing the tapes through the slots. All specimens were tested at a cross-head speed of 5 mm/min.

First a single tape connection at 0° was tested. Results for a 25 mm wide single tape are given in Figures 6.19 and 6.20 for 50 mm long tape, in Figure 6.21 for a 60 mm long tape, and in Figures 6.22 and 6.23 for a 70 mm long tape. After testing, the connections were visually inspected: no tear was detected in the 50 mm long tape, a 2 mm long tear in the 60 mm long tape, and a 7 mm tear in the 70 mm long tape were observed along the direction of the applied load.

Next, a connection with a single piece tape at +45° or −45° was tested. In this case, the width of the tape had to be reduced to fit in the slot. Results for a 17 mm wide by 75 mm long piece of tape at +45° are shown in Figure 6.24, and at −45° in Figure 6.25. No tear was observed in the tape at −45°, whereas a 2 mm long tear was observed in the other case.

Overall, it was found that the angle of the tape significantly affects the strength and stiffness of the connection. A connection with tape at +45° is three times stronger and five times stiffer than a connection with tape at 0°. However, the strength of the "complementary" connection,

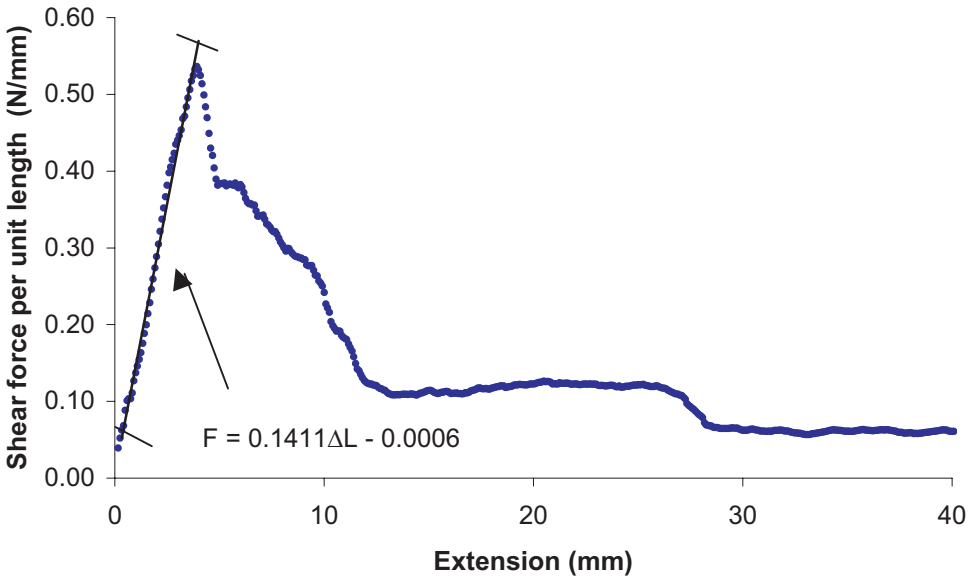

Figure 6.17: Shear test result of L-connection with a pair of tapes at ±45°.

with the tape at −45°, is half the strength of the connection with tape at 0°, and almost as stiff as one with 0° tape.

Next, the plates were connected with a pair of tapes. Results for 60 mm long by 25 mm wide pieces of tape at 0° are shown in Figure 6.26. One of the tapes was torn by 2 mm while the other was torn by 16 mm along the direction of the force.

For the tapes at ±45°, whose width is reduced to 17 mm, the length was increased to 88 mm so that the area of contact is unchanged. Results for a pair of tapes at +45°, −45°, and ±45° are given in Figures 6.27 to 6.29, respectively.

For the pair of tapes at 45°, only one of them was torn by 8 mm in the direction of loading. For the pair of tapes at −45°, no tapes were torn. For the pair of tapes at ±45° a 2 mm of tear was observed on only one of the tapes, in the direction of loading.

In comparison with the tapes applied 0°, the tape at 45° yields about 2.6 times more strength and 3 times more stiffness. The tape at −45° yields about 80% less strength and 50% less stiffness. Finally the tape at ±45° yields about 50% more strength and 25% more stiffness.

6.4 Sizing of Cut-outs in Sidewalls (Windows)

Only cut-outs for Z-folding were investigated in detail. A rectangular shape (with rounded corners) of width w_w and length L_w was assumed, see Figure 6.30.

The width of the cut-out, w_w, has to be such that the sidewall can be bent 180° along the

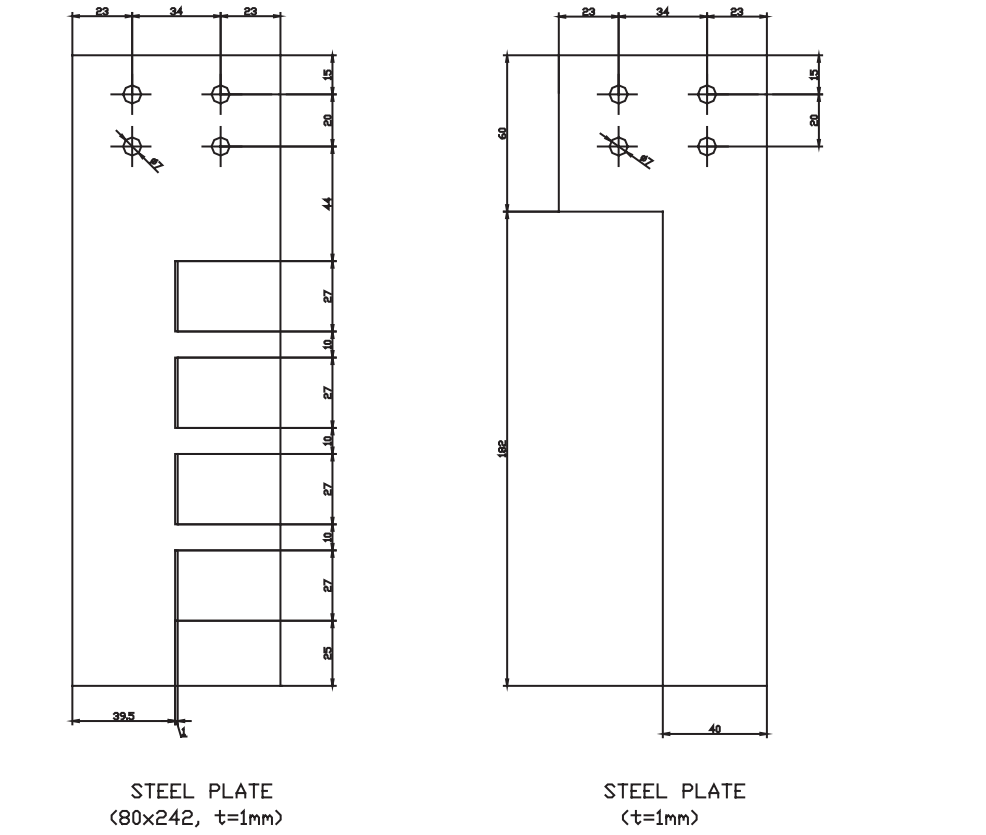

Figure 6.18: Shear testing of a T-joint.

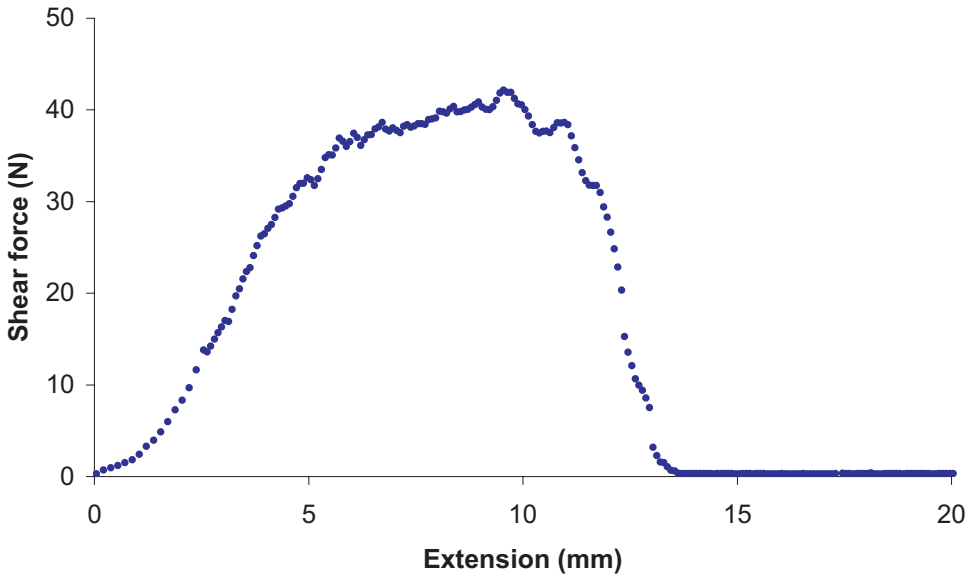

Figure 6.19: Shear test of T-joint with 50 mm × 25 mm single piece of tape at 0°, specimen 1.

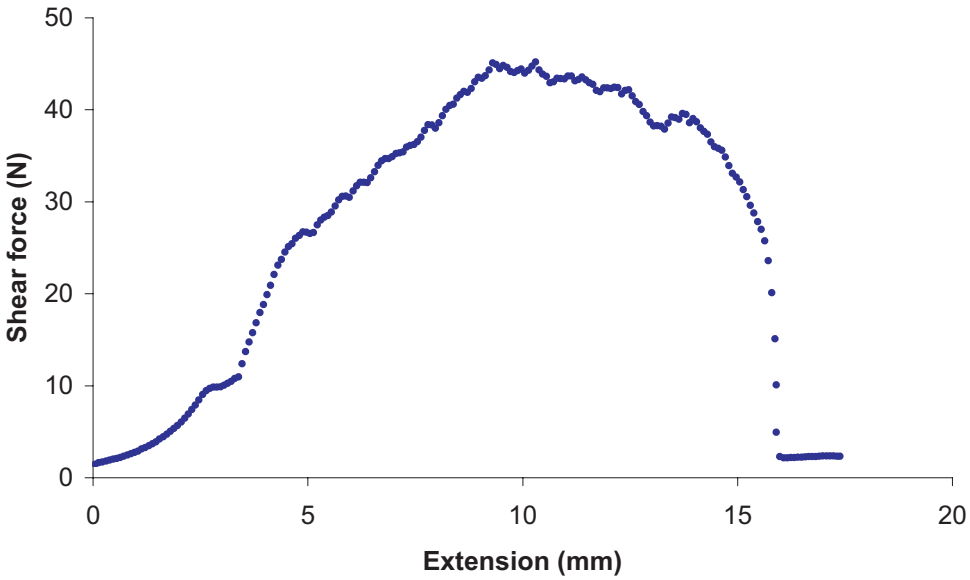

Figure 6.20: Shear test of T-joint with 50 mm × 25 mm single piece of tape at 0°, specimen 2.

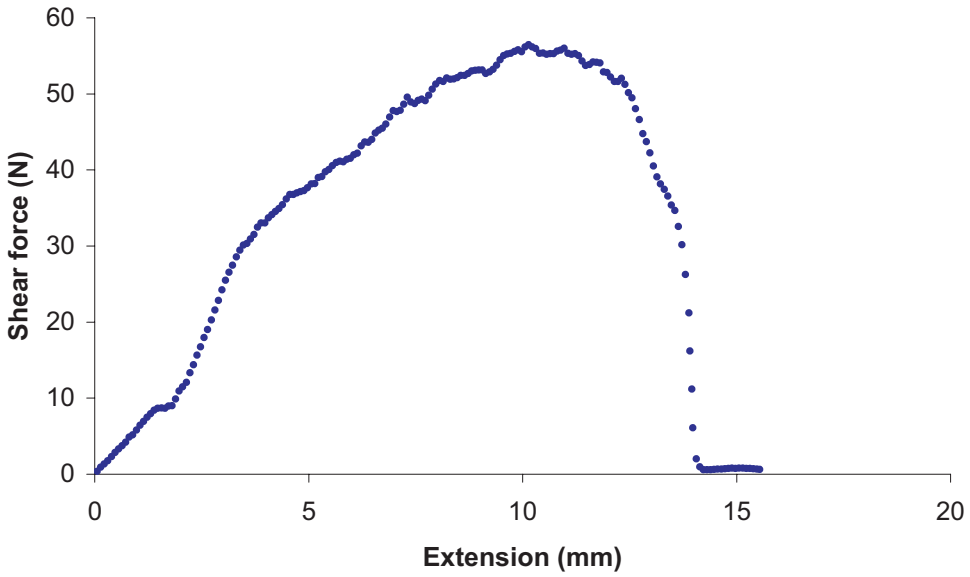

Figure 6.21: Shear test of T-joint with 60 mm × 25 mm single piece of tape at 0°.

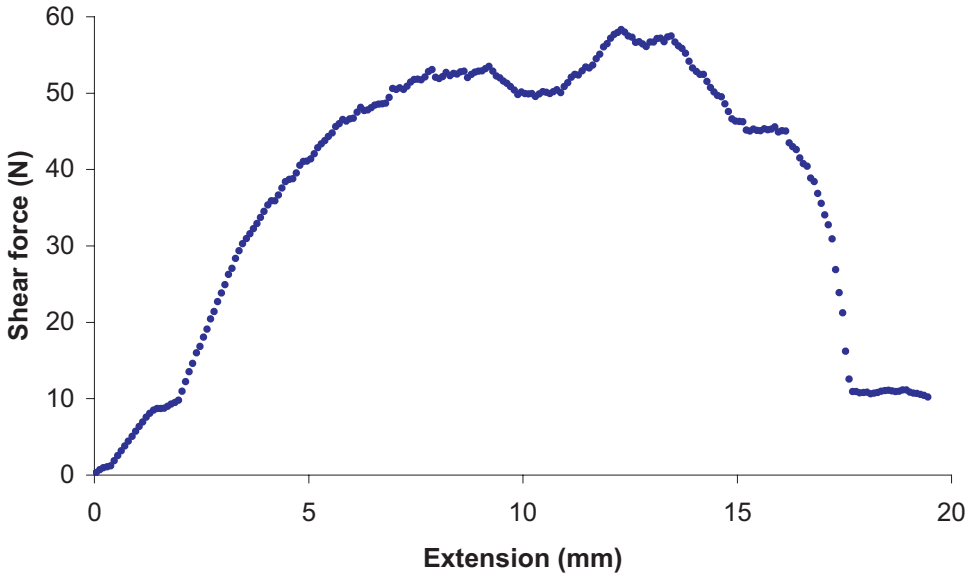

Figure 6.22: Shear test of T-joint with 70 mm × 25 mm single piece of tape at 0°, specimen 1.

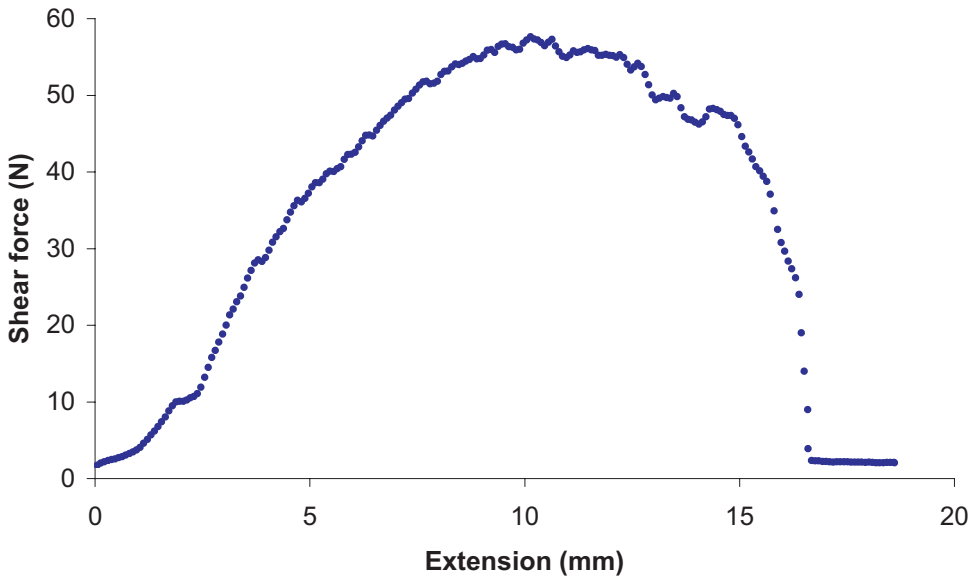

Figure 6.23: Shear test of T-joint with 70 mm × 25 mm single piece of tape at 0°, specimen 2.

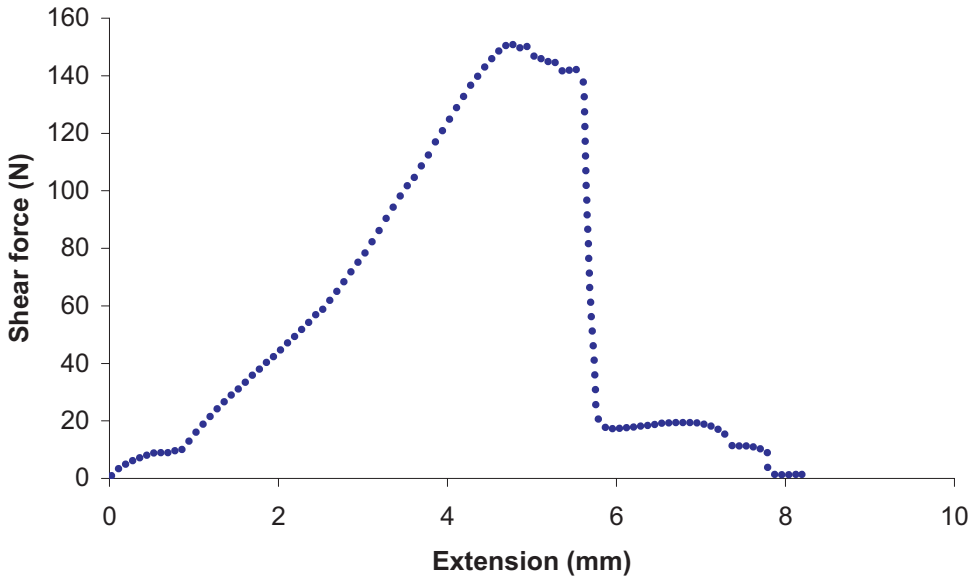

Figure 6.24: Shear test of T-joint with 75 mm × 17 mm single piece of tape at 45°.

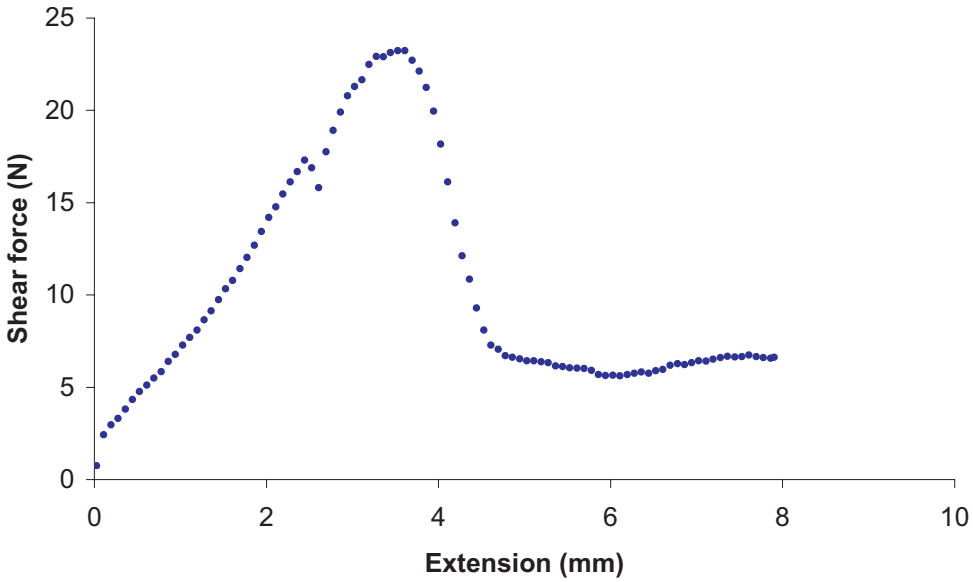

Figure 6.25: Shear test of T-joint with 75 mm × 17 mm single piece of tape at −45°.

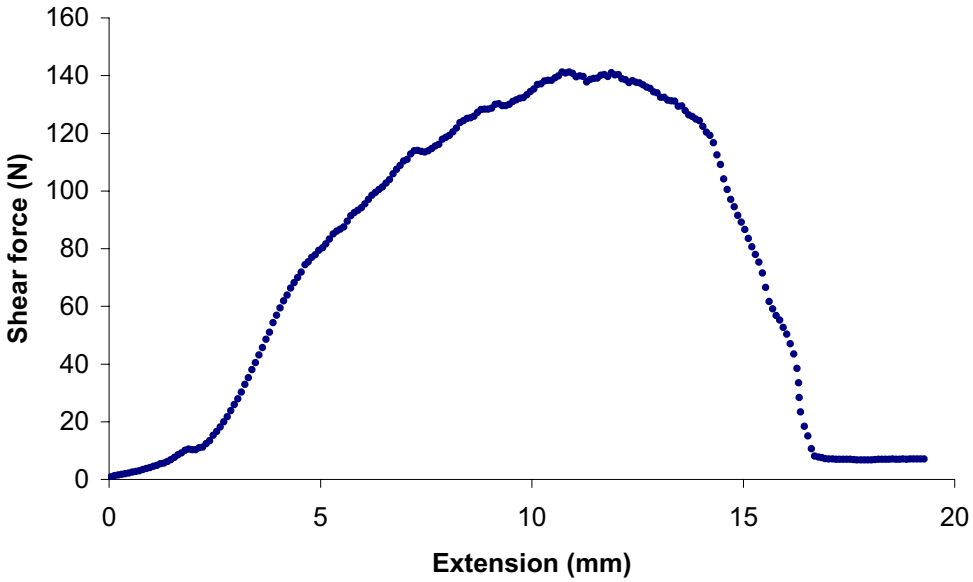

Figure 6.26: Shear test of T-joint with a pair of 60 mm × 25 mm pieces of tape at 0°.

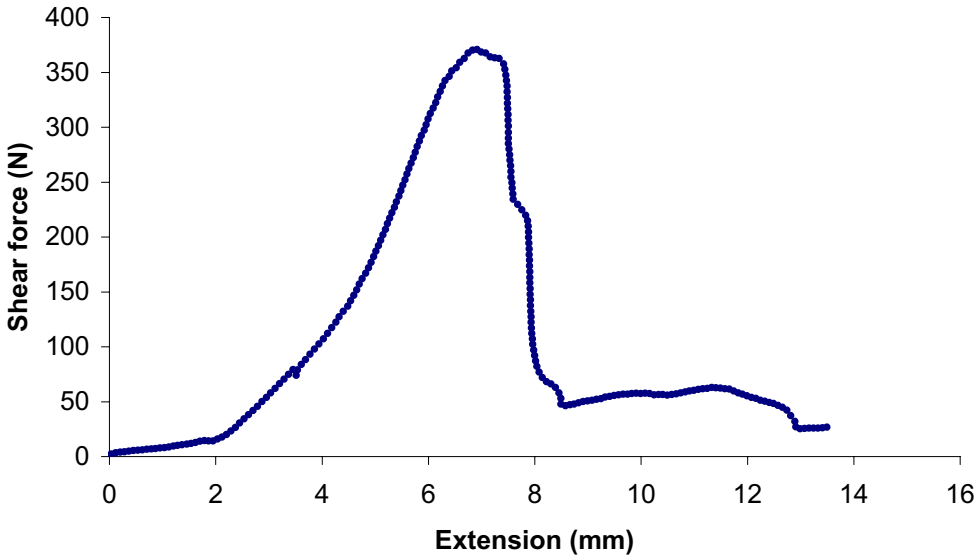

Figure 6.27: Shear test of T-joint with a pair of 88 mm × 17 mm pieces of tape at 45°.

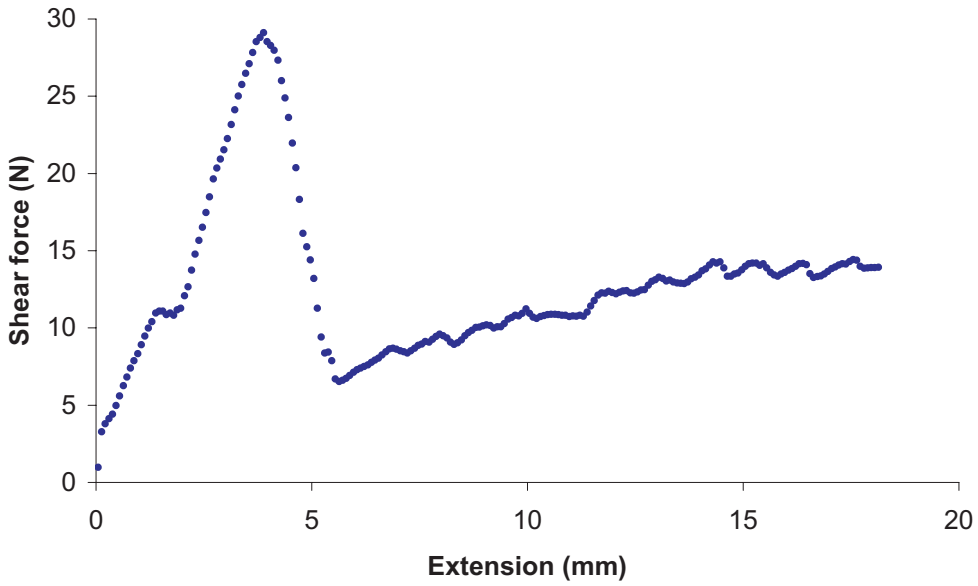

Figure 6.28: Shear test of T-joint with a pair of 88 mm × 17 mm pieces of tape at −45°.

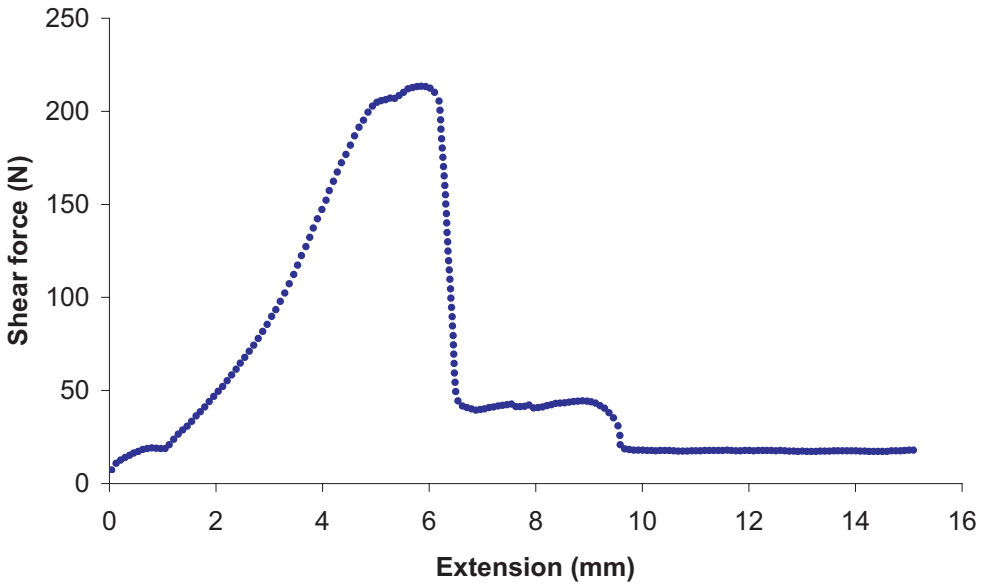

Figure 6.29: Shear test of T-joint with a pair of 88 mm × 17 mm pieces of tape at ±45°.

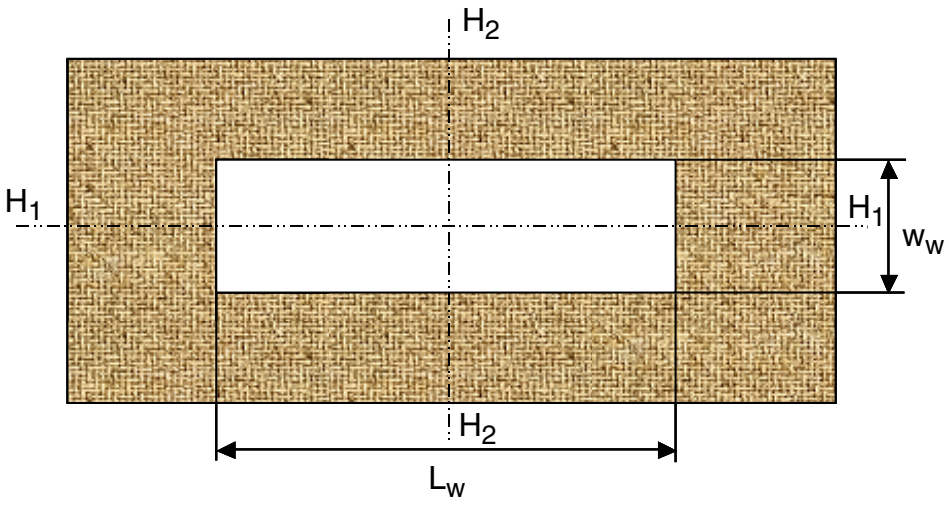

Figure 6.30: Schematic view of rectangular cut-out.

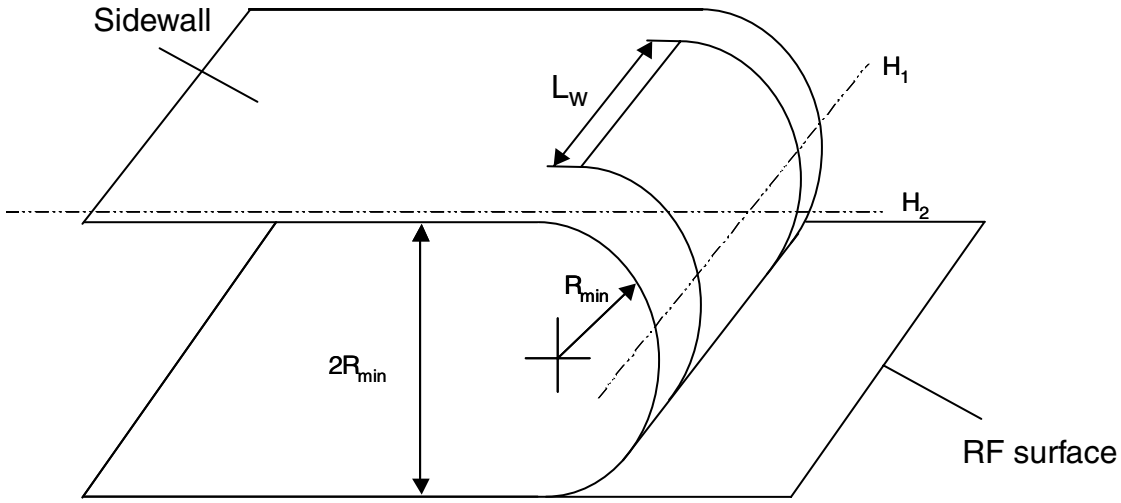

Figure 6.31: Thin plate bent 180° along hinge line H_1.

"hinge line" H_1H_1, as shown in Figure 6.31. Clearly

$$w_w \geq \pi R_{min} \tag{6.18}$$

to prevent material failure, where R_{min} is the minimum bend radius of the sidewalls.

The length of the cut-out, L_w, is needed to allow folding of the reflector structure along hinge line H_2H_2, and depends on the minimum radius of folding. Here it will be assumed that the sidewalls and the RF surface have the same thickness and material properties, and hence the same minimum radius of folding R_{min}. Note that when the thin plate shown in Figure 6.31 is bent about the "hinge line" H_2H_2, the outer part has a total thickness equal to twice the thickness of the sheet material (because the sidewall is already folded against the RF surface). However, it has already been shown in Section 6.1.3, see Table 6.4, that the minimum bend radius of two interconnected sheets on top of one another is approximately the same as that of a single sheet.

Consider Figure 6.32. The thicker surface, consisting of the RF surface plus the folded sidewall lies either on the outside or the inside of the fold. Note that the sheet on the inside of the fold needs to bend in one sense and then in the opposite sense; if the radius of curvature is assumed to be R_{min} everywhere, the inner surface would interfere with the outer one; however this can be eliminated by considering a fold with a non-uniform radius. From Figure 6.32, the length of the cut-out can be estimated to be

$$L_w \geq 2\pi R_{min} + \pi t \tag{6.19}$$

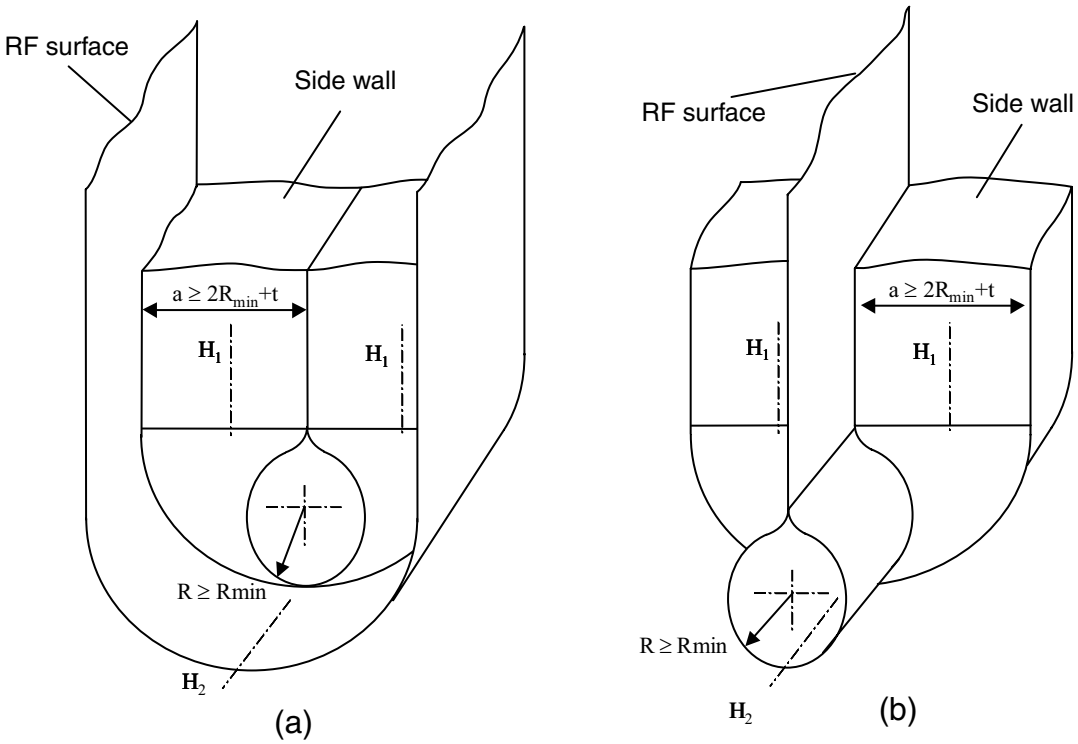

Figure 6.32: Folding of structure along hinge line H_2; (a) RF surface on the outside; (b) RF surface on the inside.

6.5 Volume of Packaged Envelope

The dimensions and volume of the packaged structure depend mainly on the minimum bend radius R_{min} of the material and the number of folds.

It will be assumed that first the sidewalls are bent 180°, thus making the whole structure substantially flat; then the flattened structure is Z-folded longitudinally. Assuming that all sheets that make up the structure have the same R_{min}, the dimensions and volume of the packaged structure are as follows:

- Folded length = $\dfrac{\text{Arc-length of parabola } (L)}{\text{1+number of folds}}$
- Packaged width = width of reflector (w)
- Packaged depth = $2R_{min}\times$ (1+number of folds)
- Packaged volume = depth × length × width = $2R_{min} \times L \times w$ =constant

Action	Required volume
	Depth×Length×Width (m^3)
Flat position (needs 180° bending of side surfaces)	$(2R_{min})\times L\times w=0.048\times 7.888\times 3.2=1.212$
One longitudinal folding	$(2R_{min}+2R_{min})\times (L/2)\times w=0.096\times 3.944\times 3.2=1.212$
Two longitudinal foldings	$(2R_{min}+4R_{min})\times (L/3)\times w=0.144\times 2.629\times 3.2=1.212$
Three longitudinal foldings	$(2R_{min}+6R_{min})\times (L/4)\times w=0.192\times 1.972\times 3.2=1.212$
Four longitudinal foldings	$(2R_{min}+8R_{min})\times (L/5)\times w=0.240\times 1.5776\times 3.2=1.212$

Table 6.6: Estimated packaged volume of full-scale reflector.

Action	Required volume
	Depth×Length×Width (m^3)
Flat position (needs 180° bending of side surfaces)	$(2R_{min})\times L\times w=0.048\times 3.944\times 1.6=0.303$
One longitudinal fold	$(2R_{min}+2R_{min})\times (L/2)\times w=0.096\times 1.972\times 1.6=0.303$
Two longitudinal folds	$(2R_{min}+4R_{min})\times (L/3)\times w=0.144\times 1.315\times 1.6=0.303$
Three longitudinal folds	$(2R_{min}+6R_{min})\times (L/4)\times w=0.192\times 0.986\times 1.6=0.303$
Four longitudinal folds	$(2R_{min}+8R_{min})\times (L/5)\times w=0.240\times 0.789\times 1.6=0.303$

Table 6.7: Estimated packaged volume of half-scale demonstrator.

Estimates of the dimensions and volume of the packaged structure are given in Table 6.6 for a full-scale reflector and Table 6.7 for the half-scale demonstrator, respectively. Both full-scale and half-scale structures are assumed to be made of 0.3 mm thick CFRP with $R_{min} = 24$ mm (including a factor of safety of 2.3). Views of the packaged half-scale structure are shown in Figure 6.33.

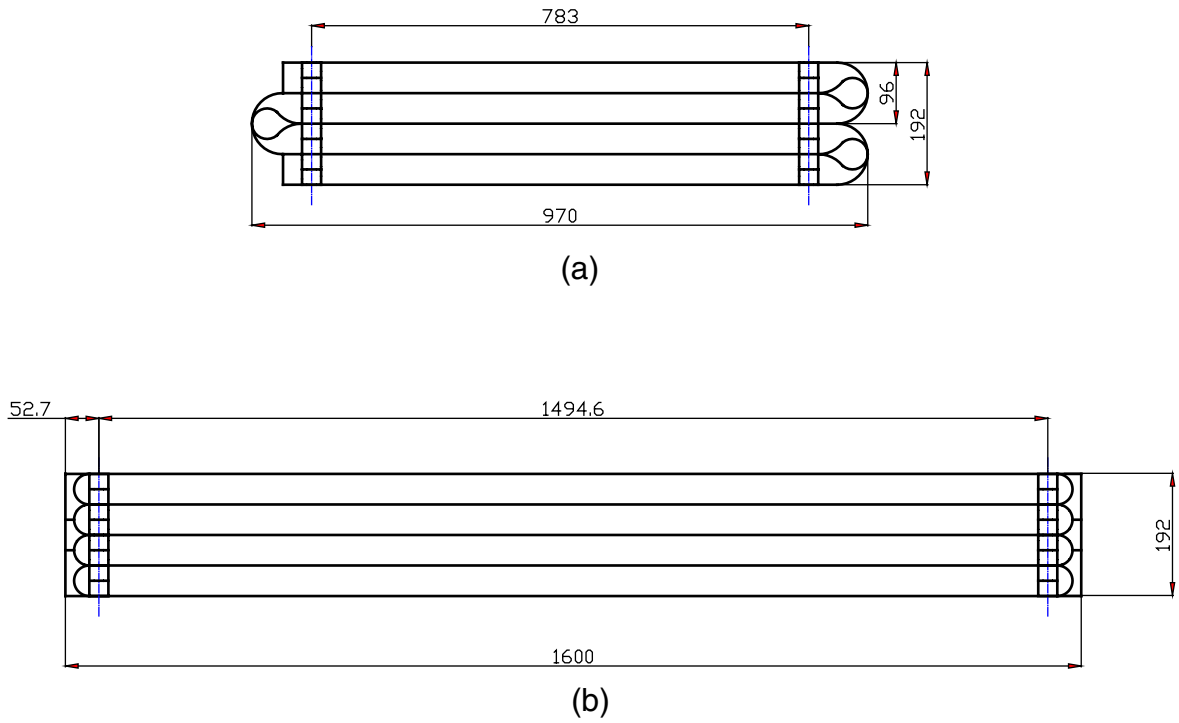

Figure 6.33: Side view and end view of half-scale reflector in packaged configuration (dimensions in mm).

Chapter 7

Manufacture and Assembly of Half-Scale Demonstrator

The half-scale demonstrator was based on the parameters selected in Section 4.2, $t_1 = t_2 = 0.3$ mm, $b_0 = b_1 = 1$ m. This chapter gives details on the individual parts of the demonstrator and the assembly process.

7.1 Parts of Demonstrator

A detailed part list for the demonstrator is given in Table 7.1 and details on each part are given in the following subsections.

Item	Material	Number of Parts	Details
Part 1	CFRP	1	RF surface
Part 2	CFRP	1	Bottom surface
Part 3	CFRP	2	Side surfaces
End beams	CFRP	3	L-type, 15 by 15, 0.83 mm thick, 1 off L=1600, 2 off L=600mm
Tape springs	Steel	18	4 off L=979, 2 off L=773, 2 off L=573, 2 off L=450, 8 off L=140
Washers	Aluminium	288	56 off type A (two holes), 40 off type B (one hole)
Bolts and nuts	Steel	304	M4x10 caphead bolts, M4 nuts
Spacers	Modelling board	32	16 pairs with 48 mm high
Disks	CFRP	32	Od=30mm, id=8mm
3M 79 Woven tape	Glass	-	12.9 m for T connection, 21.8m for L connection, 25mm wide
3M Double sided tape	Acrylic	-	10.9m for L connection 25 mm wide
Stiffeners	CFRP	6	L-type, 15 by 15, 0.41 mm thick, L=1318, 1238, 972, 1254, 1278, 964
Interface frame			
longitudinal	CFRP	2	2 off circular, od=24mm, 1.4 thick, L=750
transverse	CFRP	2	2 off L-type, L=1700;15 by 15, 0.83 mm thick
corner	Aluminium	4	4 off corner T-joint
	Total	695	

Table 7.1: Part list of demonstrator.

7.1.1 Composite Sheets

The composite material used was woven T300 carbon fibre in LTM45 epoxy resin, which is available as 94 gsm plain weave, 0.11 mm thick prepregs. According to the supplier, plain weave T300/LTM45 94 gsm has the following material properties: $E_1 = E_2$=56 GPa, G_{12}=5 GPa, ν_{12}=0.05, V_f=0.48, $\epsilon_L^{(+)} = 1\%$, $\epsilon_L^{(-)} = 1.3\%$, $S_L^{(+)}$=570 MPa, $S_L^{(-)}$=670 MPa.

To obtain sheets with an approximate thickness of 0.3 mm and high bending stiffness, a three layered 0/45/0 lay-up was selected, with an expected thickness of 0.33 mm.

Manufacturing and precision cutting of the sheets with a water-jet machine were carried out by Brookhouse Paxford Ltd, in Huntingdon. The sheets for the RF surface, the back surface (i.e. opposite to the RF surface) and the sidewalls will be called Part 1, Part 2, and Part 3 respectively, in this chapter. Drawings for each part are shown in Figures 7.1 to 7.3.

Slots for the T-connections were made in Part 1, a detail is shown in Figure 7.4. It was decided that the connecting tapes would be arranged at 0°, thus providing a shear-compliant connection, near the fold regions, and at 45°, thus providing a shear-stiff connection, away from the fold region. In order to use tape of a fixed width, the length of the slots was varied accordingly. Cut-outs in Part 3 were sized based on the minimum bend radius of the sheets, as explained in Section 6.4.

From the test results in Table 6.3, the value of the minimum bend radius is $R_{min} = 10.4$ mm. Using a **factor of safety of 2.3**, R_{min}=24 mm was adopted. Hence, from Equation 6.18

$$w_w = \pi R_{min} = 75.4 \approx 75 \text{ mm} \tag{7.1}$$

From Equation 6.19 the length of the cut-outs was calculated from

$$L_w \geq 2\pi R_{min} + \pi t = 151.8 \approx 152 \text{ mm} \tag{7.2}$$

In fact, a value of 210 mm was adopted, to include a 58 mm allowance for the width of the tape springs.

The corners of the cut-outs were rounded with a radius of 10 mm.

7.1.2 Stiffeners

15 mm by 15 mm angle-section stiffeners, made of LTM45/CFO300 woven composite 200 gsm 2 × 2 twill, were supplied by Brookhouse Paxford Ltd. These elements came in two different thicknesses. A 0.83 mm thick 4-ply layup (0/45/45/0) for the 1200 mm long stiffener connected to the tip end of the RF surface, and the 600 mm long stiffener connected to both ends of the

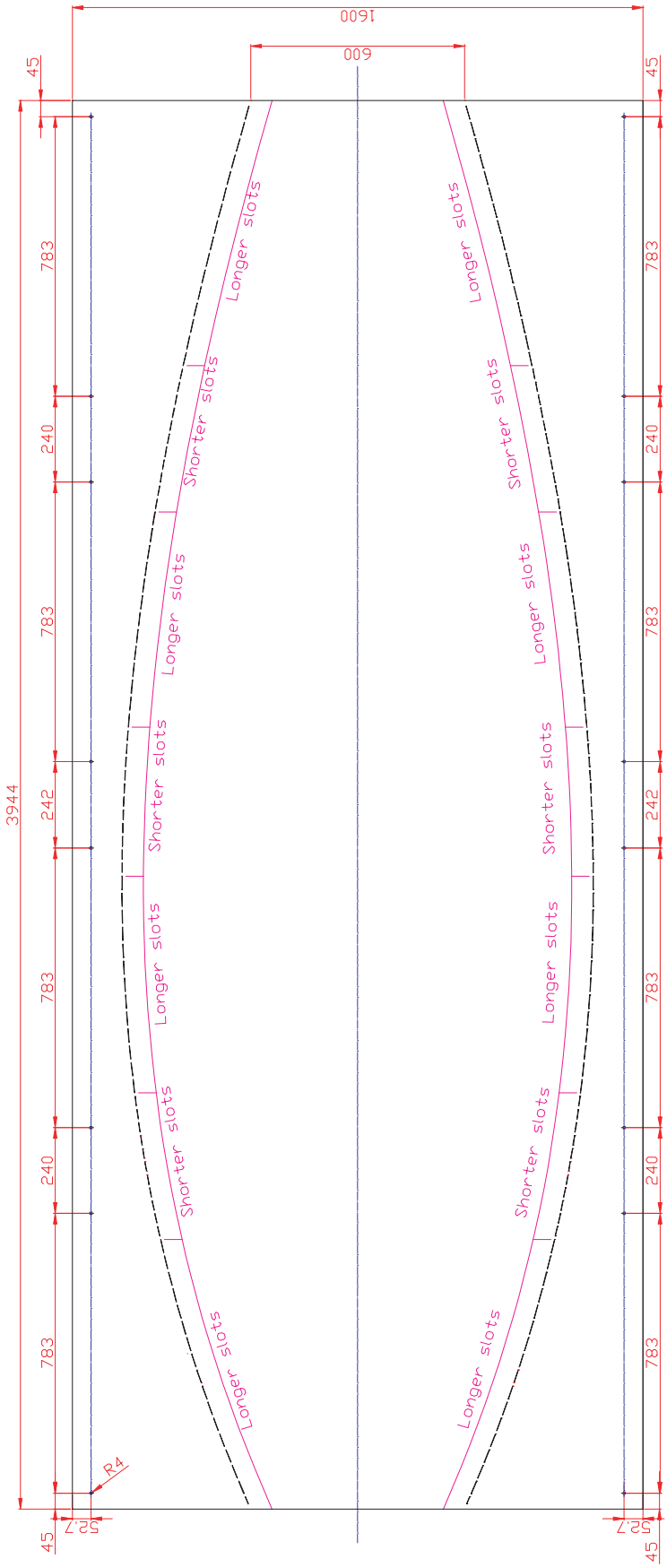

Figure 7.1: Drawing of Part 1.

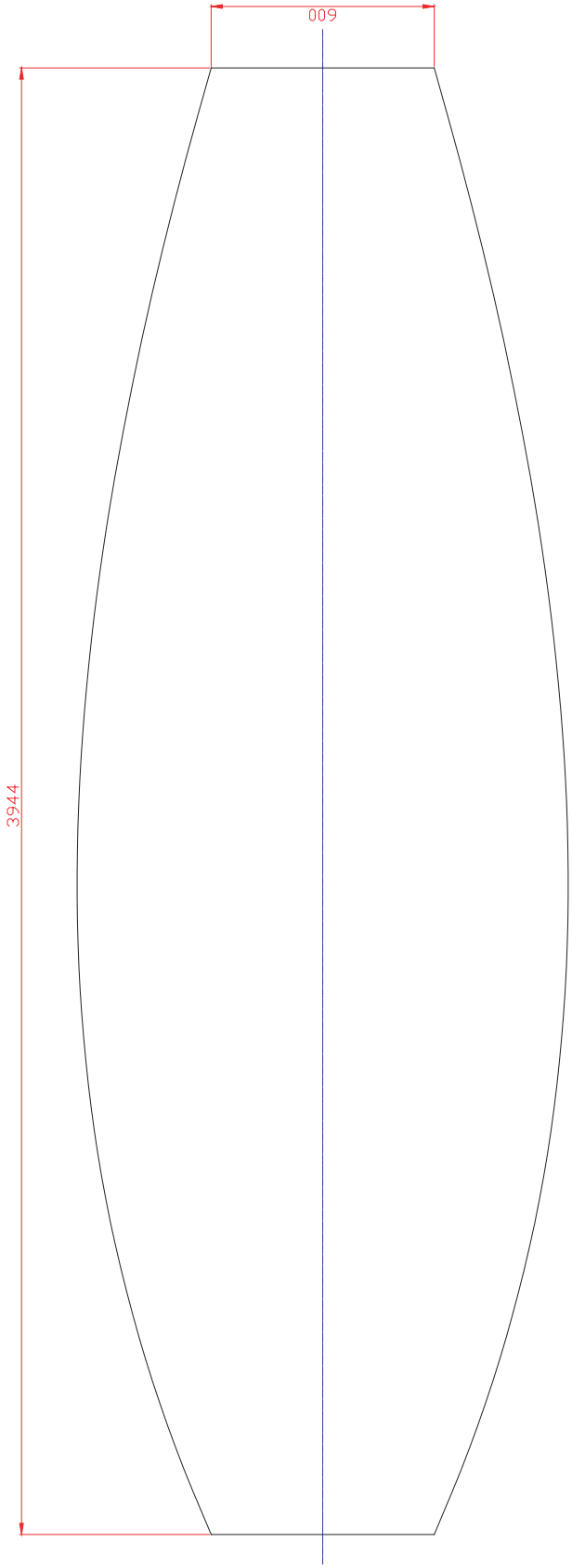

Figure 7.2: Drawing of Part 2.

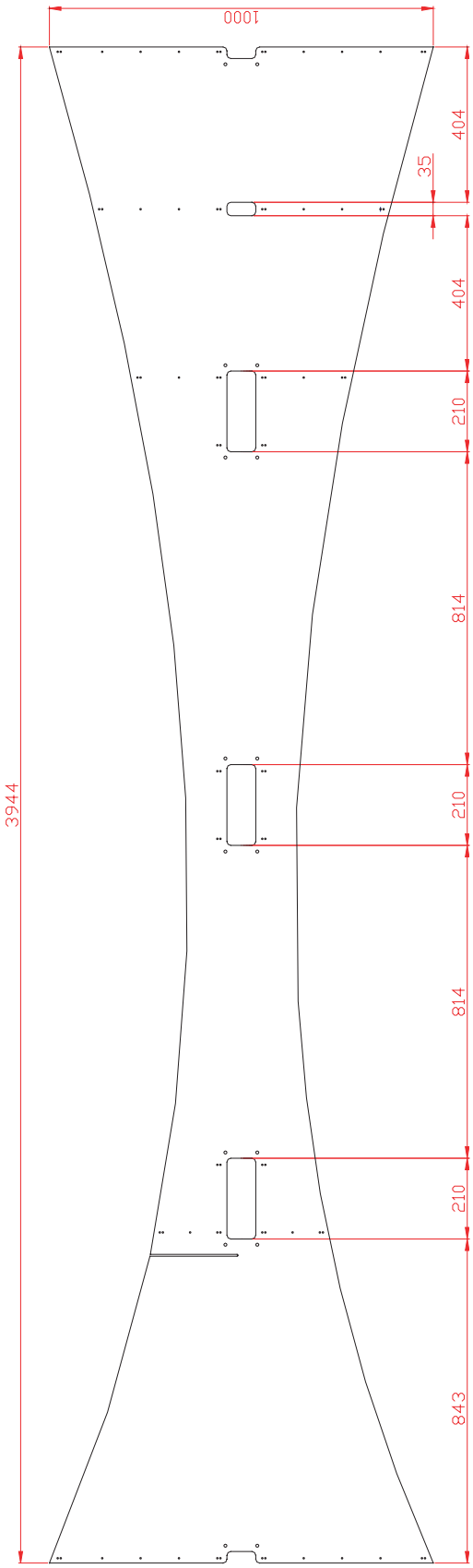

Figure 7.3: Drawing of Part 3.

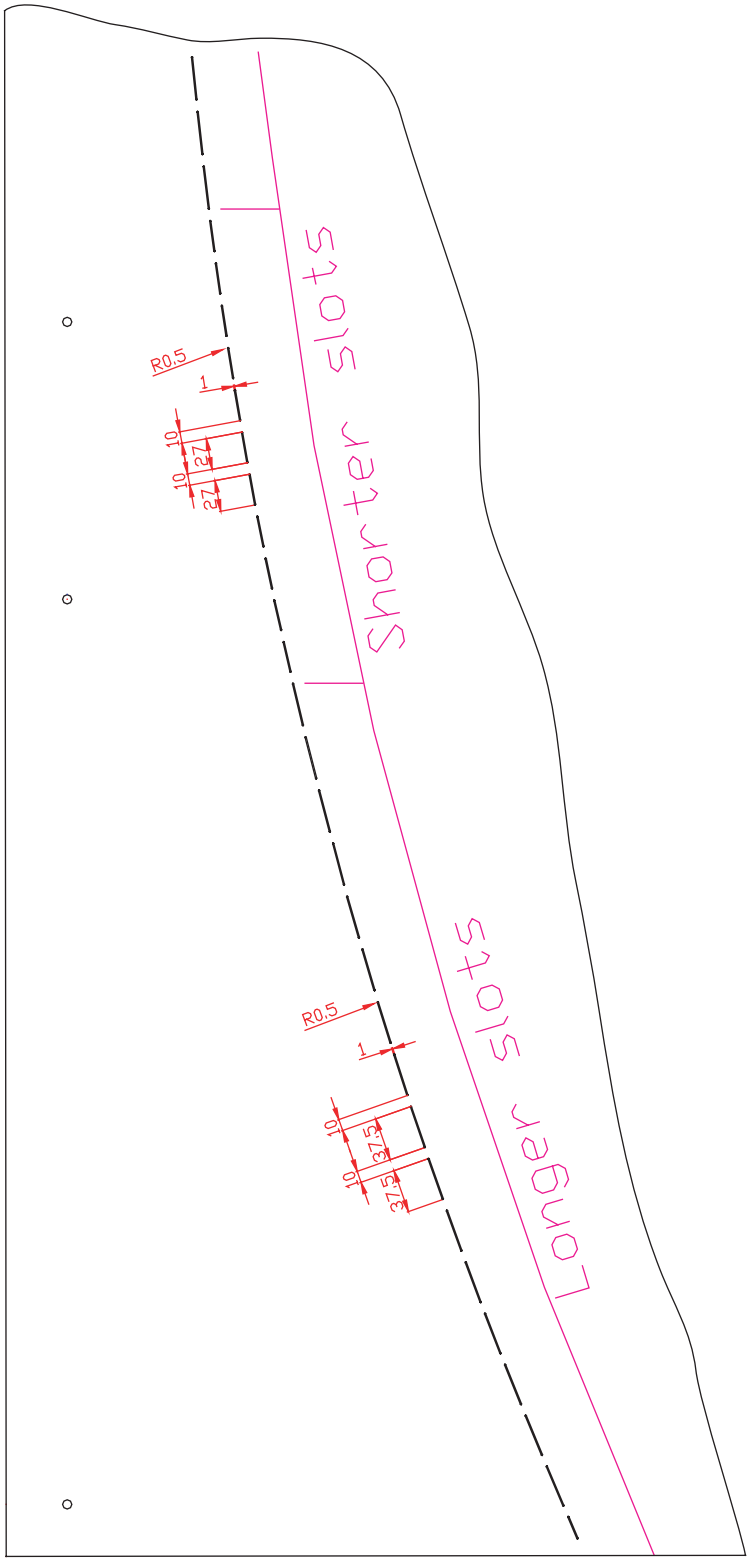

Figure 7.4: Details of slots in Part 1.

back surface. A 0.41 mm thick 2-ply layup (0/0) for the 1318 mm, 1238 mm, and 972 mm long stiffeners attached to the inside of the RF surface, respectively at a distance of 1624 mm, 2434 mm, and 3214 mm from the root end. Stiffeners with the same cross-section were also attached to the inside of the back surface; they were 1254 mm, 1278 mm, and 964 mm long, and were placed at a distance of 1184 mm, 2234 mm, 3234 mm from the root end.

All connections were made with the structural adhesive 3M Scotch-Weld DP490.

7.1.3 Interface frame

The rectangular interface frame that, in the flight system, will connect the radar structure to the deployable frame that in turn is attached to the spacecraft, consisted of two longitudinal CFRP round rolled tubes and two transverse woven CFRP angle-section beams.

The tubes had a length of 750 mm, an outside diameter of 24 mm and an inside diameter of 22.6 mm; they were supplied by Carbon Technology Ltd, Cheshire, U.K. The angle-section beams were identical to the thicker stiffeners described in Section 7.1.2, and were 1700 mm long.

The corner joints were machined from Al-alloy, see Figure 7.5.

7.1.4 Tape Springs

Tape springs were cut from a steel tape measure of the type described in Section 4.2. The layout of the holes for their connections to the sidewalls is shown in Figure 7.6. Note that only the centre section of the longer tape springs is folded, the outer sections are used only to stiffen the sidewalls.

7.1.5 Attachment of Tape Springs

To attach the tape springs to the sidewalls, Al-alloy washers with one side flat and the other side curved were used. Details are shown in Figures 7.7 and 7.8. The tape springs were sandwiched between the curved sides of the washers, and cap-head M4 bolts and nuts were used to attach them.

7.1.6 Spacers

Pairs of cap and cone spacers, made of modelling board were used to prevent the sidewalls from becoming overstressed during folding. The total height of the spacers is equal to $2R_{min} = 48$ mm. A drawing is shown in Figure 7.9.

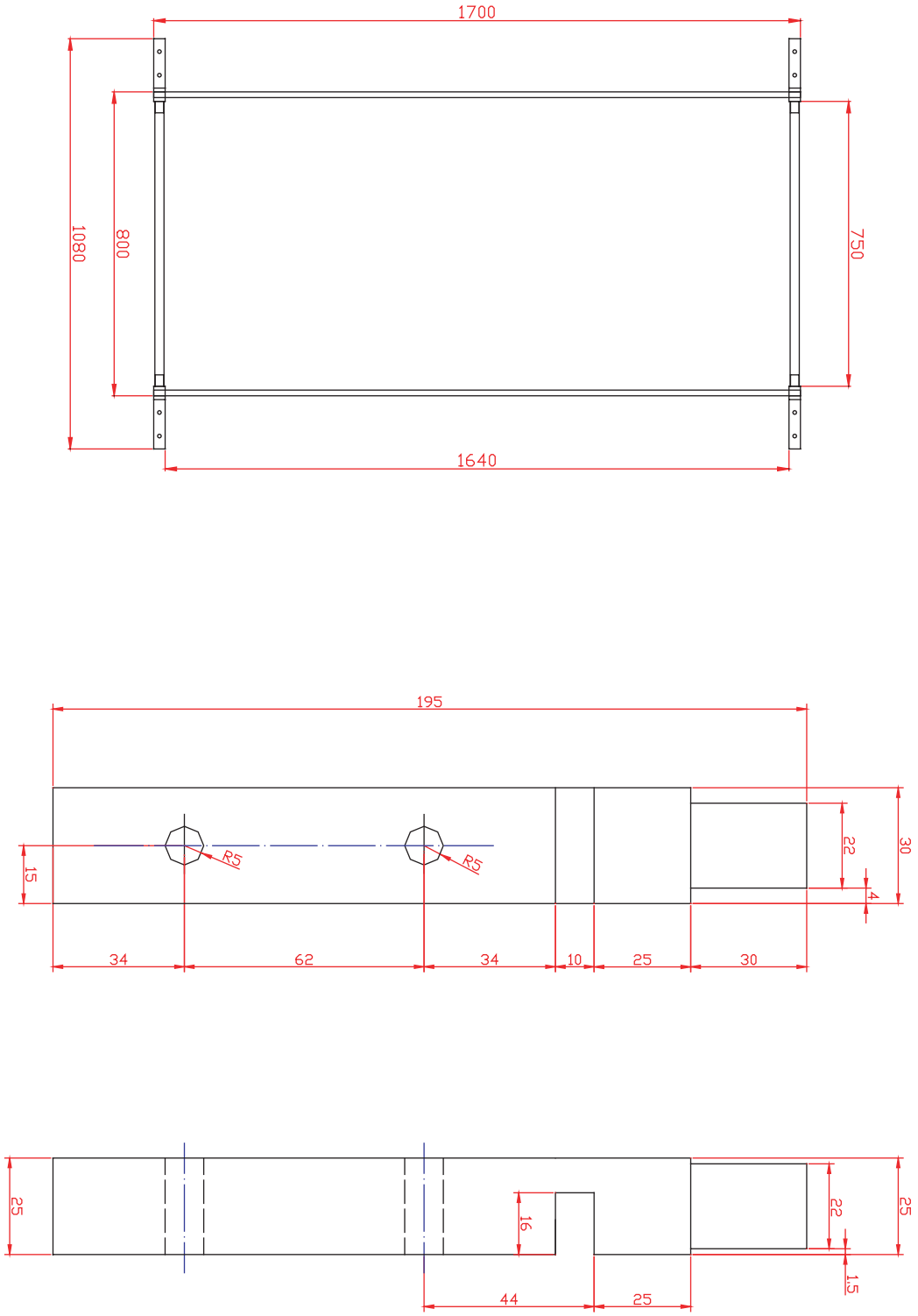

Figure 7.5: Interface frame and corner joint detail.

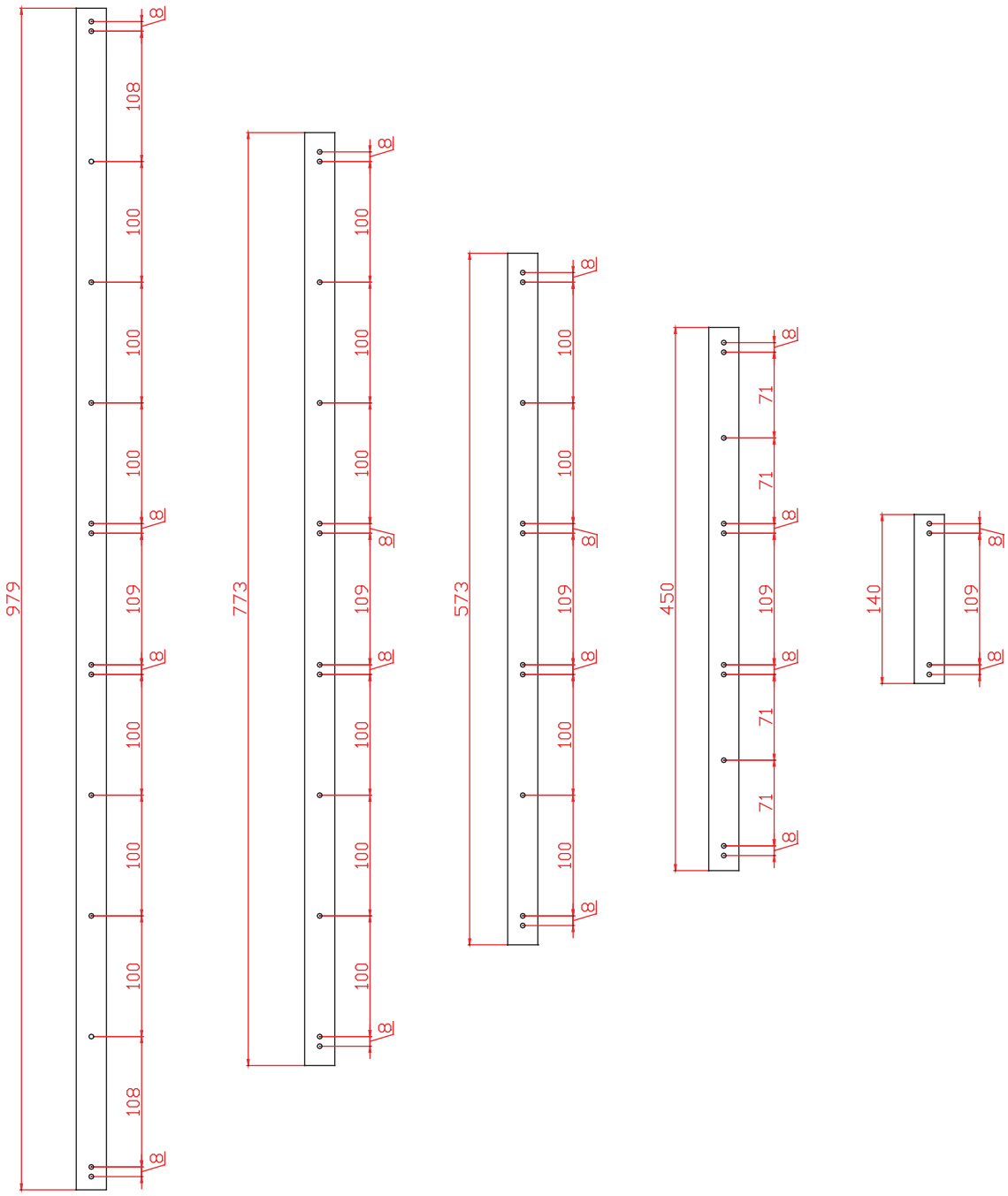

Figure 7.6: Steel tape springs.

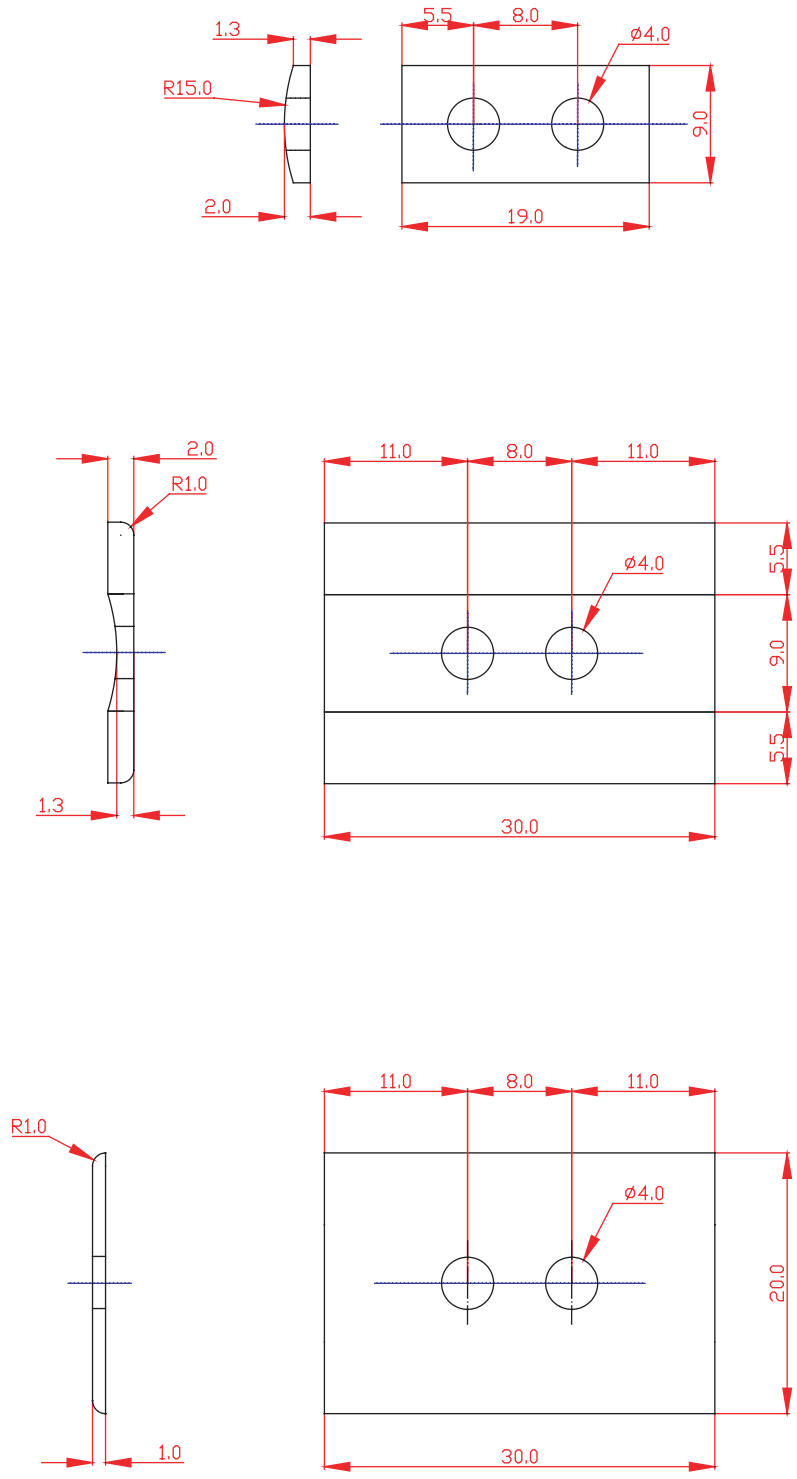

Figure 7.7: Type A washers.

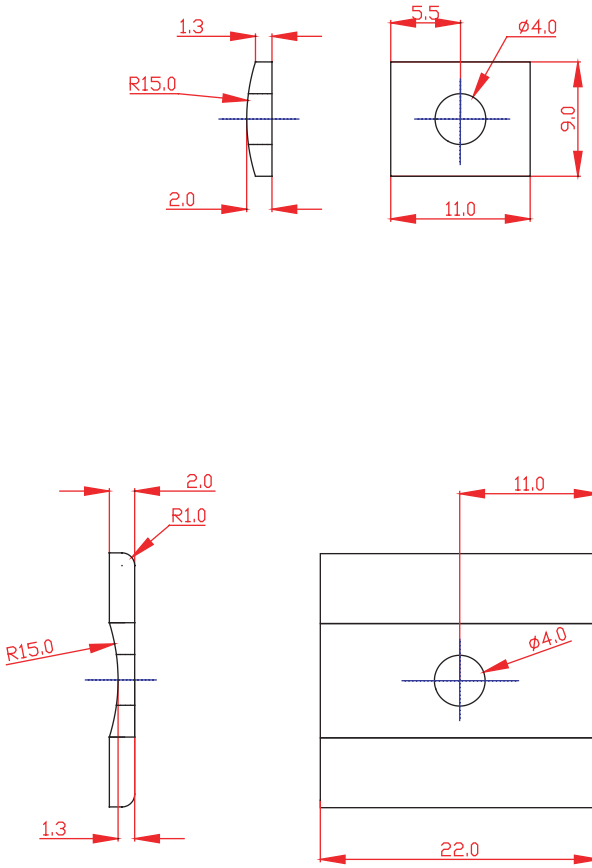

Figure 7.8: Type B washers.

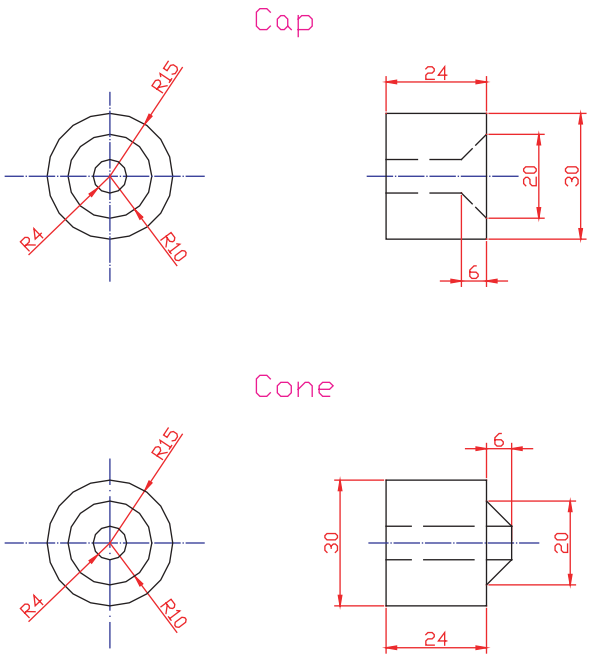

Figure 7.9: Cup and cone spacers.

The spacers were glued to the sidewalls with the structural adhesive 3M Scotch-Weld DP490.

7.1.7 Tapes and Adhesives

3M 79 woven glass tape was used for connecting the sheets. Details are given in Section 6.3.

A one-sided adhesive tape can be used to connect the sidewalls to the RF surface, but connecting the sidewalls to the back surface requires double-sided tape. Since 3M 79 tape is not available double-sided, double coated acrylic foam tape 3M VHB-4910 was used on the other side. This foam tape has a thickness of 1 mm, tensile strength (when bonded to aluminium) of 690 N/mm^2, shear strength of 7.8 N/10 mm (for a 25 mm wide strip, loaded for 10000 minutes), and 90° peel adhesion to steel of 2.6 N/10 mm.

All glued connections (end beams, stiffeners, spacers) were made with 3M Scotch-Weld DP490 structural adhesive. This adhesive has a shear strength (on etched aluminum) of 30.2 N/mm^2, a peel strength (floating roller peel) of 9.24 DaN/cm. It needs 4 to 6 hours to reach handling strength, and 7 days to reach full strength.

After fixing the tape springs to the sidewalls, the nuts were glued with “superglue”, i.e. a cyanoacrylate adhesive, supplied by Electrolube, U.K. to prevent the nuts from becoming loose.

7.2 Support Parts for Assembly

7.2.1 Mold

A curved mold made of plywood was prepared to provide the required profile for the RF surface during assembly. The mold consists of 3 pieces (root, middle and tip), and has the same parabolic shape of the RF surface, and its full length and width (3944 mm $\times$ 1600 mm). Details are shown in Figure 7.10 and an overall view can be seen in Figure 7.11.

7.2.2 Foam Plugs

Polystyrene foam plugs were made to support the back surface during the final stages of the assembly process. Each plug consists of two pieces (root and tip), see the drawings in Figure 7.12. A photo of the foam plugs on the mold is given in Figure 7.11.

After the structure had been fully assembled, the plugs were pulled out after collapsing the sidewalls by about 30° at the root and 35° at the tip, as shown in Figure 7.13. Although they were originally made just as a construction aid, the plugs were later found to be very useful to support the back surface during the early stages of folding.

7.3 Assembly of Demonstrator

The assembly of the reflector was started by sub-assembling the sheets. Next the sheets were connected to one another according to the sequence shown in Figure 7.14.

7.3.1 Subassembly of RF Surface, Back Surface and Sidewalls

Each one of these four components were sub-assembled in a flat position.

First, for precise alignment of the four sheets during the main assembly process, both faces of each sheet were marked with a fine permanent marker; transverse lines were drawn at 100 mm spacing at all locations where the connections were to be made.

Pairs of CFRP disks were glued to the inside face of Part 1, to reinforce the area around each hole. All stiffeners were glued to the inside face of Part 1. The interface frame was attached to the root end of the reflector surface (inside face).

Both root and tip end beams were glued to the outer face of Part 2, whereas all stiffeners were glued to the inner face of Part 2 as shown in Figure 7.15.

The two sidewalls, Part 3, were assembled as follows. First the spacers were glued to the inside face. Then, the full-length tape springs were bolted to the inside faces of the sidewalls

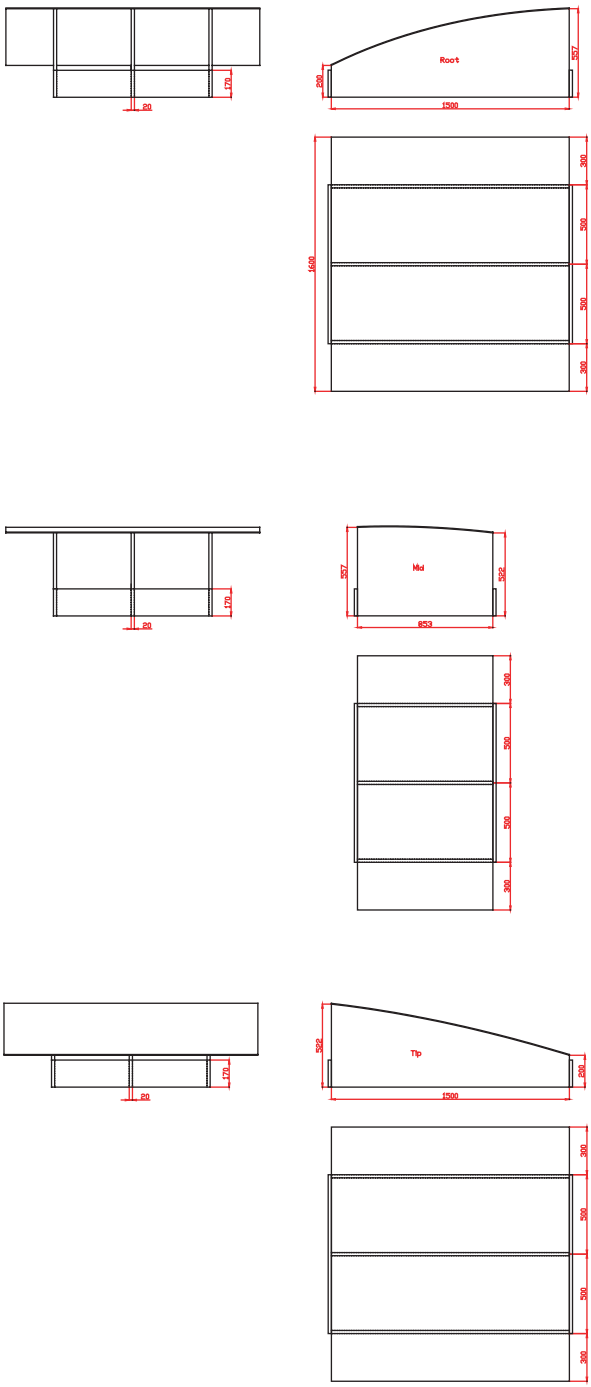

Figure 7.10: Parts of plywood mold.

Figure 7.11: View of mold and foam plugs.

(they cannot be attached to the outside face, as they could damage the RF surface when the structure is folded). The shortest tape springs were attached to the outside face of the sidewalls.

First, each tape spring was sandwiched between the curved washers, providing flat attachments for the bolts and composite sheet. Next, the tape springs were fixed with bolts and nuts. Finally, all of the nuts were locked tight with superglue.

7.3.2 Connection of Sheets

Having completed the subassembly of the sheets, first the RF surface was put on a flat assembly table, with the inside face up.

Next, one of the sidewalls was put on top of the RF surface, aligning the edge profile of the sidewall with the slots and alignment lines on the RF surface. Starting from one end, 70 mm long pieces of woven tape were applied at 45° through the longer slots, and at 0° through the shorter slots, by passing each tape through the slots, alternately from the inside and the outside faces of the RF surface.

Then the other sidewall was put on top of the RF surface. Again, starting from one end, 70 mm long pieces of woven tape were applied through the slots. A view of the sidewalls connected to the RF surface is shown in Figure 7.16.

Next, the back surface was put alongside one of the sidewalls, with all alignment lines

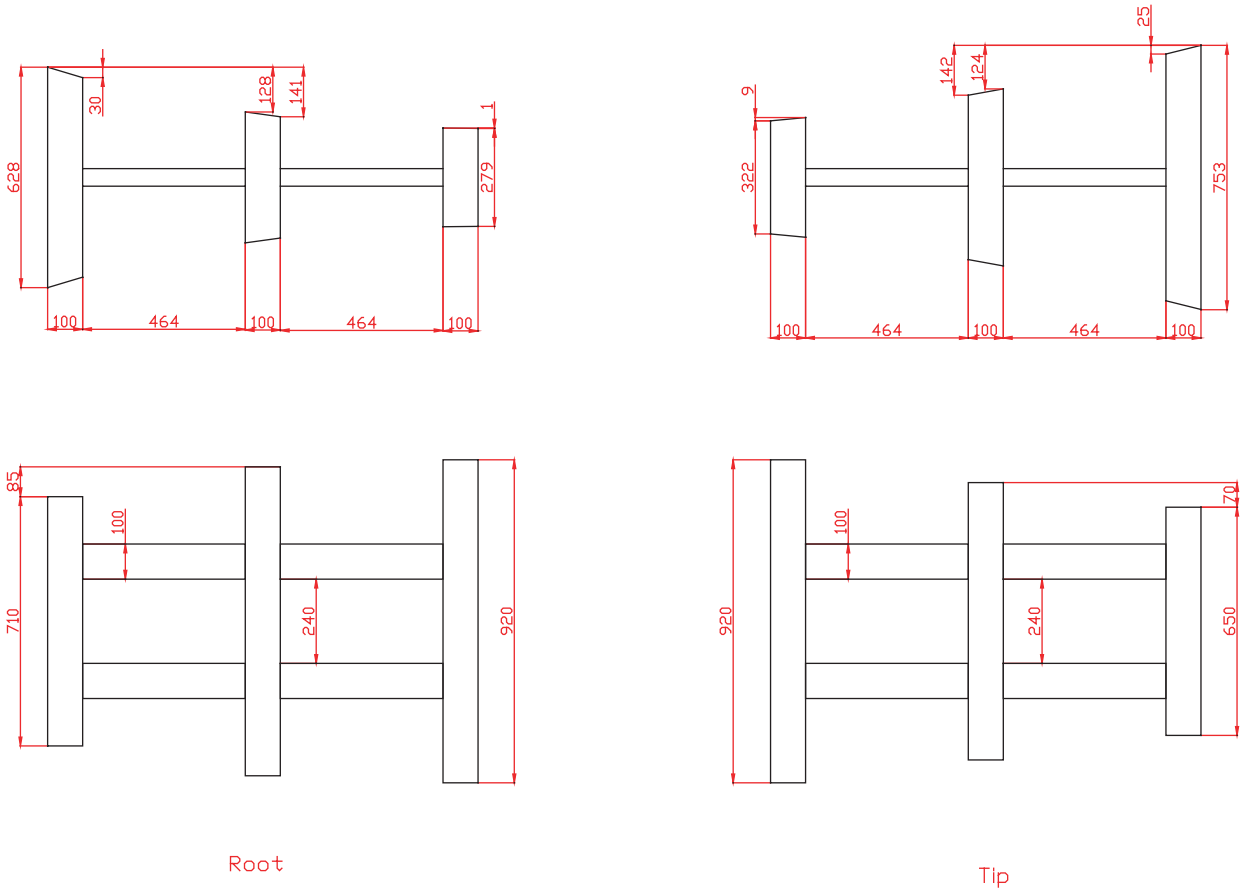

Figure 7.12: Details of foam plugs.

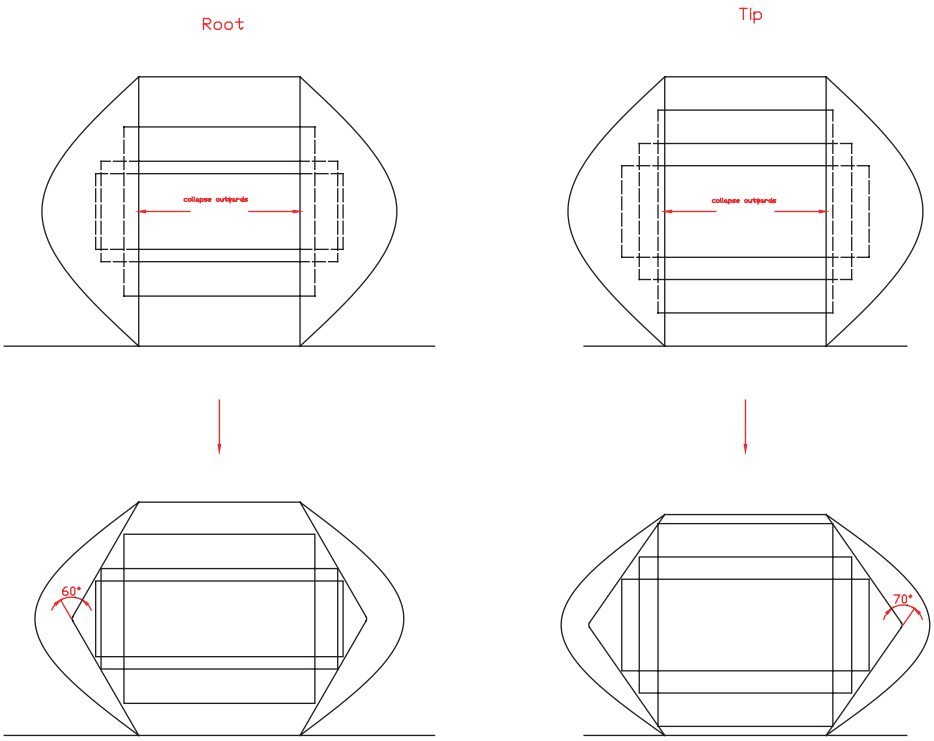

Figure 7.13: Removal of foam plugs.

matching. Again, starting from one end, the sidewall and the back surface were stitched together with woven tape and double-sided foam tape, connecting them alternately to the inside or the outside of the structure. 70 mm long pieces of tape were used to make these connections, and the acrylic foam tape was applied to the back of the woven tape, covering half of its length. The tapes were applied at 45° away from the bend regions and at 0° near the bend regions.

In order to make the final seam, the structure was moved onto the mold with all the sheets initially flat. The foam plugs were placed on top of the RF surface. Starting from the ends, the sidewalls and the back surface were rotated through 90° along the hinge line between the sidewalls and the RF surface. Then, the back surface was further rotated through 90° along the hinge line with the sidewall, to close the structure as shown in Figure 7.17.

The back surface and the sidewall were then stitched together, as explained above. Finally, the foam plugs were removed and cross-bracing wires were added at both ends. Figure 7.18 shows the fully assembled structure.

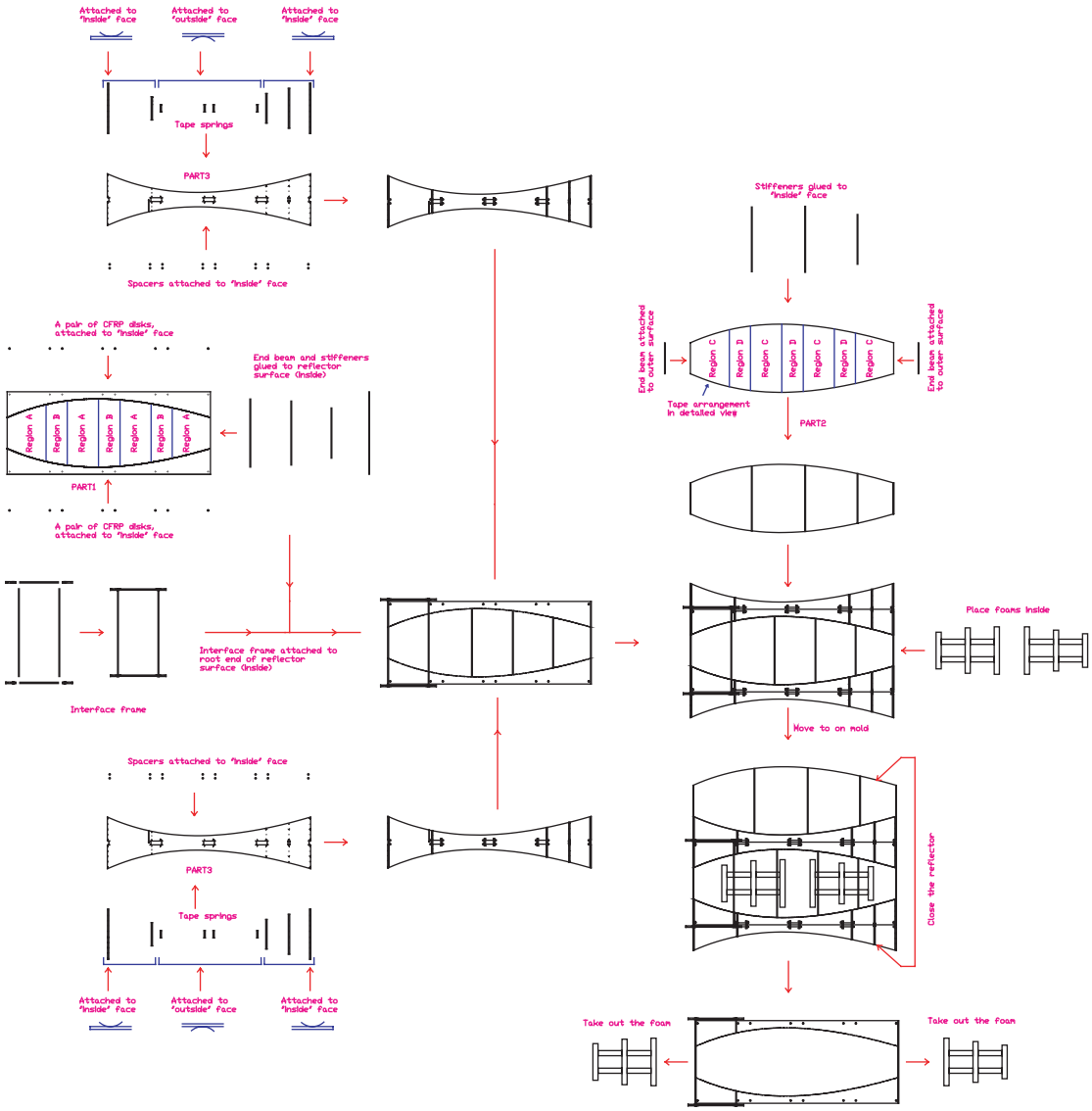

Figure 7.14: Assembly sequence.

Figure 7.15: Sub-assembly of Part 2.

Figure 7.16: Sidewalls connected to RF surface.

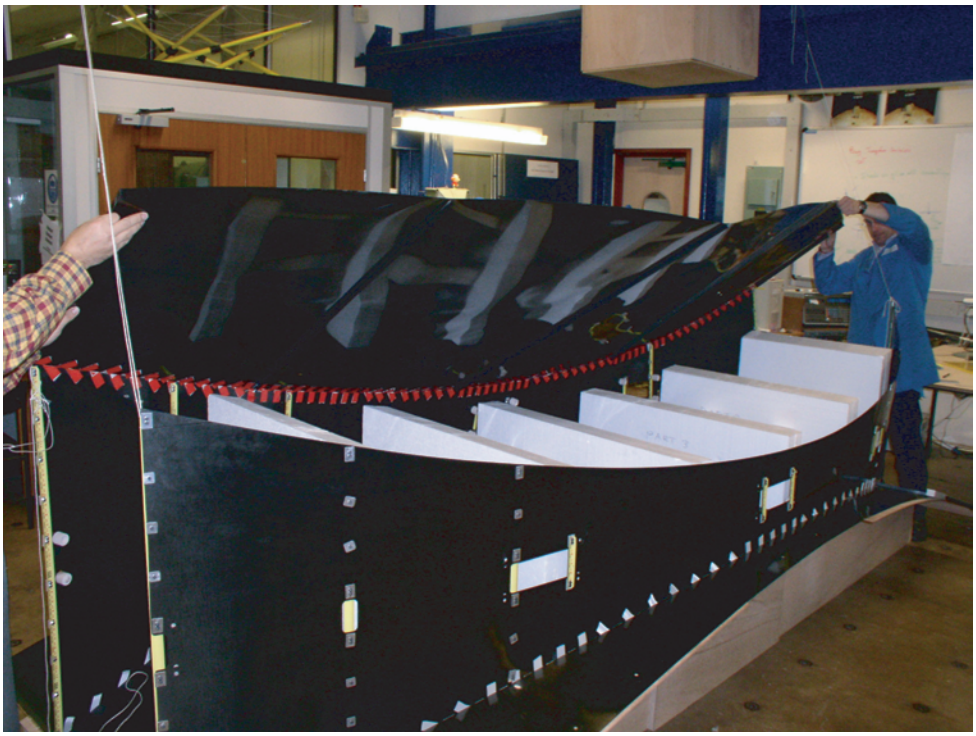

Figure 7.17: Closing the structure.

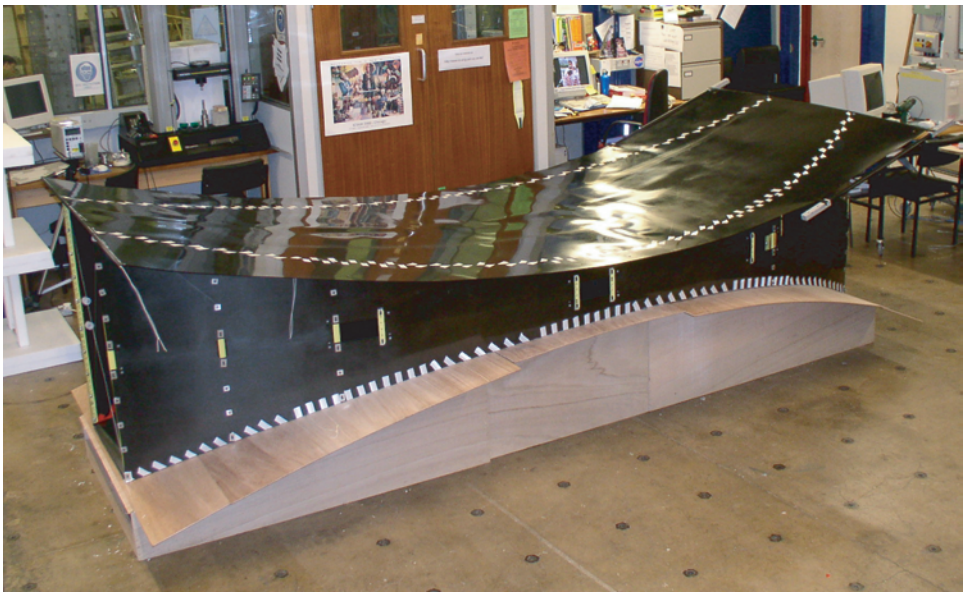

Figure 7.18: View of assembled demonstrator.

Chapter 8

Testing of Demonstrator

Measurements of mass, surface accuracy and stiffness of the demonstrator were taken in the laboratory, i.e. in a 1-g environment, in the deployed configuration. The stiffness of the demonstrator was measured before packaging. The surface accuracy was measured with a photogrammetry system both before packaging and after deployment.

8.1 Measurement of Mass

The total mass of the demonstrator was measured using a digital spring scale. The structure was suspended at both ends; one end was attached to a string which went over a pulley and then to a 5 kg counterweight; the other end was attached to the spring scale. A total mass of 11.05 kg was measured.

Mass measurements of individual parts were also taken, using offcuts and spare parts. The results are listed in Table 8.1.

8.2 Measurement of Stiffness

In the deployed configuration, displacement measurements of the tip of the structure were carried out. These measurements were taken with a LK081 (Keyence Co.) laser displacement sensor.

The structure was attached through the interface frame to a tubular steel support structure, with a 2.5 kg single-point gravity offload at the root of the back surface, and a 4 kg offload connected to the top edge of the RF and back surfaces, through a horizontal bar. The laser sensor was placed at a distance of 80 mm from the points to be measured. Static loads in out-of-plane, transverse, and longitudinal directions were applied to the tip of the reflector by means of a string and pulley system, as shown in Figures 8.1-8.3, by increasing the weight hanging from

Item	Material	Number of Parts	Unit Mass	Mass (kg)
Part 1	CFRP	1	1470 kg/m^3	3.058
Part 2	CFRP	1	1470 kg/m^3	2.060
Part 3	CFRP	2	1470 kg/m^3	1.949
End beams	CFRP	3	37.6 g/m	0.105
Tape springs	Steel	18	27.3 g/m	0.236
Washers	Aluminium	288	A:4.9 g/set, B:3.9 g/set	0.430
Bolts and nuts	Steel	304	2.35 g/pair	0.357
Spacers	Modelling board	32	633 kg/m^3	0.638
Disks	CFRP	32	0.3 g/each	0.010
3M 79 Woven tape	Glass	-	5.5 g/m	0.191
3M Double sided tape	Acrylic	-	25.0 g/m	0.273
Stiffeners	CFRP	6	20.4 g/m	0.143
Rest (glue, string, etc)				0.025
			Subtotal	9.475
Interface frame				
longitudinal	CFRP	2	83.4 g/m	0.125
transverse	CFRP	2	37.6 g/m	0.128
corner	Aluminium	4	2800 kg/m^3	1.322
			Total	11.050
		Demonstrator Mass Measured		11.050

Table 8.1: Mass of individual components.

the pulley, in 20 gram increments.

The displacement in the direction of the load was measured in each test, and in each case a linear best-fit relationship was obtained, in order to estimate the stiffness of the structure for the three load cases. Figures 8.4-8.6 compare the measured response to the results from an ABAQUS linear-elastic static analysis. The ABAQUS model is stiffer in all cases, by 15% in the out-of-plane direction, by 49% in the transverse direction, and by 232% in the longitudinal direction.

Obviously, some refinement of the model (e.g. by measuring the actual elastic properties of the composite sheets and by modelling the support conditions in more detail) would be desirable. However, note that the out-of-plane stiffness of the structure —which is the lowest stiffness— is in good agreement with the measurements.

The ABAQUS model predicts the first natural frequency of vibration of the structure at 1.5 Hz. Based on a comparison of the stiffness measurements with the ABAQUS results, its value is probably closer to 1.4 Hz, but was not measured directly.

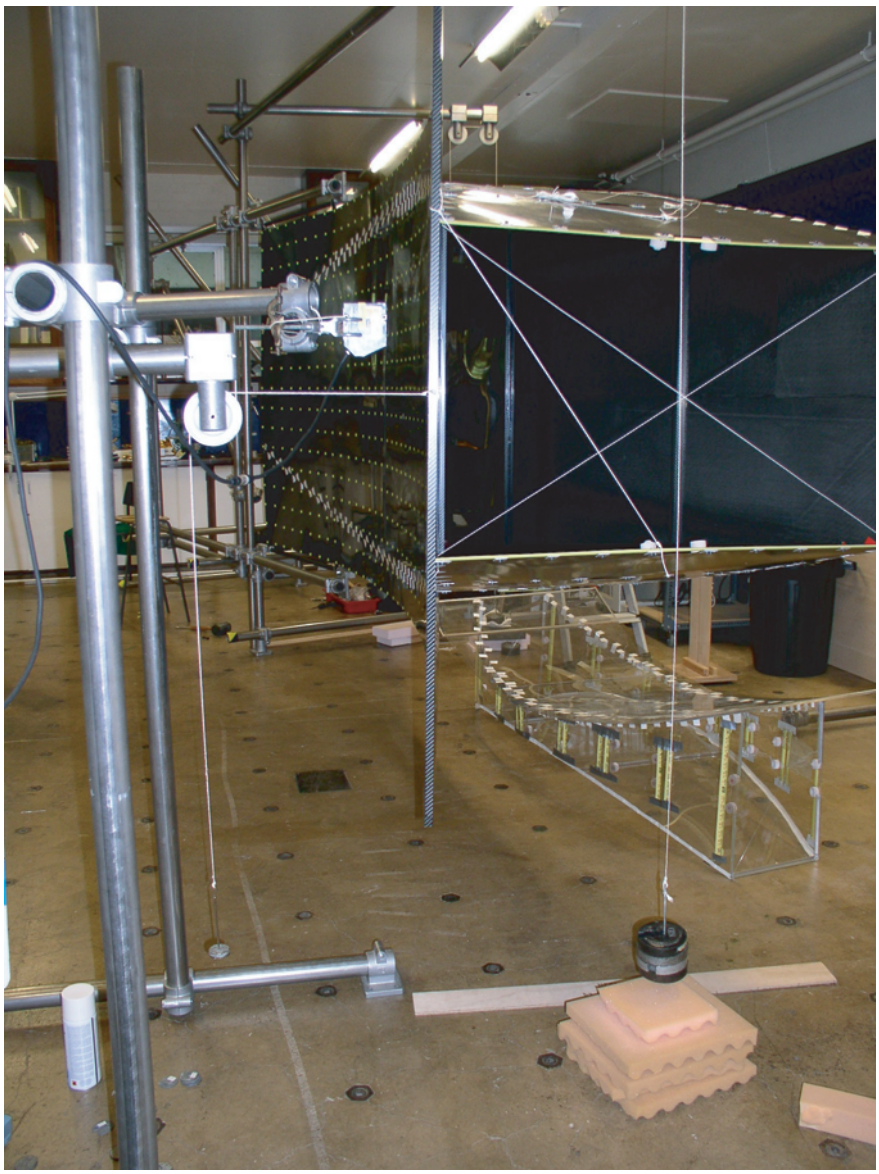

Figure 8.1: Measurement of out-of-plane displacements.

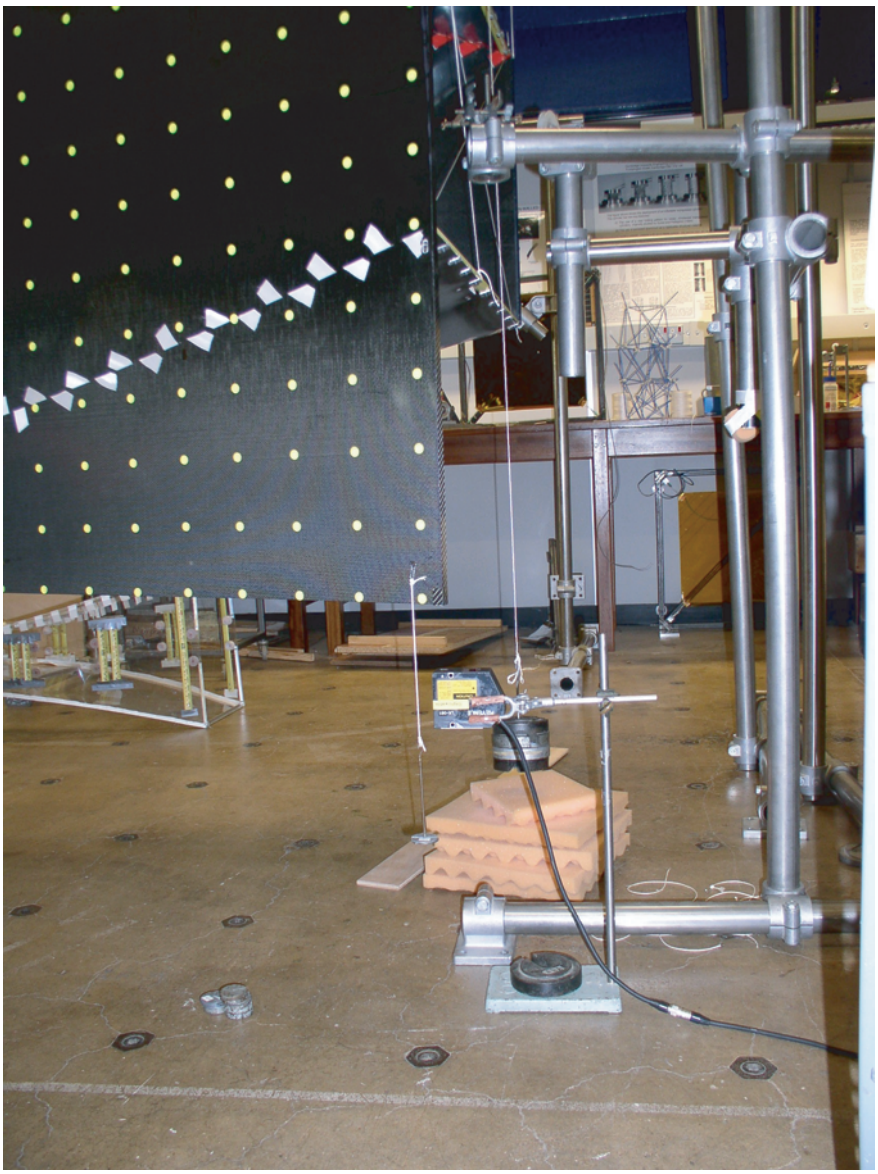

Figure 8.2: Measurement of transverse displacements.

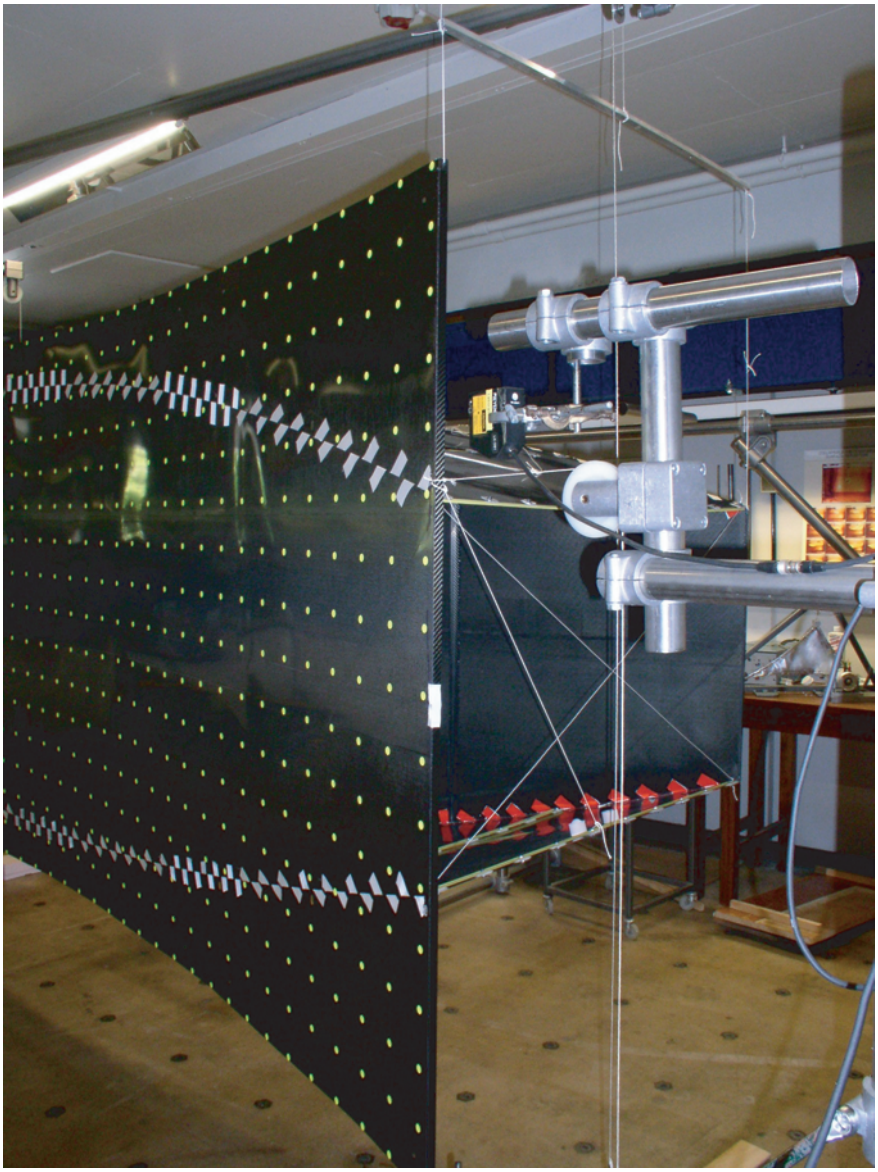

Figure 8.3: Measurement of longitudinal displacements.

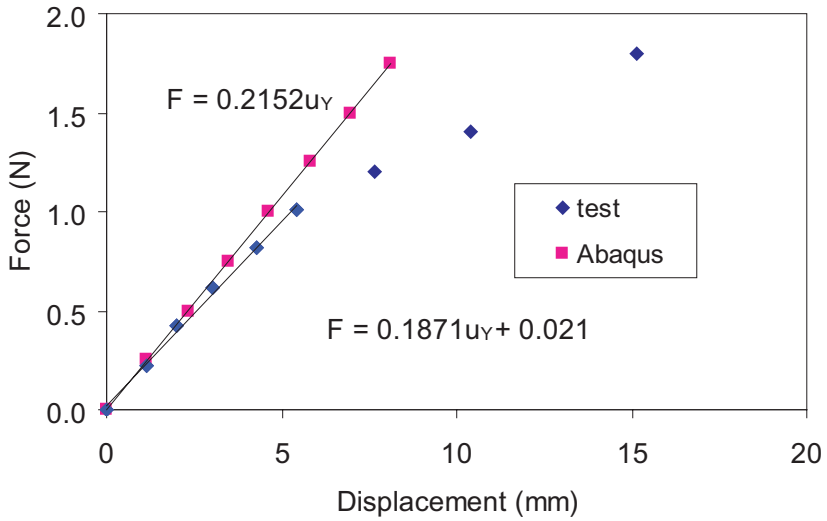

Figure 8.4: Comparison of out-of-plane displacements.

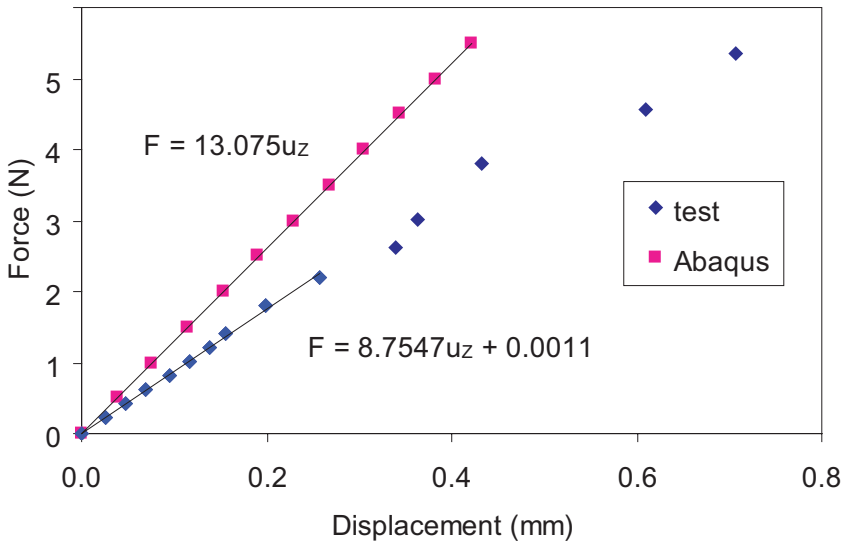

Figure 8.5: Comparison of transverse displacements.

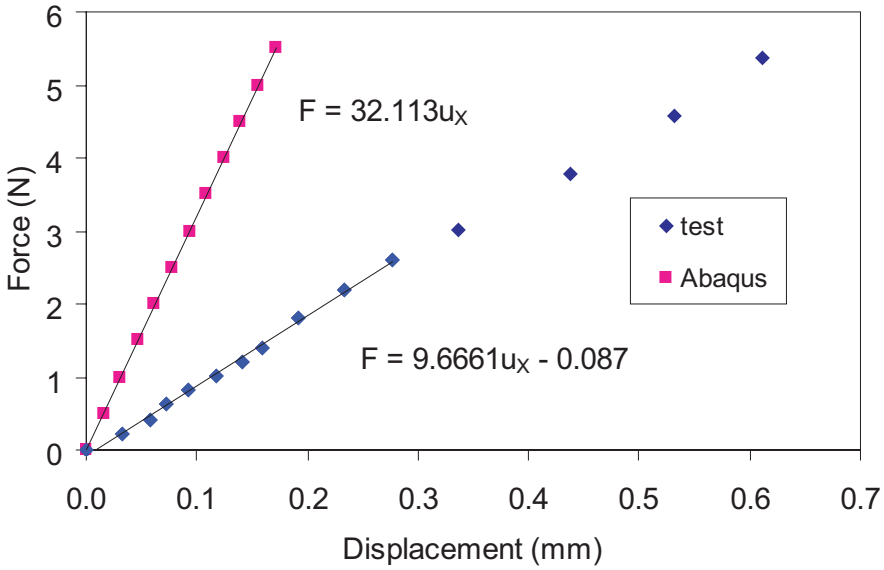

Figure 8.6: Comparison of of longitudinal displacements.

8.3 Measurement of Surface Accuracy Before Packaging

Photogrammetry, based on images from a digital camera and the software PhotoModeler Pro 4.0, developed by Eos Systems Inc., Canada, was used to measure the surface accuracy of the RF surface of the half-scale demonstrator.

The structure was attached to a tubular support structure, as shown in Figure 8.7. As in the previous section, a 2.5 kg single-point gravity offload was applied at the root of the back surface, and a 4 kg offload was applied at the tip of the RF and back surfaces.

PhotoModeler is a Windows program that extracts measurements and 3D models from photographs. There are eight steps to produce a model (PhotoModeler, 2000):

Step 1: Create a calibrated or approximate model of the camera.

Step 2: Plan the measurement project.

Step 3: Take photographs of the object.

Step 4: Import the photographs into PhotoModeler.

Step 5: Mark features on the photographs.

Step 6: Identify which points are the same.

Step 7: Process the data.

Step 8: Export the resulting 3D data to a CAD or graphics program.

In step 1, a description of the camera is needed; it can be either approximate or based on a calibration. The description includes the focal length, pixel size and number of pixels, and lens

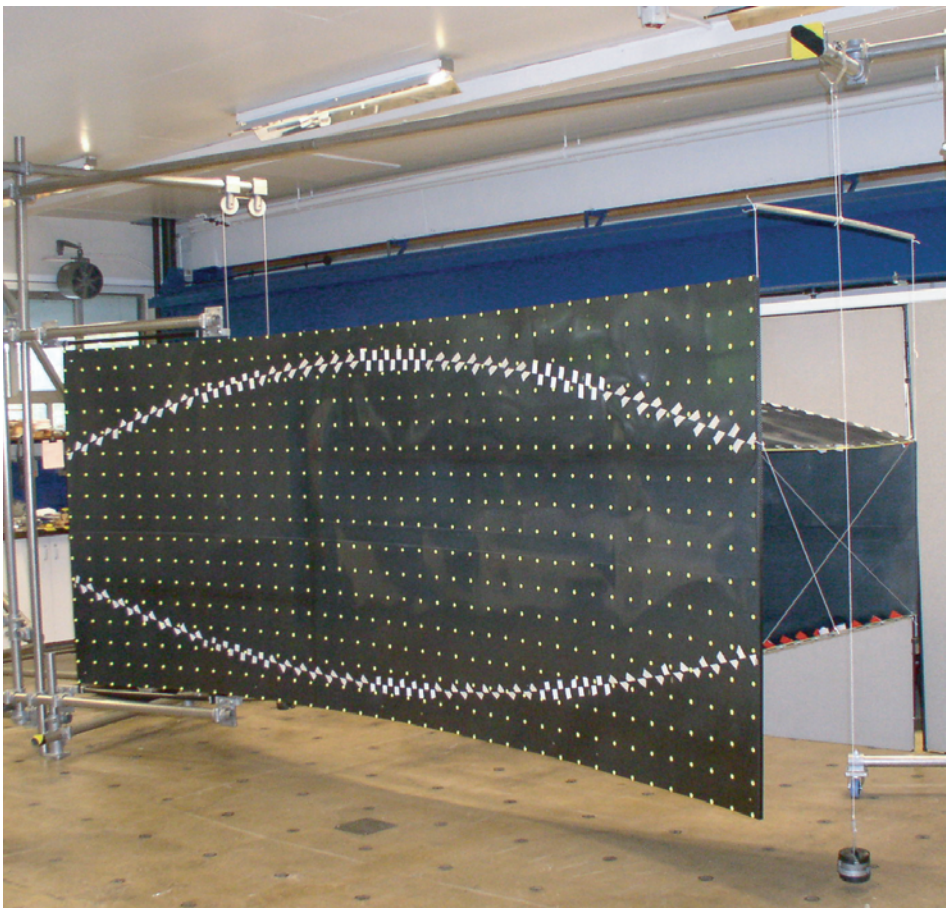

Figure 8.7: Demonstrator set up for measurement of surface accuracy.

distortion. Once the description of the camera is obtained, it can be saved to a file and re-used later on. An approximate camera model can be created by entering the description data of the camera, however its accuracy may be low.

A calibrated camera model can be created in Photomodeler by taking and analyzing photos of calibration patterns that are supplied with the software. An Olympus C4000ZOOM color digital camera with 2288 $\times$ 1712 pixels was used. This camera was calibrated within the program by projecting a calibration grid on a flat wall and taking the required calibration photos.

In step 2, planning the measurement includes deciding the target size and type, applying the targets on the object, deciding the camera positions, and the number of photos to be taken. The size of the target was based on the pixel resolution of the camera. At least 4 pixels are required to locate and mark the center of a circular dot target (this shape yields the highest precision) with the sub-pixel marker in PhotoModeler. For high precision measurements, targets that are 3 to 4 times larger are recommended. The color of the targets should provide sharp contrast with the surface on which they are located.

The target size was calculated from

$$\text{Dot target size } = \frac{4W_0}{W_I} \tag{8.1}$$

where W_0 is the width of the object and W_I is the number of pixels in the image. Using $W_0 = 4000$ mm and $W_I = 2288$ pixels, a minimum target size of $4 \times 4000/2288 = 7$ mm was obtained.

For better accuracy, yellow fluorescent self-adhesive targets with diameter of 13 mm were used. 680 targets were placed on the RF surface, at 100 mm spacing. At least two photos are required, and four or more photos are recommended for better accuracy and reliability. Therefore, six photos were planned and the camera locations were chosen such as to maximise the range of angles covered, to reduce the error in the calculation of the camera positions.

In step 3, all of the photos were taken, using the same camera. The camera was positioned in front of the RF surface at six locations: upper left, left, lower left, upper right, right, lower right. All target points were captured in all photos. In each location, several images were taken, before moving the camera to the next location. Of these images, only the best one was used.

Note that the zoom setting in the camera has to remain fixed, since any changes in the zoom setting would require a new camera calibration.

The distances between several target points were measured with a tape measure, for scaling purposes and to check the accuracy of the results.

In step 4, all photos taken were downloaded from the memory of the digital camera to a

personal computer. Then, the best photo taken at each of the six camera locations was selected and imported into PhotoModeler.

In step 5, the centers of all dot targets in the images were marked, one by one, using the sub-pixel target marking tool. Although PhotoModeler has an automatic target marking tool, to mark all targets within a selected region, it was not used because it is less accurate than the manually operated tool.

In step 6, PhotoModeler needs to know which of the marked points in two or more photos are actually the same. PhotoModeler has an automatic referencing tool that searches for unreferenced marked points and sets up this correspondence.

First, all border points on the surface were referenced manually, and the data was processed so that the camera position for each photo could be established. Next, all of the remaining unreferenced marked points were successfully referenced by use of the automatic referencing tool. The default value for the search distance parameter, i.e. the largest distance from the light ray from one marked point to the light ray from another marked point, worked fine. The results were audited to check that all the referencing had been made properly.

In step 7, PhotoModeler uses advanced mathematical techniques to process the data. There are two stages in the process: audit and adjustment. Auditing reviews the project, performs a number of calculations involving the camera station, marked points, and referenced points, and offers suggestions on how to improve the accuracy of the target points. Auditing was performed until there were no more suggestions.

The next stage is the adjustment. Several algorithms are used to determine the relative positions and angles of the camera, and of the referenced points, by minimizing the error in the three-dimensional coordinates of the target points and the camera positions and angles. There is also a self-calibration option, to further optimize the results by means of small adjustments of the camera parameters. The adjustment stage was performed by selecting all the options of orientation, 3D global optimization and self-calibration. Once the process had been completed, all of the cartesian coordinates of the target points were scaled —based on the direct length measurements supplied to Photomodeler— and transformed to a more convenient, user-defined set of cartesian coordinates.

In step 8, the results were examined for measurement precision using the RMS marking residuals and the tightness values provided by PhotoModeler.

- The *RMS residuals* are the root mean square error distances, measured in the camera image plane. Residuals of less than 1 pixel represent sub-pixel marking precision.

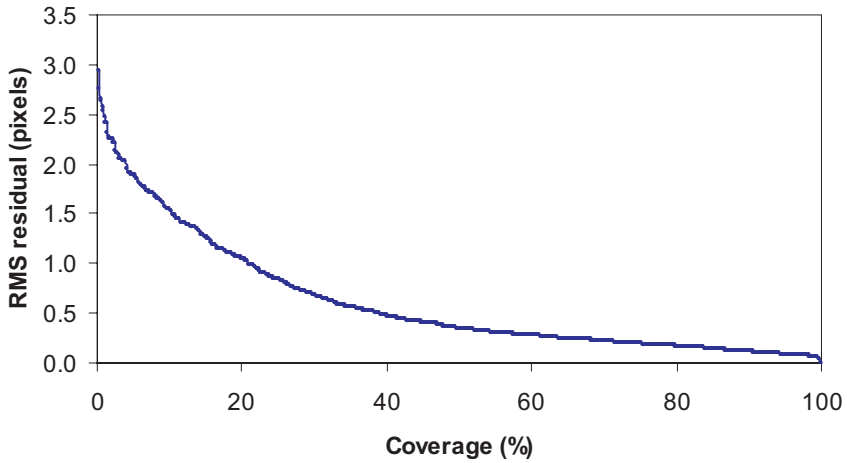

Figure 8.8: RMS marking residuals versus coverage.

- Tightness is the maximum of the smallest distances (as a percentage of the object size) between any two light rays that image the same point.

The marking residuals and the tightness of all target points were sorted in descending order, and plotted in terms of coverage of the total RF surface area, see Figures 8.8 and 8.9. 80% of the points had residuals under 1 pixel. The tightness values ranged from 0.001% to 0.069%; 90% of points had a tightness of less than 0.031% which corresponds to a precision of 1:3225.

The accuracy of some of the measurements was assessed by direct comparison with measurements with a tape measure. The difference between the largest distance on the RF surface (from the lower corner at the root to the upper corner at the tip) was found to be only 0.024%, which is equivalent to 1 part in 4152 (1:4152).

An overall view of all target points, along with the six camera stations is given in Figure 8.10. Note that there are a few holes since some targets had been placed on top of the connection tapes, and so were difficult to mark.

The three-dimensional, cartesian coordinates of all target points were transferred to a spreadsheet program to estimate the surface accuracy. The surface accuracy of a reflector is usually measured by the root-mean-square (RMS) error of half the difference between the path length of microwave rays reflecting from the distorted surface to the focus, and the corresponding path lengths for a perfect parabolic surface (Levy 1996). The performance of the reflector is not affected by distortions associated with a rigid body motion of the whole reflector, provided that

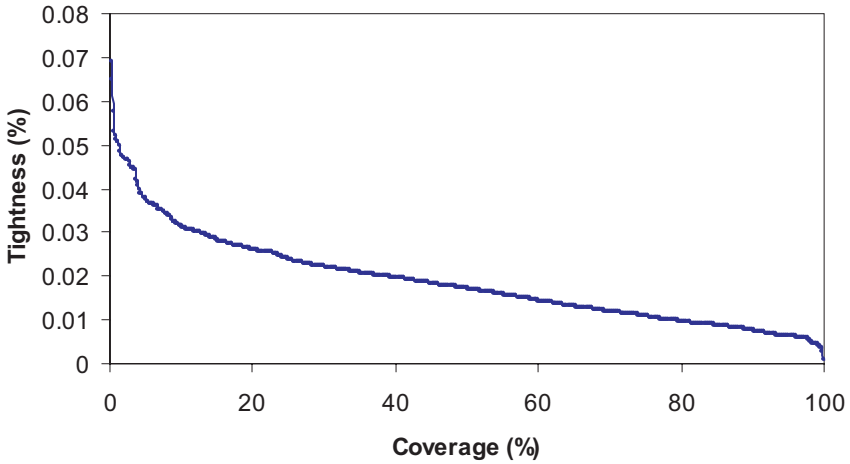

Figure 8.9: Tightness versus coverage.

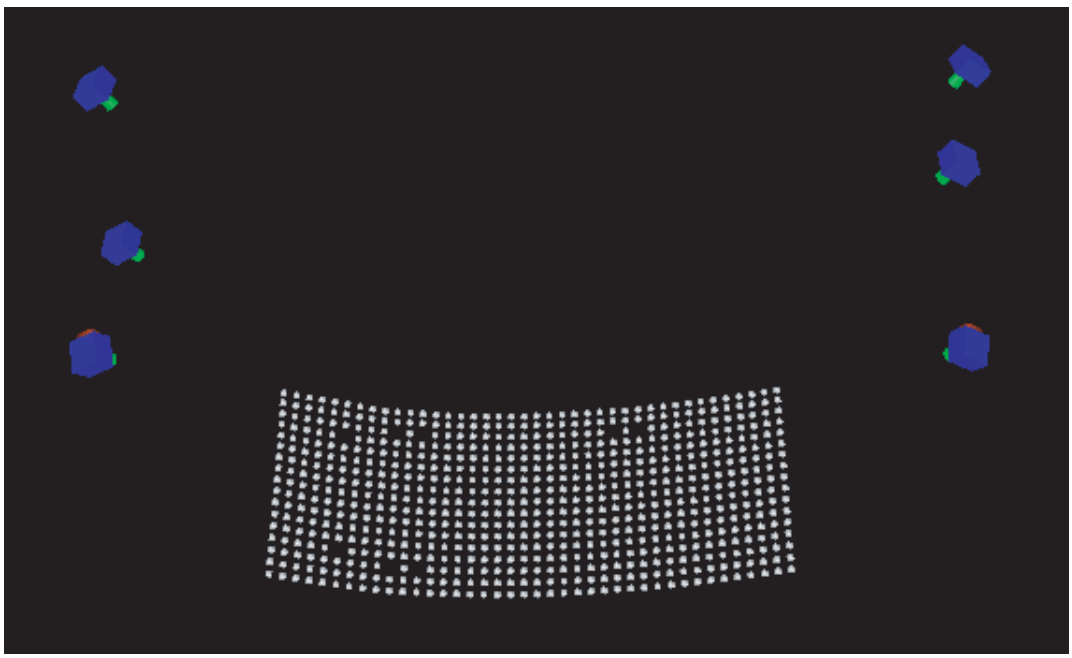

Figure 8.10: Positions of target points and camera stations.

the antenna feed is displaced accordingly. Therefore, the RMS error is calculated for the best fit parabola, thus yielding the smallest possible RMS error. The RMS error is related to the RMS error in the axial direction, δ_{ex}.

In the present case, since we are dealing with a parabolic cylinder, the problem is essentially in two dimensions and hence Z-coordinates can be disregarded during the calculation of the best fit parabola. The equation of the best fit parabola is

$$x = \frac{y^2}{4a} \tag{8.2}$$

where a is the focal distance. Equation 8.2 is converted to the coordinate system in which the measurements were taken by the translation

$$x = X - X_0$$
$$y = Y - Y_0$$

and, substituting into Equation 8.2,

$$X = \frac{1}{4a}Y^2 - \frac{Y_0}{2a}Y + \left(X_0 + \frac{Y_0^2}{4a}\right) \tag{8.3}$$

Once the best fit parabola has been obtained in the measurement coordinate system, the focal length can be worked out from the coefficient of the second order term in Equation 8.3; and Equation 8.2 can be easily obtained, if needed.

For n target points that are equally spaced on the surface, the RMS error in the axial direction X, with respect to the best fit parabola, is calculated from (Pellegrino, 2001)

$$\delta_{ex} = \sqrt{\frac{s\sum(\hat{X}_i - X_i)^2}{S}} = \sqrt{\frac{\sum(\hat{X}_i - X_i)^2}{n}} \tag{8.4}$$

where S is the total surface area of the reflector, $s = S/n$ is the surface area associated with each target point, and $\hat{X}_i$ is the axial coordinate of a general target point.

The best fit parabola was obtained using the coordinates of the targets, from PhotoModeler, and is shown in Figure 8.11. Its focal length is 1550 mm, which is very close to the focal length of the design parabola, 1544.5 mm. The RMS error of the targets points from the best fit parabola is 3.8 mm. The RMS error from the design parabola, calculated for comparison, is 4 mm.

It was noticed that the points near the upper edge of surface, between the two stiffeners that form the longer edges of the interface frame, yielded higher errors. It was thus realised that the interface frame and the RF surface had not been aligned correctly during assembly. When these points, which correspond to 6% of the surface area, were excluded from the calculations, the RMS error reduces to 3.3 mm, see Table 8.2.

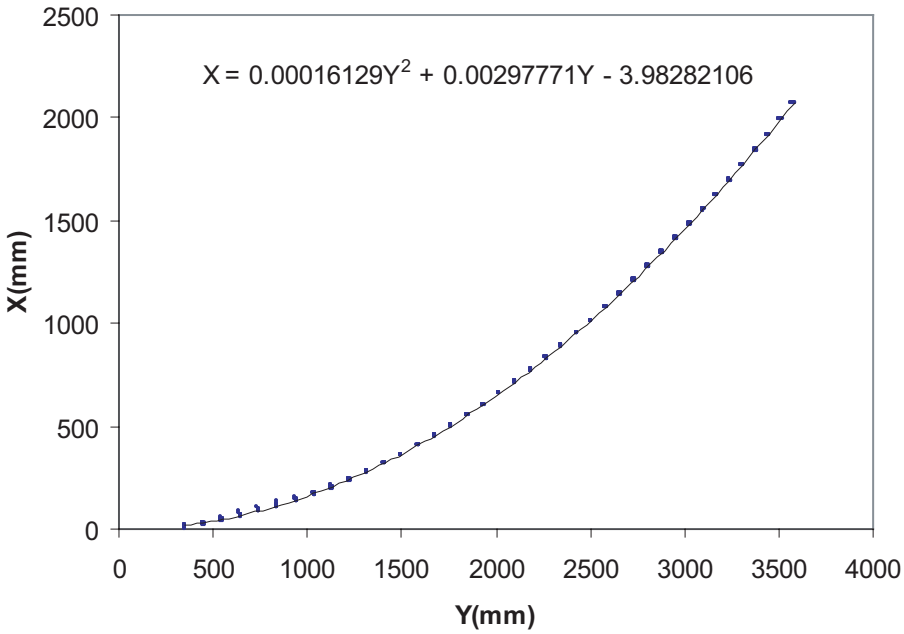

Figure 8.11: Best fit parabola.

Coverage (%)	RMS (mm)	Focal length* (mm)
100	3.8	1550.0
94	3.3	
73	3.4	
*: Design focal length: 1544.5 mm		

Table 8.2: RMS error versus coverage.

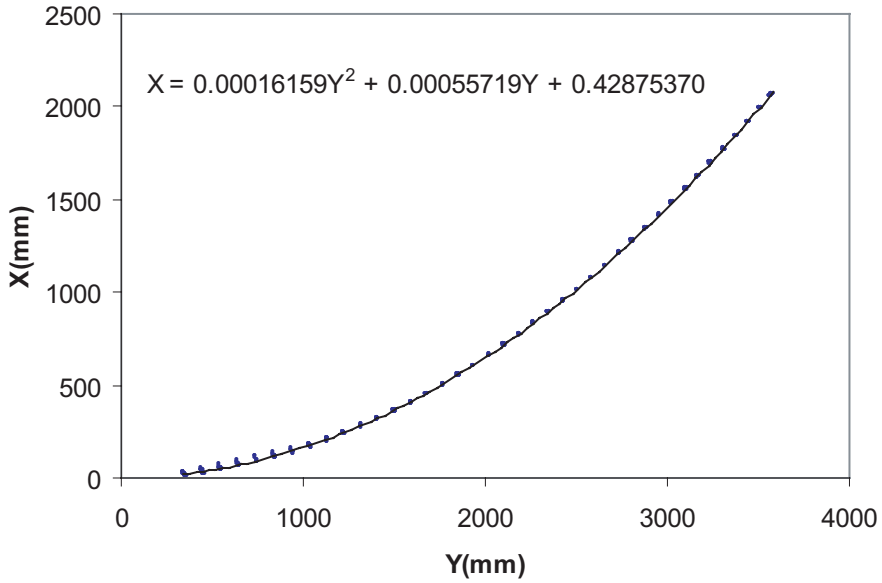

Figure 8.12: Best fit parabola after deployment.

Coverage (%)	RMS (mm)	Focal length* (mm)
100	5.1	1547.1
96	4.0	
72	3.3	
*: Design focal length: 1544.5 mm		

Table 8.3: RMS error versus coverage after deployment.

8.4 Surface Accuracy After Deployment

The surface accuracy measurements were repeated after packaging and deployment of the structure. The same steps in Photomodeler were followed again. 84% of the points had residuals under 1 pixel. The tightness values ranged from 0.002% to 0.071%; 90% of the data points had a tightness of less than 0.033%, which corresponds to a precision of 1:3030.

The best fit parabola obtained from the cartesian coordinates determined by PhotoModeler, is shown in Figure 8.12; its focal length is 1547.1 mm. The RMS error from the best fit parabola is 5.1 mm. Disregarding the same points near the interface frame already discussed in Section 8.3 reduces the error to 4.0 mm; and further disregarding all points within the interface frame reduces the RMS error to 3.3 mm, see Table 8.3.

Chapter 9

Packaging and Deployment of Demonstrator

9.1 Packaging

Packaging consists in flattening the structure and then introducing three transverse folds that allow Z-folding.

9.1.1 Flattening

Flattening the structure requires bending the sidewalls through 180°. The process through which this happens needs to be carefully controlled, to prevent damaging the structure. The main difficulty —as it was discovered through a series of unsuccessful attempts— is that the structure is very stiff in its deployed configuration, but suddenly becomes very "floppy" soon after folding begins. This behaviour resulted in a series of almost catastrophic instabilities during the early folding attempts. Next, we describe a successful folding process.

First, the demonstrator was placed on the plywood mold, with the RF surface facing down and the back surface facing up. The foam plugs were placed inside the structure to prevent its sudden collapse. Easy-release plastic cable ties, 200 mm long and 4.8 mm wide, were passed through each pair of cup and cone, and were tied to take up any slack. Next, flattening of the structure was initiated by pulling the sidewalls outwards with a pair of 1.5 m long wooden poles (with a diameter of 25 mm) placed inside the structure, between two sets of cup and cone supports. Each pole was loaded, through a cable and pulley system, with a counter weight of up to 2.8 kg, while the foam plugs were slowly pulled out to allow the back surface to some down.

Note that the back surface and the RF surface need to move symmetrically, to keep the

longitudinal fold lines in the sidewalls straight and horizontal. To ensure this, plywood sheets were gradually pushed between the mold and the structure, and slowly raised at the far ends, to move the RF surface upwards.

The structure has a tendency to "roll-over", i.e. to slew sideways during folding. This was avoided by cross-bracing both ends with cable ties attached to adjustable plastic ties, which were held taut at all times. Also, the upper edge of each end of the back surface was held by a person to prevent it from slewing.

When the structure is about half-way down, pulling on the sidewalls is no longer an efficient and safe way of bringing it down (applying excessive side forces can lead to the deformation of the structure suddenly localising in a narrow region and leading to localised damage). At this point folding is best driven by putting a few expanded polystyrene pads on top of the back surface and applying some 0.5 kg weights on top of these strips.

At a suitable point the foam plugs were taken out and replaced with several 50 mm-high expanded polystyrene pads.

When the structure was about 100 mm high, i.e. about double its expected height in the completely flattened configuration, only one layer of these pads was left in, carefully placed in the regions where no transverse fold will be forming. Also, the wooden poles were taken out.

The initial plan, when the demonstrator had been designed, was to hold it folded by means of four Kevlar cords passing through consecutive sets of cup and cone supports. However, during an early attempt at folding the demonstrator it was observed that the CFRP sheets used for the sidewalls tend to bulge out between these supports and, although their radius of curvature becomes larger away from the support —and therefore the maximum strain in the material should become smaller— the material fails due to excessive shear.

A series of simple experiments on flat sheets that were bent through 180° and then held between two sets of cup and cone supports at ends, etc. were carried out. It was found that the sheets are too stiff to be held only at the corners and hence, short of reducing the thickness of the material in the bend region, the only options were (i) to use a pair of stiff bars to prevent the sheet from bulging out, or (ii) to increase the number of points at which the sheet is held at the correct distance. Initially the first option was adopted, but this had the effect of increasing the packaged dimensions of the demonstrator due to the size of the bars. Later on it was decided to drill new holes with a diameter of 3 mm and at 150 mm spacing, along the hinge line of the sidewalls, and to hold the flattened structure with additional plastic ties passing trough these holes.

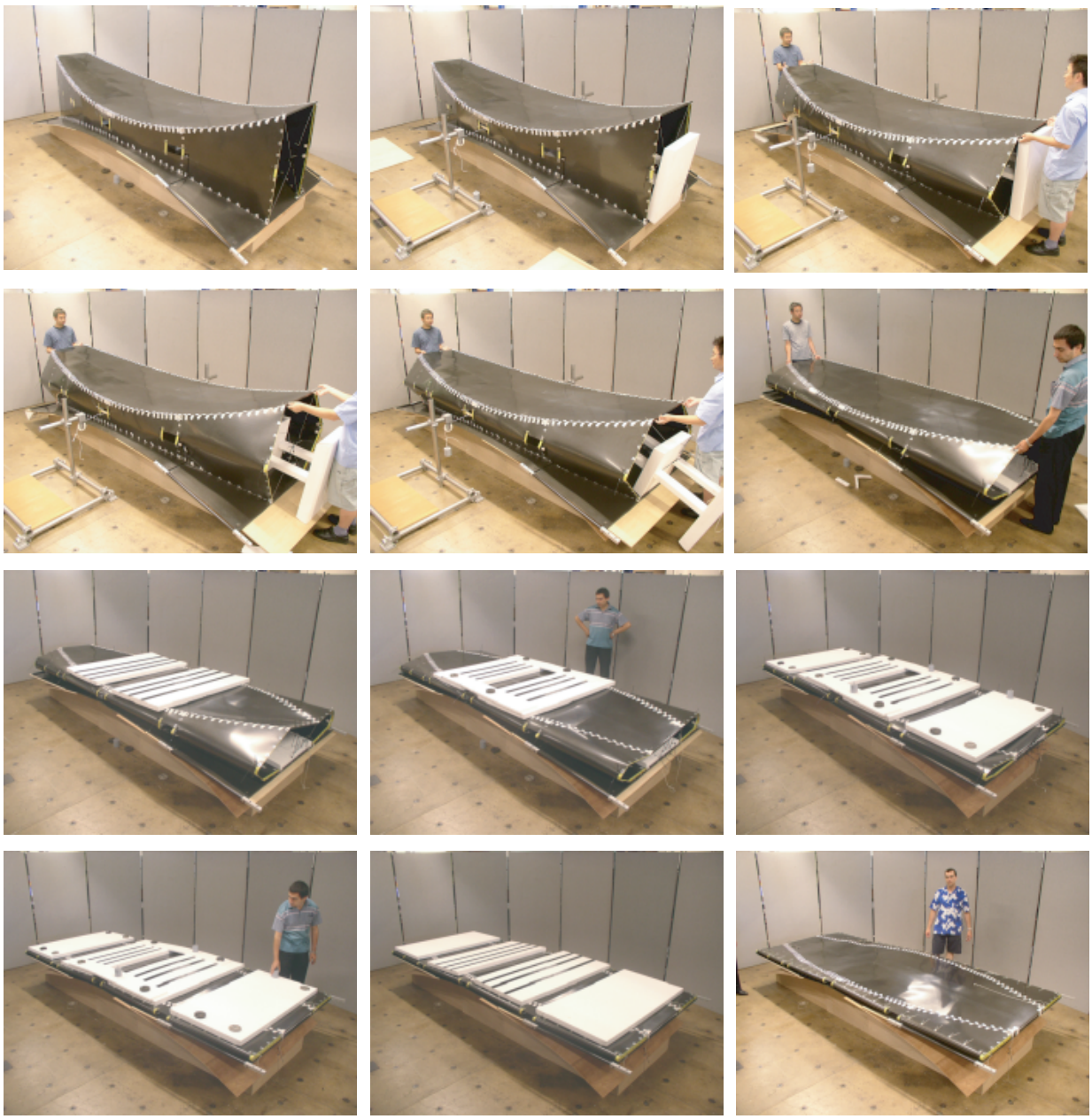

Figure 9.1: Flattening sequence, from top left to bottom right.

Once the demonstrator was flattened, 100 mm long by 2.5 mm wide plastic ties were passed through each pair of cup and cone supports, as well as through the new holes along the hinge lines. 1 mm thick, 20 mm by 22 mm flat, rectangular aluminium washers were used to distribute the loading of the plastic ties onto a larger area, and the structure was tied. Finally, all the weights and polystyrene pads were removed.

The flattening sequence is shown in Figure 9.1.

9.1.2 Z-Folding

Longitudinal folding of the demonstrator is much simpler than flattening it.

Z-folding is carried out in three steps: first, the tip end is folded with the RF surface lying on the outside; next, the root end is folded with the RF surface on the outside; finally, the central fold is introduced, so that the RF surface is inside the fold.

Expanded polystyrene strips, spanning transversely between cup and cone supports, were placed (through the windows) near the longitudinal fold regions. The first fold was created by two people lifting up the tip of the structure and thus rotating it along the hinge line. Once the first fold had been completed, overlapping sets of cup and cone supports were aligned and tied together to secure the folded part. The second fold was created in a similar way, by lifting the end of the interface frame. The third fold was created by lifting the central part of the semi-packaged structure with a 2 m long steel tube with a diameter of 50 mm. Once the third fold had been completed the whole structure was rotated 90° so that the root end was down and the tip end was up. The packaged structure fits in an envelope that is 1700 mm long, 950 mm wide, and 260 mm high.

Figure 9.2 shows the complete folding sequence. The packaged demonstrator can be seen in Figure 9.3.

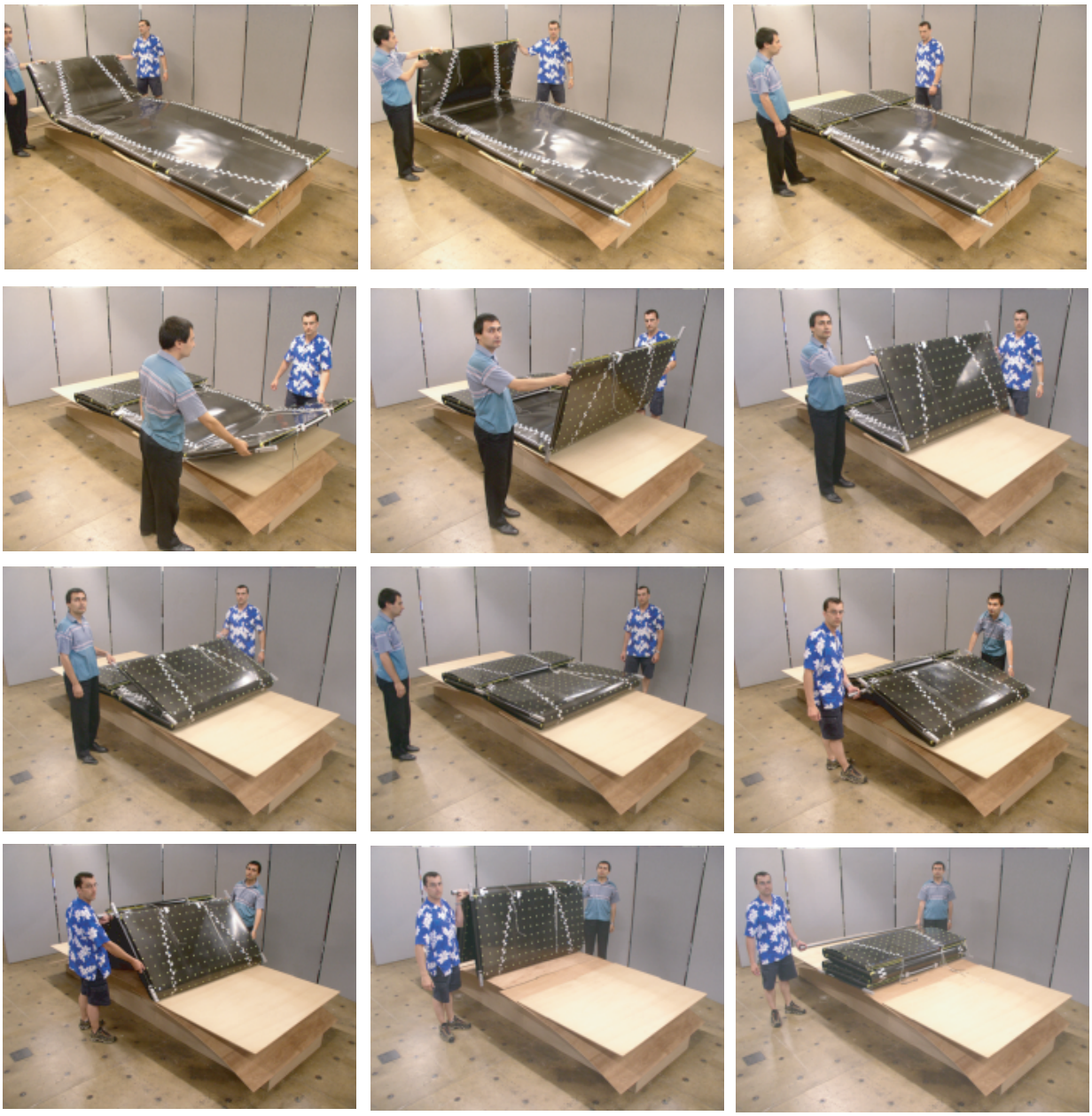

Figure 9.2: Z-folding sequence, from top left to bottom right.

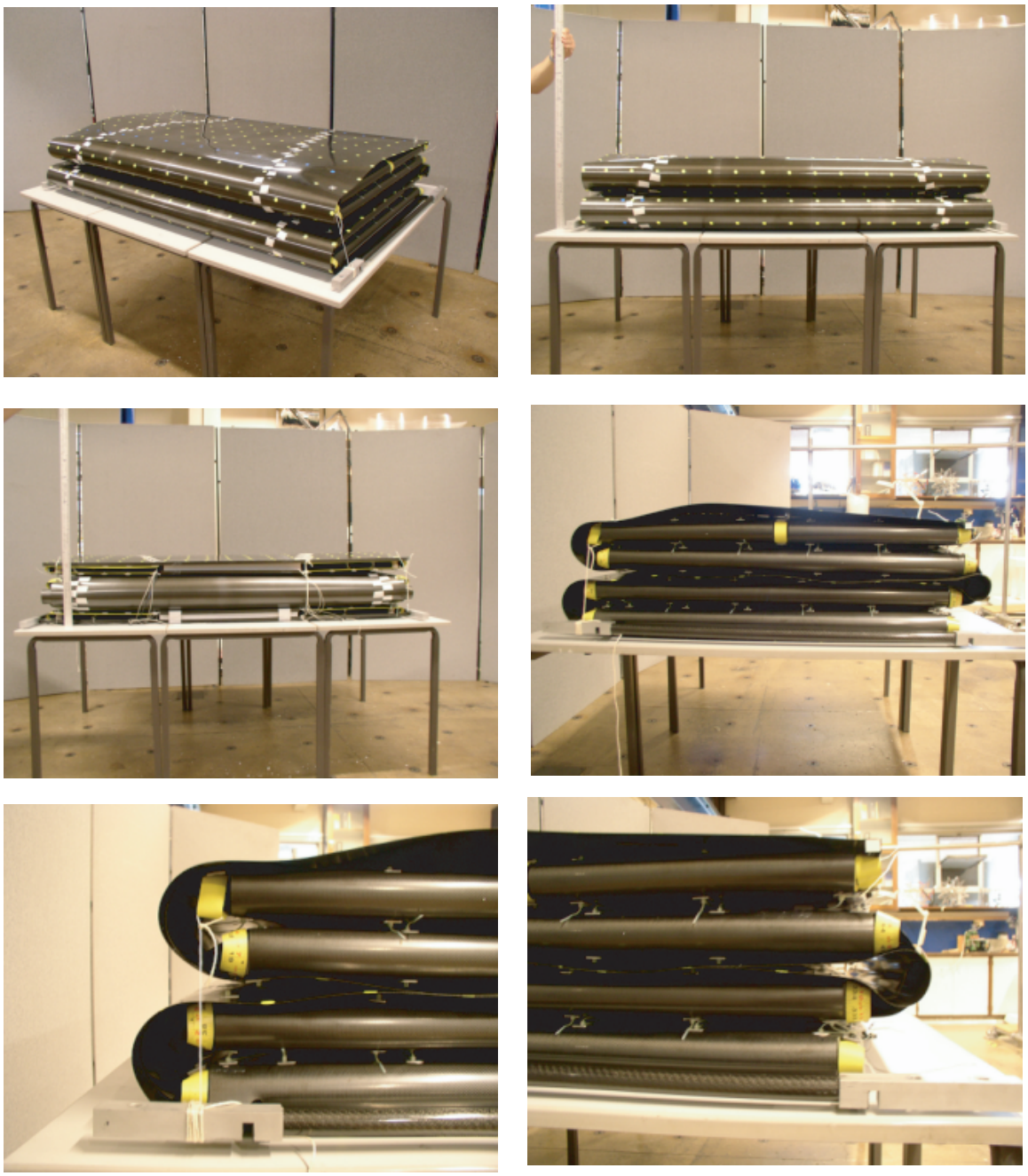

Figure 9.3: Views of packaged demonstrator.

9.2 Deployment

The packaged structure was attached to a tubular steel support structure, through the corners of the rectangular interface frame. The structure was then deployed under quasi-static conditions, in two stages, with gravity supports provided along the three transverse fold lines.

Figure 9.4 shows stage one of the deployment process, in which the structure deploys as an accordion and ends up in a flat configuration. Friction in the gravity offload system prevented the structure from deploying dynamically.

Once stage one of the deployment process had been completed, all polystyrene sheets inside the structure were removed, to avoid interference during stage two of the deployment process. Figure 9.5 shows stage two, in which the sidewalls unfold, thus separating the RF surface from the back surface.

Since the plastic ties holding the structure flat could not be released in stages, aluminium tubes were placed on either side of the fold lines in the sidewalls. These tubes were held at a fixed distance by means of adjustable cable ties on either end, see Figure 9.6. Then, the cables ties were cut, and deployment of the structure was controlled by releasing the adjustable cable ties. The structure was also cross-braced at both ends to prevent it from slewing, see Figure 9.6.

At the end of the deployment process it was found that a few tape connections, near the transverse folds, had broken due to excessive creep of the acrylic adhesive. The broken tapes were replaced to prevent further damage. Then, the gravity compensation system used for deployment were replaced with a 2.5 kg single-point suspension at the root of the back surface, and a pair of support points at the tip of the RF and back surfaces, linked to a 4 kg offload, as described in Section 8.1.

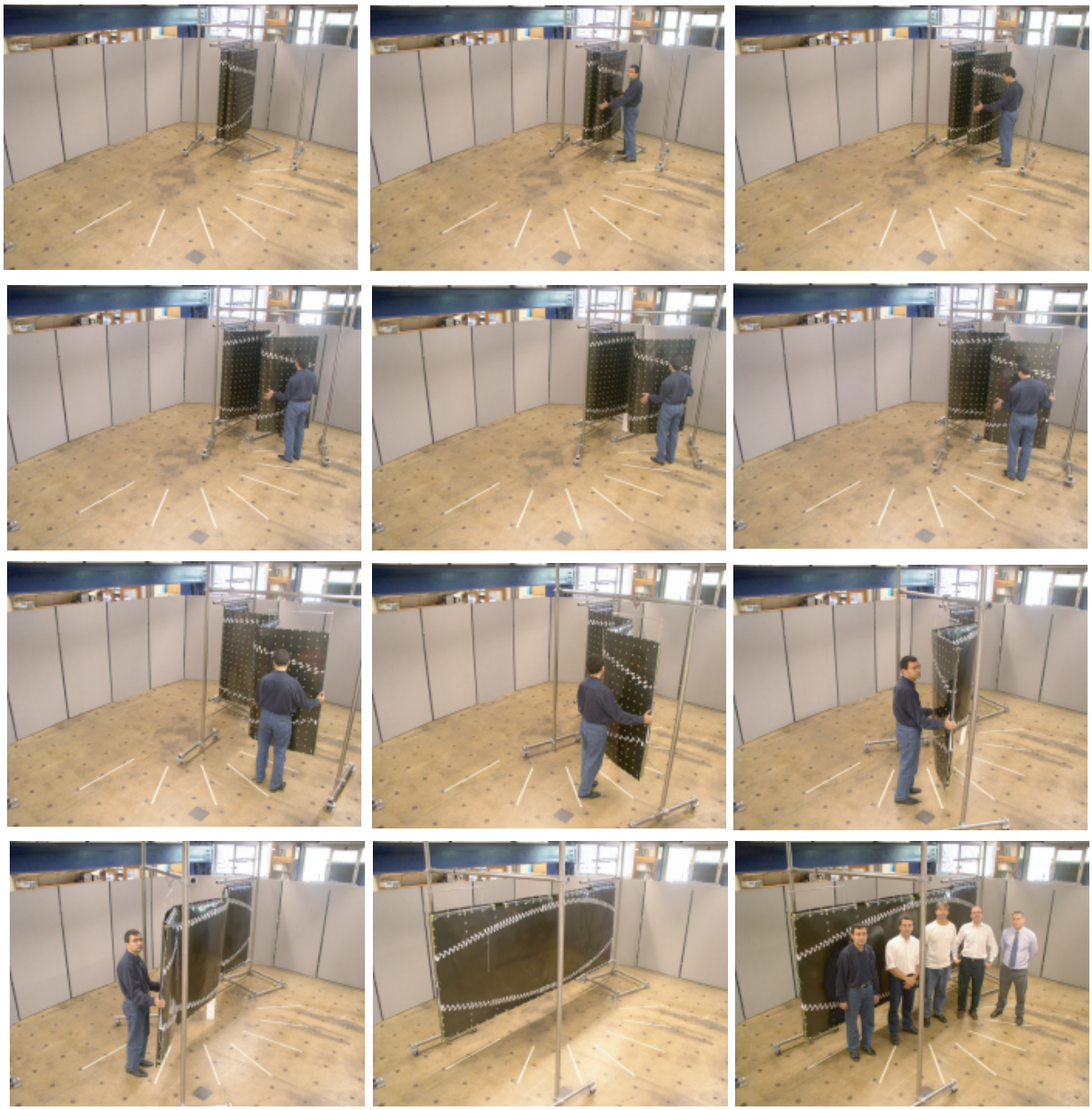

Figure 9.4: Stage one of deployment process, from top left to bottom right.

Figure 9.5: Stage two of deployment process, from top left to bottom right.

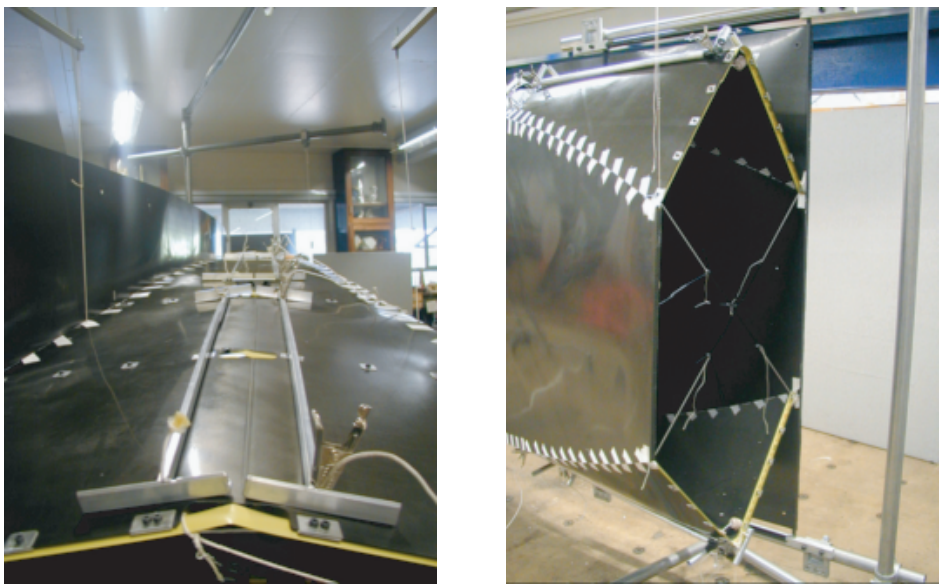

Figure 9.6: Aluminum bars on the left, cross bracing of the ends on the right.

Chapter 10

Conclusions, Lessons Learnt, and Further Work

10.1 Conclusions

An innovative concept for large deployable reflectors for synthetic aperture radar applications has been presented. This concept can deliver a parabolic profile of high accuracy with a structure of very low mass, high stiffness, and potentially very low cost.

For the particular application that was of interest in the present study, which at full scale requires a reflective surface with an aperture of 6.5×3.2 m^2 (the actual arc-length dimensions of the surface are 7.9×3.2 m^2), EADS Astrium had estimated the mass of a traditional reflector structure made from lightweight, curved panels with self-locking hinges to be around 79 kg. The corresponding figure for a reflector based on the concept proposed in this report would be 33 kg, see Section 3.4.3. Hence, the new concept promises a mass saving of the order of two-and-half times.

The new concept is based on four cylindrical surfaces, formed from thin-walled CFRP sheets hinged along their edges. This is just one particular approach, and it should be noted that there are many other ways of implementing this type of structural concept. Patent applications have been filed on this invention (Watt, Pellegrino and Howard, 2003).

The key to forming a cylindrical surface with the required shape is in the cutting pattern for the edges of the sheets. It has been shown in Section 2.2 how to compute the cutting pattern given the focal length, aperture distance, and offset distance of the reflector.

A baseline configuration for the full size reflector has been established, in Chapter 3, by carrying out a series of sensitivity studies. These studies have indicated that a structure with

open ends (each braced by a pair of cables) and with untapered sidewalls would be optimal in terms of a multi-objective performance criterion that encompasses total mass, maximum deflection, fundamental natural frequency of vibration, margin against material failure, and margin against local and global buckling.

The following phase of the study has focussed on a half-scale demonstrator, to be tested in the laboratory under gravity conditions. A preliminary design has been formulated by scaling the dimensions —but not the thickness— of the full-scale structure. This design has been gradually refined to obtain a detailed design of the structure, which includes cut-outs in the sidewalls of the structure —required to fold it— and stiffeners –to prevent local buckling.

A quarter-scale model, made of thermoplastic, has been designed and constructed. This model has been used to investigate two possible folding methods, Z-folding and coiling, and also to verify the performance of various measures for avoiding damage of the structure when it is folded, and to latch it when it is deployed. Many valuable lessons have been learnt from this model. The experience obtained from the quarter-scale model has substantially shaped the subsequent efforts to design, construct and test, a half-scale demonstrator.

The current availability of thin CFRP prepregs, and hence the range of laminates that can be procured at short notice, are rather limited. Hence, it is useful to have a way of predicting the minimum bend radius of a thin laminate, rather than having to rely solely on hard to obtain test data. It has been shown in Section 6.1 that reasonably accurate predictions of the minimum bend radius of a lamina made from woven prepregs can obtained by assuming that failure occurs when the strain at the centre of a yarn reaches an ultimate value. Hence, the minimum bend radius can be obtained from Equation 6.8 used in conjunction with the maximum strain criterion and standard suppliers data on the ultimate strains in the fibres.

The performance of the connections, made with woven-glass tape, has been investigated experimentally. On this basis, it was decided to arrange the connections in such a way as to alternate regions of shear compliance and shear resistance. A deeper understanding of the way in which shear loading is carried within the connections would have been very desirable, though.

Based on the results of these studies the detailed design of a half-scale demonstrator has been carried out. Full details of the component parts of this structure have been provided in Chapter 7, along with a novel assembly technique that has been developed.

The mass, stiffness and surface accuracy of this demonstrator have been measured. The accuracy measurements were carried out before packaging the structure for the first time and also after deploying it. The folding and deployment process were successfully demonstrated,

although manual intervention was required half-way through the deployment process— to remove the plastic ties holding the structure flat.

The half scale model has demonstrated the following:

- Surface accuracy: 3.8 mm RMS achieved immediately after construction, improving to 3.4 mm by ignoring the least accurate 25% of the surface area; 5.1 mm after folding and deployment, improving to 3.3 mm after ignoring 25% of the area.
- Typical mass achievable: 1.3 kg/m^2 of antenna.
- Fundamental frequency of 1.4 Hz. A higher value, 6.8 Hz, had been estimated at the end of the design stage, but using simplified (and actually incorrect) boundary conditions. A more refined model with the correct boundary conditions gave a value of 1.5 Hz, see Section 8.2.
- Packaging density: 1/20th of deployed volume.
- Material and process viability.
- Assembly and handling process.
- Demonstration of deployment process.

10.2 Lessons Learnt: Construction and Handling

The construction sequence worked according to plan, but it was later realised that the interface frame should have been attached to the curved RF surface. By attaching it to the RF surface while this was surface was flat, errors were introduced in the surface accuracy of the deployed antenna. This explains why comparatively large errors were observed in this area.

The glass-cloth tape with acrylic adhesive, used for all of the structural connections, has been found to creep too much. This leads to loss of accuracy and damage of the connections. A structural adhesive, such as DP490 should be used instead, and the possibility of using a Kevlar cloth, instead of glass tape, should be investigated.

The structure was found difficult to handle during folding. One problem is that the angle-section stiffeners around the end openings are insufficiently stiff and robust. The use of square section stiffeners had been considered during the design phase, but was abandoned to reduce cost, however it is recommended that they should be used in future. Another modification that would make it easier to handle the structure during folding is the use of stiffer corner hinges

at the corners of these end frames, instead of cloth connections. A key advantage of using less compliant hinges would be to improve kinematic control during folding and deployment.

10.3 Further Work

The main area where further work is required is the design of a constraint system for the folded structure which can be automatically released during deployment. The issue of the deployment behaviour of the structure should be approached in a fundamental way; it is suggested that deployment control studies should be carried out initially on a simplified version of a hollow solid that resembles the reflector structure, such as a square section tube or a tapered, circular tube. The anisotropy, both in stiffness and strength, of thin CFRP sheets also needs to be considered in this study. Hence it is recommended that these deployment studies be conducted at a relatively large scale, say one quarter of the full size of the flight model.

The sidewalls of the half-scale demonstrator presented in this report have turned out to be far too stiff, and hence they had to be held folded with closely spaced ties (or sandwiched between stiff Aluminium tubes). Such system would be far too complex to release in orbit. It seems likely that much wider windows could be used, but their effect on the overall stiffness and accuracy of the structure needs to be evaluated. With wider windows, the folded sidewalls would need to be supported only at a few points; also it may be possible to reduce the thickness of the sheets along the transverse fold lines. Finally, stiffeners on either side of a fold line, if needed, could be incorporated in the design of the structure. Their function would be similar to the Aluminium tubes used during the intermediate stages of folding, but they should become an integral part of the structure.

Another important area that needs to be investigated, but where the issues appear more a matter of detailed design than fundamental advances, is to replace all bolted connections with glued connections. As well as reducing the mass of the structure (recall that in the half-scale demonstrator almost 5 kg of the total mass of 11 kg is related to connections), this would reduce the clearance requirements in the folded state. Clearances for bolts, washers and tape springs were quite a challenge in the present design.

The mismatch between the curvature of unstiffened regions of the sidewall and the tape spring during folding (but not in the fully folded state) needs to be addressed. Also, the design of the spacers may need to be modified to reduce stress concentration at the edges. Another possibility would be to increase the thickness of the laminate near the spacers. More generally, the use of special lay-ups that aim to “stabilise” the folds should be investigated. It has been

observed that a bend parallel to the outer fibre directions in the 0/45/0 laminate (used for the half-scale demonstrator) is "unstable", i.e. under a constant force across the fold the direction of bending will tend to change because the laminate is more compliant for bending at 45° to the fibres than along the fibres.

Finally, tapered structural designs should be revisited. They did not appear to show significant advantages when they were considered in Chapter 3, but the open-ended configuration had yet to be arrived at. It is possible that the preliminary optimisation carried out in this report is not fully not applicable to our finally selected configuration.

References

ABAQUS (2000), ABAQUS/Standard User's Manual, Volume 1.

Canty P. (2002), Requirement Specification for the Deployable SAR, EADS-Astrium.

Gerngross T. (2003), Folding of Thin-Walled Composite Structures. Technical University of Munich, Munich TUM-MW 65/0331-SA.

Gibson R.F. (1994), Principles of Composite Material Mechanics, McGraw-Hill Book Co., Singapore.

PhotoModeler (2000), PhotoModeler Pro 4.0, User Manual, Eos Systems Inc, Canada.

Howard P. (2001), Technical Note: Satellite Definition File for Land Hazards Mission (WP 4200A), 3991-04660-RPZ, EADS-Astrium.

Levy R. (1996), Structural Engineering of Microwave Antennas, The Institute of Electrical and Electronics Engineers, New York.

Niu M.C. (1990), Airframe Structural Design, Conmilit Press Ltd, Hong Kong.

Peery D.J. and Azar J.J. (1982), Aircraft Structures, McGraw-Hill, Inc., USA.

Pellegrino S. (2001), Collapsible Rib-Tensioned Surface (CRTS) Technology Development Final Report, CUED/D-STRUCT/TR195, Department of Engineering, University of Cambridge.

Pellegrino, S., Green, C., Guest, S. D., and Watt, A. M. (2000). SAR Advanced Deployable Structure, CUED/D-STRUCT/TR191, Department of Engineering, University of Cambridge, Cambridge.

Pellegrino S., Kebadze E., Lefort T., and Watt A.M. (2002), Low-Cost Hinge for Deployable Structures, CUED/D-STRUCT/TR202, Department of Engineering, University of Cambridge.

Watt A.M., Pellegrino S., and Howard, P. (2003), Improvements relating to a deployable support structure, Patent Applications: UK-GB0316734.3, European-EP03254474.4.

Yee J.C.H., and Pellegrino S. (2003), Folding of composite structures, Submitted to Composites/A.